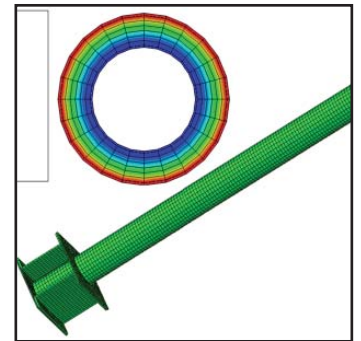
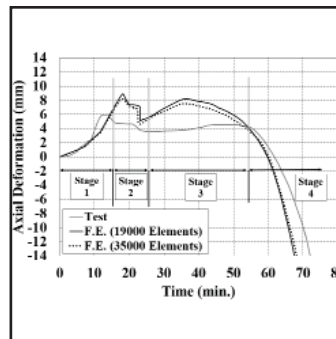
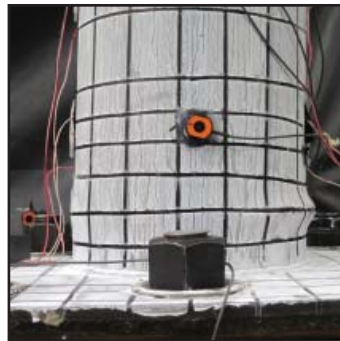


Post-Earthquake Fire Resistance of Ductile Concrete-Filled Double-Skin Tube Columns

by
Reza Imani, Gilberto Mosqueda and Michel Bruneau



Technical Report MCEER-14-0008

December 1, 2014

NOTICE

This report was prepared by the University at Buffalo, State University of New York, as a result of research sponsored by MCEER. Neither MCEER, associates of MCEER, its sponsors, the University at Buffalo, State University of New York, nor any person acting on their behalf:

- a. makes any warranty, express or implied, with respect to the use of any information, apparatus, method, or process disclosed in this report or that such use may not infringe upon privately owned rights; or
- b. assumes any liabilities of whatsoever kind with respect to the use of, or the damage resulting from the use of, any information, apparatus, method, or process disclosed in this report.

Any opinions, findings, and conclusions or recommendations expressed in this publication are those of the author(s) and do not necessarily reflect the views of MCEER, or other sponsors.

Post-Earthquake Fire Resistance of Ductile Concrete-Filled Double-Skin Tube Columns

by

Reza Imani,¹ Gilberto Mosqueda² and Michel Bruneau³

Publication Date: December 1, 2014

Submittal Date: August 21, 2014

Technical Report MCEER-14-0008

MCEER Thrust Area 2, Sustainable and Resilient Buildings

- 1 Senior Engineer, Thornton Tomasetti, San Francisco, California and former Ph.D. Candidate, Department of Civil, Structural and Environmental Engineering, University at Buffalo, State University of New York
- 2 Associate Professor, Department of Structural Engineering, University of California at San Diego
- 3 Professor, Department of Civil, Structural and Environmental Engineering, University at Buffalo, State University of New York

MCEER

University at Buffalo, State University of New York

212 Ketter Hall, Buffalo, NY 14260

E-mail: mceer@buffalo.edu; WWW Site: <http://mceer.buffalo.edu>

PREFACE

MCEER is a national center of excellence dedicated to the discovery and development of new knowledge, tools and technologies that equip communities to become more disaster resilient in the face of earthquakes and other extreme events. MCEER accomplishes this through a system of multidisciplinary, multi-hazard research, education and outreach initiatives.

Headquartered at the University at Buffalo, State University of New York, MCEER was originally established by the National Science Foundation (NSF) in 1986, as the first National Center for Earthquake Engineering Research (NCEER). In 1998, it became known as the Multidisciplinary Center for Earthquake Engineering Research (MCEER), from which the current name, MCEER, evolved.

Comprising a consortium of researchers and industry partners from numerous disciplines and institutions throughout the United States, MCEER's mission has expanded from its original focus on earthquake engineering to one which addresses the technical and socioeconomic impacts of a variety of hazards, both natural and man-made, on critical infrastructure, facilities, and society.

MCEER investigators derive support from the State of New York, National Science Foundation, Federal Highway Administration, National Institute of Standards and Technology, Department of Homeland Security/Federal Emergency Management Agency, other state governments, academic institutions, foreign governments and private industry.

This report presents the experimental, numerical and analytical studies conducted to examine the behavior of concrete-filled double-skin tube (CFDST) columns exposed to fire after being subjected to simulated seismic loads. The experiments were conducted in two separate phases, consisting of the quasi-static cyclic tests followed by fire tests. Overall, the results showed marginal differences in the fire resistance of the three specimens, providing evidence for the resilient performance of these columns under post-earthquake fire scenarios. In addition to the experimental studies, detailed finite element analyses were conducted to simulate the behavior of CFDST columns subjected to post-earthquake fires. The models were shown to be capable of replicating the experimental results with sufficient accuracy. Moreover, a simplified step by step analytical procedure was proposed for calculation of the axial load capacity of CFDST columns subjected to fire. A number of design recommendations, based on the knowledge gained from the experimental and analytical studies, were proposed for CFDST columns subjected to fire.

ABSTRACT

Fire following an earthquake has been a major cause of damage in a number of historic seismic events. Considering the amount of damage and statistics showing a high probability for the occurrence of post-earthquake ignitions, there is a need to study the effects of seismic damage on the fire resistance of structures. Concrete-Filled Double-Skin Tube (CFDST) columns, special composite structures which have shown satisfactory performance under separate seismic loading and fire conditions, were studied in this research when subjected to post-earthquake fire scenarios.

Experimental studies were conducted to examine the behavior of concrete-filled double-skin tube (CFDST) columns exposed to fire after being subjected to simulated seismic loads. The experiments were conducted in two separate phases, consisting of the quasi-static cyclic tests followed by fire tests. Three nominally identical column specimens were constructed for these studies. One of the specimens was directly tested under fire to quantify its resistance in an undamaged condition. The other two specimens were first subjected to quasi-static cyclic lateral loads, imposing varying degrees of lateral drift to simulate two different seismic events with moderate and high damage levels before being exposed to fire. Both of the specimens were pushed to the maximum drift of 6-6.5% with different residual drifts of 1.4% and 3.9% for moderate and high damage levels, respectively.

The undamaged and damaged columns were then subjected to the same fire tests following the standard ASTM E119 (ASTM 2012) temperature-time curve while sustaining an axial load until the column failed due to global buckling. Local buckling of the tubes was also observed in the specimens due to the thermal expansion and separation from the concrete. Overall, the results showed marginal differences in the fire resistance of the three specimens, providing evidence for the resilient performance of these columns under post-earthquake fire scenarios. An additional quasi-static cyclic loading test was conducted on the specimen that had been exposed to fire without any prior damage, to investigate the behavior of the column subjected to seismic loads after the fire test. Again, differences in behavior were modest, except for a 5.7% drop in strength attributed to permanent degradation in material properties due to the fire test.

In addition to the experimental studies, detailed finite element analyses were conducted using ABAQUS and LS-DYNA to simulate the behavior of CFDST columns subjected to post-earthquake fires. The models were shown to be capable of replicating the experimental results with sufficient accuracy. A simplified step by step analytical procedure was proposed for calculation of the axial load capacity of CFDST columns subjected to fire. The procedure was defined based on an analytical solution to the heat transfer problem and calculation of axial load capacity using the fire-modified material properties. A number of design recommendations, based on the knowledge gained from the experimental and analytical studies, were proposed for CFDST columns subjected to fire.

ACKNOWLEDGEMENTS

Financial support for this work was provided by MCEER, University at Buffalo. This support is gratefully acknowledged. Any opinions, conclusions or recommendations expressed in this report are those of the authors and do not necessarily reflect the views of MCEER.

TABLE OF CONTENTS

SECTION 1	INTRODUCTION	1
1.1	Introduction	1
1.2	Objectives and Scope of Work	2
1.2.1	Experimental Phase	2
1.2.2	Analytical Phase	3
1.3	Outline of the Report	4
SECTION 2	LITERATURE REVIEW	7
2.1	Post-Earthquake Fires	7
2.2	Concrete-Filled Double-Skin Tube (CFDST) Columns	9
2.2.1	The Advantages of Traditional Concrete-Filled Steel Tube (CFST) Columns	9
2.2.2	Concrete-Filled Double-Skin Tube (CFDST) Columns Subjected to Monotonic and Cyclic Loading	12
2.2.3	Concrete-Filled Double-Skin Tube (CFDST) Columns Subjected to Fire	17
2.3	Summary	20
SECTION 3	FINITE ELEMENT MODELING OF CONCRETE-FILLED DOUBLE SKIN STEEL TUBES	21
3.1	Introduction	21
3.2	Finite Element Model for Simulation Cyclic Inelastic Flexural Response	22
3.2.1	Steel Material	22
3.2.2	Concrete Material	24
3.2.3	Steel-Concrete Interface	27
3.3	Pre-test Verification for Cyclic Lateral Loading	28
3.3.1	Hardening Model for Steel Material	28
3.3.2	Element Type for the Steel Tube	29
3.3.3	Modification of Concrete Damaged Plasticity Model to Include the Confinement Effects	31
3.3.4	Verification of Modeling Assumptions for Cyclic Lateral Loading	33
3.4	Finite Element Model for Simulating the Effect of Fire on a Steel-concrete Composite Member	40

3.4.1	Introduction to Thermal-Stress Problems	40
3.4.2	Developing the Finite Element Model for Heat Transfer Analysis	43
3.4.2.1	Theory of Heat Transfer Analysis.....	43
3.4.2.2	Thermal Properties of Materials at Elevated Temperatures.....	45
3.4.2.3	Element Type and Mesh Size for Heat Transfer Analysis	49
3.4.2.4	Thermal Loads and Boundary Conditions	50
3.4.2.5	Heat Transfer Mechanisms inside a Composite Member	52
3.4.3	Developing the Finite Element Model for Stress/Deformation Analysis	53
3.4.3.1	Structural Properties of Materials at Elevated Temperatures.....	53
3.4.3.2	Steel-Concrete Interface.....	61
3.4.3.3	Loads and Boundary Conditions.....	62
3.4.3.4	Buckling Issues and Geometric Imperfection	62
3.4.3.5	Element Types and Meshing.....	63
3.5	Pre-test Verification of the Finite Element Model for Thermal Stress Problem	63
3.5.1	Verification of Heat Transfer Analysis.....	65
3.5.2	Verification of Stress/Deformation Analysis	67
 SECTION 4 CYCLIC TESTING TO DAMAGE CFDST COLUMNS (PRIOR TO FIRE		
	TESTS).....	75
4.1	General	75
4.2	Specimen Design.....	76
4.2.1	Geometry of the Specimens	76
4.2.2	Materials	78
4.2.2.1	Steel.....	78
4.2.2.2	Concrete	78
4.2.3	Calculation of Section properties	80
4.3	Description of the Experimental Setup for Cyclic Tests	85
4.3.1	General.....	85
4.3.2	Design of the Setup	86
4.3.2.1	Assumptions.....	86
4.3.2.2	Calculation of the Maximum Lateral Load Applied to the Specimen	87
4.3.2.3	Transfer Element (Connecting the Actuator to the Specimen)	88
4.3.2.4	Connection of the Cap Plate to the Specimen.....	90
4.3.2.5	Design of the Box Section at the Base of the Specimen	90

4.3.2.6	Welds Connecting Top and Bottom Plates of the Box Section to the Outer Tube	91
4.3.2.7	Effects of Axial Load on the Specimen and the Box Section	92
4.3.2.8	Threaded Rods at the Base and the Supporting Tubes.....	92
4.3.2.9	Effects of Out of Plane Deformations.....	93
4.4	Construction	94
4.5	Instrumentation.....	96
4.5.1	General.....	96
4.5.2	Strain Gauges	97
4.5.3	String Potentiometers.....	99
4.5.4	Krypton Dynamic Measurement Machine.....	101
4.5.5	Load Cells.....	102
4.6	Experimental Protocol.....	102
4.7	Cyclic Test Results.....	103
4.7.1	Test 1: Specimen S1.....	103
4.7.2	Test 2: Specimen S2.....	106
SECTION 5	FIRE TESTS ON DAMAGED AND UNDAMAGED CFDST COLUMNS.....	109
5.1	General	109
5.2	Experimental Setup for Fire Tests.....	109
5.2.1	Description of the Setup.....	109
5.2.2	Preparation of the Specimens for the Fire Tests	111
5.3	Instrumentation.....	114
5.3.1	Thermal Instrumentation.....	114
5.3.2	Structural Instrumentation	117
5.4	Experimental Protocol.....	117
5.5	Fire Test Results.....	119
5.5.1	Test 1: Specimen S3 (Undamaged specimen).....	119
5.5.2	Test 2: Specimen S1 (Damage Level 1).....	123
5.5.3	Test 3: Specimen S2 (High-damage specimen)	127
5.5.4	Results from Stub Columns	132
5.5.5	Post-Fire Lateral Cyclic Testing of Specimen S3	134
SECTION 6	FINITE ELEMENT SIMULATION OF EXPERIMENTAL RESULTS	137
6.1	General	137

6.2	Simulation of the Cyclic Tests	138
6.2.1	Finite Element Models	138
6.2.2	Push-over Analysis of Specimen S1	141
6.2.3	Cyclic Analysis of Specimen S1	142
6.2.4	Push-over Analysis of Specimen S2	150
6.2.5	Cyclic Analysis of Specimen S2	151
6.3	Simulation of the Fire Tests	154
6.3.1	General	154
6.3.2	Fire Testing of the Undamaged Specimen (S3)	155
6.3.2.1	Heat Transfer Analysis of Specimen S3	155
6.3.2.2	Stress/deformation Analysis of Specimen S3	161
6.3.3	Fire Testing of the Moderately Damaged Specimen (S1)	169
6.3.3.1	Heat Transfer Analysis of Specimen S1	169
6.3.3.2	Stress/deformation Analysis of Specimen S1	170
6.3.4	Fire Testing of the Highly Damaged Specimen (S2)	172
6.3.4.1	Modification of the Finite Element Model	172
6.3.4.2	Heat Transfer Analysis of Specimen S2	173
6.3.4.3	Stress/deformation Analysis of Specimen S2	175
6.3.5	Fully Coupled Approach versus Sequentially Coupled Approach	176
6.4	Simulation of the Post-Fire Cyclic Test	177
6.5	Summary	180
SECTION 7 SIMPLIFIED ANALYTICAL SOLUTION FOR FIRE RESISTANCE OF CFDST COLUMNS		183
7.1	General	183
7.2	Analytical Solution for the Heat Transfer Problem	184
7.2.1	General Solution for Heat Conduction Differential Equation	184
7.2.2	Simplification of the Solution for Heat Transfer Problem for Practical Purposes	192
7.2.3	Verification of the Heat Transfer Solution	196
7.3	Calculation of the Axial Load Capacity of CFDST Columns Subjected to Fire	202
7.3.1	Development of the Analytical Procedure	202
7.3.2	Simplified Step by Step Procedure to Calculate the Axial Load Capacity for CFDST Columns under Fire	211

7.3.3	Verification of the Analytical Approach to Calculate the Axial Load Capacity for CFDST Columns under Fire	216
7.4	Design Recommendations for Fire Resistance of CFDST Columns Subjected to Fire ..	225
7.4.1	Inner Steel Tube	225
7.4.2	Concrete Core	225
7.4.3	Outer Steel Tube	228
7.4.4	Examples: Investigating the Effect of Different Section Geometry Parameters on the Axial Load Capacity of CFDST Columns Subjected to Fire.....	228
SECTION 8 SUMMARY AND CONCLUSIONS		233
SECTION 9 REFERENCES.....		239
APPENDIX A		
A COMPARISON BETWEEN SOLID AND SHELL ELEMENTS		247
A.1	Accuracy Assessment Based on the Simulation of an Experimental Study.....	247
A.1.1	Experiment Description	247
A.1.2	Experimental Results	248
A.1.3	Simulation with 3D Shell Elements	249
A.1.4	Simulation with 3D Solid Elements.....	250
A.2	Accuracy Assessment Based on the Classical Pinched Cylinder Problem	251
A.2.1	Problem Description.....	252
A.2.2	Analysis with Shell Elements.....	252
A.3	Summary	254
APPENDIX B		
THE WINFRITH CONCRETE MODEL		257
APPENDIX C		
CASE STUDY: FINITE ELEMENT SIMULATION OF THE FIRST FIRE TEST (CONDUCTED ON SPECIMEN S3) USING A FULLY COUPLED TEMPERATURE- DISPLACEMENT APPROACH.....		259

LIST OF FIGURES

Figure 2- 1	Cross-section of a circular: a) CFST and b) CFDST column.....	10
Figure 2- 2	Effect of void ratio (χ) on the ductility of CFDST columns (Tao et al. 2004)	14
Figure 2- 3	Typical lateral load vs lateral displacement results for a CFDST column subjected to combined axial and cyclic flexural loading (Han et al. 2006)	16
Figure 2- 4	Envelope curves for the lateral load versus lateral displacement results from hollow steel tube, CFST and CFDST column subjected to cyclic bending (Han et al. 2006).....	17
Figure 2- 5	Effect of different parameters on the time-temperature curve of the inner tube in CFDST columns subjected to the standard ISO-834 curve: a) diameter of the outer steel tube (D_o) and b) void ratio (ϕ) (Yang and Han 2008).....	18
Figure 3- 1	Uniaxial behavior of Concrete Damaged Plasticity model (a) in tension, (b) in compression from ABAQUS theory manual (SIMULIA 2012)	26
Figure 3- 2	Uniaxial load cycle (tension-compression-tension) for Concrete Damaged Plasticity model from ABAQUS theory manual (SIMULIA 2012)	26
Figure 3- 3	Yield surface for Concrete Damaged Plasticity model in plane stress conditions from ABAQUS theory manual (SIMULIA 2012)	27
Figure 3- 4	Lateral load vs lateral displacement hysteresis curve for bare steel tube (a) Experimental and analytical results (Goto et al. 1998) (Dashed line shows experimental results) (b) Finite element analysis results for different hardening models	29
Figure 3- 5	Moment-rotation results for cyclic tests of steel tubes: (a) Test results by McCormick et al. (2010), (b) model with C3D8R solid elements, (c) model with C3D20R solid elements (d) model with S4R shell elements	30
Figure 3- 6	Strain curves for unconfined and confined concrete enclosed in steel tube	32
Figure 3- 7	Schematic View of Test Setup (Han et al. 2006)	34
Figure 3- 8	Circular Section of cc-23 Specimen.....	35
Figure 3- 9	Meshed Model of cc-23 Specimen.....	35
Figure 3- 10	Stress-strain relationships used in Concrete Damaged Plasticity model: (a) confined concrete in compression, and (b) concrete in tension	36
Figure 3- 11	Stress-strain relationships used for the steel material model with linear kinematic hardening: (a) outer steel tube, and (b) inner steel tube	37
Figure 3- 12	Free body diagram of the steel tube section used for confinement (Usami et al. 2001)	38

Figure 3- 13	Applied cyclic displacement pattern	39
Figure 3- 14	Cyclic load versus lateral displacement for cc-23 specimen: a) ABAQUS analysis results for models with different mesh sizes, (b) Experimental results (Han et al. 2006).....	39
Figure 3- 15	Specific heat of steel as a function of temperature (CEN 2005)	46
Figure 3- 16	Specific heat of normal weight (NC) and light weight (LC) concrete as a function of temperature (CEN 2005).....	47
Figure 3- 17	Thermal conductance of steel as a function of temperature (CEN 2005)	48
Figure 3- 18	Thermal conductance of normal weight (NC) and light weight (LC) concrete as a function of temperature (CEN 2005).....	49
Figure 3- 19	Standard fire curve (ASTM 2012).....	50
Figure 3- 20	Stress-strain relationship for steel at elevated temperatures (CEN 2005)	54
Figure 3- 21	Graphs of Eng. stress vs. Eng. strain as predicted using the NIST approach, the Eurocode equations, and NIST experimental data for ASTM A572 Gr. 50 structural steel (NIST 2010).....	57
Figure 3- 22	Young’s modulus for steel as a function of temperature (different models).....	58
Figure 3- 23	Stress-strain relationship for concrete at elevated temperatures (CEN 2005).....	59
Figure 3- 24	Strain in compression curves for concrete at elevated temperatures (Harmathy and Allen 1973)	60
Figure 3- 25	Thermal elongation of steel as a function of temperature (CEN 2005).....	61
Figure 3- 26	Geometry of the model.....	64
Figure 3- 27	Visualized results of heat transfer analysis showing nodal temperatures (in °C) at the end of the fire event (from ABAQUS).....	66
Figure 3- 28	Comparison of the heat transfer analysis results with experimental data from Chabot and Lie (1992).....	67
Figure 3- 29	Visualized final displacement result of the structural analysis – Eurocode steel and concrete models (from ABAQUS).....	69
Figure 3- 30	Ratio of the axial load carried by steel tube/concrete core to the total axial load during the fire test	70
Figure 3- 31	Axial displacement results from ABAQUS compared with experimental data (Chabot and Lie 1992).....	70
Figure 3- 32	Axial displacement results from ABAQUS compared with experimental data (Chabot and Lie 1992): checking sensitivity to the mesh sizing and thermal properties of steel material (MP1: modified coeff. of thermal expansion, MP2: modified coeff. of thermal expansion and yield strength of steel at high temp.)	72

Figure 3- 33	Axial displacement results from ABAQUS with NIST steel model compared with experimental data (Chabot and Lie 1992) and simulation results with Eurocode steel model.....	73
Figure 4- 1	Cross-section of the Specimen	78
Figure 4- 2	Stress-strain Curve for Inner and Outer Tube Steel Materials	79
Figure 4- 3	Cross-section of the Specimen with the Assumed N.A.....	80
Figure 4- 4	Differential Element for Calculation of Tensile and Compressive Forces of a Tubular Section.....	81
Figure 4- 5	Moment Arm for Total Compressive Force of a Tubular Section	82
Figure 4- 6	Differential Force and Moment Calculation for a Circular Section (Above N.A.)	83
Figure 4- 7	Experimental setup for Cyclic Tests	85
Figure 4- 8	Details of the Additional Parts to the Specimen’s Base (built-up box section)	86
Figure 4- 9	Complete Free Body Diagram of the Specimen.....	87
Figure 4- 10	Built-up Transfer Element.....	88
Figure 4- 11	Failure Modes for Anchor Bolts in Tension (ACI 318-11).....	89
Figure 4- 12	Failure Modes for Anchor Bolts in Shear (ACI 318-11).....	89
Figure 4- 13	Circular Welding of the Additional Elements to the Column’s Base	94
Figure 4- 14	Thermocouple Wires Coming out of the Specimens.....	95
Figure 4- 15	Threaded Rods fixed on the Cap Plate to Be Embedded in Concrete	96
Figure 4- 16	Specimen S1 after Instrumentation	98
Figure 4- 17	Strain Gauge Layout.....	99
Figure 4- 18	String Pot Layout	100
Figure 4- 19	LED Layout.....	101
Figure 4- 20	Load Cell Used to Monitor the Tensile Load of the Threaded Rod.....	102
Figure 4- 21	Cyclic Displacement Controlled Test Protocol (ATC-24).....	103
Figure 4- 22	Lateral Force vs. Drift Ratio Results– Specimen S1	105
Figure 4- 23	Local Buckling at the Base of Specimen S1	105
Figure 4- 24	Specimen S1 at the End of the Cyclic Test	106
Figure 4- 25	Lateral Force vs. Drift Ratio Results– Specimen S2.....	107
Figure 4- 26	Local Buckling at the Base of Specimen S2	108
Figure 4- 27	Specimen S2 at the End of the Cyclic Test	108
Figure 5- 1	Specimen S3 in the Vertical Furnace	111

Figure 5- 2	Built-up Elements for Connection of Column Ends to the Top and Bottom Beams of the furnace.....	112
Figure 5- 3	Built-up Channels Added to the Ends of the Specimens for the Fire Test.....	113
Figure 5- 4	Built-up Member Used at the Top End Connection.....	113
Figure 5- 5	Vertical Furnace Thermocouple Layout (view looking into the furnace, S: south side, N: north side)	115
Figure 5- 6	Locations of Thermocouples in the Cross-section of the Specimen and Stub Columns ...	115
Figure 5- 7	Wires Carrying Temperature Data Connected to the Channels at the Back of the Furnace Wall.....	116
Figure 5- 8	Temperature Data Acquisition System.....	116
Figure 5- 9	Mechanical Dial Gauges Placed under the Bottom Beam.....	117
Figure 5- 10	Standard ASTM E119 Fire (ASTM 2012).....	118
Figure 5- 11	Temperature Data Measured in the Fire Test of Specimen S3.....	120
Figure 5- 12	Axial Displacement Results from Fire Test of Specimen S3	120
Figure 5- 13	Local Buckling of Specimen S3 Close to the Top Beam of the Furnace	121
Figure 5- 14	Out of Plane Global Buckling of Specimen S3	122
Figure 5- 15	Inclined Connection of the Column with Residual Displacement to the Built-up Channels.....	123
Figure 5- 16	Specimen S1 Installed in the Furnace in Preparation for the Fire Test.....	124
Figure 5- 17	Temperature Data Measured in the Fire Test of Specimen S1	125
Figure 5- 18	Axial Displacement Results from Fire Test of Specimen S1	126
Figure 5- 19	Local Buckling of Specimen S1 Close to the Top Beam of the Furnace	126
Figure 5- 20	Out of Plane Global Buckling of Specimen S1	127
Figure 5- 21	Temperature Data Measured in the Fire Test of Specimen S2.....	129
Figure 5- 22	Axial Displacement Results from Fire Test of Specimen S2	130
Figure 5- 23	Local Buckling of Specimen S2 Close to the Top Beam of the Furnace	131
Figure 5- 24	Out of Plane Global Buckling of Specimen S2.....	131
Figure 5- 25	Temperature Data Measured from the Two Short Columns (SC1, SC2).....	132
Figure 5- 26	Time history of Temperature Recorded by Nine Thermocouples Installed in Different Parts of the Furnace during Fire Test 2.....	133
Figure 5- 27	Post-fire cyclic testing of specimen S3: a) lateral force vs. lateral drift ratio results and b) fractures at the end of the test	135

Figure 6- 1	Uniaxial stress-strain relationship used for the modeling of steel material: a) inner tube b) outer tube	138
Figure 6- 2	Uniaxial stress-strain relationship used for the modeling of concrete material for specimen S1 in: a) compression (used for FE-CDP and FE-CDP-DS), b) tension (used for FE-CDP)	139
Figure 6- 3	Finite element model built for the numerical simulation of cyclic loading tests	140
Figure 6- 4	Lateral force vs. drift ratio results from the push-over analysis of specimen S1 using the FE-CDP model (compared with the test results).....	142
Figure 6- 5	Lateral force vs. drift ratio results from the cyclic loading analysis of specimen S1 (FE-CDP model) compared with the test results	143
Figure 6- 6	Uniaxial tensile stress-displacement relationship used for modeling the concrete material of specimen S1 (used in FE-CDP-DS model).....	145
Figure 6- 7	Lateral force vs. drift ratio results from the cyclic loading analysis of specimen S1 (from the FE-CDP-DS model) compared with the test results.....	146
Figure 6- 8	Stress-displacement relationship used for the tensile behavior of concrete in the FE-W model.....	148
Figure 6- 9	Lateral force vs. drift ratio results from the analysis of the FE-W models of specimen S1: a) comparison with the experimental results b) mesh sensitivity analysis.....	149
Figure 6- 10	Local buckling of specimen S1 at the end of cyclic testing: a) FE-CDP-DS model b) FE-W model and c) photo from the test	150
Figure 6- 11	Lateral force vs. drift ratio results from the finite element push-over analysis (compared with results from cyclic testing of specimen S2)	151
Figure 6- 12	Lateral force vs. drift ratio results from the cyclic loading analysis of specimen S2 (FE-CDP-DS model) compared with the test results	152
Figure 6- 13	Results from the cyclic loading analysis of the FE-W model of specimen S2: a) Lateral force vs. drift ratio (comparison with the experimental results) and b) opening and closing of concrete tensile cracks while the column goes from +5 to -5% lateral drift ratio	153
Figure 6- 14	Local buckling of specimen S2 at the end of cyclic testing: a) FE-CDP-DS model, b) FE-W model and c) photo from the test	154
Figure 6- 15	Finite element model built for the thermal stress analysis of specimen S3 along with the final visualized results of the heat transfer analysis for a section chosen at mid-height of the column (from ABAQUS).....	157

Figure 6- 16	Analysis results for the temperature time-history of the inner tube for cases without and with its connectivity to the end plates for a point at: a) mid-height and b) close to the top end of specimen S3	158
Figure 6- 17	Analysis results for the temperature time-history for a point in mid-width of the concrete core of specimen S3 (compared with test results).....	159
Figure 6- 18	Analysis results of the temperature time-history for a point on the inner tube of specimen S3 (compared with test results).....	160
Figure 6- 19	Analysis results of the axial displacement of the bottom plate of specimen S3 (compared with test results)	162
Figure 6- 20	Final deformed shape of specimen S3 from: a) finite element analysis (ABAQUS) in the force-controlled mode and b) experimental results.....	164
Figure 6- 21	Global buckling of specimen S3 from the displacement-controlled ABAQUS analysis..	166
Figure 6- 22	Axial load versus axial contraction results from the displacement controlled analysis of specimen S3 after being exposed to different durations of the standard ASTM E119 fire	167
Figure 6- 23	Local buckling of the top end of the outer tube from: a) finite element analysis (ABAQUS) and b,c,d) test results of Specimen S3	168
Figure 6- 24	Analysis results of the temperature time-history for a point in mid-width of the concrete core of specimen S1 (compared with test results).....	169
Figure 6- 25	Analysis results of the temperature time-history for a point on the inner tube of specimen S1 (compared with test results).....	170
Figure 6- 26	Analysis results of the axial displacement of the bottom plate of specimen S1 (compared with test results)	171
Figure 6- 27	Final deformed shape of specimen S1 from: a) finite element analysis (ABAQUS) and b) experimental results	172
Figure 6- 28	Analysis results for the temperature time-history of a point at mid-width of the concrete core of specimen S3 (compared with test results).....	174
Figure 6- 29	Analysis results for the temperature time-history of a point on the inner tube of specimen S3 (compared with test results).....	174
Figure 6- 30	Analysis results of the axial displacement of the bottom plate of specimen S2 (compared with test results)	176
Figure 6- 31	Local buckling of specimen S2 before and after fire testing: a) ABAQUS result before fire test b) ABAQUS result after fire test c) photo of the highly damaged specimen (S2) before fire test d) photo of the highly damaged specimen after fire test.....	177

Figure 6- 32	Lateral force vs. drift ratio results from the finite element analyses of post-fire cyclic loading of specimen S3 from: a) FE-CDP-DS model and b) FE-W model (compared with experimental results).....	179
Figure 6- 33	Lateral force vs. drift ratio results from the simulation of the post-fire cyclic loading of specimen S3 (FE-W model with element deletion compared with experimental results)	181
Figure 7- 1	Cross-section of a CFDST column for the heat transfer problem: a) with steel tubes and b) without steel tubes (assuming uniform temperature for steel sections).....	185
Figure 7- 2	Comparison of the exact and approximated values calculated for the function, $J_0(x)$	193
Figure 7- 3	ASTM E119 Standard fire curve compared with its bilinear approximation.....	194
Figure 7- 4	Time-temperature curve measured for the outer tube of specimen S3 along with the curve from the fitted bilinear function	198
Figure 7- 5	Temperature dependent vs. constant values of: a) specific heat and b) thermal conductivity for concrete (Eurocode 2005).....	199
Figure 7- 6	Time-temperature curves for a point at mid-width of the concrete section for specimen S3 from the test, finite element analysis and analytical (Eq. 7.54) results.....	200
Figure 7- 7	Time-temperature curves for a point on the surface of inner tube for specimen S3 from the test, finite element analysis and analytical (Eq. 7.54) results	201
Figure 7- 8	Variation of temperature through the thickness of the Specimen S3's cross-section for different points in time (finite element results compared with the analytical solution)....	202
Figure 7- 9	Steel and concrete regions with uniform temperature distribution	203
Figure 7- 10	Stress-strain curve of steel in uniaxial tension at temperature T (Eurocode curve compared with the simplified function (Eq. 7.73)	204
Figure 7- 11	Reduction factor for the elastic modulus of steel at high temperatures (tabulated data from Eurocode compared with calculated values from the proposed fitted function	205
Figure 7- 12	Reduction factor for the yield stress of steel at high temperatures (tabulated data from Eurocode compared with calculated values from the proposed fitted function	206
Figure 7- 13	Reduction factor for the proportional limit stress of steel at high temperatures (tabulated data from Eurocode compared with calculated values from the proposed fitted function	206
Figure 7- 14	Reduction factor for the maximum compressive strength of concrete (tabulated data from Eurocode compared with calculated values from the proposed fitted function).....	207
Figure 7- 15	Strain at maximum compressive stress for concrete at high temperatures (tabulated data from Eurocode compared with calculated values from the proposed fitted function)	207

Figure 7- 16	Strain at zero compressive stress (ultimate strain) for concrete at high temperatures (tabulated data from Eurocode compared with calculated values from the proposed fitted function).....	208
Figure 7- 17	Generic plots of the $P_{axial}(\epsilon, T)$ and $P_{critical}(\epsilon, T)$ functions for a fixed T and varying ϵ (the axial load capacity is determined by the load at the intersection of the two curves).....	210
Figure 7- 18	Generic plot of the $P_{critical}^*(\epsilon, T)$ functions for a fixed T and varying ϵ (Eq. 7.78).....	213
Figure 7- 19	Strain values needed for the calculation of $P_{critical_0}^*, P_{critical_1}^*, \dots$	215
Figure 7- 20	Graphical explanation for calculating the axial load capacity using Eq. 7.81 for the cases where: a) $P_{critical_{2i-1}}^* < P_{critical_i}^*$ and b) $P_{critical_{2i}}^* \leq P_{critical_i}^* \leq P_{critical_{2i-1}}^*$	215
Figure 7- 21	Buckling deformation of Specimen S3 with the rigid part at the bottom end subjected to different boundary conditions: a) fixed-fixed and b) fixed-pinned.....	218
Figure 7- 22	Free body diagram of Specimen S3 with the added rigid part after buckling with the fixed-pinned end conditions.....	219
Figure 7- 23	P_{axial} and $P_{critical}$ functions plotted for Specimen S3 after 65 minutes of exposure to the ASTM E119 standard fire curve assuming: a) fixed-fixed and b) fixed-pinned end conditions for cases with different number of defined concrete layers ($n = 2$ and $n = 3$).....	221
Figure 7- 24	Minimum concrete thickness values required to keep the temperature of inner tubes with different diameter sizes below the critical limit (i.e., 300 C) for 1, 2 and 3 hours of exposure to the standard ASTM E119 fire.....	226
Figure 7- 25	Variation of $\ln(r/r_1)$ for different values of r_1 and $r - r_1$ (r_1 : inner tube radius, $r - r_1$: concrete layer thickness).....	227
Figure 7- 26	Results of inner tube temperature calculated for a CFDST column with the outer tube section AA for different values of concrete layer thickness after 1,2 and 3 hours of exposure to the ASTM E119 fire curve	230
Figure 7- 27	Effects of changes in the thickness of inner and outer tubes on the axial load capacity of CFDST columns subjected to the first hour of ASTM E119 fire curve.....	232
Figure 7- 28	Effects of changes in the outer tube diameter, on the axial load capacity of the CFDST column, assuming that all of the other section geometry properties are selected as such to maximize the axial resistance	232

Figure A- 1	Test setup (McCormick et al., 2010).....	248
Figure A- 2	Protocol for applied displacement cycles (McCormick et al., 2010)	248
Figure A- 3	Moment vs. rotation results for HSS 304.8x152.4x6.4 (McCormick et al., 2010).....	249
Figure A- 4	Moment vs. rotation results obtained from the model using S8R shell elements.....	250
Figure A- 5	Moment vs. rotation results obtained from the model using S4R shell elements.....	251
Figure A- 6	Moment vs. rotation results obtained from the models using 3D solid elements: a) C3D8R; b) C3D20R.....	252
Figure A- 7	The Pinched Cylinder Problem (ABAQUS benchmark examples manual).....	253
Figure C- 1	Comparison between the heat transfer results from the sequentially coupled (FE-SC) and fully coupled (FE-FC) finite element analyses: a) mid-width of concrete; b) inner tube	260
Figure C- 2	Comparison between the axial deformation results from the sequentially coupled (FE-SC) and fully coupled (FE-FC) finite element analyses.....	260

LIST OF TABLES

Table 2- 1	Post-earthquake Ignitions for some of the 20th Century U.S. events.....	7
Table 3- 1	Thermal Constants and Parameters Used in Heat Transfer Modeling.....	52
Table 3- 2	Formulation of stress-strain relationship for steel at elevated temperatures.....	55
Table 3- 3	Parameters for equations 3.24 and 3.25.....	56
Table 3- 4	Two main parameters of the stress-strain relationship for normal weight (NC) and light weight (LC) concrete at elevated temperatures (CEN 2005).....	59
Table 3- 5	Geometry and material properties (Espinosa et al., 2010)	64
Table 4- 1	Compactness and Ductility Criteria for Round Filled Composite Elements (AISC2010a, b) – Limiting values are calculated based on nominal material properties $E=29,000$ ksi (200,000 MPa) and $f_y= 32$ ksi(220MPa)).....	77
Table 4- 2	Geometry of the Specimen	77
Table 4- 3	Concrete Cylinder Test Results	79
Table 7- 1	Summary of the parameters needed for the calculation of the temperature field using Eq. 7.54	197
Table 7- 2	Uniform temperature and material prop. calculated for different parts of the cross-section of specimen S3 after 50, 65 and 80 min. of exposure to the ASTM E119 fire.....	217
Table 7- 3	Axial load capacity calculated for Specimen S3 using the Analytical Approach (Eq. 7.72) compared with finite element analysis and test results for different cases (force unit: kips).....	221
Table 7- 4	$P^*_{critical}$ and P^*_{axial} loads calculated at different strain levels for Specimen S3 after 65 minutes of exposure to the ASTM E119 fire (n: no. of concrete layers).....	223
Table 7- 5	Geometric properties of the selected profiles for the outer steel tube	229
Table 7- 6	CFDST design cases with their calculated axial load capacity	231
Table A- 1	Properties of the HSS member used in analyses.....	247
Table A- 2	Comparison of the displacement results gained by different types of shell elements	254

SECTION 1

INTRODUCTION

1.1 Introduction

Several conflagrations following earthquakes have been documented throughout the history. In the twentieth century alone, the destructive fires that followed the San Francisco 1906 and Tokyo 1923 earthquakes rank as the two largest peace time urban fires. These two events caused significant damage to both of the cities (Scawthorn et al. 2005). Damage and losses from the subsequent fires reportedly exceeded damage from the shaking itself (NOAA 1972). While these large conflagrations have not been observed in more recent earthquakes, there have been numerous separate fires confined to single structures that have caused significant damage (Cousins and Smith 2004; Scawthorn 2008). Hundreds of fires were reported after the 1989 Loma Prieta, 1994 Northridge and 1995 Kobe earthquakes (NIST 1996). More recently, several post-earthquake fires were reported from the aftermath of Tohoko 2011 earthquake (Davidson 2012). The resistance of buildings to fire has been an active area of research; however, little information exists on whether structural elements damaged to various degrees, by the earthquake itself, can retain all or some of their fire resistance.

Although the problem of fire following earthquakes seems important, it has not received much attention from researchers in the past. There have been substantial efforts to investigate the effectiveness of various fire protection methods and to establish fire-ratings for various protected and unprotected structures. However, the involvement of earthquake engineers in this field of research has been limited. More research is needed to develop the design basis for structures that can resist a fire event occurring right after an earthquake or to determine if repairs may be required to the fire protection system.

Concrete-Filled Steel Tube (CFST) columns have been shown to be a promising multi-hazard resistant structural system exhibiting high performance for different types of extreme events. Several past studies have demonstrated the desirable seismic performance of CFSTs (Hajjar 2000; Marson and Bruneau 2004; Han and Yang 2005), while a number of separate studies have addressed the fire resistance of CFSTs (Kodur 1998; Han 2001; Han et al. 2003; Hong and Varma 2009; Moliner et al. 2013). It has been observed that these columns can achieve relatively high fire-ratings without using external protection. Low heat conductivity of concrete delays the temperature rise through the cross-section confined by the steel tube, helping the structure to enhance its fire resistance.

Observing acceptable results from CFST columns, a new but similar composite column was developed by adding a second tube inside the first one with the confined concrete sandwiched in between. The behavior of the new column type, referred to as the ductile Concrete-Filled Double-Skin Tube (CFDST) column, has been studied separately for seismic (Zhao and Grzebieta 2002; Han et al. 2004; Uenaka et al. 2008) and fire (Yang and Han 2008; Lu et al. 2010) and has showed desirable performance under both conditions. More recently, CFDST columns have also been investigated under both seismic and blast loadings and found to provide good performance under these different loading conditions (Fouché and Bruneau 2010).

The main goal in this project is to study the behavior of CFDST columns subjected to fire following earthquake scenarios. For this purpose, the behavior of CFDST columns with various degrees of simulated seismic damage is examined under the standard ASTM E119 (ASTM 2012) fire, using both experimental and numerical approaches. Moreover, to get a preliminary understanding of the reverse scenario (i.e., a post-fire earthquake), the effect of fire on the seismic capacity of a CFDST column is experimentally studied.

1.2 Objectives and Scope of Work

The principal aim of this research is to study the behavior of ductile CFDST columns subjected to post-earthquake fire scenarios. Towards this purpose, experiments and finite element analyses have been conducted to simulate a number of scenarios in which different levels of seismic damage are imposed on the CFDST column prior to the fire phase. The study started with preliminary finite element modeling and analyses conducted to acquire the essential knowledge for the design of the experimental program and setup. Objectives and scope of the following experimental and analytical phases are briefly presented here.

1.2.1 Experimental Phase

The experimental phase of this research is divided into two parts, including the cyclic loading and the fire simulation tests. Three CFDST columns were tested under cyclic lateral loading with different intensities to impose different levels (zero, moderate and high) of simulated seismic damage on the specimens. The specimens were built as identical quarter scale circular CFDST columns, such as to limit their prior-to-fire differences to be only the severity of the simulated seismic damage. The seismic loading simulation was achieved through quasi-static lateral loading of the columns under a constant axial load. The intensity of

the damage was judged based on the column's residual drift ratio (quantitatively) and the severity of local buckling observed in the outer tube (qualitatively).

In the fire simulation experiments, the specimens were exposed to direct flames inside a furnace and subjected to the standard ASTM E119 fire curve. The objective of these tests was to study the behavior and fire resistance of damaged and undamaged CFDST specimens under constant axial load and fire. The specimens were equipped with thermocouples embedded at different locations of their cross-section to record temperature data to be used in the investigation of the heat transfer process.

In addition to the main specimen columns, a number of 12 inches long stub columns were tested in fire to gain additional knowledge about the heat transfer process, effect of fire on the moisture content of concrete and possible permanent loss in the structural properties of CFDST columns due to fire exposure. No structural loads were applied to the stub columns during the fire tests.

The last part in the experimental program of this research was dedicated to the investigation of the post-fire behavior of CFDST columns subjected to lateral cyclic loading. After being exposed to the standard ASTM E119 curve and cooled down to room temperature, the specimen which was previously tested under fire as the reference (undamaged) case was tested under cyclic loading to study the effects of fire exposure on the flexural behavior of the column. The post-fire axial load capacity of CFDST columns was also evaluated by conducting axial loading tests on the stub columns which were previously tested in fire. An additional axial loading test was conducted on a reference stub column (not tested in fire) to determine the severity of possible permanent losses in the axial capacity of the columns due to fire.

1.2.2 Analytical Phase

The main goal of the analytical phase of this research was to build finite element models capable of simulating the behavior of CFDST columns subjected to a post-earthquake fire scenario. The objective of the finite element simulation of the cyclic loading tests was to replicate the experimental hysteretic load-displacement curves and specimen deformations with sufficient accuracy.

For fire test simulations, finite element models were built to account for the degradation of structural properties of steel and concrete at elevated temperatures. The models had to be capable of simulating the during-fire behavior of the columns (i.e. heat transfer process, load carrying capacity and deformations) and providing a sufficiently accurate estimation of the fire resistance time.

The finite element models built for the simulation of the cyclic loading and fire tests were verified using experimental results from similar studies in the past and validated based on the tests conducted in this research. The validated model was also used to simulate the behavior of the CFDST column subjected to a post-fire cyclic lateral loading scenario.

A simplified analytical procedure was developed to calculate the axial load capacity of CFDST columns subjected to any selected duration of any predefined fire curve. The procedure was defined in two parts, consisting of the analytical solution for the heat transfer problem for the cross-section of CFDST columns exposed to fire, followed by an analytical method to calculate the column's axial load capacity using the modified material properties at elevated temperatures. The procedure was simplified as such to be useful for practical design purposes without using specialized structural analysis software. The proposed method was used in a process to develop design recommendations for CFDST columns subjected to fire.

1.3 Outline of the Report

This report provides a detailed description of the analytical and experimental work conducted to study the behavior of CFDST columns subjected to post-earthquake fires.

Section 2 presents a brief review of previous related studies. The review starts on the subject of post-earthquake fires and continues to present a summary of studies conducted on the performance of Concrete Filled Steel Tube (CFST) and Concrete-Filled Double-Skin Tube (CFDST) columns under seismic and fire loadings. The review includes both analytical and experimental studies and addresses the motivations for this research. Section 3 presents preliminary finite element modeling of CFDST columns subjected to cyclic loading and fire. This section is completed by conducting verification analyses on the numerical models using experimental results from past studies.

Section 4 describes the cyclic loading tests conducted to impose seismic damage on the column specimens. Construction of the specimens, experimental setup for cyclic loading tests, observations of behavior and results are presented. Section 5 is dedicated to the fire testing part of the experimental program. The fire test setup is described and results are presented for different specimens tested under fire. The last sections of this section describes the post-fire lateral cyclic and axial loading tests conducted on the specimen and stub columns that were previously tested in fire.

Section 6 presents the finite element simulation of the experiments presented in Sections 4 and 5. The modeling techniques verified in Section 3 are initially used and further enhanced to numerically replicate the experimental results observed in cyclic loading and fire tests. The section also includes the simulation analysis for the post-fire lateral cyclic loading of CFDST columns.

Section 7 describes a simplified analytical procedure proposed to calculate the axial load capacity of CFDST columns subjected to fire. The section presents the analytical derivation of the solution for the heat transfer problem and explains a step by step procedure to determine the axial load capacity of the column at elevated temperatures. Section 7 concludes with a few examples of how to apply the proposed procedure (verifying its accuracy using the experimental and finite element analysis results) and some design recommendations for CFDST columns subjected to fire.

Section 8 contains final remarks and conclusions from this research, including comments on the accuracy of different material models and analysis techniques in an effort to guide future research tackling similar analytical studies. Finally, a summary of the improved understanding of the behavior of the CFDST columns in post-earthquake fires gained throughout the project is provided.

SECTION 2

LITERATURE REVIEW

2.1 Post-Earthquake Fires

Although much attention has been given to protect structures against damage from earthquake shaking, fire following an earthquake can be considered a significant contributor to total losses based on historic seismic events in the United States and Japan in the twentieth century (Scawthorn et al. 2005). The 1906 San Francisco and the 1923 Tokyo earthquakes caused severe damage due to the ground shaking; however, damage and losses from the subsequent fires reportedly exceeded damage from the shaking itself (NOAA 1972). In terms of life and economic loss, the 1906 San Francisco earthquake caused over 3,000 deaths and the destruction of more than 28,000 buildings (Scawthorn et al. 2005). In the 1923 Tokyo earthquake, a similar situation occurred with 140,000 people killed and 575,000 buildings destroyed. The aftermath reports showed that 77% of the building destructions were caused by fire (Scawthorn et al. 2005).

Table 2.1 lists some of the most significant 20th Century seismic events in the United States, which had a number of post-earthquake ignitions. Large number of ignitions reported in the aftermath of earthquakes in large populated cities emphasizes the threat of possible conflagrations, particularly for structures that are probably already impaired because of the shaking damage.

**Table 2- 1 Post-earthquake Ignitions for some of the 20th Century U.S. events
(Scawthorn et al. 2005)**

Date	Earthquake	Magnitude	City	No. of Ignitions
04/18/1906	San Francisco	8.3	San Francisco	52
03/11/1933	Long Beach	6.3	Long Beach	19
02/09/1971	San Fernando	6.7	Los Angeles	128
08/17/1989	Loma Prieta	7.1	San Francisco	26
01/17/1994	Northridge	6.8	Los Angeles	77

Despite the historical records of massive damage caused by post-earthquake fires and statistics showing a large number of ignitions that occur following earthquakes in large cities, little attentions has been given to the effects of post-earthquake fires on structures. One possible reason might be the lack of interactions between the earthquake engineers and fire protection engineers, who have dealt separately with the earthquake and fire hazards, ignoring their possible combined effects. Another reason can be related to the fact that the 1906 event was considered as a conflagration, which was a common experience in the U.S. at

the time, rather than a side effect of an earthquake. Moreover, improvements in the fire protection services have created a general notion that such events are unlikely to occur again (Scawthorn et al 2005).

Vulnerability of structures to the threat from post-earthquake fires should remain an important concern because buildings are not normally designed for combined seismic and fire effects. Moreover, damage to the firefighting and water supply systems caused by earthquake can result in longer response times in the ensuing fires. Little information exists on whether structural elements with various degrees of seismic damage can retain all or some of their fire resistance, when subjected to a fire following earthquake scenario. Considering the risk of fire either locally within buildings, or conflagrations following an earthquake, the effects of seismic damage on the fire resistance of structural members need to be better understood if resilient structural design is to be achieved.

A number of recent studies have looked into the behavior of structures subjected to post-earthquake fires. Yassin et al. (2010) conducted an analytical study on the performance of steel moment resisting frames in post-earthquake fires. The general finite element analysis software, ANSYS, was used to apply the 1940 El Centro earthquake to one- and two-story steel moment resisting frames. After the simulation of seismic damage and deformations, the structures were subjected to the Canadian standard fire curve (CSA 1989). The study revealed that the performance of the structure (in fire following earthquake scenarios) is strongly related to the residual lateral deformations caused by the seismic action. This was because the fire induced deformations, which occur due to the degradation of material properties, were asymmetrically added to severely increase the residual displacements caused by seismic loading. For frames with no residual displacement from a prior seismic action, the fire induced displacements were imposed symmetrically, taking a relatively longer time to cause failure. In a more general study, Yassin et al (2010) assessed the estimation and mitigation of the risk associated with fire following earthquake events.

Mostafaei and Kabeyasawa (2010) conducted a 3D simulation of the behavior of a 6-story reinforced concrete structure subjected to a post-earthquake fire scenario. Seismic damage was simulated by applying the 1995 Kobe ground motion to the structure. Subsequently, the ground level was subjected to the standard ASTM E119 fire. The study revealed that fire resistance of the structure reduced considerably due to the earthquake damage to the structural elements such as columns. This was because cracks in the concrete provided exposure of the column reinforcement to the fire temperature. Analysis showed that heat penetration caused relatively large load capacity reductions.

Memari et al. (2013) studied the effects of local behavior of reduced beam section (RBS) connections during fire following earthquakes on the global response of steel moment resisting frames using nonlinear finite element analysis. Results showed that the residual drift after the fire loading was orders of magnitude higher than the one from the seismic loading. Looking into the localized behavior of the connections, it was revealed that the local Mises stress values had approximately reached the yield stress of the material because of the effects of the post-earthquake fire.

For reinforced concrete structures, Lazarov et al. (2013) looked into the fire resistance of a reinforced concrete frame subjected to post-earthquake fire. A two-story three-bay planar reinforced concrete frame was analyzed under different loading cases using a finite element program developed by the authors. The defined load cases included cases with only gravity loads, gravity loads combined with standard fire, gravity loads combined with a push-over analysis and a subsequent standard fire, and a last case which was similar to the third one except for the push-over loading that was replaced with a 1-cycle push-over scenario (i.e., loading + unloading + opposite loading + unloading). Results showed that applying the fire load after a push-over loading caused higher residual displacements in the frame compared to the case that did not have a push-over loading part. Also the fire resistance time was longer for the latter compared to the former.

To better understand the effects of post-earthquake fires on the behavior of structures (specifically at the level of structural elements), a special type of columns, namely the concrete-filled double-skin tube columns, is studied in this project under different post-earthquake fire scenarios. Existing information on the fire and seismic performance of concrete-filled composite columns is presented in the following sections.

2.2 Concrete-Filled Double-Skin Tube (CFDST) Columns

2.2.1 The Advantages of Traditional Concrete-Filled Steel Tube (CFST) Columns

Concrete-filled steel tube columns are composite members constructed (as the name implies) from a steel tube filled with concrete. The combination of the steel and concrete sections creates a number of advantages for the CFST column compared to its equivalent steel or reinforced concrete counterpart. The steel tube is away from the center of the section (creating a larger moment of inertia), and performs well under tension and flexure, whereas the concrete core can sustain the axial compressive loads. Fig. 2.1a shows a typical circular CFST column.

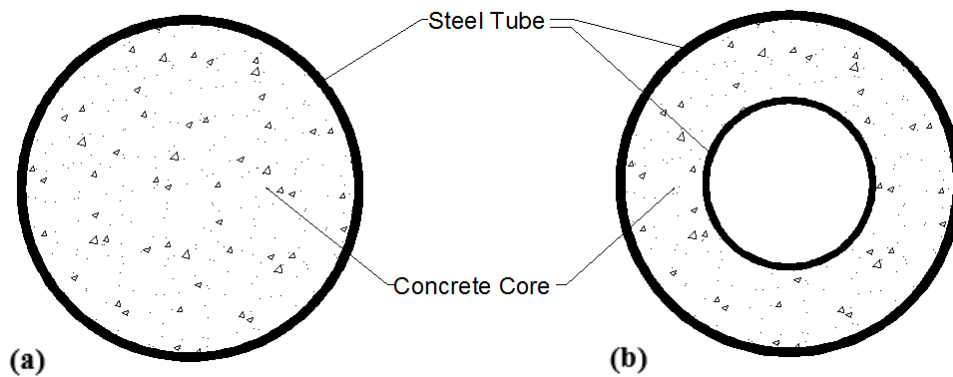


Figure 2- 1 Cross-section of a circular: a) CFST and b) CFDST column

The concrete core in a CFST column also works as a support for the steel tube, preventing it from inward local buckling. This delays the strength loss that can be seen in the cyclic loading of a bare steel tube. The steel tube, on the other hand, can provide confinement for the concrete core under compression, which leads to strength and ductility enhancements for the CFST column. The steel tube also prevents the spalling of concrete, which can be beneficial for seismic applications.

Much research has been conducted on the behavior of CFDST columns subjected to different load types. A complete summary of the experimental and analytical studies on CFST columns can be found in the online database for steel-concrete composite structures created by Hajjar et al. (2013), which contains more than approximately 1000 references for this type of structural element alone. Generally, past studies have demonstrated the desirable seismic performance of CFST columns; a few such key studies are summarized below.

In a review conducted by Hajjar (2000) on the behavior of circular and rectangular concrete-filled steel tube beam-columns subjected to cyclic seismic loading (based on the past experimental studies), a superior behavior was reported for CFST beam-columns compared to their equivalent bare steel or reinforced concrete members. This was because the added concrete delayed local buckling and the column could go through an increased number of cycles before failure leading to a larger amount of energy dissipation. The concrete part also benefits from the confinement effect caused by the steel tube. Similarly, Marson and Bruneau (2004) conducted a series of cyclic loading tests on full scale concrete-filled circular steel piers. The results showed a satisfactory ductility for the tested columns, and no significant loss in moment capacity was noticed up to a drift ratio of 7%. Likewise, research by Han and Yang (2005) on the behavior

of CFST columns subjected to combined axial and cyclic bending loads, confirmed that such columns exhibited relatively high stiffness, capacity and ductility for seismic applications.

As briefly mentioned above, one of the most important advantages of the CFST columns is the confinement effect from the steel tube that enhances the strength and ductility of the concrete core. Usami et al. (2001) proposed a method to predict the complete stress-strain curve of concrete subjected to triaxial compressive stresses caused by axial loads and confining pressures applied by the steel tube, for different CFST shapes (e.g., circular, rectangular). Specifically, for the circular CFSTs, empirical formulas were used to calculate the lateral pressure applied to the concrete core. The authors also proposed approximate expressions for determining the post-peak behavior of concrete based on experimental results of past studies. The post-peak behavior was defined by a linear descending branch starting from the maximum strength point and ending at a certain calculated strain value, beyond which the cross-section was able to sustain a low by constant stress. Analyses conducted using the proposed model showed good agreement with the test results. Additional details from this model are presented in Section 3 for the finite element models used in this study.

CFST columns have also shown positive behavior when subjected to fire. Kodur (1998) showed that concrete filling is significantly effective in producing fire resistance for HSS columns. Experimental results from this study also suggested that there is a significant difference between the behavior of high strength concrete-filled tube columns and that of the normal strength CFSTs. Results showed that high strength concrete reaches the critical temperature limits (that cause significant strength reductions) relatively sooner than the normal strength type. To compensate for this shortcoming when high strength concrete has to be used, the study suggested that adding fiber reinforcement can significantly improve the column's behavior by enhancing its ductility. Han (2001) and Han et al. (2003), in two successive studies, conducted both experimental and analytical works on the fire resistance of axially loaded CFST columns subjected to the standard ASTM E119 fire curve. The studies showed that the diameter of the steel tube and slenderness of the columns are the two most influencing parameters for the fire resistance. Larger diameter of the steel tube simply creates a larger concrete core which can delay the heating of the inner parts of the column.

Hong and Varma (2009) conducted a complete 3D finite element modeling of different CFST columns tested in past experimental studies. Sensitivity analysis results from this study showed that linear thermal expansion models can be used for the steel and concrete materials. Also it was revealed that full composite action may be used to model the CFST column specimens, because results from the models with full

bonding at the interaction of the steel and concrete surfaces were not significantly different compared to the ones from the models that allowed for slipping.

In a more recent work, Moliner et al. (2013) studied the behavior of eccentrically loaded CFST columns of high slenderness subjected to standard ISO-834 fire curve, which is similar to the ASTM E119 curve (ISO 1980). Results showed that for both normal and high strength concrete, shorter fire resistance time values were recorded for the columns with larger values of load eccentricity, because global buckling was expedited for these cases.

2.2.2 Concrete Filled Double-Skin Tube (CFDST) Columns Subjected to Monotonic and Cyclic Loading

Concrete Filled Double-Skin Tube (CFDST) column is a new type of composite construction that modifies the traditional CFST by adding a second steel tube to the section to sandwich the concrete between the two tubes and create a hollow part in the middle. Both circular and rectangular sections can be used as the inner and outer tubes for the CFDST columns. Fig. 2.1b shows the cross section of a circular CFDST column. This type of column can be used in high-rise buildings, sea-bed vessels, and offshore platforms. Recently it has been used for high-rise bridge piers in Japan to reduce the structure's weight while maintaining an acceptable energy absorption capacity (Zhao et al. 2002).

CFDST columns can perform better than the traditional CFST columns under different types of monotonic and cyclic loading because of the structural contribution of the inner tube and their larger stiffness, and larger strength-to-weight ratios (due to the material being distributed farther from the center of the cross-section).

Zhao and Grzebieta (2002) conducted a series of compression and bending tests on square CFDST columns. The specimens had outer tubes with width-to-thickness ratios in the range of 16.7 to 25 and inner tubes with a constant width-to-thickness ratio of 20. For compression tests, a total of 8 CFDST stub columns were tested along with 5 empty single-skin tube columns under axial load. The failure modes from the axial loading tests showed outward local buckling for the outer tube (similar to what occurs for CFST columns) and inward local buckling for the inner tube.

For bending, Zhao and Grzebieta used a four point bending rig to apply a monotonic moment to the CFDST columns (2002). Similar to the results of axial compression loading, the failure mode showed outward local

buckling of the outer tube. The inner tube, on the other hand, showed deflections similar to those of a compact empty tube. A more ductile behavior, both in compression and bending, was seen for the CFDST column compared to the empty single-skin tubes.

Elchalakani et al. (2002) conducted axial loading tests on CFDST columns with circular outer and square inner tubes. The outer tubes had diameter-to-thickness ratios in the range of 19 to 55. The inner tubes were chosen from sections with width-to-thickness ratios ranging from 20 to 26. The CFDST columns were shown to have significant increase in strength, ductility and energy absorption compared to the hollow steel tube columns.

In a number of extensive experimental studies (Han et al. 2004; Tao et al. 2004; Tao and Han 2006), a series of both circular and rectangular CFDST columns were tested under different types of static loading. The studies included testing of 37 specimens under axial compression, 42 columns under eccentric axial compression and 13 specimens subjected to bending. Results showed behavior of CFDST columns similar to that of traditional CFST columns, meaning that the sandwiched concrete gets the same confinement effects in both cases. A brief review from these studies is presented in the following paragraphs.

The axial loading tests, conducted on CFDST stub columns, showed typical failure mode of local (outward) buckling of the outer tube (similar to what occurs in CFST columns). Results showed that the behavior of the inner tube and its failure mode can be different according to its D_i/t_i ratio. For larger D_i/t_i 's, the inner tube failed with inward local buckling, while for tubes with smaller D_i/t_i 's no local buckling was reported from the tests. In terms of the outer tube, smaller D_o/t_o ratios led to more ductile behavior of the column.

The authors also studied the effect of the void (hollow) ratio (χ) on the ductility of CFDST columns. The void (hollow) ratio is defined as:

$$\chi = \frac{D_i}{(D_o - 2t_o)} \quad (2.1)$$

in which D_i and D_o are the diameters for the inner and outer tubes, and t_o is the outer tube thickness. The ductility of each section was quantified using the Ductility Index (DI), defined by Lin and Tsai (2001) as:

$$DI = \frac{\varepsilon_{95\%}}{\varepsilon_y} \quad (2.2)$$

in which $\varepsilon_{95\%}$ is the axial strain at the point where the axial load falls to 95% of the maximum load, ε_y is equal to $\varepsilon_{75\%}/0.75$, and $\varepsilon_{75\%}$ is the axial strain when the load reaches 75% of the maximum load in the pre-peak stage. Fig. 2.2 shows the DI values calculated for CFDST columns tested with different void (hollow) ratios and a fixed D_o/t_o of 60. Results showed that the void ratio did not significantly affect the ductility of the CFDST specimens. Note that the data point with ($\chi = 0$) refers to a conventional CFST specimen that was tested as a reference. The results show that the creation of a hollow space in the middle of the section did not negatively affect the overall ductility of the columns.

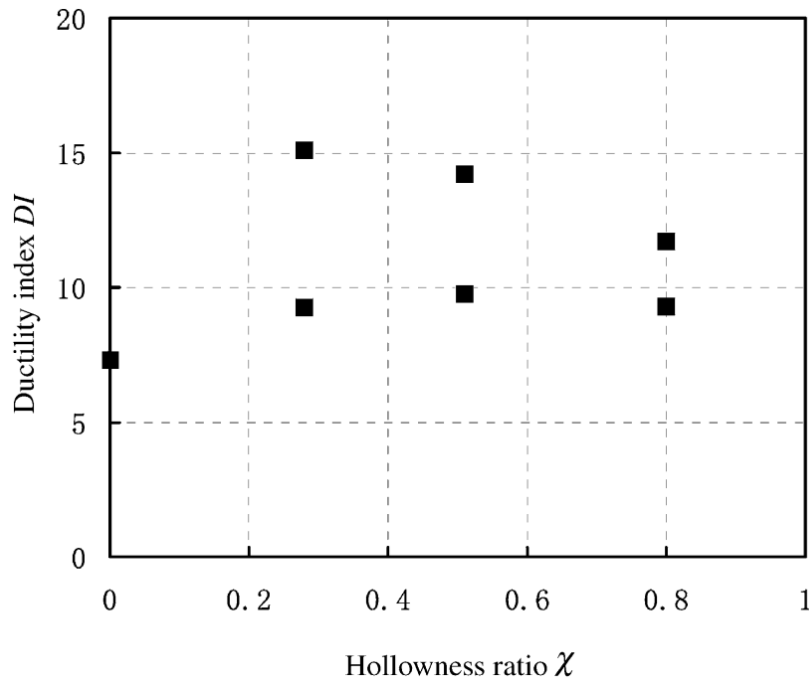


Figure 2- 2 Effect of void ratio (χ) on the ductility of CFDST columns (Tao et al. 2004)

For the CFDST beam-column tests, the specimens were subjected to eccentric axial loads in a pinned-pinned end support system and loading was increased up to failure. All of the specimens failed due to global buckling and, as expected, the maximum sustained load and the flexural stiffness was smaller for the specimens with larger slenderness ratio or load eccentricity. The specimens showed an overall ductile behavior and no local buckling was seen in the failure modes.

The interaction between the steel tubes and the sandwiched concrete can be explained in a few steps. At the initial stages of the axial loading, the lower Poisson's ratio of concrete (of 0.2) compared to steel (with a ratio of 0.3) leads to its smaller lateral expansion compared to that of the outer tube. Therefore, no

confinement pressure is applied to the concrete by the outside tube at that time. As the axial strain further increases, the longitudinal cracking of concrete leads to its increasing lateral expansion, gradually becoming greater than that of steel and a contact pressure force builds up between the surfaces of the two materials similarly to what occurs in a CFST column (Tao et al. 2004).

The sandwiched concrete in CFDST columns limits local buckling of the steel, as the outer tube is only allowed to buckle outward and the inner tube can only buckle inward. Note that this would be true only as long as the concrete layer is thick enough to provide enough rigidity to support the tubes. Based on experimental results, Tao et al. (2004) suggested keeping the void (hollow ratio) below the maximum limit of 0.8 for an adequate concrete layer thickness.

Tao et al. (2004) also defined a theoretical parameter to describe the composite action between the outer steel tube and concrete. The parameter was called the confinement factor (ξ), defined as:

$$\xi = \frac{A_{so} \cdot f_{yo}}{A_{c,nominal} \cdot f'_c} \quad (2.3)$$

in which A_{so} is the cross-sectional area of the outer steel tube, $A_{c,nominal}$ is the nominal cross-sectional area of the concrete core (equal to the hollow area inside the outer tube), f_{yo} is the yield strength of the outer tube, and f'_c is the compressive strength of concrete. Comparison between the results of different specimens showed that an increase in the confinement factor led to both strength and ductility enhancements for the CFDST column.

Uenaka et al. (2010) tested a total of 11 CFDST stub columns under axial loading. An additional CFST specimen was built for comparison. All of the CFDST columns had smaller weights (W) compared to the reference CFST column (the W_{CFDST}/W_{CFST} ratio was ranging from 0.57 to 0.99). Results showed that the strength-to-weight ratio was improved significantly by replacing the central part of concrete in a CFST column with a hollow steel (inner) tube.

In addition to the monotonic axial loading and bending tests mentioned above, CFDST columns have been also studied in a number of cyclic loading tests. Han et al. (2006) conducted a number of cyclic loading tests on both circular and square CFDST column with void ratios ranging from 0 to 0.77. A total of 28 column specimens, including 16 circular and 12 square CFDSTs, were subjected to a constant axial and cyclically increasing flexural loading. The specimens were set up in pinned-pinned end conditions, in which

one of the ends was allowed to move in the axial direction (to apply the axial load) and a load stub was used to apply the cyclic lateral loading to a short portion at the mid-length of the columns.

Typical failure mode of the CFDST columns subjected to cyclic bending included outward local buckling of the outer tube on each side of the rigid lateral loading stub, crushing of the sandwiched concrete and inward local buckling of the inner tube. Hysteretic lateral load versus lateral displacement curves showed a desirable energy dissipation capability for the CFDST columns. Fig. 2.3 shows the measured lateral force versus lateral displacement curve for one of the tested specimens (Han et al. 2006)

Han et al. (2006) concluded that under a similar axial load level, the shape and changing trend of the hysteretic curves of the CFDST columns are similar to those of CFSTs, meaning that the void ratio did not negatively affect the behavior of the specimen. To better understand the effect of the void ratio on the ductility of CFDST columns, the envelope curves for lateral load versus lateral displacement results were plotted together for a hollow steel tube, a CFST column ($\chi = 0$) and three different CFDST columns (Han et al. 2006). Comparison between the mentioned cases (shown in Fig. 2.4) revealed that except for the case with a relatively large void ratio ($\chi = 0.77$), in which a less ductile behavior was reported, the differences in the ductility of CFDST columns with void ratios of 0.25 and 0.51 with that of the CFST column were marginal (the CFDSTs were slightly more ductile).

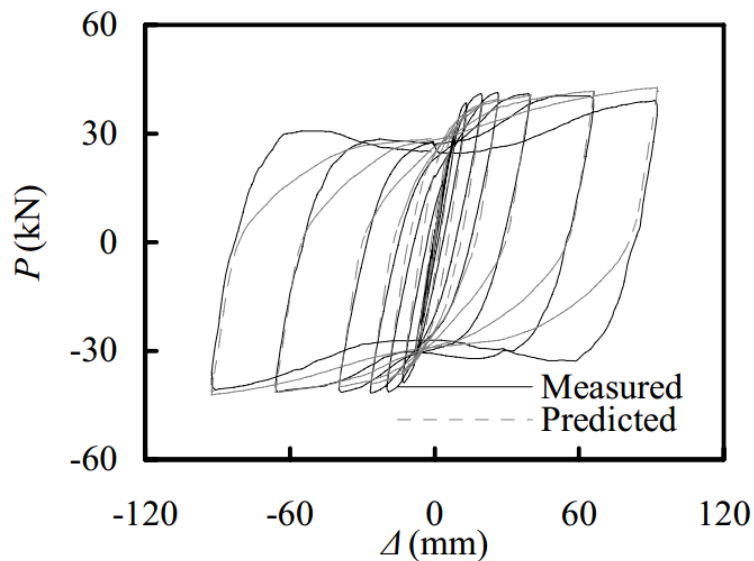


Figure 2- 3 Typical lateral load vs lateral displacement results for a CFDST column subjected to combined axial and cyclic flexural loading (Han et al. 2006)

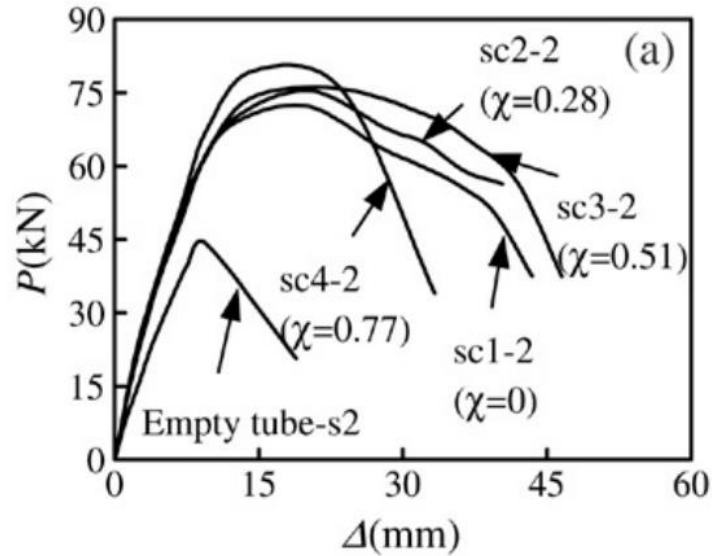


Figure 2- 4 Envelope curves for the lateral load versus lateral displacement results from hollow steel tube, CFST and CFDST column subjected to cyclic bending (Han et al. 2006)

Han et al. (2006) proposed a numerical model to predict the hysteretic curves of CFDST columns subjected to constant axial and cyclic flexural loading. The model predicted the curves based on different parameters including the axial load level, strengths and D/t ratios of the outer and inner tubes and the void (hollow) ratio. Fig. 2.3 shows the comparison between the predicted versus measured load-displacement hysteretic curves for one of the tested CFDST columns.

2.2.3 Concrete Filled Double-Skin Tube (CFDST) Columns Subjected to Fire

A CFDST column generally performs better than a traditional CFST when subjected to fire. This is mainly because the inner steel tube is thermally protected by the surrounding concrete and its temperature remains relatively lower for a longer time. Lower temperature leads to less strength and stiffness degradation of the inner tube, thus making it capable of sustaining the applied axial load for a longer duration (Yang and Han 2008). Compared to CFST columns, a limited number of studies have been dedicated to investigate the behavior of CFDST columns subjected to fire.

Yang and Han (2008) used a theoretical model to assess the performance of CFDST columns subjected to the standard ISO-834 fire curve. The proposed model, which was previously developed and used for CFST columns (Han 2001), consisted of a temperature distribution analysis in the column cross-section followed by a process to estimate the load carrying capacity of the column. The temperature distribution analysis

was conducted using the finite element method. The authors studied the effects of the outer steel tube diameter and the void ratio on the temperature of the inner tube in CFDST columns subjected to the standard ISO-834 fire. Fig. 2.5 shows the plots of calculated temperature for the inner tubes of CFDST columns with varying outer steel tube diameter (Fig. 2.5a) and void ratio (Fig. 2.5b), while all of the other parameters are kept constant.

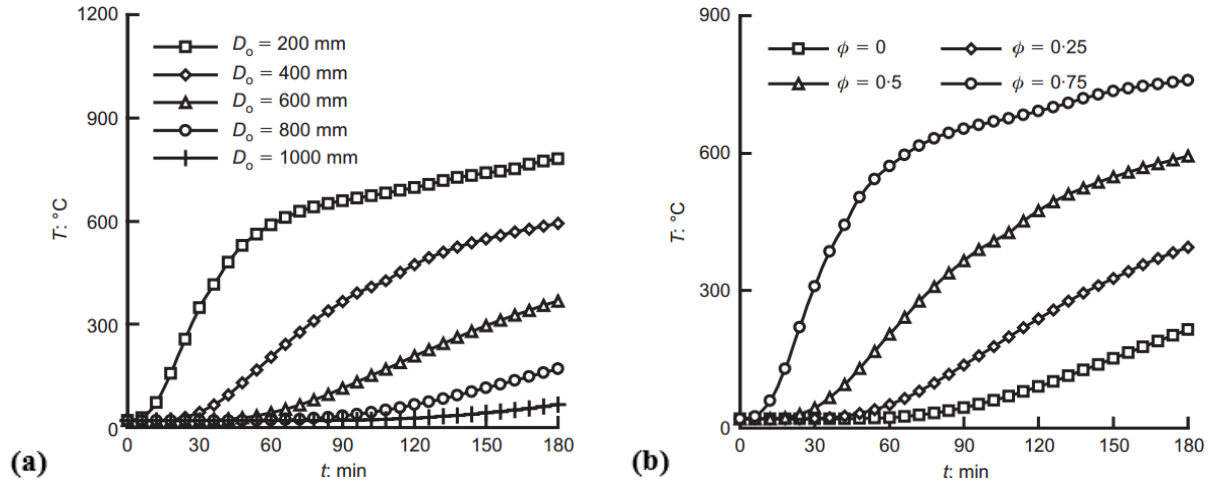


Figure 2- 5 Effect of different parameters on the time-temperature curve of the inner tube in CFDST columns subjected to the standard ISO-834 curve: a) diameter of the outer steel tube (D_o) and b) void ratio (ϕ) (Yang and Han 2008)

Note that the void ratio in this study is the same parameter as the one that was defined earlier in this section for CFDST columns (the only difference here is the use of ϕ instead of χ for the void ratio). Results in Fig. 2.5 show that the temperature of the inner tube is significantly lower for CFDST columns with larger outer diameters and smaller void ratios. In both cases, if all of the other geometric parameters are kept constant, the section has a thicker concrete layer that better insulated the inner tube during the heating period.

Knowing the temperature distribution results for a number of CFDST columns, Yang and Han (2008) calculated the columns' axial load capacities by conducting stability analyses on the models using material properties modified for elevated temperatures. Using regression analysis, the authors suggested a strength index, referred to as k_s , for the axial load capacity of CFDST columns subjected to the standard ISO-834 fire. The strength index, k_s , was defined as:

$$k_s = \frac{N_u(t)}{N_u} \quad (2.4)$$

in which $N_u(t)$ is the ultimate axial strength of the column at the fire duration time, t , and N_u is the axial strength at room temperature. The k_s index, which is calculated from a formula derived from regression analysis, is smaller for longer fire durations and depends on the outer diameter (D_o), void ratio ($= D_i/(D_o - 2t_o)$), column's slenderness ratio, thickness of the outer tube (t_o), and fire duration time (t). Results from parametric analyses showed that the diameter of the outer tube, void ratio, and the slenderness ratio have significant effects on the fire resistance of CFDST columns.

Lu et al. (2010) conducted standard fire tests on a total of 6 full size CFDST columns. The specimens were constructed using different combinations of circular and rectangular sections for the inner and outer steel tubes. Self-compacting concrete was used. Global buckling was observed as the final failure mode for all of the specimens. The "limiting temperature" value, T_{cr} , was defined as the temperature of the outer steel tube when the specimen reaches failure under the axial load. Results showed that the CFDST columns had higher "limiting temperatures" than the unfilled and conventional concrete filled tubular columns. This showed the superior performance of CFDST columns compared to the CFST and hollow tubes.

Lu et al. (2010) also argued that although a bit of composite action between the concrete and outer steel tube might have been lost because of the steel's higher thermal expansion rate, lower temperatures of the inner tube kept it in composite action after the yielding of the outer tube. Looking into the effects of different parameters affecting the fire resistance of CFDST columns, it was found that the diameter of the outer tube and the void ratio (which affects the thickness of the concrete layer) were the most influential.

In a more recent study, Lu et al. (2011) built finite element models to simulate a series of fire tests conducted on CFDST columns under axial loads. The models were used in a sequentially-coupled thermal stress analysis procedure, consisting of a heat transfer analysis, followed by a stress/deformation analysis. Note that a detailed description of the thermal stress analysis using the finite element method will be presented in Section 3. Using validated finite element models, a series of analyses were conducted to analyze the influence of different parameters on the fire resistance of CFDST columns. The selected parameters included the axial load level, capacities of the inner and outer tubes, use of fire protection material, effective length, the perimeter of the outer tube, and use of fiber reinforced concrete.

The axial load level was defined as the ratio of the applied axial load to the axial capacity of the column at room temperature. Results from the study by Lu et al. (2011) showed that fire resistance of CFDST columns decreases significantly as the axial load level increases. This is due to the fact that a column with a higher axial load ratio is closer to reaching its capacity, which is reduced because of the degradation of material at

elevated temperatures. Results from additional analyses showed that for a set of assumed values for the effective column length and diameters of outer and inner tubes, the inner tube thickness was the most influential parameter on the fire resistance of the CFDST column.

Apart from the separate seismic loading and fire conditions, CFDST columns have been also shown to perform well under other types of multi-hazard conditions. In a recent study, ductile concrete filled double-skin tube (CFDST) columns have been investigated under both seismic and blast loadings and found to provide good performance under these two different loading conditions (Fouché and Bruneau 2010). Finite element models were developed to simulate the behavior of CFST columns under seismic and blast loading and validated based on the experimental results. The modeling techniques verified in the mentioned process were then used to study the behavior of CFDST columns under seismic and blast loads. These analyses confirmed the good behavior of CFDSTs under those two hazards.

2.3 Summary

According to the past studies reviewed above, the performance of CFDST columns has been assessed separately when subjected to: first, different types of monotonic and cyclic loads and second, standard ASTM E119 (or ISO-834) fire curve. Results showed good behavior for the CFDST columns under both (structural load and fire) conditions. Although these results suggest that CFDST column may be an effective solution providing good performance in fire following earthquake scenarios, no specific experimental or analytical study has assessed their performance in such situations.

The research presented in the following sections expands on these previous studies by investigating the behavior of CFDSTs when exposed to fire following an earthquake. More specifically, the behavior of such columns under fire is examined after being subjected to various levels of damage from simulated earthquake loading. In addition, to a limited degree, the effect of fire on the seismic capacity of structural column is also investigated.

SECTION 3

FINITE ELEMENT MODELING OF CONCRETE FILLED DOUBLE SKIN STEEL TUBES

3.1 Introduction

This section presents the details of the finite element models used for simulating the behavior of double skin concrete filled steel tubes subjected to lateral cyclic and fire loading, and the calibration work (if needed) and rationale for selecting specific modeling approaches. The finite element software ABAQUS is used to build the numerical models, which are expected to be capable of simulating realistic conditions. Verification and validation of the models are accomplished in two steps.

The first step presented in this section consists of developing the models and comparing the simulation results with data from past experiments. These models will be used to predict the results of the tests conducted in this study (described in Sections 4 to 5). The second step of the model validation will be done using the recorded data from experiments first presented in this report (Section 6). As such, this second step will allow for assessing the validity of the numerical models built in this section using new data, and performing minor calibrations to the models if necessary. After the completion of this step, the models will be used for further numerical studies and parametric analyses.

In this section, Section 3.2 focuses on developing a model to simulate the cyclic inelastic response of CFDSTs (relevant to the seismic-related part of this study) obtained by applying constant axial and cyclic lateral loads to the specimens. The modeling assumptions are chosen from different options available in ABAQUS in an attempt to get as realistic results as possible. Some of the parameters adopted here are suggested in the literature and have been shown to adequately reproduce experimental results. Simulations of the material behavior is mostly based on choosing one of the existing models that has been shown to work best for the problem at hand, and defined using parameters that are directly measured in the lab. Minor calibrations were planned to be done to increase the suitability of the models to this specific problem and get closer to the experimental results from this project. The results of the models built in section 3.2 are verified with past experimental studies in section 3.3.

The next step focuses on the development of finite element models to simulate the behavior of CFDST specimens during a fire event. This simulation falls in the category of thermal-stress problems which can

be divided into heat transfer and stress/displacement parts. These two aspects will be discussed separately in section 3.4 in a way similar to the aforementioned approach for the cyclic loading model. Section 3.5 presents the verification analyses for the whole thermal-stress model using experimental data from past studies. The main objective of this section is to build numerical models for both cyclic and fire tests that can provide overall acceptable results. Further discussions on enhancing the accuracy of the models in simulating the experimental works of this project are presented in Section 6.

3.2 Finite Element Model for Simulation Cyclic Inelastic Flexural Response

The specimens tested as part of this project are composite columns consisting of two coaxial steel tubes filled with plain concrete. The finite element model should be able to simulate the inelastic behavior of these two materials and their bond under combined axial and cyclic loads. The modeling process consists of several steps, starting from material modeling to interactions at the steel-concrete interface, to loads and boundary conditions discussed in detail in the following paragraphs.

3.2.1 Steel Material

A bilinear model is used for the steel material consisting of a linear elastic phase and a post-yield linear hardening phase with stiffness equal to 2-3% of the initial stiffness. Based on experience from similar analyses on CFST columns, this simple material model can provide reasonable results for monotonic loading. A von Mises yield surface is considered for this steel material. Various hardening rules are considered for modeling under cyclic inelastic loading (i.e. with reversals of tension and compression yield excursions).

In addition to the elastic perfectly plastic model with no hardening, three hardening models are considered here, namely the isotropic, kinematic and two-surface models. The last one combines characteristics of both previous models to build two-surface yield criteria. Isotropic hardening models the yield surface as expanding with work hardening, neglecting movement of the center of the yield surface. While isotropic hardening material is easy to use, the loading surface expands uniformly and remains self-similar while the plastic deformation increases. Therefore, it cannot account for the Bauschinger effect exhibited by most structural materials. Considering that plastic deformation is an anisotropic process, it is predictable that the theory of isotropic hardening will not provide realistic results when complex loading paths with stress reversals are considered (Chen and Han 1988).

Kinematic hardening models shift the yield surface in the stress space such that straining in one direction reduces the yield stress in the opposite direction, simulating the Bauschinger effect and possible anisotropy induced by work hardening. The two-surface model, which is a combined isotropic/kinematic hardening model provides the flexibility to model both effects, which can be useful in some instances (e.g. to model phenomena such as ratcheting, relaxation of the mean stress, and cyclic hardening for materials subjected to cyclic loading). It is also possible to superpose several kinematic hardening models, when the range of changes in strain is significant to better model ratcheting effects.

At this stage it was decided to leave the sophisticated two-surface model for the second step of model development and verification, which will be done to simulate the experiments conducted in this project. The first step of model development and verification is done by using the simple no hardening, isotropic hardening, and linear kinematic hardening for steel material and comparing the results with experimental data from past studies. These simple models have been shown to provide acceptable replications of experimental works in the past. Therefore, a number of analyses have been conducted trying to simulate a tested specimen's behavior with these models; results and observations are presented in the following section.

The library of most finite element programs (including ABAQUS which is used here), include many types of elements that can use the above material models. Obviously some type of stress/displacement elements should be selected here, because the problem is the simulation of a structure subjected to cyclic loading. Typically to model a 3D structural member, solid elements are used. These elements have different number of nodes with displacement degrees of freedom and can be defined by materials which are homogeneous (like is case with steel) or layered. However in the modeling of steel tubes, solid elements are not the only choice. Another class of elements referred to as shell elements should also be considered. Shell elements are used to model structures in which one dimension, the thickness, is significantly smaller than the other dimensions (Simulia 2012). Shell elements are appropriate for use with thin tubes (such as the specimens considered in this project, which have thickness of 3mm or less). Using conventional shell elements is convenient as the thickness is taken care of numerically (meaning not modeled by the element dimensions), which avoids problems that could arise when solid elements are used to model thin elements (problems that could include having a few integration points across thickness, and issues of improper aspect ratios in term of length-to-thickness ratio of the solid elements).

Using solid elements has the benefit of better capturing deformations and contact surfaces, because these elements have real dimensions along the thickness of the tube. Also, solid elements provide better

visualizations in the ABAQUS outputs. However the problem of generating elements that are very thin in one dimension, mentioned above can occur in thin tubes such as those used in this study. Practically, in a thin tube, there will be only one solid element used along the thickness of the tube and it will produce aspect ratios that are considerably bigger than the common value of two, recommended for solid models. In some of the analyses considered below, the maximum aspect ratio of brick elements approximately reached a value of ten. To investigate which type of elements was best suited to the problem at hand, both shell and solid elements were used in attempts to replicate existing solutions for classical problems and cyclic test results of bare steel tubes tested by other researchers. The verification analyses and results are presented in section 3.3.2.

3.2.2 Concrete Material

Non-linear cyclic behavior of concrete is typically modeled using stress/displacement elements. Since the concrete elements does not have the problem of being thin in one direction, (as was discussed for the steel tube), 3D solid elements are the best choice for modeling. The solid (or continuum) elements in ABAQUS can be used for linear analysis and for complex nonlinear analyses involving contact, plasticity, and large deformations (Simulia 2012). Solid elements include the types with first-order and second order interpolation functions, referred to as 8-node and 20-node elements, respectively. According to the ABAQUS analysis user's manual, the 20-node element is very effective in bending-dominated problems and can model a curved surface with fewer elements. On the other hand, using 20-node solid elements appears to be considerably expensive in terms of the needed computational time. In order to get as close as possible to a model that would be both sufficiently accurate and efficient, the 8-node linear 3D solid element with reduced integration was selected for the modeling of concrete part, considering that the models will go through mesh refinement stages to get to the desired accuracy level. This element type is referred to as C3D8R in the ABAQUS element library. It should be mentioned that reduced integration uses a lower-order integration to form the element stiffness. Therefore, it reduces the running time and avoids the shear locking problem. Note that proper hourglass control techniques must be used for the C3D8R elements to avoid singularities in the stiffness matrix (SIMULIA 2012).

Having selected the element type, the material model needs to be defined for concrete. The Concrete Damaged Plasticity model implemented in ABAQUS is based on developments by Lubliner et al. (1989) and by Lee and Fenves (1998) and is able to model the following properties:

- Different yield strengths in tension and compression, with the initial yield stress in compression being a factor of 10 or higher than the initial yield stress in tension;
- Softening stiffness and strength in tension;
- Initial hardening followed by softening stiffness and strength in compression;
- Different degradation of the elastic stiffness in tension and compression upon unloading;
- Stiffness recovery at load reversals to consider the effects of closed cracks, and;
- Rate sensitivity, especially peak strength as a function of strain rate.

The Concrete Damaged Plasticity model expresses behavior in terms of effective stress and hardening variables, such that:

$$\sigma = (1 - d)D_0^{el} : (\varepsilon - \varepsilon^{pl}) = D^{el} : (\varepsilon - \varepsilon^{pl}) \quad (3.1)$$

$$\bar{\sigma} = D_0^{el} : (\varepsilon - \varepsilon^{pl}) \in \{\bar{\sigma} | F(\bar{\sigma}, \tilde{\varepsilon}^{pl}) \leq 0\} \quad (3.2)$$

$$\tilde{\varepsilon}^{pl} = h(\bar{\sigma}, \tilde{\varepsilon}^{pl}) \cdot \varepsilon^{pl} \quad (3.3)$$

$$\dot{\varepsilon}^{pl} = \dot{\lambda} \frac{\partial G(\bar{\sigma})}{\partial \bar{\sigma}} \quad (3.4)$$

where σ is the Cauchy stress, $\bar{\sigma}$ is the effective stress, D_0^{el} is the initial undamaged elastic stiffness, d is a scalar stiffness degradation variable, (which can vary between zero for undamaged material to one for fully damaged material), ε and ε^{pl} are total strain and plastic strain, $(\bar{\sigma}, \tilde{\varepsilon}^{pl}) \leq 0$ is the yield function, $\tilde{\varepsilon}^{pl}$ is the hardening variable which is also referred to as the equivalent plastic strain, h defines the evolution of hardening variables, and G is a flow potential which governs the plastic flow.

Figures 3.1a, 3.1b, and 3.2 show the uniaxial behavior of concrete in this model while subjected to tension, compression and cyclic loads respectively. The stiffness degradation upon unloading and stiffness recovery at load reversals can be seen in the figures. Parameters d_c and d_t account for stiffness degradation upon unloading. When concrete undergoes plastic strains in tension and compression, it typically loses a portion of its initial stiffness in the unloading phase, which can be modeled by the stiffness degradation parameters (using values of d_t and d_c less than 1), as shown in Fig. 3.1. At end of the unloading process, when the loading starts in the reverse direction, it is sometimes possible to recover the lost stiffness when the cracks that have opened in tension start to close and resist load again under compression, leading to stiffness recovery (modeled using w_c as shown in Fig. 3.2). This process cannot happen when going from compression to tension ($w_t=0$). Additional details about the formulation of this constitutive model can be found in ABAQUS theory manual (SIMULIA 2012). The Concrete Damaged Plasticity model uses a yield

condition based on the yield function proposed by Lubliner et al. (1989) and incorporates the modifications proposed by Lee and Fenves (1998) to account for different evolution of strength under tension and compression. Fig. 3.3 show the model's yield surface in plane stress conditions.

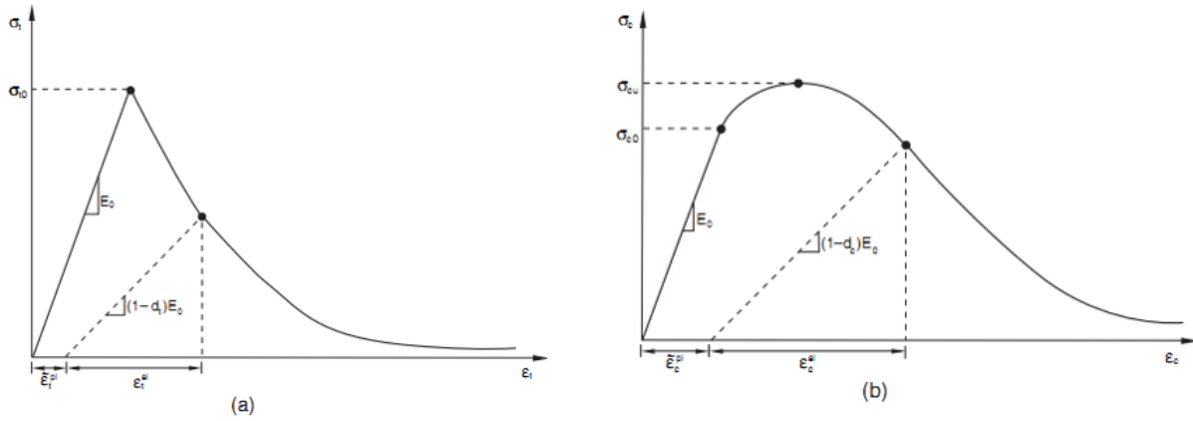


Figure 3- 1 Uniaxial behavior of Concrete Damaged Plasticity model (a) in tension, (b) in compression from ABAQUS theory manual (SIMULIA 2012)

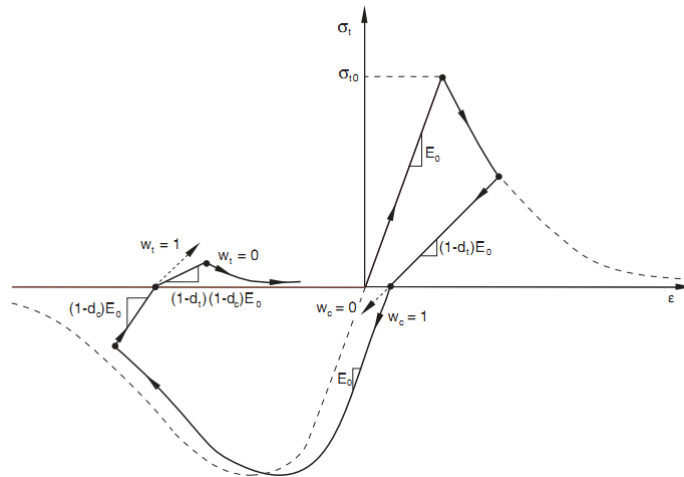


Figure 3- 2 Uniaxial load cycle (tension-compression-tension) for Concrete Damaged Plasticity model from ABAQUS theory manual (SIMULIA 2012)

One important issue, according to the ABAQUS theory manual, is that, simulating the behavior of concrete subjected to extreme confinement pressures is beyond the validated range of the Damaged Plasticity model. Therefore it is important to have an estimation of the confinement pressure applied to the concrete in different problems before using this model. According to the manual if the pressure is above 4 to 5 times the ultimate compressive strength under uniaxial direction, the model is unlikely to give reasonable results.

This issue will be checked for the specimens considered in this project in the pre-test verifications of the model in section 3.3.

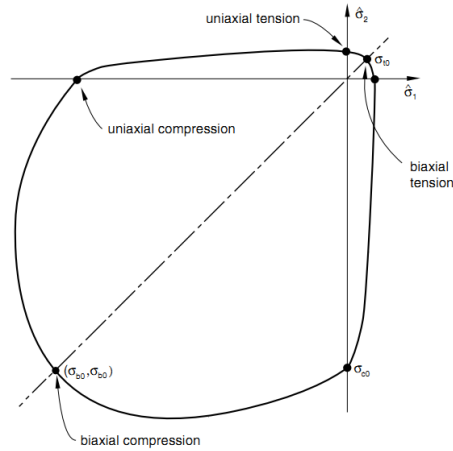


Figure 3- 3 Yield surface for Concrete Damaged Plasticity model in plane stress conditions from ABAQUS theory manual (SIMULIA 2012)

3.2.3 Steel-Concrete Interface

Contact between steel and concrete must be modeled in concrete filled steel tubes, as well as in double skin concrete filled tubes. The models used for this purpose must be able to account for the forces to be transferred at the interface when these surfaces are in contact, while allowing the two materials to separate from each other if needed. Two situations are possible for these surfaces through the whole loading process, including the times that they are actually in contact and times they are separated from each other because of the deformations of the tubes and concrete core.

Typically, this contact interface is modeled by generating a surface based interaction in the finite element program, (which is ABAQUS in this study), with two sets of properties for the normal and tangent directions. In the direction normal to the contact surfaces, the contact elements are able to transfer pressure when the surfaces are in contact with each other, and allow them to separate without any pressure between the two materials. This can be achieved simply by defining a hard contact property for the normal direction in ABAQUS. In the tangent direction, coulomb friction is used to model the tangent forces transferred in the interface when there is a normal pressure between the two surfaces; these are shear forces developed in the tangent direction, corresponding to the normal pressure multiplied by a friction coefficient. This was defined in ABAQUS by creating a tangential behavior property for the interaction with a penalty friction formulation. In this stage the only parameter needed to complete the interaction model is the friction coefficient. According to a study by Baltay and Gjelsvik (1990), the coefficient of friction between steel

and concrete can be between 0.2 and 0.6. In past studies, a friction coefficient value of 0.20-0.3 has been typically used, showing acceptable results compared to experiments (Johansson and Gylltoft 2001; Espinos et al. 2010). Friction coefficient of 0.2 is accepted to be used in the finite element models of this project.

3.3 Pre-test Verification for Cyclic Lateral Loading

This section first examines different options for finite element models to determine which modeling alternatives best represent past analytical and experimental studies. Next, the selected modeling options are combined with the material and interface models discussed in the previous section to build a complete finite element model of a CFDST column. Finally, the adequacy of this model to replicate the experimentally observed behavior of specimens subjected to cyclic lateral loading is verified.

3.3.1 Hardening Model for Steel Material

To investigate the effectiveness of different strain hardening models in capturing the cyclic behavior of interest here, past experiments of a bare steel tube subjected to cyclic lateral loading are replicated in ABAQUS using the three aforementioned hardening options, namely the elastic perfectly plastic with no hardening, linear isotropic hardening and linear kinematic hardening.

Fig. 3.4 shows the results from the experimental study by Goto et al. (1998) (shown with dashed line in Fig. 3.4a), and the results from numerical simulations done here (Fig. 3.4b). The peak value of H/H_y (normalized lateral load) is about 1.3-1.4 for the experimental results, where H is the lateral load and H_y is the yield lateral load. Comparing with the results from finite element analyses, the model with elastic-perfectly plastic (no hardening), and the model with linear kinematic hardening show a similar peak H/H_y value of 1.4, but the case with isotropic hardening shows a peak value of 1.5. Another observation is that the peak negative values of lateral load occur at negative displacements for the experimental results similar to the models with no hardening and linear kinematic hardening. The model with isotropic hardening, however, has its negative peak lateral load at a positive displacement. Note that the models with no hardening and linear kinematic hardening better replicate the experimental results, and between these two, kinematic hardening provides the better overall match, as shown in Fig. 3.4.

Numerical simulations by Goto et al. also suggested that apart from their proposed sophisticated three-surface hardening model which provided satisfactory results, the kinematic hardening model may be used

as an acceptable alternative for practical purposes. Therefore, the linear kinematic hardening model for steel was selected at this stage to be used in the finite element analyses in this project.

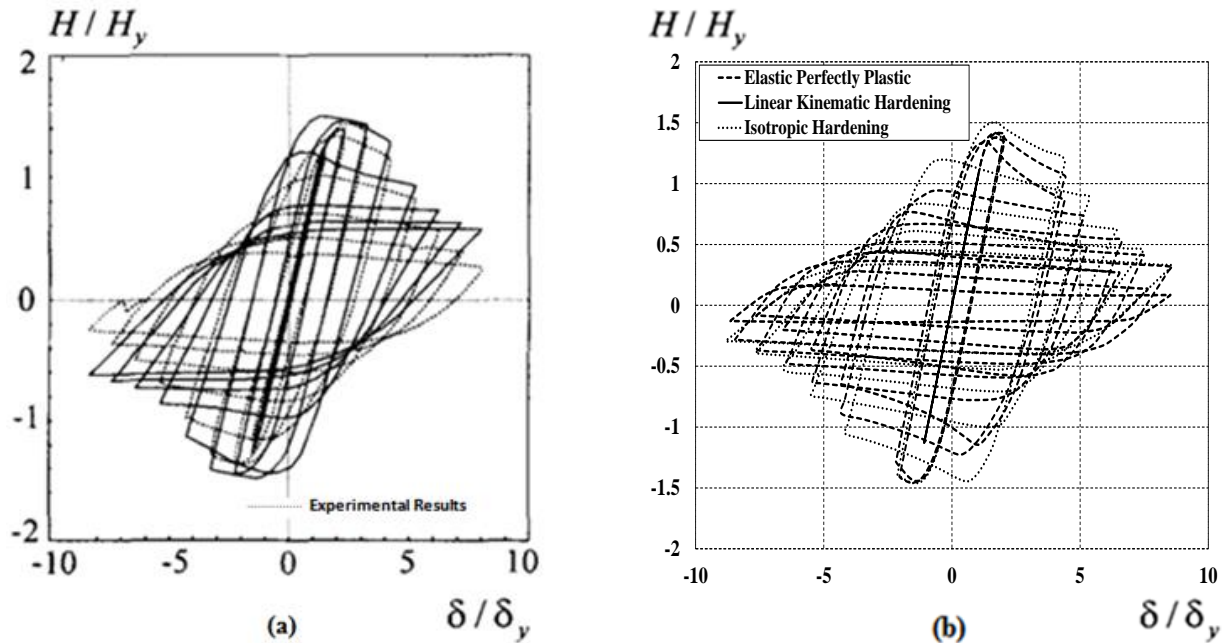


Figure 3- 4 Lateral load vs lateral displacement hysteresis curve for bare steel tube

- (a) Experimental and analytical results (Goto et al. 1998) (Dashed line shows experimental results)**
- (b) Finite element analysis results for different hardening models**

3.3.2 Element Type for the Steel Tube

The selection of elements to model the steel tube was evaluated by two examples including a classical problem with an analytical solution and a specimen from past experimental studies by McCormick et al. (2010). Both of these examples have thin cylindrical steel sections that are subject to bending. This is similar to the conditions of the steel tubes used in the CFDST columns. Finite element analyses were conducted for these examples using both the shell and solid elements. The shell element types selected for the analyses included the 4-node general purpose, 8-node thin, and 8-node thick shell elements. As for solid elements, the 8-node linear and 20-node quadratic types were selected. These elements were checked with and without reduced integration formulation. Detailed discussion of the results for these analyses to select the best element type to capture the inelastic cyclic behavior of a steel tube, is presented in appendix A. Fig. 3.5 shows a few examples of the results of these analyses, including the moment-rotation results from experiments by McCormick et al. (2010) and the numerical results obtained using different shell and solid

elements in the finite element models developed here. Mesh refinement was performed separately to reach the best results for each particular element type.

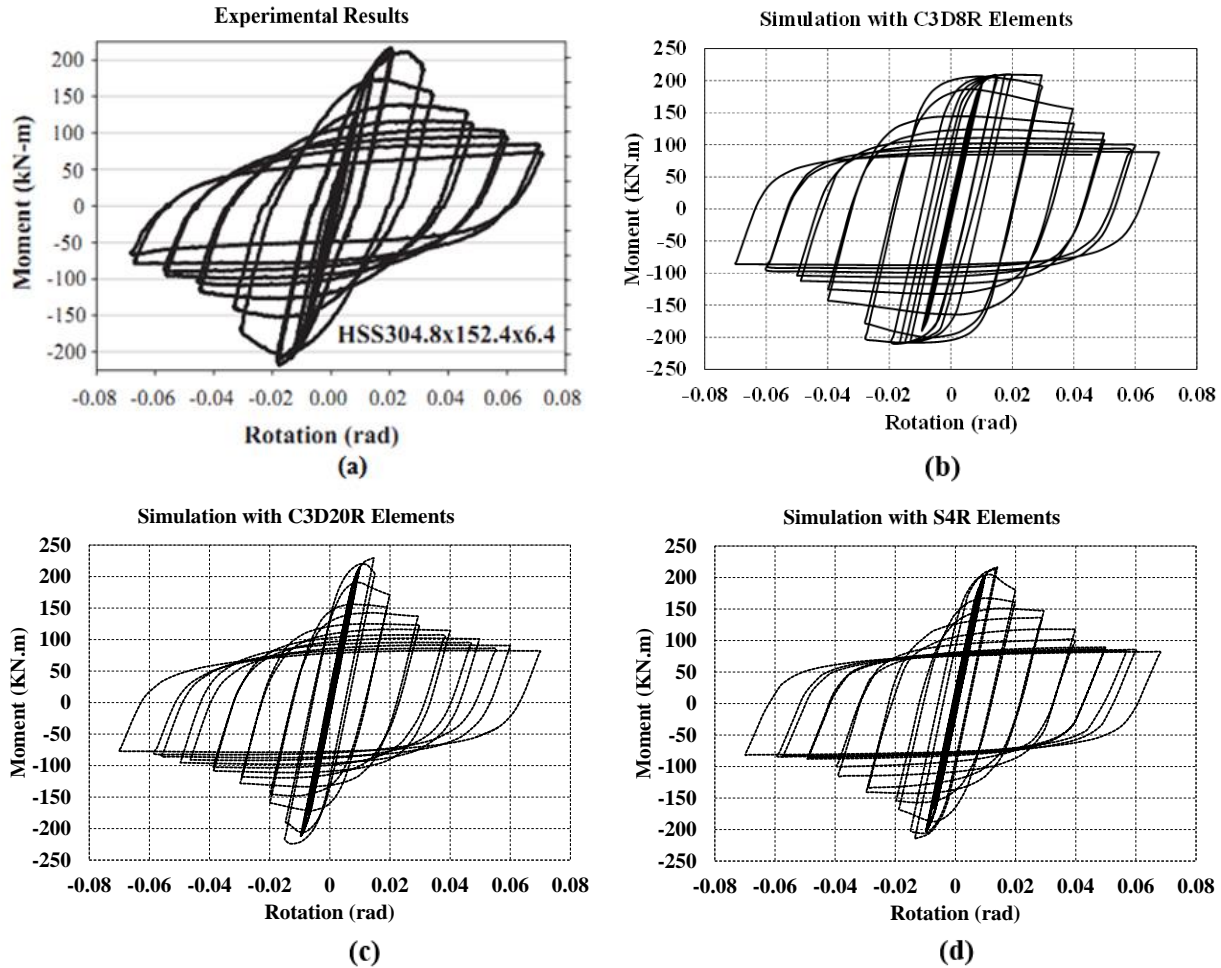


Figure 3- 5 Moment-rotation results for cyclic tests of steel tubes: (a) Test results by McCormick et al. (2010), (b) model with C3D8R solid elements, (c) model with C3D20R solid elements (d) model with S4R shell elements

In Fig. 3.5, C3D8R refers to the 8-node 3D solid element, C3D20R refers to 20-node 3D solid element and S4R refers to the 4-node shell element. All of these element types use the reduced integration formulation, which is identified by the letter “R” in their code name. Fig. 3.5 shows that all of the element types were able to provide relatively accurate results after mesh refinement. Note that the 20-node solid element provided acceptable results using a relatively coarser mesh compared to the 8-node solid and 4-node shell elements. However, the 20-node solid (and similarly 8-node shell) elements use quadratic equations and

are computationally more expensive to be used in complex structures compared to the 8-node solid and 4-node shell elements.

Comparing the summarized results shown in Fig. 3.5 (discussed in detail in Appendix A), it was inferred that both the 4-node shell (S4R) and 8-node solid (CD38R) elements were able to provide acceptable results if used with suitable mesh pattern for the specific problem. Note that this is contingent on identifying the parts of the structural members that will be subject to local buckling and large inelastic deformations and using a finer mesh pattern at those areas (solid elements need to be finer than shell elements at the locally buckling areas). Inability to capture these excessive deformations, stress concentrations and local instabilities will negatively impact the results. Therefore, the 4-node shell element with reduced integration (S4R) was selected as the first choice for the modeling of the steel tube in the following parts of this study, because, compared to the solid element, it needed less mesh refinements at the locally buckling areas. Note that the 8-node solid elements were also used in a number occasions, where there was a possibility of improvement in the simulation results and also for comparative purposes.

3.3.3 Modification of Concrete Damaged Plasticity Model to Include the Confinement Effects

Although it is expected that the confinement pressure applied to concrete in the specimens of this project will be low enough to keep the results from the Concrete Damaged Plasticity model valid, it will still have some effects on the material's behavior that can be considered in the analyses by a few modifications. Many researcher (Mander et al. 1988; Usami et al. 2001; Sakino et al. 2004) have shown that concrete confined by a circular steel tube can exhibit increased strength and ductility as illustrated in Fig. 3.6.

These effects can be considered in the Damaged Plasticity model by modifying the stress-strain expression ($f_c - \varepsilon$) of concrete in uniaxial compression defined by Popovics (1973) and later modified by Mander et al. (1988), to become:

$$f_c = f'_{cc} \frac{x^r}{r - 1 + x^r} \quad (3.5)$$

$$x = \frac{\varepsilon}{\varepsilon_{cc}} \quad (3.6)$$

$$r = \frac{E_c}{(E_c - f'_{cc}/\varepsilon_{cc})} \quad (3.7)$$

$$\epsilon_{cc} = \epsilon_c \left[1 + 5 \left(\frac{f'_{cc}}{f'_c} - 1 \right) \right], f'_{cc} = f'_c + m f_{rp} \quad (3.8)$$

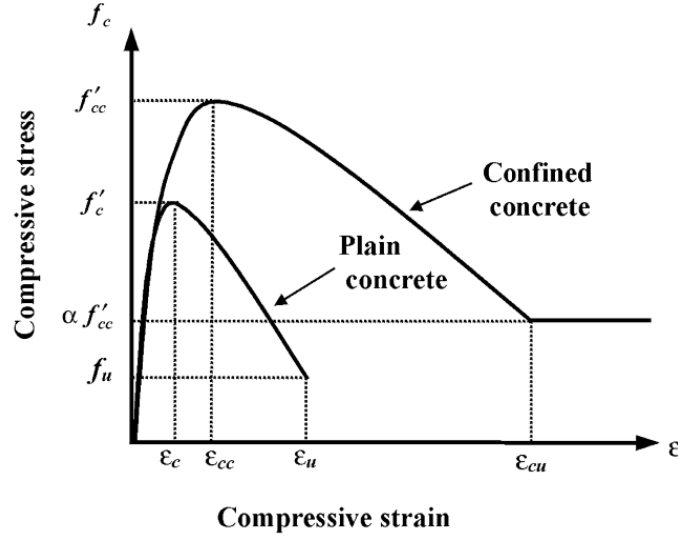


**Figure 3- 6 Strain curves for unconfined and confined concrete enclosed in steel tube
(Usami et al. 2001)**

where f'_c and ϵ_c are the maximum strength and corresponding strain value for unconfined concrete, f'_{cc} and ϵ_{cc} refer to the same parameters for confined concrete, and E_c stands for the modulus of elasticity of concrete. f_{rp} is the maximum radial pressure on concrete and m is an empirical coefficient (in the range of 4-6). It should be mentioned that this expression works for the whole uniaxial curve (before and after peak), but it is also common to model the post-peak behavior as a linear descending branch, starting from the peak point and ending at the point with the coordinates $(\epsilon_{cu}, \alpha f'_{cc})$, after which the material is taken to have a constant stress $\alpha f'_{cc}$ referred to as the residual stress.

Since it is difficult to come up with a mathematical expression for the parameter ϵ_{cu} , it is considered here as having a constant value of 0.025 in all cases, which can be considered acceptable based on the analyses done by Usami et al. The α multiplier is determined by calculating the softening slope (Z), from the peak point; for concrete confined having circular sections, and Usami et al. have proposed the following equations to calculate Z , based on calibration with experimental data:

$$Z = \begin{cases} 0 & \text{for } R_t(f'_c/f_y) \leq 0.006 \\ 1.0 \times 10^5 R_t \frac{f'_c}{f_y} - 600 & \text{for } R_t(f'_c/f_y) \geq 0.006 \text{ and } f_y \leq 283 \text{ MPa} \\ 1.0 \times 10^5 R_t \frac{f'_c}{f_y} - 6000 & \text{for } R_t(f'_c/f_y) \geq 0.006 \text{ and } f_y \geq 283 \text{ MPa} \\ \left(\frac{f_y}{283}\right)^{13.4} \left[1.0 \times 10^5 R_t \frac{f'_c}{f_y} - 600\right] & \text{for } R_t(f'_c/f_y) \geq 0.006 \text{ and } 283 \text{ MPa} \leq f_y \leq 336 \text{ MPa} \end{cases} \quad (3.9)$$

where f_y is the yield stress of steel, and R_t is the radius to thickness ratio parameter defined by:

$$R_t = \sqrt{3(1 - \nu^2)} \frac{f_y D}{E_s 2t} \quad (3.10)$$

in which D and t are the outer steel tube's diameter and thickness respectively. After calculation of Z , the parameter, α , is given by:

$$\alpha = 1 - \frac{Z(\varepsilon_{cu} - \varepsilon_{cc})}{f'_{cc}} \quad (3.11)$$

It should be mentioned that Usami et al. recommend the use of a reduction factor of 0.85 for the strength of unconfined concrete, similar to what is used in design specifications of ACI 318. Now the next step is to implement these confinement effects in ABAQUS's Concrete Damaged Plasticity model. Based on experience it is known that ABAQUS can capture the increase in the compressive strength due to confinement but is incapable of capturing the added ductility. Therefore, instead of using a modified stress-strain relationship like Usami et al.'s model, a new relationship must be defined which has the added ductility without the added strength. This is possible by making minor modifications to the model proposed by Usami et al. A scale factor can be applied to Usami's confined concrete stress-strain relationship to get back to the compressive strength of the unconfined concrete, or a plateau can be added to the stress-strain curve of unconfined concrete.

3.3.4 Verification of Modeling Assumptions for Cyclic Lateral Loading

A CFDST previously tested by Han et al. (2006) was selected for verification of the model that was developed based on the modeling assumptions discussed in the previous sections. Han et al. (2006) studied

different double skin concrete filled steel sections with circular and rectangular shapes subjected to axial load and cyclic bending. The specimen labeled cc-23 was selected here because of its similarities with this project's specimens.

The 1500mm long column was built with outer and inner circular steel tubes with diameters of 114mm and 32mm, respectively. Both of the tubes were 3mm thick. The outer and inner tubes were made of steel materials with different yield strength values, which were reported equal to 308MPa and 422.3 MPa, respectively. A constant axial load of 306kN was applied to the specimen, which was equal to 43% of the ultimate axial strength of the column. The ultimate lateral strength of the specimen, P_{uc} , was calculated by the authors to be equal to 38.8kN.m based on the assumption of fully plastic section (Han et al. 2006).

Fig. 3.7 shows the experimental setup used by Han et al. to test this specimen. The column was placed in a horizontal position, and its end plates were attached to clevises that could rotate in plane simulating pin-pin boundary conditions. The axial load and the cyclic lateral loads were applied using two hydraulic rams as shown in Fig. 3.7. Cyclic load was applied in a displacement-controlled mode, while the axial load was applied in a force-controlled manner. Fig. 3.8 shows the section of the cc-23 specimen including the inner and outer steel tubes and the infill concrete. Han et al. assumed the modulus of elasticity of steel to be 200,000 MPa and the concrete compression strength was measured to be about 40 MPa for the specimens.

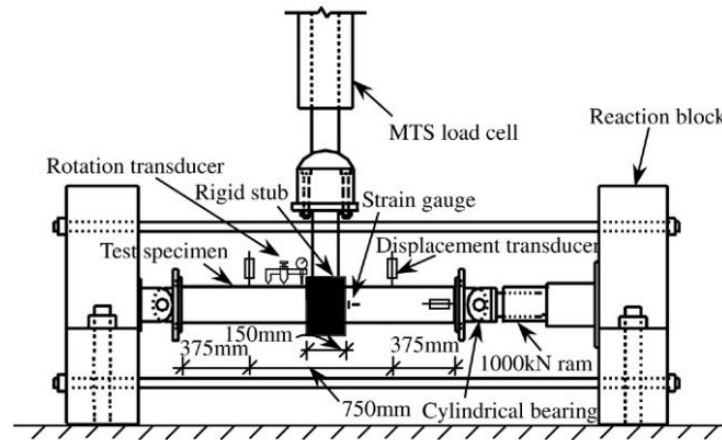


Figure 3- 7 Schematic View of Test Setup (Han et al. 2006)

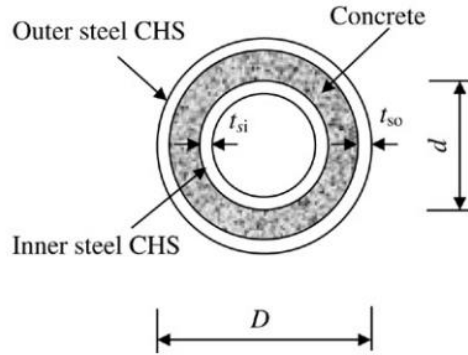


Figure 3- 8 Circular Section of cc-23 Specimen

The FEM model was built according to the assumptions and techniques explained in the previous sections. Both of the steel tubes were modeled using 4-node shell elements (S4R) and the concrete core was meshed using the 8-node solid elements (C3D8R). To reduce computation time, the model was meshed with a non-uniform mesh size, with finer meshing in the regions with expected inelastic response. For specimen cc-23, it is known from the experiments that these regions are the stub ends at the center, where, yielding and local buckling developed. Fig. 3.9 shows the meshed model.

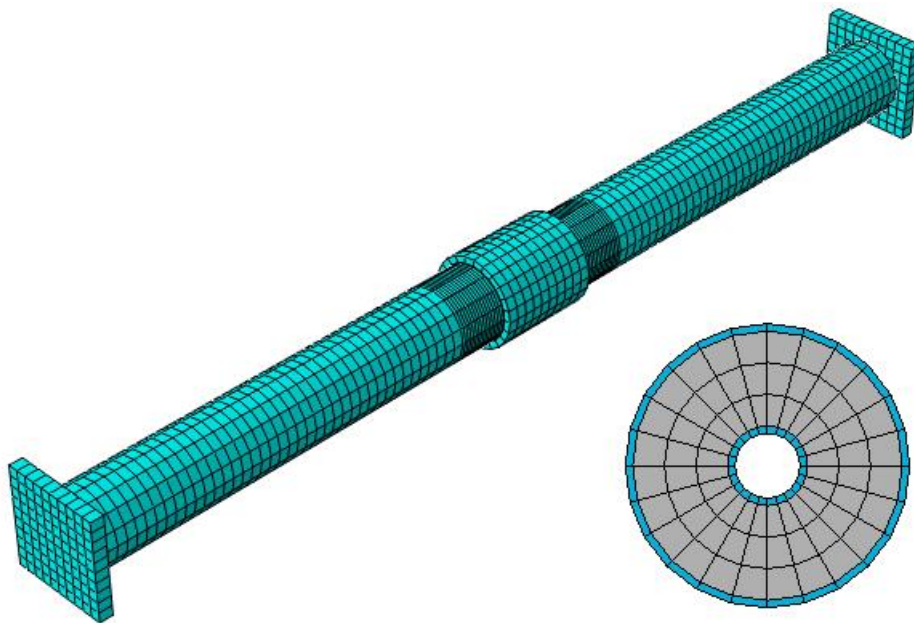


Figure 3- 9 Meshed Model of cc-23 Specimen

Steel plates at both ends of the specimen were used to apply the loads and boundary conditions to the columns. The boundary conditions applied to the model are pinned-pinned at both ends while one end is

allowed to have axial displacement as in the test setup. Axial load was applied as a constant pressure on the end plate and the lateral load was directly applied to the stub, which was modeled to act nearly rigid. This rigidity can be simulated by a relatively high modulus of elasticity for the stub's steel material, compared to the other parts of the model. Lateral load was defined by a displacement history based on the ATC-24 guidelines for cyclic testing of structural steel components. The secant stiffness of the specimen when the lateral load reached the value of $0.7P_{uc}$ for the first time was used to determine the yield level lateral displacement ($\Delta_y = \frac{0.7P_{uc}}{K_{sec}}$). P_{uc} is the theoretical ultimate lateral strength of the specimen calculated based on the assumption of fully plastic section.

Steel and concrete were modeled using the material properties mentioned in Han et al. For steel, a simple bilinear model with linear kinematic hardening was implemented. Strain hardening rate was selected to be equal to 3% of the initial elastic stiffness of the steel material. Concrete was modeled using the Damaged Plasticity model. Figures 3.10 and 3.11 show the stress-strain relationships used for concrete and steel in the finite element model.

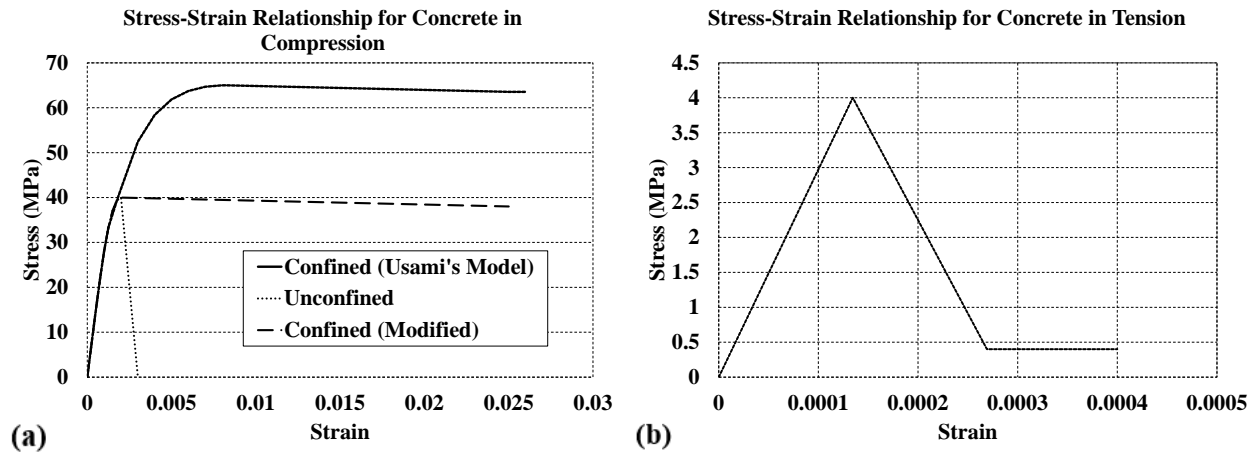


Figure 3- 10 Stress-strain relationships used in Concrete Damaged Plasticity model:

(a) confined concrete in compression, and (b) concrete in tension

Fig. 3.10a shows three stress-strain relationships for concrete material in compression (i.e. curve for unconfined condition, Usami's confined model, and the modified confined model). The modified model for confined concrete (used in this study) has the ductility enhancement caused by the confinement and not the strength enhancement, since the latter is accounted for in the analysis by ABAQUS. For the behavior of concrete in tension (shown in Fig. 3.10b), the tensile strength of concrete, f_t , was assumed equal to 10% of the compressive strength, with an elastic modulus equal to one used for compression ($4700 \sqrt{f'_c(MPa)}$).

The post-peak behavior was modeled with a linear descending branch, which continues up to two times the cracking strain (the strain at the end of the elastic part) and maintains a residual strength of $0.1f_t$. Note that the strain value at the end of the descending branch (two times the cracking strain) was chosen conservatively. The residual tensile strength does not have any physical significance and was selected to be slightly above zero to facilitate the computational process.

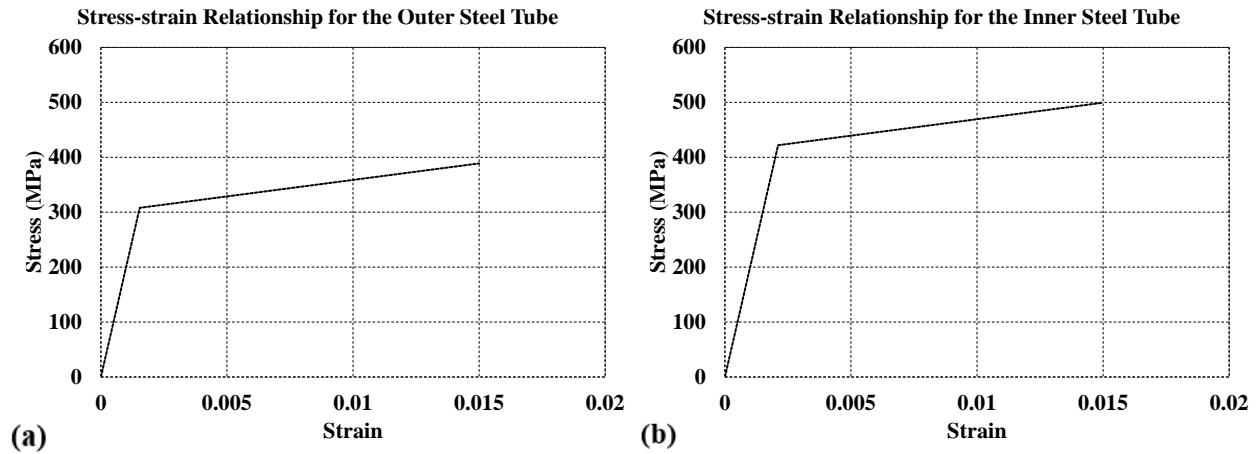


Figure 3- 11 Stress-strain relationships used for the steel material model with linear kinematic hardening: (a) outer steel tube, and (b) inner steel tube

Damage parameters needed for the Damaged Plasticity model were calculated based on the stress-strain curves given in Fig. 3.10 for compression and tension sides. Considering the strain corresponding to the maximum stress in compressive and tensile uniaxial stress-strain curves to be referred to as $\varepsilon_{f'_c}$ and ε_{f_t} , damage parameters for compression and tension (d_c and d_t) for a given strain value, ε , were assumed to be equal to zero if $\varepsilon \leq \varepsilon_{f'_c}$ or ε_{f_t} . For values of $\varepsilon > \varepsilon_{f'_c}$ or ε_{f_t} , the damage parameters were calculated as $d_c = 1 - \sigma_\varepsilon / f'_c$ and $d_t = 1 - \sigma_\varepsilon / f_t$, where σ_ε is the value of stress corresponding to the strain, ε , in the compressive or tensile uniaxial stress-strain curve.

As mentioned in section 3.2.2, the Concrete Damaged Plasticity model may not capture the behavior of concrete material correctly at high confinement pressures. Maximum confinement pressure equal to 4 to 5 times the uniaxial compressive strength is recommended in the ABAQUS theory manual to be the limit for reliable performance of the Concrete Damaged Plasticity model. To approximately check this condition for the specimen considered in this verification example, the confinement pressure can be calculated based on the free body diagram shown in Fig. 3.12.

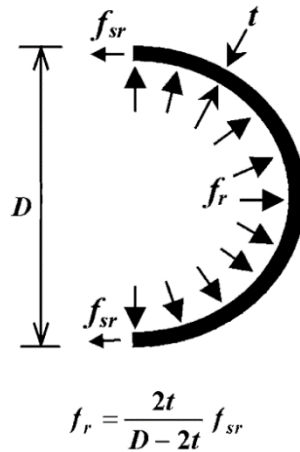


Figure 3- 12 Free body diagram of the steel tube section used for confinement (Usami et al. 2001)

In Fig. 3.12, f_r is the radial pressure (confinement pressure), and f_{sr} refers to the hoop stress in steel tube. The maximum possible hoop stress happens at the yield stress of steel material, f_y . Based on the formula shown in Fig. 3.12, for a steel tube with yield stress of 308MPa, diameter of 114mm, and thickness of 3mm, maximum confinement pressure equals 17.11MPa. This pressure is about 40% of the maximum uniaxial compressive strength of the concrete. This is below the maximum limit by a large margin, and it is calculated for the yield limit of the steel tube. The confinement pressure will be in lower levels most of the time during the cyclic loading and the validity issues of the Concrete Damaged Plasticity model due to high confinement pressures can be neglected here.

The interaction at the steel-concrete interface was modeled using the assumptions and modeling techniques presented in section 3.2.3. A surface based interaction was defined with hard contact properties in the normal direction allowing the separation of the surfaces. In the tangent direction, a coulomb friction model was used, with a coefficient of friction equal to 0.2 that produces shear resistance in the presence of normal pressure. The top and bottom plates were tied to the steel tubes and just a hard contact interaction was defined for the interface between the steel plates and concrete. To replicate the test by Han et al., two analyses were conducted here on the model. First, a monotonic lateral loading analysis was conducted to determine the yield level lateral displacement of the model. The lateral yield displacement was used to create the displacement history for the cyclic loading based on the ATC-24 specifications for cyclic tests of metals. Next, the analysis with the cyclic lateral load was conducted in a displacement controlled mode. According to ATC-24 the applied displacement was defined with cycles that follow an increasing pattern. The applied displacement history is shown in Fig. 3.13.

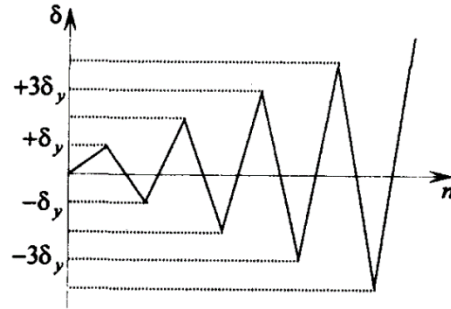


Figure 3- 13 Applied cyclic displacement pattern

Figures 3.14a and 3.14b show the lateral load versus displacement hysteresis curves for the cc-23 specimen from experimental data (Han et al. 2006) and analysis results (conducted in this study), respectively. Note that Fig. 3.14a also shows the results of the numerical analysis conducted by Han et al. in the same reference. The graphs in Fig. 3.14b indicate that the finite element model has replicated the experimental results with sufficient accuracy. The model captured the stiffness and strength of the specimen going through increasing amplitudes of cyclic displacements. The two curves plotted in Fig. 14b are from two similar finite element models with different mesh sizes, which were analyzed to check the mesh-sensitivity of the results. Results showed only a marginal difference, thus approving the proper choice of the mesh size.

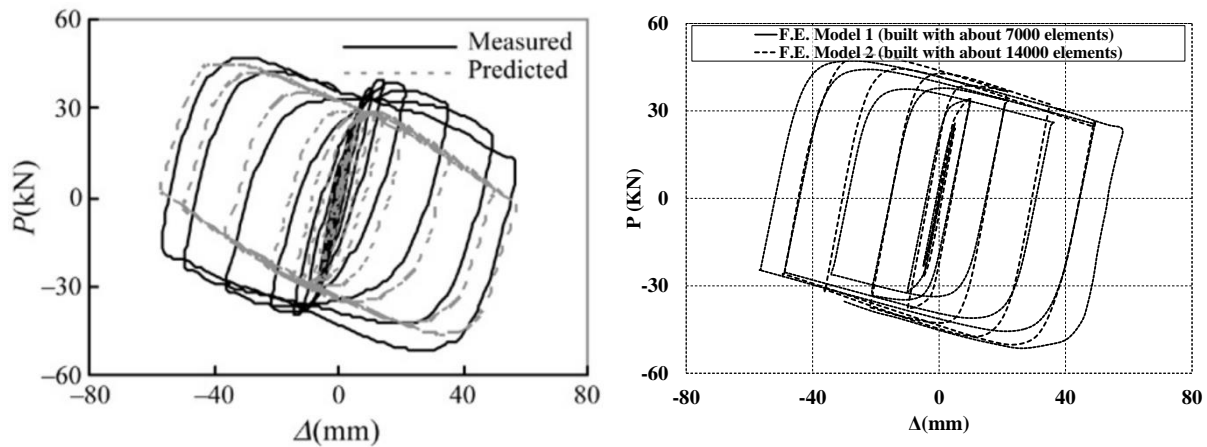


Figure 3- 14 Cyclic load versus lateral displacement for cc-23 specimen: a) ABAQUS analysis results for models with different mesh sizes, (b) Experimental results (Han et al. 2006)

Note that the initial mesh size was selected after conducting a few number of analyses to reach a close replication of the experimental results. Upon reaching an acceptable numerical result, the mesh size was refined one step further for sensitivity checks. Results presented above complete the pre-test verification of

the modeling assumptions and material types chosen for the numerical simulation of the cyclic testing of CFDST columns. Further investigation of the finite element model was left for the post-test validation process, presented in Section 6, using the experimental results from the tests conducted and in this study (presented in Sections 4 and 5).

3.4 Finite Element Model for Simulating the Effect of Fire on a Steel-concrete Composite Member

3.4.1 Introduction to Thermal-Stress Problems

The effect of fire on a structural member can be simulated by conducting finite element analysis of that member subjected to a thermal load. This kind of thermal-stress problem includes both thermal and structural aspects, taking into account changes in temperature, thermal expansion, heat transfer, stress/deformation, and issues related to the simultaneous application of thermal and structural loads. An important issue to capture is the interaction between thermal and structural loads.

Applying thermal loads to a structure leads to changes (over time) in the distribution of temperatures within the structure itself. Increasing temperature will cause stresses and deformations in the structure due to thermal expansion of the material. Additionally, most materials have thermal and mechanical properties that are dependent on temperatures. Therefore, when temperature changes, the material will behave differently and more complicated models are necessary to capture these effects.

Considering the issues mentioned above, a complete thermal stress analysis can be performed in two different ways. The first approach is to perform a fully coupled thermal stress analysis in which the stress/displacement and temperature fields are solved simultaneously. The second approach is to perform a sequentially coupled thermal stress analysis in which the stress/displacement field is dependent on the temperature field but the inverse dependency is not considered. Although the first approach is more realistic, it is computationally intensive. Previous studies have shown that the second approach can give reasonably acceptable results (Hong and Varma 2009; Espinos et al. 2010).

To further examine the interaction between thermal and structural loading, an example is studied here. A double skin concrete filled column with a constant axial load is subjected to a standard fire to create an example of thermal stress problems. Time plays an important role in this scenario because as the column heats continuously and reaches higher temperatures, degradation occurs in materials properties (for both

steel and concrete), until the point when the column is no longer able to resist its axial load, leading to its failure.

The fully coupled thermal stress analysis captures the two-way dependency of the temperature field and stress/deformation field. The dependency of the stress/deformation field on the temperature field was discussed above and is a general aspect of any thermal-stress problem. This dependency in the reverse direction should be studied specifically for the structural members that are examined in this project.

One of the parameters that affect the heat transfer mechanism in the CFT columns is the rate of heat conductance from the steel tube to the concrete core. While the column is subjected to thermal and structural loads, the steel tube and the concrete core can be in contact or separated because of the relative displacements and expansion of the material. When they are separated, heat has to transfer through that gap mainly by radiation and convection mechanisms. This transfer happens at a lower rate compared to the situation in which the two materials are in contact. The varying rate of conductance between the steel tube and concrete core is referred to as the “gap conductance” and is the source of dependency of the temperature field on the stress/deformation field.

The main reason for the changes in the gap conductance value is the changes in the void size at the location of the separation. Therefore, the heat transfer between the steel and concrete will occur at a different rate, affecting the results of the temperature field. Considering this situation, a fully coupled approach will provide better results, but this added complexity may not be necessary in the current context, because if the changes in gap conductance value are considered, a sophisticated and reliable equation relating the gap conductance to the clearance between the steel and concrete surfaces should be provided. Even though there are some models in the literature defining a linear or nonlinear relation for gap conductance as a function of clearance, the fact remains that, by using any of these models, a new source of uncertainty will be added to the problem, making the situation more complicated without necessarily improving the accuracy of the results.

Moreover, the dependence of temperature field on stress/deformation solution that controls the gap conductance is not strong in this case, as has been shown by results from previous experimental and analytical studies (Hong and Varma 2009; Espinos et al. 2010). Finally, although a lesser concern, the computational time required for analysis is also a factor. Performing a fully coupled thermal stress analysis for a complicated model takes a relatively longer time because the thermal and structural equations must be solved simultaneously. This makes the sequentially coupled analysis approach preferable.

For all of the above reasons, the current research project only considers the one-way dependency of stress/deformation solution to the temperature field and neglects the reverse dependency. It is noteworthy that past studies, in which finite element simulations of CFDSTs or CFSTs under fire were conducted, did not use fully coupled analyses. In this regard, Hong and Varma (2009) reported extensive convergence problems of the fully coupled method for the finite element simulation of CFST columns under fire, but showed that the sequentially coupled method produced results that matched the experimental data. To account for gap conductance, a constant average value will be used to compensate for the changes due to different clearance values through the real test. This procedure has been used and shown to be acceptable by other researchers in the past (Hong and Varma 2009; Espinos et al. 2010).

In this section, the modeling procedure for the problem at hand is done in two parts, i.e. using the sequentially coupled analysis. The first part is dedicated to the heat transfer analysis while neglecting the stress/deformation field. Section 3.4.2 starts with a summary of the background theory of heat transfer analysis and a brief survey of thermal properties of materials and different models available (as implemented in ABAQUS), followed by a description of modeling of the specimen with thermal material properties and definition of the thermal loads and boundary conditions. Results of this analysis are the history of nodal temperature values for the whole specimen through the thermal loading time.

The second part of Section 3.4.2 starts with a brief survey of how some structural material properties vary with temperature. Different material models exist in the literature and the ones best suited to the problem at hand were selected to determine the model's structural properties. Results from this phase include the stress/deformation solution during the burning time and the fire resisting time for the specimen.

Most of the modeling assumptions made here are based on previous numerical studies that have been shown to provide reasonably accurate simulations of experiments. These assumptions will be verified by comparing the results of a selected example thermal-stress problem modeled here to replicate past experimental results. It is understood that analyses conducted after the experiments will also be done, to verify and possibly correct these modeling assumptions. Incidentally, the experiments may also provide information on some modeling parameters that have not been extensively studied in the past; hopefully, at some points through calibration, finite element analyses may be able to closely replicate the experimental results.

3.4.2 Developing the Finite Element Model for Heat Transfer Analysis

3.4.2.1 Theory of Heat Transfer Analysis

The uncoupled heat transfer analysis in ABAQUS is capable of modeling the heat conduction in solid bodies with a general material conductivity coefficient that can change as a function of temperature. The effects of internal energy can be considered in the formulations through the use of specific heat and latent heat terms. Different types of thermal loads and boundary conditions, including general convection and radiation, can be defined for the model. A summary of formulations used in ABAQUS, including the basic energy balance, constitutive model, boundary conditions, finite element discretization, and time integration is presented in the following paragraphs. Some of the important elements of heat transfer analysis theory are presented here.

3.4.2.1.1 Energy Balance

The basic energy balance equation is based on the works of Green and Naghdi (1965):

$$\int_V \rho \dot{U} dV - \int_S q dS + \int_V r dV \quad (3.12)$$

In this equation, V is the volume of the solid material, S is the area of the surface defining the boundary of the volume, ρ is the material density, \dot{U} is the rate of material's internal energy with respect to time, q is the heat flux per unit area of the body flowing into it, and r is the heat per unit volume supplied to the body. Considering the analogy between this equation and a typical stress formulation for a 3D body, q can be considered as surface pressure/traction while r is similar to body forces (e.g. inertial forces). Eq. 3.12 considers that U is only a function of θ (temperature), which means that the thermal and mechanical parts are uncoupled. Also, q and r do not depend on the strains/displacements of the body. The formulation is done in a Lagrangian framework, so that volume and surface are defined with respect to the reference configuration.

Heat transfer analysis can be performed in steady state and transient modes. The difference between the two is that in the steady state formulation, the internal energy effects from the specific heat terms are neglected in the formulations. Therefore, the problem has no intrinsic physically meaningful time scale. The specific heat is the amount of heat per unit mass required to raise the temperature of the material by

one degree. In a transient mode, the specific heat terms are not neglected, which means that an amount of heat flow during a period of time changes the temperature of the material based on its specific heat. In this research project, the analysis is performed in transient mode because the fire scenario is defined with a time scale raising the temperature from room conditions up to 1000°C.

3.4.2.1.2 Constitutive Definition

Ignoring the coupling between thermal and mechanical problems, the constitutive relation is written as:

$$c(T) = \frac{dU}{dT} \quad (3.13)$$

where, c is the specific heat, U is the internal energy and T represents the temperature. Based on Eq. 3.13, the internal energy will be defined in terms of specific heat. This formula will change for the cases of thermal problems that include a material phase change. In these problems, the effects of latent heat, defined as the total internal energy associated with the phase change, should also be considered. No solid to liquid phase change will happen to steel and concrete at the temperatures expected to develop in a fire. The only phase changes will happen for the water in the concrete vaporizing during the fire, and for steel at temperatures above 700°C that changes the positioning pattern of its atoms. These will be accounted for by simple modifications of the specific heat functions of the concrete and steel.

3.4.2.1.3 Heat conduction

Heat conduction in a solid material is defined based on the Fourier law,

$$f = -k \frac{\partial T}{\partial x} \quad (3.14)$$

where k is the conductivity matrix and can be a function of temperature, f is the heat flux and x is the position. The conductivity matrix has the options to be defined as fully anisotropic, orthotropic, and isotropic. For steel and concrete, it is usually isotropic.

3.4.2.1.4 Boundary conduction

Boundary conditions can be defined as prescribed temperature, prescribed surface heat flux, or prescribed volumetric heat flux, all with respect to time and position. Surface convection is also possible to define:

$$q = h(T - T^0) \quad (3.15)$$

where h is the film coefficient, q refers to the heat flux and T^0 is the sink temperature, all of which can be dependent on time and position. Surface radiation can also be applied by:

$$q = A[(T - T^z)^4 - (T^0 - T^z)^4] \quad (3.16)$$

in which A is the radiation constant (emissivity time the Stefan-Boltzmann constant) and T^z is the value of absolute zero on the temperature scale being used. Cavity radiation effects can also be defined for surfaces but this feature is beyond the scope of this project. More information about the implementation of heat transfer theory in the finite element method, spatial discretization and time integration can be found in the ABAQUS theory manual (Holman 2009; SIMULIA 2012).

3.4.2.2 Thermal Properties of Materials at Elevated Temperatures

Fire analysis of a structure investigates its performance at extremely elevated temperatures. For that purpose, different material models at elevated temperatures have been proposed for steel and concrete. Two of the most frequently used sources are the models provided by Eurocode 4 general rules for structural fire design (CEN 2005), and NIST (2010). The thermal properties used in the models for heat transfer analysis are the specific heat and thermal conductance of the material. Thermal expansion can also be considered among these properties but due to its effects on stress/deformation field, it will be discussed in the next section of the report.

3.4.2.2.1 Specific Heat

As defined before, the specific heat is the amount of heat per unit mass required to raise the temperature of the material by one degree. Specific heat of steel, c_a , is given in Eurocode 4 as a nonlinear function of temperature as shown in Fig. 3.15 defined at different levels of temperatures by Eq. 3.17. There is a spike in the specific heat value of steel around the temperature of 750 °C. This sudden increase is due to the phase change that occurs in steel in which the atoms transition from a face centered cubic to a body centered cubic structure (steel with carbon content of 0.25% transfers from pearlite to austenite). This process absorbs considerable energy, thus accounting for the spike around 750 °C (Kodur et al. 2010).

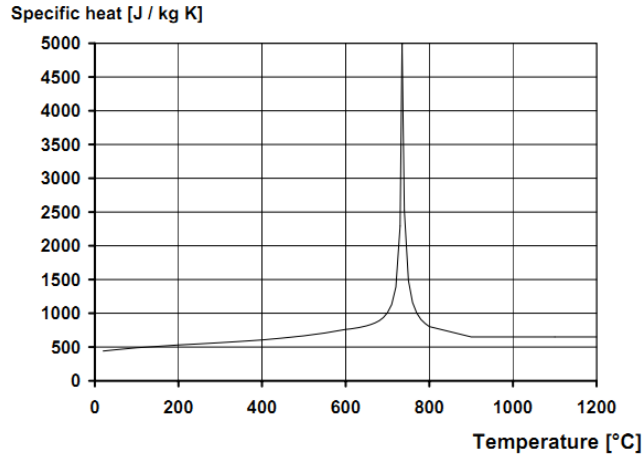


Figure 3- 15 Specific heat of steel as a function of temperature (CEN 2005)

$$c_a = \begin{cases} 425 + 7.73 \times 10^{-1} T_a - 1.69 \times 10^{-4} T_a^2 + 2.22 \times 10^{-6} T_a^3 \frac{J}{kg \text{ } ^\circ C}, & 20^\circ C \leq T_a \leq 600^\circ C \\ 666 + \frac{13002}{738 - T_a} \frac{J}{kg \text{ } ^\circ C}, & 600^\circ C \leq T_a \leq 735^\circ C \\ 545 + \frac{17820}{T_a - 731} \frac{J}{kg \text{ } ^\circ C}, & 735^\circ C \leq T_a \leq 900^\circ C \\ 650 \frac{J}{kg \text{ } ^\circ C}, & 900^\circ C \leq T_a \leq 1200^\circ C \end{cases} \quad (3.17)$$

T_a : Steel temperature, $^\circ C$

Changes in specific heat of concrete with respect to temperature can be seen in Fig. 3.16 which is taken from Eurocode 4 general rules for structural fire design (CEN 2005). As it can be seen in Fig. 3.16, there is a peak at specific heat values for concrete around the temperature of 100-115 $^\circ C$. This peak is inserted in the curve because of the moisture content of the concrete material. Around the temperature value of 100 $^\circ C$, the water content of the concrete mixture starts to evaporate, consuming a portion of the thermal energy. At this stage, thermal energy will be absorbed for the material “phase change” (to the extent that evaporating water in concrete can be assumed to be a phase change), without contribution to the temperature rise. A very large value of specific heat in the curve will consume relatively large amount of thermal energy for just one degree of change in the concrete temperature, simulating the real conditions indirectly. According to the Eurocode 4, specific heat (C_c), for normal weight concrete for different ranges of temperature is given by:

$$C_c = \begin{cases} 900 \frac{J}{kg^\circ C}, & 20^\circ C \leq T_c \leq 100^\circ C \\ 900 + (T_c - 100) \frac{J}{kg^\circ C}, & 100^\circ C \leq T_c \leq 200^\circ C \\ 1000 + (T_c - 200)/2 \frac{J}{kg^\circ C}, & 200^\circ C \leq T_c \leq 400^\circ C \\ 1100 \frac{J}{kg^\circ C}, & 400^\circ C \leq T_c \leq 1200^\circ C \end{cases} \quad (3.18)$$

T_c : Concrete temperature, °C

The effects of moisture content can be considered in the model through the latent heat effects in a more sophisticated analysis, but, for the purposes of this project and in most applications to structural engineering problems, this effect is defined in the model as an artificial peak of specific heat at 100-115°C. Therefore, when the model's temperature reaches that level, an extra amount of energy will be used to cross that peak, compensating for the latent heat effects.

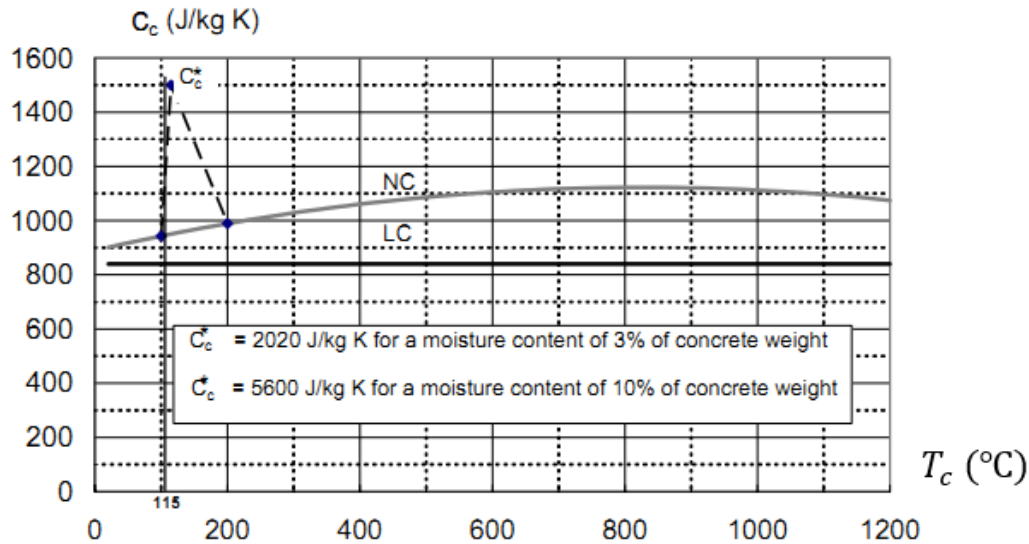


Figure 3- 16 Specific heat of normal weight (NC) and light weight (LC) concrete as a function of temperature (CEN 2005)

3.4.2.2.2 Thermal Conductance

Thermal conductance, λ_a , is a measure of the ability of a material to transfer heat per unit time, given one unit area of the material and a temperature gradient through the thickness of the material. Figs. 3.17 and

3.18 show the thermal conductance of steel (λ_a) and concrete (c_c) as a function of temperature. These curves are defined with Eq. 3.19 and 3.20 for steel and concrete respectively (CEN 2005).

$$\lambda_a = \begin{cases} 54 - 3.33 \times 10^{-2} T_a \text{ W/m}^\circ\text{C}, & 20^\circ\text{C} \leq T_a \leq 800^\circ\text{C} \\ 2.73 \text{ W/m}^\circ\text{C}, & 800^\circ\text{C} \leq T_a \leq 1200^\circ\text{C} \end{cases} \quad (3.19)$$

T_a : Steel temperature, °C

$$c_c = 890 + 56.2 \left(\frac{T_c}{100} \right) - 3.4 \left(\frac{T_c}{100} \right)^2 \quad (3.20)$$

T_c : Concrete temperature, °C

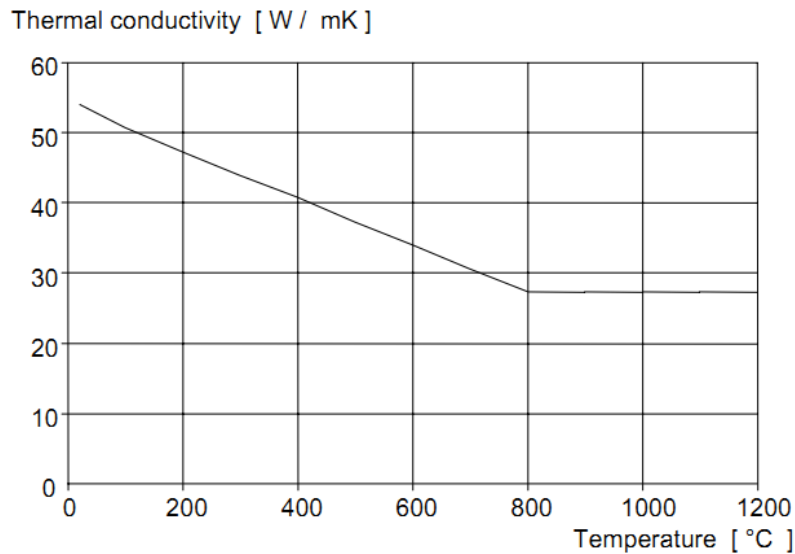


Figure 3- 17 Thermal conductance of steel as a function of temperature (CEN 2005)

As can be seen in the figures, thermal conductance has a similar trend for both steel and concrete at elevated temperatures: It decreases for both of the materials until temperature values approach 800 degrees Celsius and stays constant from there on. The difference for the two materials is in the order of magnitude of the conductivity values. As shown on the graphs, the conductivity values for steel are more than twenty times larger than values for concrete. NIST adopted the Eurocode 4's formulation for specific heat and thermal conductance of steel in its guidelines for structural fire design (NIST 2010).

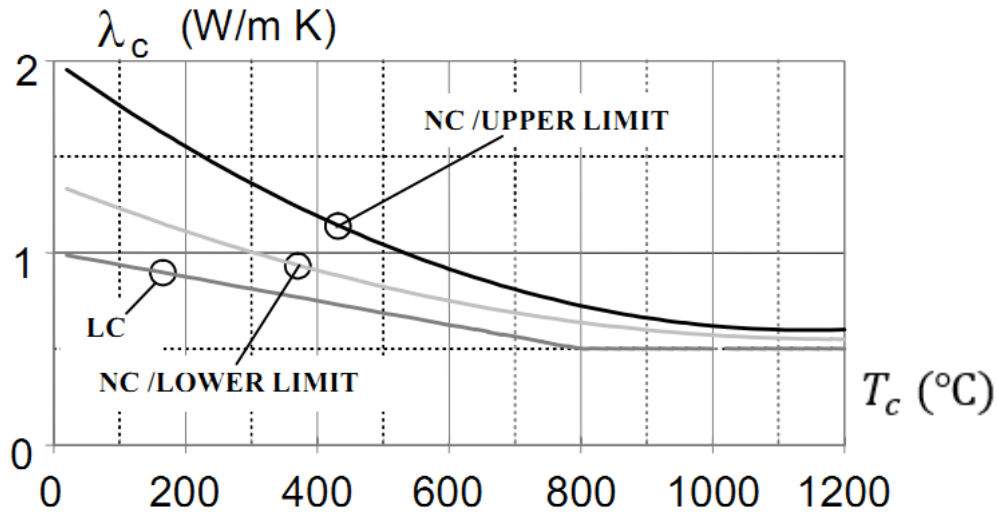


Figure 3- 18 Thermal conductance of normal weight (NC) and light weight (LC) concrete as a function of temperature (CEN 2005)

3.4.2.3 Element Type and Mesh Size for Heat Transfer Analysis

Different types of heat transfer elements are available in ABAQUS, including solid elements with choices of 8 and 20-node types, and shell elements with choices of 4 and 8-node types. Similar to the discussion in the 3D stress analysis part (section 3.3), elements with higher number of nodes use equations of higher order and can provide better accuracy compared to the elements with lower number of nodes, while adding significant computational cost to the analysis. Considering the fact that acceptable results can be gained using the simpler elements (8-node solid and 4-node shell), provided that proper mesh refinement is done at the critical areas, 8-node solid heat transfer elements (DC3D8) were used in the modeling of the concrete core of the structures in this study. The steel tube was modeled using both 4-node shell (DS4) and 8-node solid (DC3D8) heat transfer elements depending on the type of application and also for comparative studies. Note that irrespective of element type, mesh size should be fine enough to ensure satisfactory solution, and mesh sensitivity analysis must be conducted to establish convergence of the solution.

Another issue about meshing to consider is the selection of a proper mesh pattern for the second part of the modeling, which deals with the stress/deformation analysis. Since the result of the heat transfer analysis is used as a predefined temperature field for the subsequent stress analysis part, it is important to have a compatible mesh pattern for the two parts. In this project the meshing pattern for the heat transfer and stress/deformation parts are defined to match.

The next steps to develop a complete heat transfer system are the definition of thermal loads, boundary conditions, and heat transfer mechanisms that carry the heat into the specimen. These steps are discussed in the following sections.

3.4.2.4 Thermal Loads and Boundary Conditions

For a typical finite element analysis thermal analysis problem, after building the geometry and mesh of the structural element, thermal loads and boundary conditions must be defined. The thermal load in many problems is a fire load defined based on the standard fire curve proposed in ASTM E119 (Fig. 3.19), which is frequently used in structural fire engineering studies (ASTM 2012).

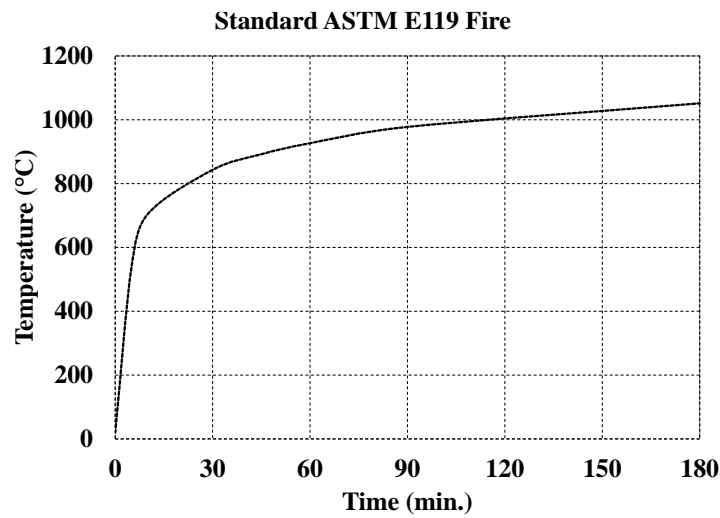


Figure 3- 19 Standard fire curve (ASTM 2012)

Applying the fire load to the model can be done in different ways. The first approach, which is the simplest, is to apply the history of nodal temperature values to the nodes on the exposed surface of the model, as a boundary condition that varies through time. In this method, heat transfer analysis will start from the exposed surface with known temperatures and track progress of the heat through the material. The problem with this method is that the standard fire curve is defined as the temperature of the gas surrounding the specimen. Therefore, the temperature values on the exposed surface of the structure will be slightly different with information about the difference between these values available from previous experimental studies. In most cases, real data measured by thermocouples on specimens during tests can be used here.

The second method is to define the fire load as an interaction between the exposed surface of the specimen and the ambient space surrounding it. In this approach the standard fire curve will be defined as the ambient temperature. The thermal energy will transfer to specimen's exposed surface via radiation and convection mechanisms. While this seems more realistic, it needs some additional information about the parameters that affect the radiation and convection processes.

Another method is to model the fire at its origin and follow it from there to the specimen's exposed surface. This is the most sophisticated approach and can be done by Computational Fluid Dynamics (CFD) calculations for the temperature of the gas in the path from the fire location to the exposed surface (starting from the fire ignition time). It can be done by general CFD analysis programs or some especially designed programs like Fire Dynamics Solution (FDS) by NIST.

For the purposes of this section, it was decided to use the second method for all fire simulations. In the pre-test verification process of the heat transfer modeling, the standard fire curve is given as an ambient temperature changing with respect to time, and transferred to the specimen through surface radiation and convection. This method assumes that the history of temperature values on the exposed surface of the specimen are unknown, limiting the information to the history of temperature values for the surrounding air (the resulted nodal temperature values on the exposed surface can be compared with the measured values to check the accuracy of the simulation).

To define the surface radiation and convection mechanisms, a few constants must be provided as input to the software, including the coefficient of convection at the exposed surface, the Stephan Boltzmann constant, the emissivity of fire and exposed surface, and the coefficient factor for radiation at the exposed surface. Proper values for these constants can be found from previous experimental and analytical studies. The values recommended by Eurocode 4 (CEN 2005) were adopted to be used in this research and are listed in Table 3.1.

The effects of the parameters defined in Table 3.1 on the heat transfer mechanisms will be discussed briefly in the following sections. The model also requires initial conditions. Here it is assumed that all of the nodes of the steel and concrete model are at room temperature (20°C) before the fire. Now that the initial conditions are defined and the fire load is applied to the exposed surface, the next step is to define the heat transfer mechanisms inside the specimen.

Table 3- 1 Thermal Constants and Parameters Used in Heat Transfer Modeling

Parameter	Definition	Value
h	Coeff. of convection at exposed surf.	25 W/m ² k
φ	Config. factor for radiation at exposed surf.	1
σ	Stephan-Boltzmann const	5.67E-8 W/m ² k ⁴
ϵ_m	Emissivity of exposed surf.	0.7
ϵ_f	Emissivity of fire	1
T_0	Initial temp.	20 C
k_{gap}	Average gap conductance	200 W/m ² k

3.4.2.5 Heat Transfer Mechanisms inside a Composite Member

When heat reaches the exposed surface of a material, it will propagate through the material column in accordance to the heat transfer mechanisms described here. When thermal energy has to go through a solid material (e.g. steel or concrete), the main transfer mechanism is conductance. As mentioned in the previous section, the conductance rate is much higher in steel compared to concrete.

At times when no solid element is present in the thermal energy's path, heat is transferred via convection and radiation. This happens for example at a gap in the steel-concrete interface when the two solids are separated from each other. The average gap conductance rate, k_{gap} is equal to 200 W/m²k based on studies by Ding and Wang (2008). The conductance rate can be defined in a more sophisticated way by using equations proposed in past studies as a function of clearance and temperature, which seems more realistic. Eq. 3.21, taken from a study by Ghojel (2004), considers the dependency of gap conductance on temperature:

$$h_j = 160.5 - 63.8e^{-339.9T^{-14}} \text{ W/m}^2\text{C} \quad (3.21)$$

In this equation, h_j is the gap conductance, T is temperature and e is the Euler's number. Since past studies have shown that using the average conductance rate provides enough accuracy for the problem in hand while keeping the equations simple, it was adopted to be used in this project. Another heat transfer mechanism that should be defined at the steel-concrete interface is radiation. Emissivities of both steel and concrete surfaces are considered to be 0.7 based on the recommendations by Eurocode 4 (CEN 2005). After

the transfer of thermal energy through the interface between steel and concrete, the transfer mechanism will change to conductance through concrete. This will take a relatively longer time because of the low heat conductance rate of concrete.

After completion of the above stages, the heat transfer analysis is complete and the output provides the history of nodal temperature values for all of the nodes in a model through the burning time. These results can then be used as input for the next part of the solution, which deals with the stress/deformation field.

3.4.3 Developing the Finite Element Model for Stress/Deformation Analysis

3.4.3.1 Structural Properties of Materials at Elevated Temperatures

Experiments have shown that structural properties of materials can change when exposed to varying temperatures. These changes can have substantial effects on the results of analysis for structures exposed to fire. In a fire scenario, structural members can achieve temperatures of up to 1000 °C for a relatively long period of time. Modeling temperature effects on stress-strain properties is therefore required for this kind of analysis.

Several models have been proposed by different researchers to simulate the behavior of steel and concrete at elevated temperatures. Most of these models are based on fitting curves to experimental results. The material properties needed for this kind of analysis are stress-strain relationships as a function of temperature, and the coefficient of thermal expansion, each discussed separately in the sections that follow.

3.4.3.1.1 Stress-strain Relationship for Steel

Several stress-strain relationships that consider the effects of varying temperatures for steel material can be found in the literature. Some of the most frequently used are those by Lie (1994), Poh (2001), Eurocode 4 (CEN 2005), Yin et al. (2006) and NIST (2010). Based on the sensitivity analysis done by Espinos et al. (2010) on all of the models mentioned above, except the NIST model which was not available at the time of Espinos' study, the Eurocode model was reported to give the best results compared to experimental data when used for modeling the behavior of concrete filled steel tubes subjected to fire.

Therefore, the Eurocode steel model was selected here in developing finite element models as part of this project, along with the more recent NIST model for comparison purposes. Fig. 3.20 and Table 3.2 show the

stress-strain behavior of steel according to the Eurocode specifications. The formulation is defined in a general way that accounts for the effect of temperature by varying both the elastic modulus and the yield strength of the material, per the relationships presented in Table 3.2. In support of the World Trade Center investigation, NIST developed high temperature stress-strain curves using the materials recovered from the collapse site. The following expression was obtained for the modulus of elasticity of structural steel.

$$E(T) = e_0 + e_1T + e_2T^2 + e_3T^3 \text{ where,}$$

$$e_0 = 206 \text{ GPa,}$$

$$e_1 = -0.043 \text{ GPa}/^\circ\text{C,}$$

$$e_2 = -3.5 \times 10^{-5} \text{ GPa}/^\circ\text{C}^2,$$

$$e_3 = -6.6 \times 10^{-8} \text{ GPa}/^\circ\text{C}^3$$
(3.22)

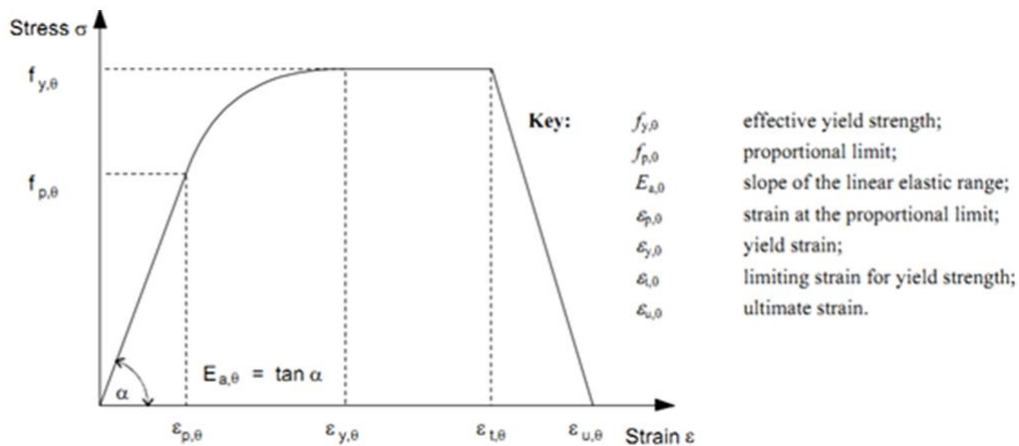


Figure 3- 20 Stress-strain relationship for steel at elevated temperatures (CEN 2005)

**Table 3- 2 Formulation of stress-strain relationship for steel at elevated temperatures
(CEN 2005)**

Strain Range	Stress σ	Tangent Modulus
$\varepsilon \leq \varepsilon_{p,T}$	$\varepsilon E_{a,T}$	$E_{a,T}$
$\varepsilon_{p,T} < \varepsilon < \varepsilon_{y,T}$	$f_{y,T} - c + (b/a) [a^2 - (\varepsilon_{y,T} - \varepsilon)^2]^{0.5}$	$\frac{b(\varepsilon_{y,T} - \varepsilon)}{a [a^2 - (\varepsilon_{y,T} - \varepsilon)^2]^{0.5}}$
$\varepsilon_{y,T} \leq \varepsilon \leq \varepsilon_{t,T}$	$f_{y,T}$	0
$\varepsilon_{t,T} < \varepsilon < \varepsilon_{u,T}$	$f_{y,T} [1 - (\varepsilon - \varepsilon_{t,T}) / (\varepsilon_{u,T} - \varepsilon_{t,T})]$	-
$\varepsilon = \varepsilon_{u,T}$	0	-
Parameters		
$\varepsilon_{p,T} = f_{p,T} / E_{a,T} \quad \varepsilon_{y,T} = 0.02 \quad \varepsilon_{t,T} = 0.15 \quad \varepsilon_{u,T} = 0.20$		
Functions		
$a^2 = (\varepsilon_{y,T} - \varepsilon_{p,T}) \left(\varepsilon_{y,T} - \varepsilon_{p,T} + \frac{c}{E_{a,T}} \right)$		
$b^2 = c(\varepsilon_{y,T} - \varepsilon_{p,T}) E_{a,T} + c^2$		
$c = \frac{(f_{y,T} - f_{p,T})^2}{(\varepsilon_{y,T} - \varepsilon_{p,T}) E_{a,T} - 2(f_{y,T} - f_{p,T})}$		

A simple phenomenological model was selected for the true stress – true strain relation given by

$$\sigma = K \varepsilon^n \quad (3.23)$$

in which K and n are defined as functions of temperature by equations 3.24 and 3.25,

$$n = (n_3 + n_4 f_y) e^{(-\frac{T}{n_2})^{n_1}} \quad (3.25)$$

$$K = (k_3 + k_4 f_y) e^{(-\frac{T}{k_2})^{k_1}} \quad (3.24)$$

where f_y is the specified yield strength of steel (i.e., at room temperature), and the remaining parameters in Eqs. 3.24 and 3.25 were obtained by fitting curves to the experimental data. Table 3.3 shows the values for

these parameters, which are expected to give good results for steels with room temperature yield strengths in the range of 36-65ksi (248-448 MPa).

Table 3- 3 Parameters for equations 3.24 and 3.25

Parameter	Value	Units
k ₁	4.92	
k ₂	575	°C
k ₃	734	MPa
k ₄	0.315	
n ₁	4.51	
n ₂	637	°C
n ₃	0.329	
n ₄	-4.23×10^{-4}	MPa ⁻¹

Eqs. 3.26 and 3.27 are used to convert the true stress and true strain values to engineering stress and strain

$$\sigma_E = \frac{\sigma}{e^\varepsilon} \quad (3.26)$$

$$\varepsilon_E = \frac{\sigma}{\sigma_E} - 1 \quad (3.27)$$

For illustration purposes, the engineering stress-engineering strain values for an A572 Gr. 50 steel computed per the NIST equations are plotted (Fig. 3.21) for temperature values of 60, 200 and 400 °C, along with the experimental results obtained as part of the NIST study, and the Eurocode curves (NIST 2010). It can be seen in the figure that the model proposed by NIST better matches the experimental results compared to the Eurocode equations, which is somewhat expected since the NIST model was calibrated for the steel material that was tested in their experimental studies (NIST 2010; Bruneau et al. 2011).

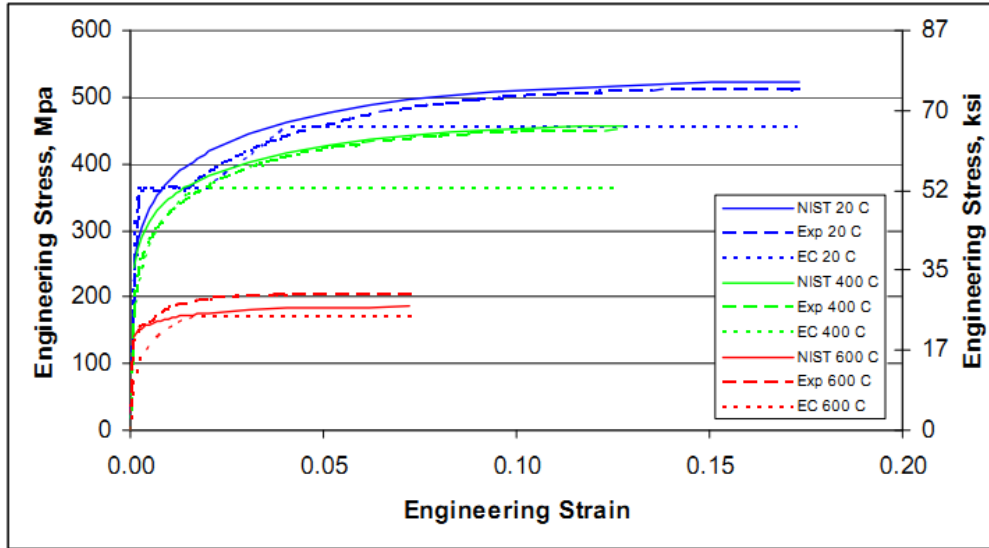


Figure 3- 21 Graphs of Eng. stress vs. Eng. strain as predicted using the NIST approach, the Eurocode equations, and NIST experimental data for ASTM A572 Gr. 50 structural steel (NIST 2010)

According to the NIST technical note 1681 (2010), since the formulation above is based on curve fitting over a large strain range (from zero to 0.15), it will work well for large strains but is likely to fail in capturing the linear elastic behavior of steel at small strains. Therefore it is suggested that for analysis purposes, the linear elastic part of the behavior can be modeled separately up to the yield stress (as defined by a 0.002 strain offset), and the proposed power law (Eq. 3.23) can be used for providing the stress-strain data beyond the yield stress. To obtain the yield stress value for different temperatures, Eq. (3.28) proposed by Luecke (CEN 2005) is suggested by NIST, which assumes that yield stress will occur at the strain of 0.002 for all temperature levels. In this equation, $A_2=0.075$, $m_1=8.07$, $m_2=1.0$, $s_1=635$ °C, and $s_2=539$ °C.

$$R = \frac{f_y(T)}{f_y(20\text{ }^\circ\text{C})} = (1 - A_2)e^{\left(\frac{1}{2}\left(\frac{T}{s_1}\right)^{m_1} - \frac{1}{2}\left(\frac{T}{s_2}\right)^{m_2}\right)} + A_2 \quad (3.28)$$

Looking at the steel models for varying temperatures, it is obvious that as the temperature increases, both stiffness and strength of the material degrade to lower values. Fig. 3.22 shows the degradation of elastic stiffness at higher temperatures. According to the two models shown above (i.e. NIST and Eurocode), steel has nearly a zero elastic stiffness when it reaches the temperature of 1000 °C. Fig. 3.22 includes another model for steel at varying temperatures proposed by Poh (2001). Among the three models, the NIST

approach gives the highest values for Young's modulus, which indicates that analyses using the Eurocode model will give more conservative results.

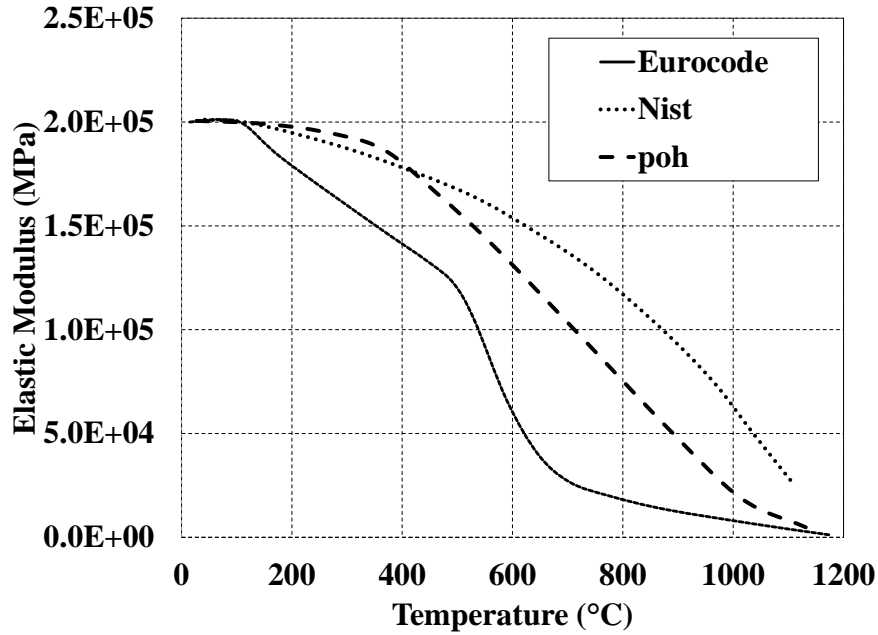
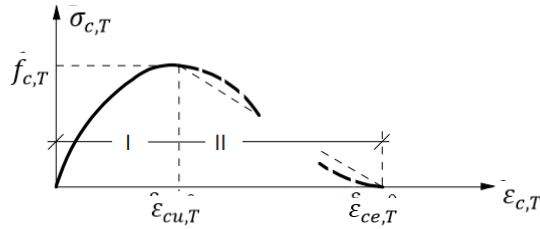


Figure 3- 22 Young's modulus for steel as a function of temperature (different models)

3.4.3.1.2 Stress-strain Relationship for Concrete

To account for temperature effects on the stress-strain relationship of the concrete model, among the several models proposed by researchers in the past, the study by Espinos et al. (2010) concluded that the models proposed by Lie (1994) and Eurocode 4 general rules for structural fire design (CEN 2005) can provide reasonable results (slightly conservative for the Eurocode model) when used for modeling the behavior of concrete filled steel tubes subjected to fire. Fig. 3.23 and Table 3.4 show the definition of the temperature dependent stress-strain model for concrete by Eurocode 4.

Similar to steel, concrete loses both its stiffness and strength when subjected to high temperatures. Fig. 3.24 shows the stiffness and strength values at varying temperatures. It can be seen that at temperatures close to 800°C, concrete has only 10% of its initial compressive strength at room temperature.



RANGE I:

$$\bar{\sigma}_{c,T} = \hat{f}_{c,T} \left[\frac{3 \left(\frac{\hat{\varepsilon}_{c,T}}{\hat{\varepsilon}_{cu,T}} \right)}{\left\{ 2 + \left(\frac{\hat{\varepsilon}_{c,T}}{\hat{\varepsilon}_{cu,T}} \right)^3 \right\}} \right]$$

$$k_{c,\theta} = \left. \begin{array}{l} \hat{f}_{c,T} \\ f_c \end{array} \right\} \text{ to be chosen according to the values of Table 3.3}$$

and $\hat{\varepsilon}_{cu,T}$

RANGE II:

For numerical purposes a descending branch should be adopted

Figure 3- 23 Stress-strain relationship for concrete at elevated temperatures (CEN 2005)

Table 3- 4 Two main parameters of the stress-strain relationship for normal weight (NC) and light weight (LC) concrete at elevated temperatures (CEN 2005)

Concrete Temperature re T_c ($^{\circ}C$)	$k_{c,\theta} = f'_{c,T}/f'c$		$\varepsilon_{cu,T} \times 10^3$
	Normal Weight Concrete te	Light Weight Concrete e	Normal Weight Concrete ete
20	1.00	1.00	2.5
100	1.00	1.00	4.0
200	0.95	1.00	5.5
300	0.85	1.00	7.0
400	0.75	0.88	10.0
500	0.60	0.76	15.0
600	0.45	0.64	25.0
700	0.30	0.52	25.0
800	0.15	0.40	25.0
900	0.08	0.28	25.0
1000	0.04	0.16	25.0
1100	0.01	0.04	25.0
1200	0.00	0.00	-

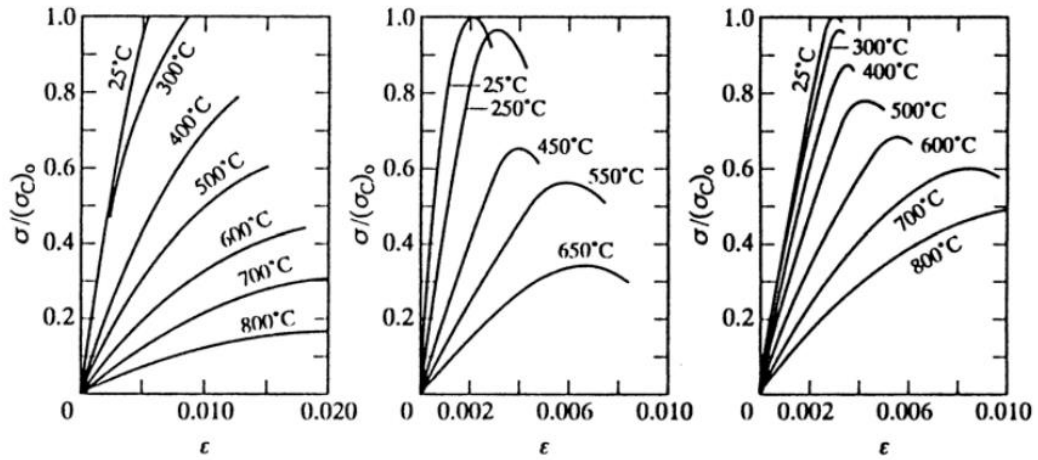


**Figure 3- 24 Strain in compression curves for concrete at elevated temperatures
(Harmathy and Allen 1973)**

NIST also provides a concrete stress-strain relationship expression as a function of temperature. The relationship is based on the simple equation by Lie (1994) for the compressive strength of concrete at various temperatures (Eq. 3.29).

$$f_{c,T} = \begin{cases} f_{c,20^{\circ}C}, & T \leq 450^{\circ}C \\ f_{c,20^{\circ}C} \left[2.011 - 2.353 \frac{T - 20}{1000} \right], & T > 450^{\circ}C \end{cases} \quad (3.29)$$

The other properties of the model, including the elastic modulus, tensile strength and the stress-strain curve, are defined based on the compressive stress value. The model is expected to provide conservative results. The Eurocode model has been shown to provide acceptable and slightly conservative results in past studies (Espinosa et al. 2010) and was selected to be used for concrete modeling in this research.

3.4.3.1.3 Thermal Expansion

Eurocode 4 general rules for structural fire design (CEN 2005) provides thermal expansion coefficient values for both steel and concrete as a function of temperature. This parameter can play an important role in the analysis of CFT columns because of the relative difference between the amount of expansion in the steel and concrete at high temperatures. Although coefficient of expansion for concrete can be defined as a function of temperature, past studies have shown that assuming a constant value for all temperatures can

provide enough accuracy in the results (Espinosa et al. 2010). Therefore, in order to avoid adding complexities to the model that will not necessarily improve accuracy of the results, it was decided to use a constant value of $\alpha_c = 6 \times 10^{-6} \frac{1}{^\circ\text{C}}$ as the expansion coefficient of concrete for all temperatures. Since steel material will have considerably more amount of expansion relative to concrete, its thermal elongation, $\frac{\Delta l}{l}$, was defined as a function of temperature based on the Eq. 3.30. Fig. 3.25 shows the relation for thermal elongation provided by Eurocode 4.

$$\frac{\Delta l}{l}(\text{steel}) = \begin{cases} -2.416 \times 10^{-4} + 1.2 \times 10^{-5}T_a + 4.0 \times 10^{-9}T_a^2, & 20 \text{ }^\circ\text{C} \leq T_a \leq 750 \text{ }^\circ\text{C} \\ 11 \times 10^{-3}, & 750 \text{ }^\circ\text{C} \leq T_a \leq 860 \text{ }^\circ\text{C} \\ -6.2 \times 10^{-3} + 2.0 \times 10^{-5}T_a, & 860 \text{ }^\circ\text{C} \leq T_a \leq 1200 \text{ }^\circ\text{C} \end{cases} \quad (3.30)$$

T_a : Steel temperature, $^\circ\text{C}$

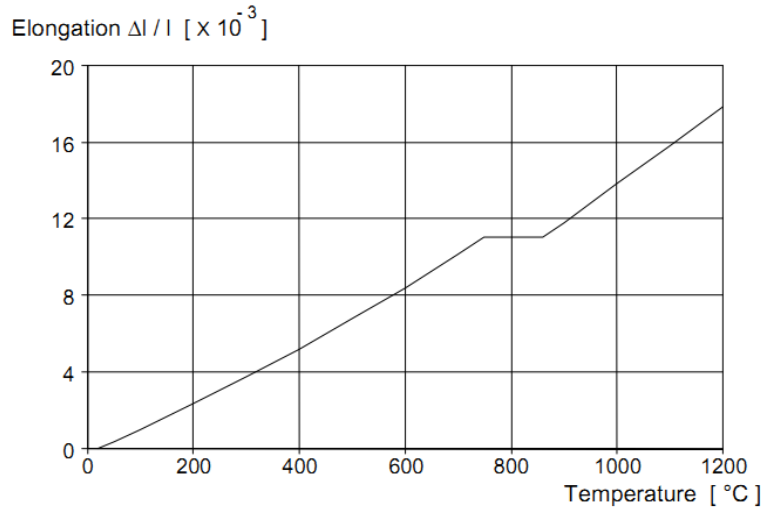


Figure 3- 25 Thermal elongation of steel as a function of temperature (CEN 2005)

3.4.3.2 Steel-Concrete Interface

The modeling of the steel-concrete interface for thermal-stress problem is similar to the model built in Sec. 3.2.3 for the cyclic loading test. Considering the little amount of sliding that is likely occur between the surfaces of steel and concrete in the problem examined in this project, no changes in friction properties between the surfaces will be considered in this project.

3.4.3.3 Loads and Boundary Conditions

When subjecting a column specimen to a fire, as done in this study, the intent is to keep it under a constant axial load. This is assumed to be similar to the real conditions that represent a building column during a fire. However, in a real building, thermal expansion occurs in all structural members, including the columns, which may lead to redistribution of the gravity loads among all columns, thus possibly changing the amount of axial load on a specific column. However, even though the axial load may not remain constant in the real conditions, it is a fair assumption to consider that most of it remains on the column until it collapses. In buildings, it is also often assumed that the amount of axial load acting on a column during a fire will be approximately equal to 30% of its axial strength. In experiments, practice has been to maintain the high temperatures until the column loses its resistance to a constant axial load and buckles.

Since the failure mode is in the form of buckling, modeling the boundary conditions of the columns is significantly important. A column with fixed-fixed conditions at its ends will be able to survive a fire relatively longer than a column with pinned-pinned ends.

For the verification process described in Section 3.5, the end conditions of the column will be modeled as stated by authors of the reference experiment. However, for modeling the fire tests conducted as part of this project, the end conditions will be more complicated because of the special conditions of the test setup at the fire lab (as described in Section 4). The approach to model those specific end conditions will be discussed in Section 5.

3.4.3.4 Buckling Issues and Geometric Imperfection

Based on the experience from previous experimental and analytical studies, a column subjected to a fire is vulnerable to both local and global buckling (Hong and Varma 2009; Espinos et al. 2010). In addition, concrete-filled tubes having a fixed-fixed configuration at their ends can exhibit localized buckling at these ends. This happens because the steel tube expands more than its concrete core; as a result, at its ends, the steel becomes longer than the concrete and bears alone the entire applied axial load. Therefore, the elements at these critical locations will have excessive deformations and stresses, leading to local buckling of the steel tube at column ends. This does not necessarily jeopardize the strength of the column, but rather introduces some local damage at the column ends.

Eventually, at the high temperatures developed during a fire, the stiffness and strength of the materials will become low enough to trigger global buckling of the column. This is the most common failure mode reported for concrete-filled columns in experimental studies. In order to develop a model capable of predicting this behavior, geometric imperfections must be defined for the specimen. Geometric imperfections are basically due to the initial out-of-straightness of the structural elements that promote buckling to develop at loads lower than what would otherwise be the case with a perfectly straight structure. Since imperfections are always present in actual specimens, they should be considered in the modeling process. Initial imperfections are also needed for computational reasons in buckling problems, to help trigger buckling modes that would not otherwise develop for idealized structures.

For available specimens, the engineer can actually measure the imperfections and impose them on the numerical model. When the specimen is not available, an alternative numerical approach commonly used consists of performing an eigenvalue analysis of the model to get the first few mode shapes of the structure, to multiply these mode shapes by scale factors, and to impose them as initial displacements to the model. This approach makes it possible to capture global buckling of a structural member. Here, a scale factor of $L/1000$ was used in all analyses, where L is the length of the column.

3.4.3.5 Element Types and Meshing

Similar to the heat transfer modeling, the 8-node solid and 4-node shell elements with reduced integration was used to build the model. The only modification needed was to change the element types from heat transfer to stress/displacement elements. As discussed before, the mesh pattern was chosen to match that of the heat transfer model, making it possible to use the nodal output values from the heat transfer analysis.

3.5 Pre-test Verification of the Finite Element Model for Thermal Stress Problem

A specimen similar to the columns examined in this project was selected from past experimental studies to be modeled using the same assumptions and techniques explained above to check the accuracy of the numerical results compared to the experimental data. The specimen was selected from a study by Espinos et al. (2010) on an advanced FEM model for predicting the fire response of CFT columns. Espinos et al. numerically simulate a number of tests done by other researchers including the particular specimen selected here from a test by Chabot and Lie (1992).

It should be mentioned that although a few studies were available on the fire performance of double skin concrete filled tube columns, an example of conventional CFT columns was selected to be used in the model verification process. A CFT column was examined because of the completeness of the information available about both the experimental and numerical analyses done on this particular specimen, which could help in verifying the modeling process. The addition of the second tube definitely makes the problem more complicated but for the purposes of pre-test verification of the thermal-stress model, a simple CFT column has everything necessary to check the performance of the numerical simulation. Table 3.5 contains information about the dimensions, material properties, boundary conditions and loads regarding the selected specimen. Fig. 3.26 shows the geometry of the specimen which basically consists of a steel tube filled with plain concrete. Two steel plates are attached to the top and bottom faces of the column to be used as equipment for applying the loads and boundary conditions.

Table 3- 5 Geometry and material properties (Espinos et al., 2010)

Length (mm)	Outer Diameter (mm)	Thickness of the Tube (mm)	f_y (MPa)	f'_c (MPa)
3810	219.1	4.78	350	31
End Conditions	Axial Load (KN)	Eccentricity (mm)	Burning Time (min.)	
Fixed - Fixed	492	0	80	

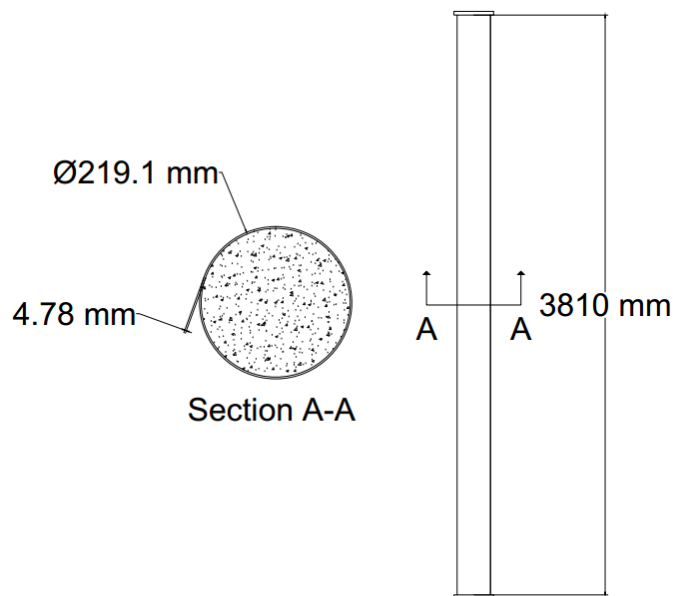


Figure 3- 26 Geometry of the model

The selected example can be considered as a complete thermal-stress problem. The CFT column will be subjected to a constant axial load and undergo a standard fire, burning until the time that it no longer can resist the axial load. As it was discussed in the previous sections, the analysis will be conducted with a sequentially coupled approach, starting with a heat transfer analysis and followed by a stress/deformation solution. The second part will be affected by the history of nodal temperature results gained from the first part.

3.5.1 Verification of Heat Transfer Analysis

The specimen was modeled in ABAQUS considering the issues discussed in Sec. 3.3. Thermal properties for steel and concrete were adopted from Eurocode 4. The 8-node solid heat transfer elements (DC3D8) were used for both the steel tube and concrete core. Note that in order to be consistent with the numerical studies conducted by Espinos et al. (2010) and for comparative purposes, solid elements were preferred to the shell elements for the modeling of the steel tubes. Taking advantage of symmetry, only half of the specimen was modeled. The fire load, which was the standard ASTM E119 curve, was applied as the ambient air temperature transferred to the specimen through convection and radiation. Heat transfer mechanisms defined for the steel-concrete interface were conduction, which was based on an average conduction factor (to account for the gaps), and radiation from the inner surface of the steel tube to outer surface of the concrete core. A complete list of the parameters and constants used for the modeling are shown in Table 3.1 in Sec. 3.3.

The final visualized results of the heat transfer analysis are shown in Fig. 3.27. The top and bottom plates have been removed from this part of the analysis assuming that those parts won't be exposed to the fire with the help of protective materials. This is usually done in the tests to keep the connecting parts of the specimen and the test machine safe.

According to the colors in the figure, all of the nodes defined for the steel tube member have reached the maximum temperature level caused by fire because of the high conductance rate of steel. On the other hand going through the specimen, the colors change into colder ones showing that the thermal energy has some difficulties going through the interface and especially into the concrete with a low conductance rate. The coldest point which is at the center of the specimen has stopped at the temperature of 320 °C at the end of the 80-minute heating time.

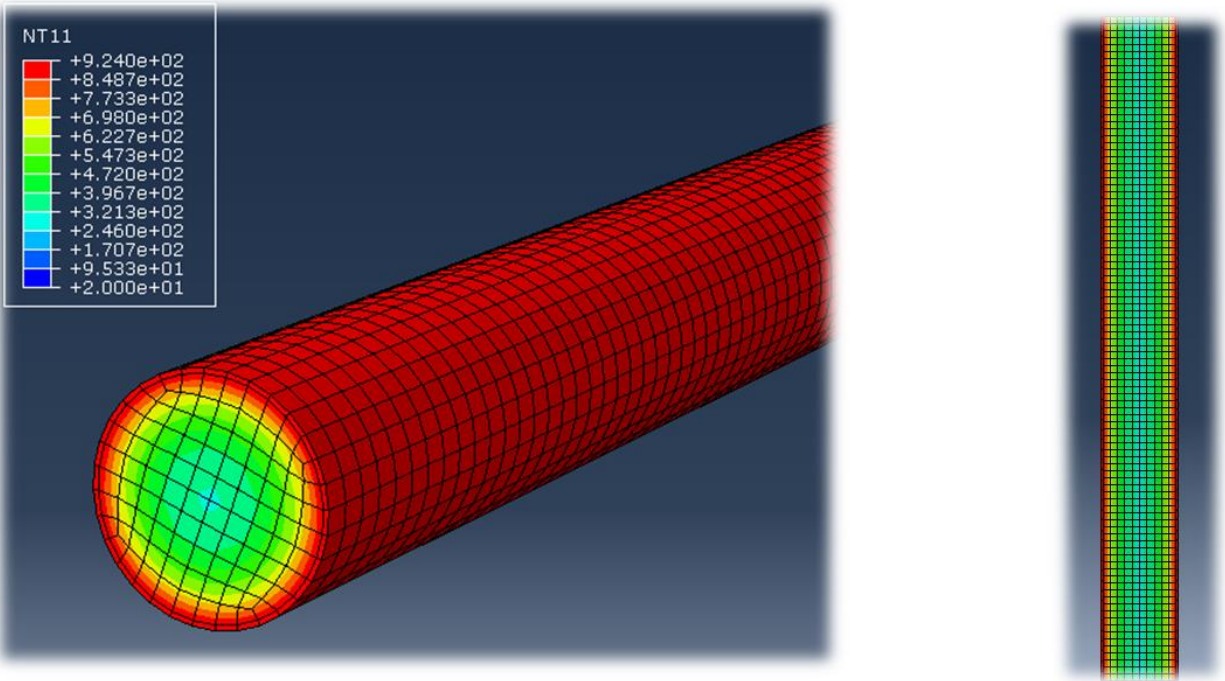


Figure 3- 27 Visualized results of heat transfer analysis showing nodal temperatures (in °C) at the end of the fire event (from ABAQUS)

Fig. 3.28 shows the history of temperature for a few selected nodes located at the outer surface of the steel tube, mid-way through the concrete core and the center point. The experimental data are also plotted for comparison. Generally the simulation has provided reasonable results considering several sources of uncertainty in the modeling process. During the initial minutes of burning, the experimental data show faster increase in the temperatures of mid-way concrete and center points. This is followed by a relatively constant temperature phase. Simulated results however, show a gradual increase from room temperature to higher levels without any steep or constant portions. The curves fit well for the second half of the burning time for all of the three sample points.

Results indicate that accuracy of the finite element heat transfer analysis is sufficient for the purposes of this project. Note that in the post-test validation of the heat transfer models, the fire load will be imposed on the exposed surface of the specimens using the recorded data from the experiments conducted in this study (to minimize the simulation errors). Another issue to be considered in the post-test validation process is the effect of end plates of the column on the heat transfer process. If the end plates are exposed to fire and allowed to provide a short path for heat to get to the inner parts of the column, they can change the temperature distribution close to the column ends. This issue along with the effects of concrete's moisture

content on the heat transfer process will be discussed further in Section 5, where the tests conducted in this project will be simulated numerically.

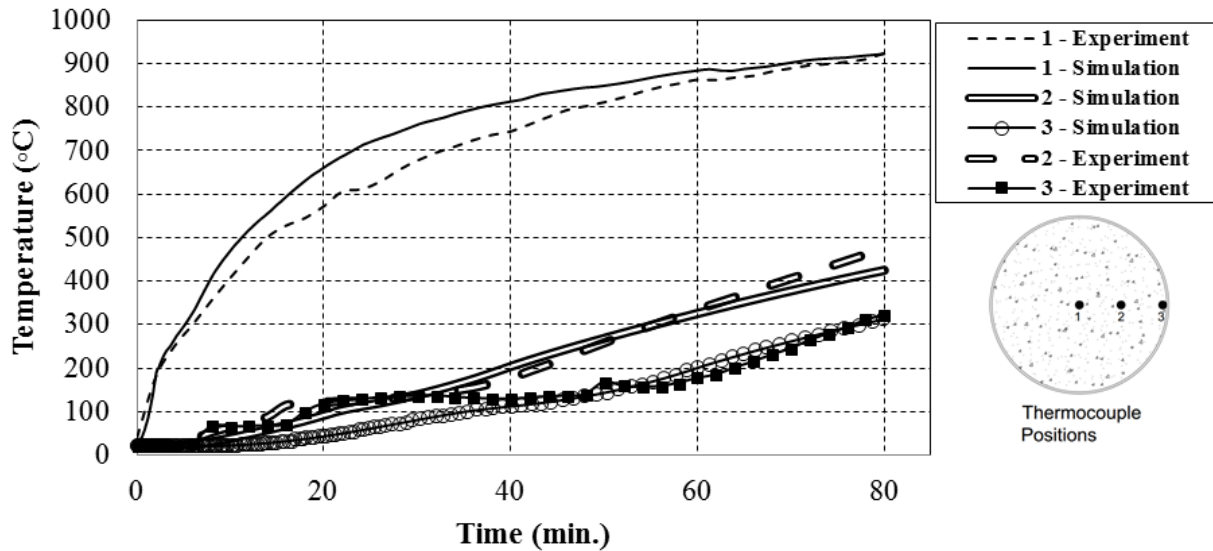


Figure 3- 28 Comparison of the heat transfer analysis results with experimental data from Chabot and Lie (1992)

3.5.2 Verification of Stress/Deformation Analysis

The same model with the exact geometry and mesh size was used here for verification of the finite element analysis results in the stress/deformation field with experimental data. The only difference was adding the structural properties to the existing thermal properties of the model. The mesh pattern was kept the same as the one built for heat transfer analysis because the results for history of nodal temperatures were given as input to the stress/deformation model. Since the stress/deformation analysis is more complicated than the heat transfer analysis in this problem, the mesh pattern that was found suitable for the former was copied exactly for the latter.

The element types were changed to 8-node 3D stress solid elements (C3D8R). A static general analysis should be conducted considering the effects of geometric nonlinearities because of the buckling possibilities. Two steel plates are added to the top and bottom ends of the column to be used for imposing the loads and boundary conditions.

The analysis started with applying the constant axial load of 492KN as a pressure to the top plate. Next, the structure was exposed to the first 80 minutes of the standard ASTM E199 fire curve. To consider the effects

of geometric imperfections, a buckling analysis was conducted prior to the main analysis to calculate the first five buckling modes of the model. These mode shapes were applied as an initial displacement to the model with an amplification factor of $L/1000$. (L is the total length of specimen which is equal to 3810mm in this case). The finite element model needs an initial imperfection to be able to initiate the global buckling of the column when the applied axial load reaches the critical limit. However, no initial imperfections were imposed on the model to capture the possible local buckling of the steel tube, as the model was considered to be capable of triggering local buckling based on the conditions that are applied to different elements throughout the analysis (e.g. local distortions induced as a consequence of boundary conditions restraint to expansion, and other similar constraints at high plastic strains during the simulation). The validity of this assumption will be checked based on the results of this simulation.

Thermal properties needed in the analysis were chosen from Eurocode 4 specifications similar to what has been used in the heat transfer analysis. In terms of structural properties, two cases will be considered. First case will be done using Eurocode material models for steel and concrete whereas the second case will use the NIST material model for steel at high temperatures. Eurocode models have been used by many researchers in the past and they seem to provide acceptable results, but it may be useful to check their differences with the NIST model which has come out of a more recent study. It should be mentioned that in terms of thermal properties, NIST and Eurocode provide similar specifications.

Final visualized result of the model built with Eurocode 4 specifications is shown in Fig. 3.29. Only half of the specimen was modeled because of symmetry. Local buckling of the steel tube happened near the fixed end. The analysis was aborted due to the global buckling of the specimen. The buckled shape can be seen up to a certain level in Fig. 3.29 and will go on to larger displacements in a real test. It should be mentioned that this type of global buckling is triggered because of the presence of initial geometric imperfection. The model goes towards the buckling state with gradual increases in the displacements rather than a sudden instability.

Fig. 3.30 shows the roles of the steel tube and concrete core in carrying the constant axial load through the burning time. They start with carrying a nearly equal portion of the load but soon after, the load is resisted by steel tube alone. This is because the steel tube expands more than concrete, leading to the separation of the end plates and the concrete core. This continues until local buckling occurs for the steel tube near the ends and it starts to shorten until a point that concrete starts to take load again. From this point on, concrete continues to carry the load until it degrades enough due to high temperatures to lose its ability to resist the load, leading to the buckling of specimen.



Figure 3- 29 Visualized final displacement result of the structural analysis – Eurocode steel and concrete models (from ABAQUS)

Fig. 3.31 shows the results of axial displacement of the column's end plate, which is equivalent to the column's extension or contraction in this case, versus the heating time from the analysis done here along with the experimental results from the study by (Chabot and Lie 1992). The simulation results are reasonably close to the measured data. One noticeable difference is that in the experiment, the expansion period starts at a slower rate and lasts longer than the numerical simulation. Since the numerical model generally follows a pattern that is similar to what has occurred during the test, the slight deviation of the axial displacement curves might be due to the fact that the thermal properties defined for the steel material in the analysis (e.g. coefficient of thermal expansion and yield stress of steel at higher temperatures) did not represent the exact properties of the tested material.

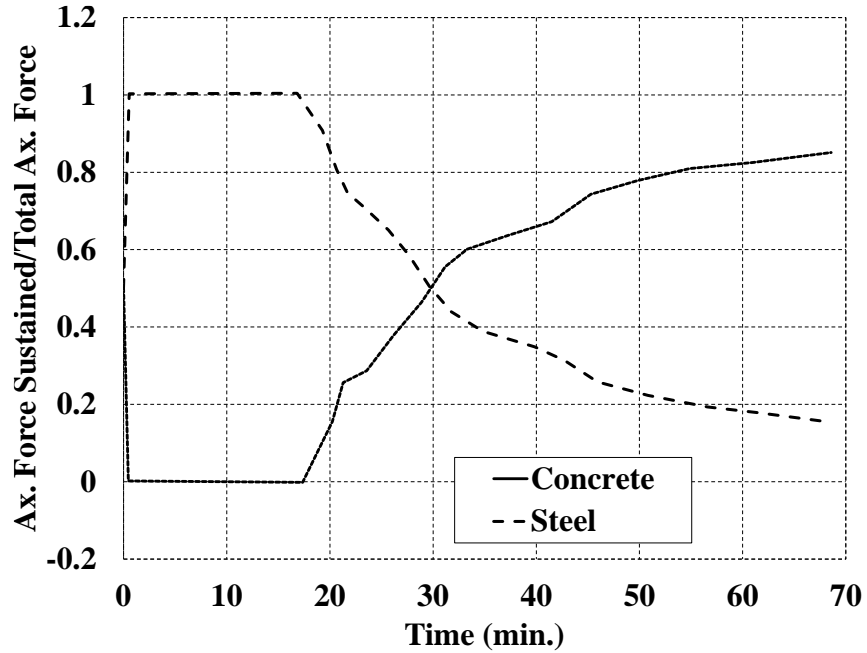


Figure 3- 30 Ratio of the axial load carried by steel tube/concrete core to the total axial load during the fire test

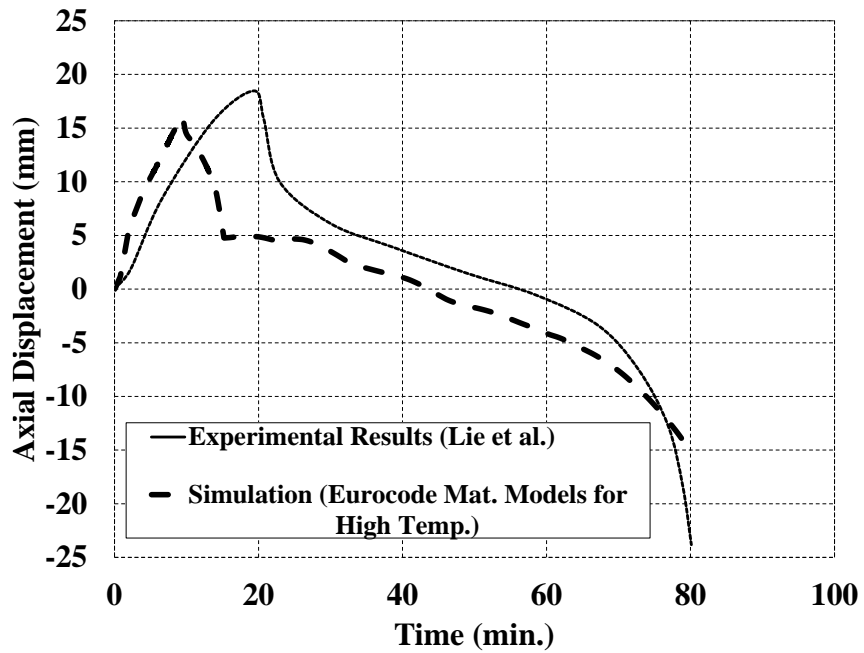


Figure 3- 31 Axial displacement results from ABAQUS compared with experimental data (Chabot and Lie 1992)

Additional analyses were conducted to check the sensitivity of the results to a number of parameters including the mesh size, temperature dependent coefficient of thermal expansion and yield stress of steel material at high temperatures. Fig. 3.32 shows the curves from Fig. 3.31 along with the results from additional analyses with changes in the mentioned parameters. Results from the model with a refined mesh size followed the same path as the original simulation curve, indicating the convergence of the finite element results.

The curve MP1 is from a model with modified values for coefficient of thermal expansion at different temperatures for steel material (i.e. a 20% reduction in the coefficient for all temperatures). The reduction in the expansion coefficient decreased the slope of axial displacement curve in the early moments of the fire, which more closely replicates the experimental results in the initial expansion phase.

Note that the axial displacement curve from the model MP1 reaches its peak value sooner than the experimental curve. The peak time is controlled by the yield strength of the steel tube at higher temperatures and occurs at the moment when the strength is decreased as much that the tube cannot bear the axial load alone. The curve MP2 was obtained from another model, which had the changes made for MP1 along with a modified set of reduction factors for the yield stress of steel at high temperatures (20% less reduction compared to Eurocode 4 specifications). Result from MP2 follows the experimental curve with an acceptable accuracy.

Fig. 3.32 shows that results from the finite element model (at the current mesh size) are not sensitive to the changes in the mesh size but can be sensitive to modifications in the definition of certain material properties. Note that apart from minor differences in the time and amplitude of the maximum axial displacement, the original finite element model (built with material properties adapted from the Eurocode) provided a relatively accurate replication of the experimental results. Therefore, the small arbitrary modifications mentioned above, which can be made as part of calibration to improve the accuracy of the results for a specific problem (but cannot be justified in general solutions), were unnecessary for the purposes of this study.

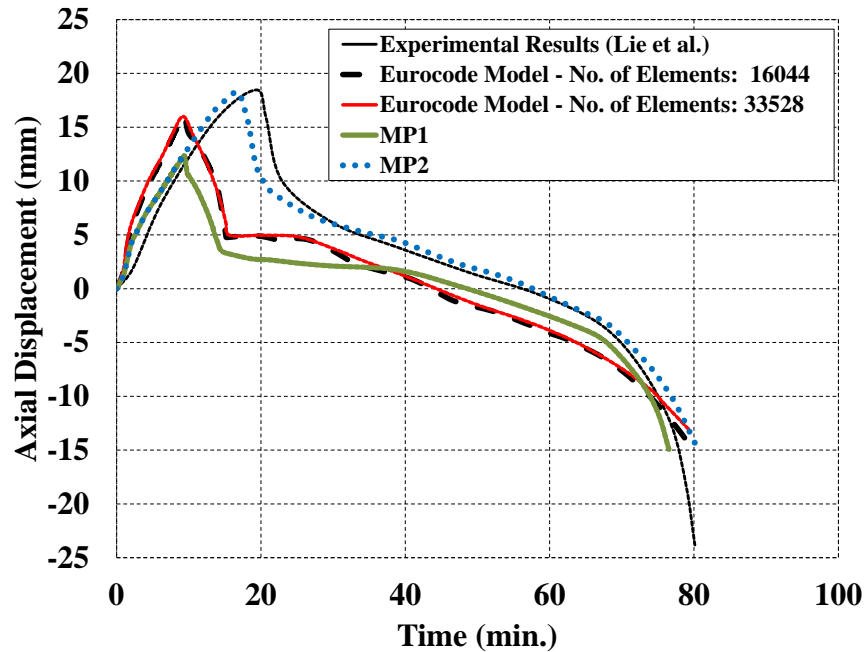


Figure 3- 32 Axial displacement results from ABAQUS compared with experimental data (Chabot and Lie 1992): checking sensitivity to the mesh sizing and thermal properties of steel material (MP1: modified coeff. of thermal expansion, MP2: modified coeff. of thermal expansion and yield strength of steel at high temp.)

The material model for steel proposed by NIST (2010) provides higher stiffness and strength values compared to the Eurocode model for the same temperature levels. Considering that the Eurocode model may be conservative, the analysis was repeated by changing the steel material's structural properties to NIST specifications. The new analysis just had the stress/displacement part replaced because the heat transfer process was exactly the same as the one for the Eurocode model. The analysis results are plotted in Fig. 3.33 along with the experimental and simulation results repeated from Fig. 3.31.

Using the NIST steel model, the expansion period lasted for a few more minutes. This is because the material has enough strength and stiffness at higher temperatures to resist the axial load for a relatively longer time. A longer expansion period leads to a higher peak in the axial displacement curve. Comparing the simulation results from the NIST and Eurocode models, it is inferred that while both models predict a similar total fire resistance time for the tested column, the Eurocode model provides a better estimation for the maximum axial displacement.

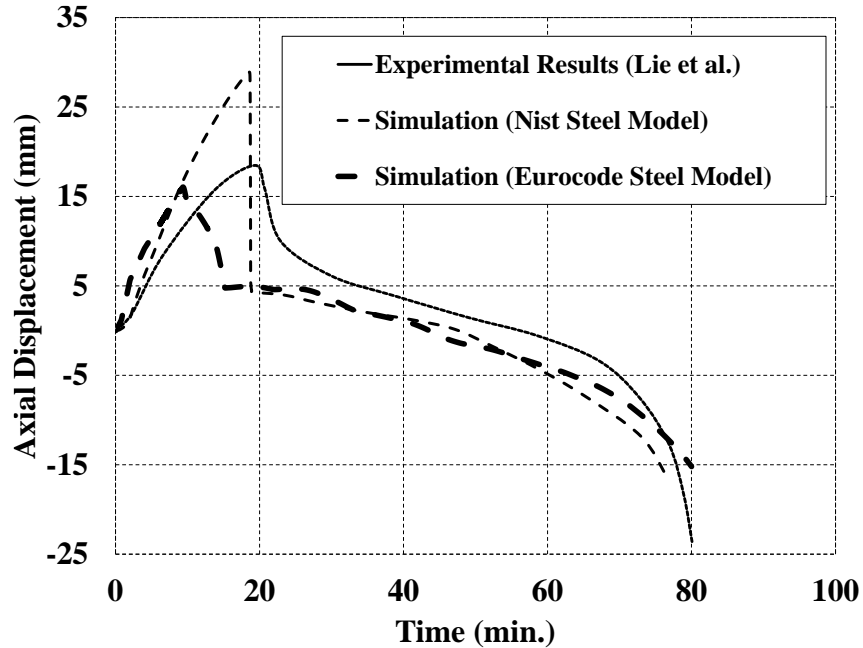


Figure 3- 33 Axial displacement results from ABAQUS with NIST steel model compared with experimental data (Chabot and Lie 1992) and simulation results with Eurocode steel model

The thermal and structural temperature-dependent material properties of steel and concrete will be adopted from the Eurocode models (mentioned above) in the following studies presented in this report, unless stated otherwise for specific reasons. Based on the comparisons made between the results from numerical analyses and the experimental data, the accuracy of the thermal-stress model is considered to be acceptable for the pre-test verification process. The models will be revisited and checked again in post-test validation analyses to check the accuracy of their results in simulating the fire tests conducted in this project.

SECTION 4

CYCLIC TESTING TO DAMAGE CFDST COLUMNS (PRIOR TO FIRE TESTS)

4.1 General

This section presents the first part of the experimental work conducted to study the behavior of concrete-filled double-skin tubes subjected to post-earthquake fires. The first part of testing was designed to simulate the effects of seismic damage on the specimens by subjecting them to cyclic lateral loading. The second part examines the behavior of seismically damaged specimens under fire and is presented in Section 5. The main objective of the cyclic loading tests was to impose different levels of seismic damage to the specimens, resulting in columns with different initial conditions for the fire resistance tests.

Three identical one-quarter scale column specimens were built and two of those were subjected to different levels of cyclic loading. The specimen not subjected to seismic loading served as a reference undamaged column, going directly to the fire test (i.e., to be fire tested without prior earthquake damage). The other two specimens were subjected to cyclic lateral loading. In order to study the effects of different levels of seismic damage on the performance of the specimens under fire, the cyclic tests were designed to impose two different damage levels on the specimens. One of the cyclic tests was conducted until the point when the onset of inelastic local buckling became visible in the specimen. The other test was continued further beyond that point, up to a higher damage level (i.e., developing more severe local buckling), and ended leaving a higher residual drift ratio for the column.

Section 4.2 presents the details of specimen design. A full description of the specimens' geometry, material selection and calculation of section properties is presented along with details of the construction procedure. Section 4.3 describes the experimental setup for conducting cyclic tests on the specimens, and how it was designed. Section 4.4 presents information on the construction and preparation of the test setup. Section 4.5 describes specimen instrumentation and its intended purpose. Sections 4.6 and 4.7 respectively present the protocol followed in the cyclic tests, and the experimental results obtained for all the specimens.

4.2 Specimen Design

Due to the importance of studying the effects of different seismic damage levels on the specimens' fire resistance and the limitations of the project in terms of number of fire tests that could be conducted within the available budget, it was decided to design and build three identical specimens. The only changing variable in the fire tests thus became the specimens' different initial conditions, in terms of seismic damage prior to the fire. Concrete-filled double-skin tube columns were selected for this project, as an extension of studies by Fouché and Bruneau (2010), which showed that these columns had superior performances compared to conventional bridge columns when subjected to multi-hazard (earthquake and blast) conditions.

The specimens used for the current studies were selected to be identical to one of those examined by Fouché and Bruneau (2010), which were a quarter scale of the prototype columns they considered. The geometry of the specimen was also chosen to be compatible with the limitations of the experimental setup for cyclic and fire testing procedures of this project. Note that the selected specimens satisfied the compactness criteria defined in AISC specifications for steel structures (AISC 2010a) and the ductility requirements for round filled composite members in AISC seismic provisions (AISC 2010b) as described in the following sections.

4.2.1 Geometry of the Specimens

To insure ductile behavior for concrete-filled steel tubes, the AISC specifications for steel structures and the AISC seismic provisions (AISC 2010a, b) provide limits on the diameter to thickness ratios (D/t) of the tubes. These values which are shown in Table 4.1 were complied with, particularly the first column in the row of compactness criteria and the first two columns in the row of ductility criteria, in the design of concrete-filled double-skin tubes in this project due to the similarities of the two design alternatives. In Table 4.1, f_y and E refer to the yield strength and Young's modulus of the steel material used for the steel tube. The main geometric features of the single design for all three column specimens of this project are summarized in Table 4.2.

Note that the inner tube has a diameter-to-thickness ratio (D_i/t_i) equal to 55.6, which satisfies the compactness limit for high ductility (per Table 4.1), while the outer tube has a diameter-to-thickness ratio (D_o/t_o) equal to 72.2, which makes it a compact for moderately ductility. Both are acceptable as the AISC

seismic provisions allows this type of composite members to be either highly or moderately ductile (defined per the limits in Table 4.1).

Table 4- 1 Compactness and Ductility Criteria for Round Filled Composite Elements (AISC2010a, b) – Limiting values are calculated based on nominal material properties (E=29,000 ksi (200,000 MPa) and fy= 32 ksi(220MPa))

Width to Thickness Ratio Limits			
Compactness Criteria for Round Filled Composite Elements	λ_p Compact/ Non-Compact	λ_r Non-Compact/ Slender	λ_{max} Maximum Permitted
	$\frac{0.09E}{f_y} = 81.8$	$\frac{0.31E}{f_y} = 281.8$	$\frac{0.31E}{f_y} = 281.8$
Ductility Criteria for Round Filled Composite Elements	λ_{hd} Highly Ductile	λ_{md} Moderately Ductile	λ_{maxd} Maximum Permitted
	$\frac{0.076E}{f_y} = 69.1$	$\frac{0.15E}{f_y} = 120.8$	$\frac{0.15E}{f_y} = 120.8$

Table 4- 2 Geometry of the Specimen

Height	Diameter of Outer Tube	Diameter of Inner Tube	Thickness of Outer Tube	Thickness of Inner Tube	D_o/t_o	D_i/t_i	Void Ratio	Ductility Class	
	H (in.)	D_o (in.)	D_i (in.)	t_o (in.)				t_i (in.)	Outer Tube
106.5	8	5	0.11	0.09	72.2	55.6	0.63	MD	HD

Fig. 4.1 shows the section of the specimen. The section has a void ratio of 0.63, which is a relatively high value. The large void ratio was chosen for the specimen mainly to provide more space in the middle for construction purposes, as will be explained in the following sections. The height of the specimen was determined based on the limitations of the experimental setups for the cyclic and fire tests. The fire testing furnace required a total height of 10' for the specimen to fit. Considering the additions to the column at its

top and bottom, which were designed for installation purposes in both of the cyclic and fire test setups (explained later in this report), the column height was calculated to be 106.5”.

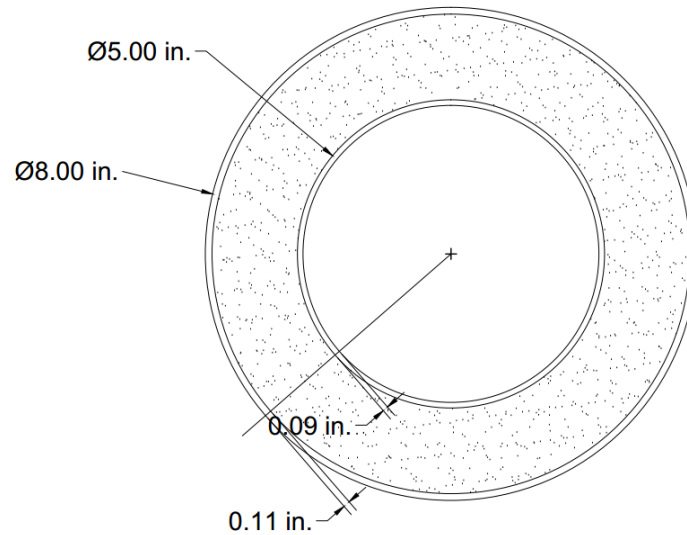


Figure 4- 1 Cross-section of the Specimen

4.2.2 Materials

4.2.2.1 Steel

Specimens were constructed of electric resistance welded tubes manufactured from ASTM A513 type 1 steel. The nominal yield and tensile strength for this steel are 32ksi (220.6 MPa) and 45ksi (310.3 MPa), respectively. The material is expected to have a minimum of 15% elongation at failure. Measured stress-strain curves from coupons tested separately for the outer and inner tubes are shown in Fig. 4.2. ASTM A36 steel was used to build the parts of the experimental setup connected to the columns (i.e. end plates, fixed base, etc.). The nominal yield and tensile strength for this A36 steel are 36ksi (248.2 MPa) and 58ksi (399.9 MPa), respectively. This type of steel is expected to have a minimum elongation of 20% at failure.

4.2.2.2 Concrete

For the chosen concrete-filled double-skin tubes geometry, the two steel tubes were only 1.5” apart from each other, making it impossible to use a vibrator to compact the concrete during construction. Therefore, a self-compacting concrete was used, with nominal compressive strength of 5.0ksi (34.5 MPa), maximum

aggregate size of ½”, and a spread of 18”-30” during the slump test. All of the specimens were built from the same concrete batch and concrete cylinders were casted on the construction day to be tested on the day of specimen testing. The average compression strength obtained from those cylinder tests was in the range of 8-10ksi (55.2-68.9 MPa) depending on the length of curing (results are reported in Table 4.3). The significant difference between the nominal and actual values is considered to be a consequence of the use of super plasticizers by the concrete provider to achieve the high workability requirements.

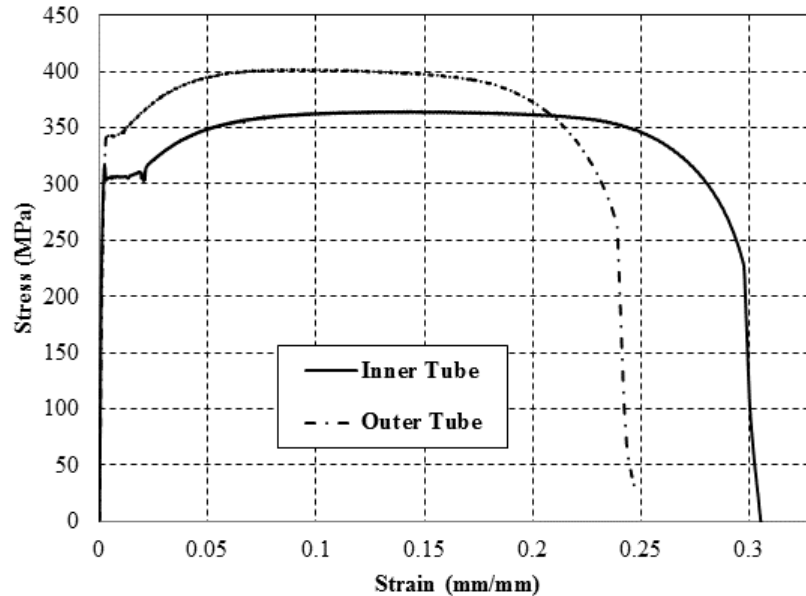


Figure 4- 2 Stress-strain Curve for Inner and Outer Tube Steel Materials

Table 4- 3 Concrete Cylinder Test Results

Specimen	Cylinder Tests Conducted on the Day of	Compressive Stress Results			
		Cylinder 1	Cylinder 2	Cylinder 3	Ave.
S1	First Cyclic Test	7.9 ksi (54.5 MPa)	8.0 ksi (55.2 MPa)	8.2 ksi (56.8 MPa)	8.0 ksi (55.8 MPa)
S2	Second Cyclic Test	8.9 ksi (61.3 MPa)	8.7 ksi (59.9 MPa)	8.5 ksi (58.6 MPa)	8.7 ksi (60.0 MPa)
S3	First Fire Test	9.6 ksi (66.2 MPa)	9.5 ksi (65.5 MPa)	10 ksi (68.9 MPa)	9.7 ksi (66.9 MPa)

4.2.3 Calculation of Section properties

The full plastic moment strength (M_p) of the specimens was calculated based on the nominal material properties. The calculation was done using the plastic stress distribution method, assuming the steel to be fully yielded and the concrete to have reached its strength, f'_c , where in compression while being cracked and providing no strength in tension. It was decided to use the full f'_c , instead of $0.95f'_c$ mentioned in AISC provisions, to indirectly account for some of the confinement provided by both the inner and outer tubes. Fig. 4.3 shows the cross-section with an assumed position for the neutral axis (N.A.).

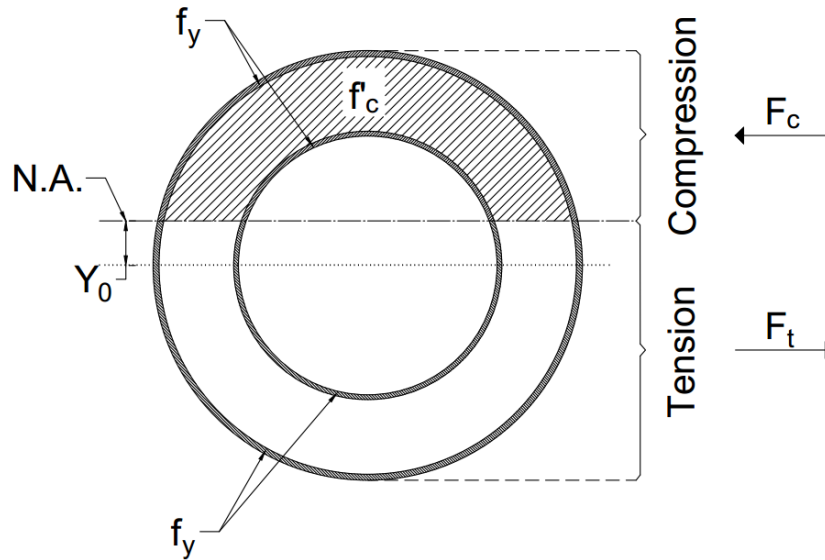


Figure 4- 3 Cross-section of the Specimen with the Assumed N.A.

The plastic moment for the section is calculated by summation of the contributions from the concrete, inner tube and the outer tube, as expressed by:

$$M_p = M_{P_{Concrete}} + M_{P_{Outer Tube}} + M_{P_{Inner Tube}} \quad (4.1)$$

Total compressive and tensile forces acting on the parts of the thin-walled tube above and below the N.A. (Fig. 4.4) can be calculated by:

$$F_c = f_y(\pi r t - 2 r \gamma t) = 2 f_y r t \left(\frac{\pi}{2} - \gamma \right) \quad (4.2)$$

$$F_T = f_y(\pi r t + 2r\gamma t) = 2f_y r t \left(\frac{\pi}{2} + \gamma\right)$$

where f_y is the plastic stress, r is average radius, t is the wall thickness and γ is the angle determining the position of the N.A. in radians (Fig. 4.4).

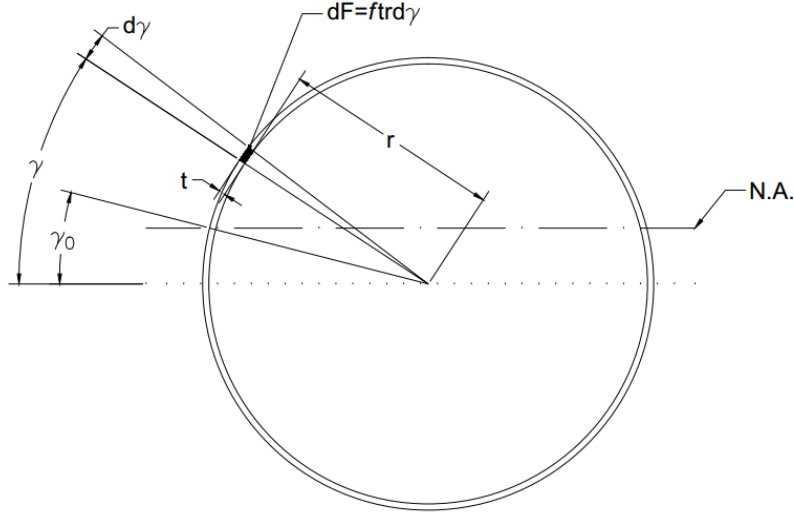


Figure 4- 4 Differential Element for Calculation of Tensile and Compressive Forces of a Tubular Section

Equation 4.2 is used to calculate total forces for both the inner and outer tubes. These forces are multiplied by their moment arms to calculate their contribution to the plastic moment of the section. For a given tube, the moment arm for the compressive force, d_c , (shown in Fig. 4.5) is given by:

$$d_c = \frac{r \sin\left(\frac{\pi}{2} - \gamma\right)}{\left(\frac{\pi}{2} - \gamma\right)} = \frac{r \cos \gamma}{\left(\frac{\pi}{2} - \gamma\right)} \quad (4.4)$$

and the plastic moment component coming from the compression side of the tube is:

$$M_C = F_C d_c = 2f r t \left(\frac{\pi}{2} - \gamma_0\right) \cdot \frac{r \cos \gamma_0}{\left(\frac{\pi}{2} - \gamma_0\right)} = 2f r^2 t \cos \gamma_0 \quad (4.5)$$

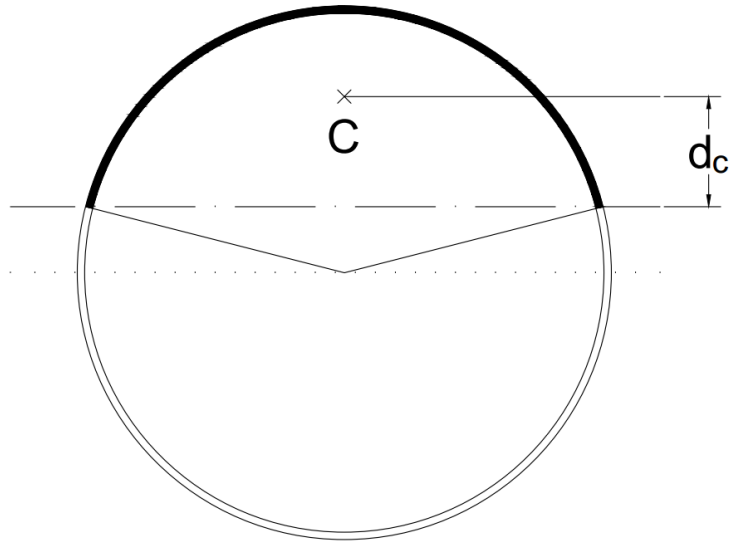


Figure 4- 5 Moment Arm for Total Compressive Force of a Tubular Section

Similarly, for the tension side the lever arm, d_t , and the plastic moment component, M_T , are given by:

$$d_t = \frac{rcos\gamma_0}{\left(\frac{\pi}{2} + \gamma_0\right)} \quad (4.5)$$

$$M_T = F_T d_t = 2f r t \left(\frac{\pi}{2} + \gamma_0\right) \cdot \frac{rcos\gamma_0}{\left(\frac{\pi}{2} + \gamma_0\right)} = 2f r^2 t \cos \gamma_0 \quad (4.6)$$

The resulting contribution to the total plastic moment for one tube is:

$$M_{Tube} = M_C + M_T = 4f r^2 t \cos \gamma_0 \quad (4.7)$$

Total compressive force and the resultant moment for the concrete part of the section is calculated by subtracting the results for a circular section defined by the inner radius of the concrete section, r_{ci} , from the results for a larger circular section defined by the outer radius of the concrete section, r_{co} . The total force and moment corresponding to the part of a circular section above the N.A. are calculated by integration using the differential elements shown in Fig. 4.6.

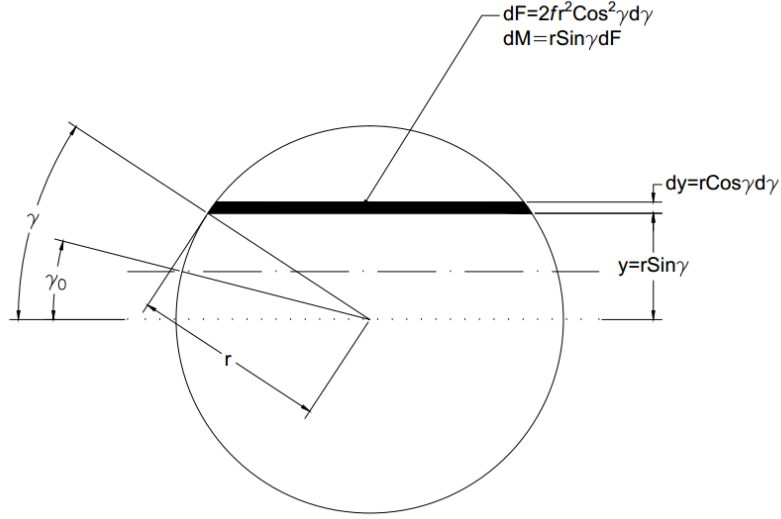


Figure 4- 6 Differential Force and Moment Calculation for a Circular Section (Above N.A.)

Since f'_c is the stress value for all of the elements, total force and moment values are given by:

$$F = \int_{\gamma_0}^{\frac{\pi}{2}} 2fr^2 \cos^2 \gamma d\gamma = \frac{fr^2}{2} (\pi - 2\gamma_0 - \sin 2\gamma_0) \quad (4.8)$$

$$M = \int_{\gamma_0}^{\frac{\pi}{2}} 2fr^3 \cos^2 \gamma \sin \gamma d\gamma = \frac{2}{3} fr^3 \cos^3 \gamma_0 \quad (4.9)$$

Solving Eqs. 4.8 and 4.9, the total force and plastic moment resulting from the concrete part of the specimen are given by:

$$F_{Conc.Comp} = \frac{f}{2} (\pi - 2\gamma_0 - \sin 2\gamma_0) (r_{co}^2 - r_{ci}^2) \quad (4.10)$$

$$M_{Conc.} = \frac{2}{3} f \cos^3 \gamma_0 (r_{co}^3 - r_{ci}^3) \quad (4.11)$$

The location of the N.A. can be found by satisfying equilibrium for all the above axial forces acting on the cross-section, namely:

$$F_{C,Inner Tube} + F_{C,Outer Tube} + F_{Conc.Comp.} = F_{T,Inner Tube.} + F_{T,Outer Tube} \quad (4.12)$$

where, using Eqs. 4.2 to 4.10, the components of Eq. 4.12 can be calculated as:

$$F_{C,Inner Tube} = 2F_y r_i t_i \left(\frac{\pi}{2} - \gamma_0 \right) \quad (4.13a)$$

$$F_{C,Outer Tube} = 2F_y r_o t_o \left(\frac{\pi}{2} - \gamma_0 \right) \quad (4.13b)$$

$$F_{C,conc.Comp.} = \frac{f_c}{2} (\pi - 2\gamma_0 - \sin 2\gamma_0) (r_{co}^2 - r_{ci}^2) \quad (4.13c)$$

$$F_{T,Inner Tube} = 2F_y r_i t_i \left(\frac{\pi}{2} + \gamma_0 \right) \quad (4.13d)$$

$$F_{T,Outer Tube} = 2F_y r_o t_o \left(\frac{\pi}{2} + \gamma_0 \right) \quad (4.13e)$$

Substituting Eq. 4.13 into 4.12, γ is left as the only unknown of the equation, and can be calculated, giving both the position of the N.A. and the value of the plastic moment for the cross-section. Using Eqs. 4.7 and 4.11, the total plastic moment is given by:

$$M_p = 4F_y r_i^2 t_i \cos \gamma_0 + 4F_y r_o^2 t_o \cos \gamma_0 + \frac{2}{3} f_c \cos^3 \gamma_0 (r_{co}^3 - r_{ci}^3) \quad (4.14)$$

Using the geometric and nominal material properties of the section mentioned above, total plastic moment was calculated to be 360kip.in (4.07×10^4 KN.m). However, for experimental purposes, to design the test set-up from a capacity design perspective, a greater maximum specimen flexural strength was conservatively calculated using Equation 4.14 considering both an over strength factor of 1.5 for the nominal yield strength and a strain hardening factor of 1.5 for the steel tubes, and both a factor of 1.7 for the concrete compressive strength to account for the higher expected values along with a factor of 1.5 to consider the added strength due to confinement effects, for the concrete core.

Using the new material strength values, the conservative maximum flexural strength was calculated to be 816kip.in (9.22×10^4 KN.mm) and was used in a capacity design approach to design the experimental setup (as described in the following sections). Note that shear capacity of the specimen was not an issue (for the specimen geometry chosen) and that design of the experimental setup was dictated by developing flexural failure of the column.

4.3 Description of the Experimental Setup for Cyclic Tests

4.3.1 General

The specimens were designed to be fixed at their base on a lateral foundation beam to form a vertical cantilever condition. The base beam constructed from a W14x211 section was attached to the strong floor of the lab. One end of the base beam was welded to an A-shaped reaction frame, from which lateral forces could be applied to the specimens using a 50kip MTS actuator. Fig. 4.7 illustrates this experimental setup.

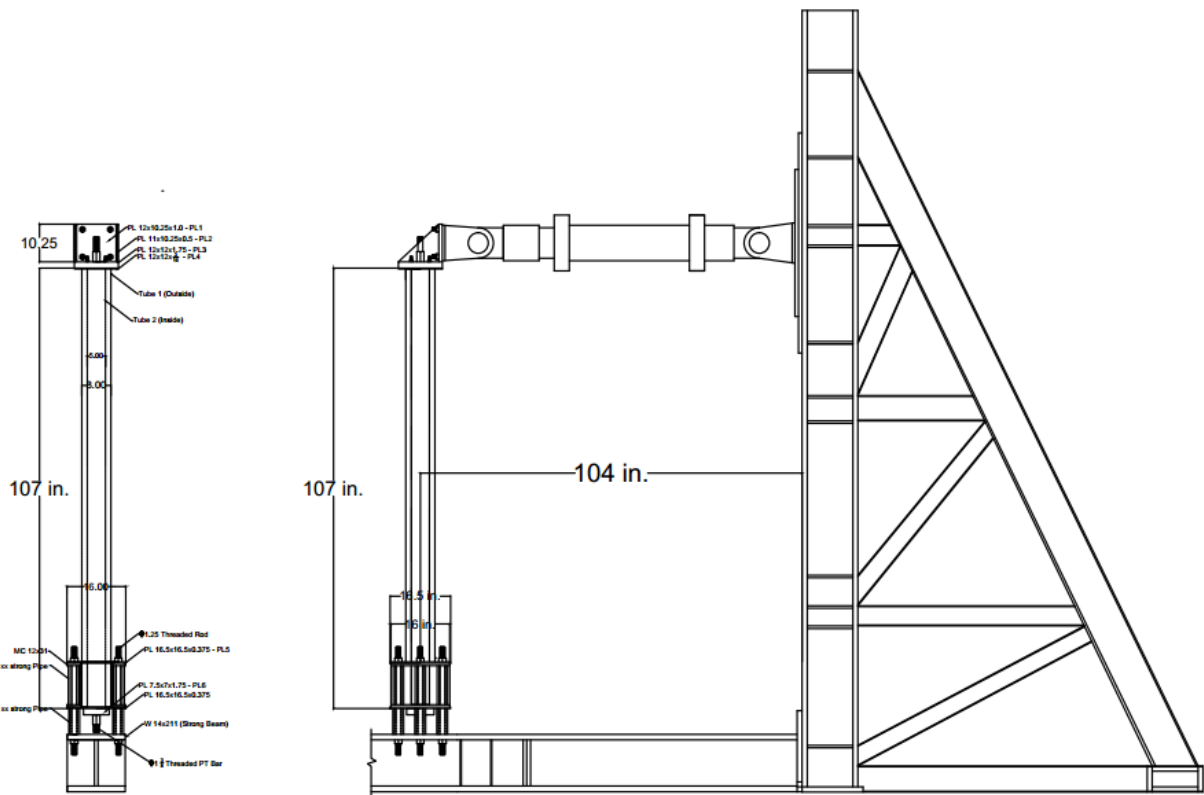


Figure 4- 7 Experimental setup for Cyclic Tests

An additional part was designed to be added to the base of each specimen in order to move the position of the maximum moment from the connection point on the base beam to the top of that additional part welded to the column base. This configuration also prevented damage from occurring to the base beam during the cyclic loading process. The additional part welded to the base of the columns consisted of two channels with their flanges facing outward and two plates welded to all free edges of the channel flanges on their top and bottom. The details of this additional part are shown in Fig. 4.8. For convenience, this built-up part will be referred to as the box section from now on in this report.

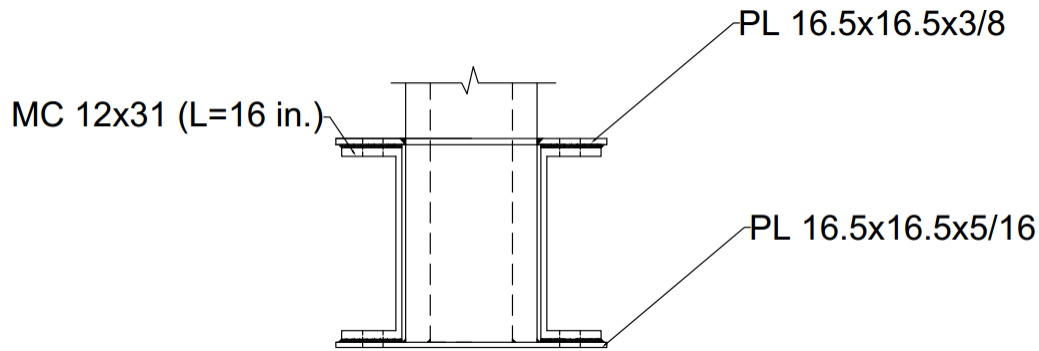


Figure 4- 8 Details of the Additional Parts to the Specimen's Base (built-up box section)

4.3.2 Design of the Setup

4.3.2.1 Assumptions

This section describes the transfer of the loads (lateral and axial) from the top of the specimen all the way to the foundation beam. Structural elements along this load path are designed to resist those loads. A complete free body diagram showing the assumed load transfer mechanism is shown in Fig. 4.9.

The lateral load is transferred from the actuator to the transfer element on top of the specimen. This load is distributed to the full composite section mainly by bearing of the threaded rods coming out of concrete and also by the friction forces at the interface of horizontal plate of the transfer element and the top plate of the specimen.

The load applied at the top of the composite section produces bending and shear forces acting on top of the channels at the bottom of the specimen. The load goes from the column to the plate by bearing against the thickness of the plate at the circular welded connection. Stresses in the plate are transferred to top flanges of the channels on both sides through the welds and the connecting rods. To satisfy equilibrium, equal forces are developed in the bottom flanges of the channels in the opposite direction. These opposite forces at the top and bottom flanges create a bending moment resisted by the channels. This moment is transmitted to the bottom plate of the specimen and, from there, resisted by tension in the rods going into the foundation beam and compression by the hard contact between the bottom plate and the top flange of the foundation beam. Design process of the experimental setup for the cyclic test is presented in the following sections.

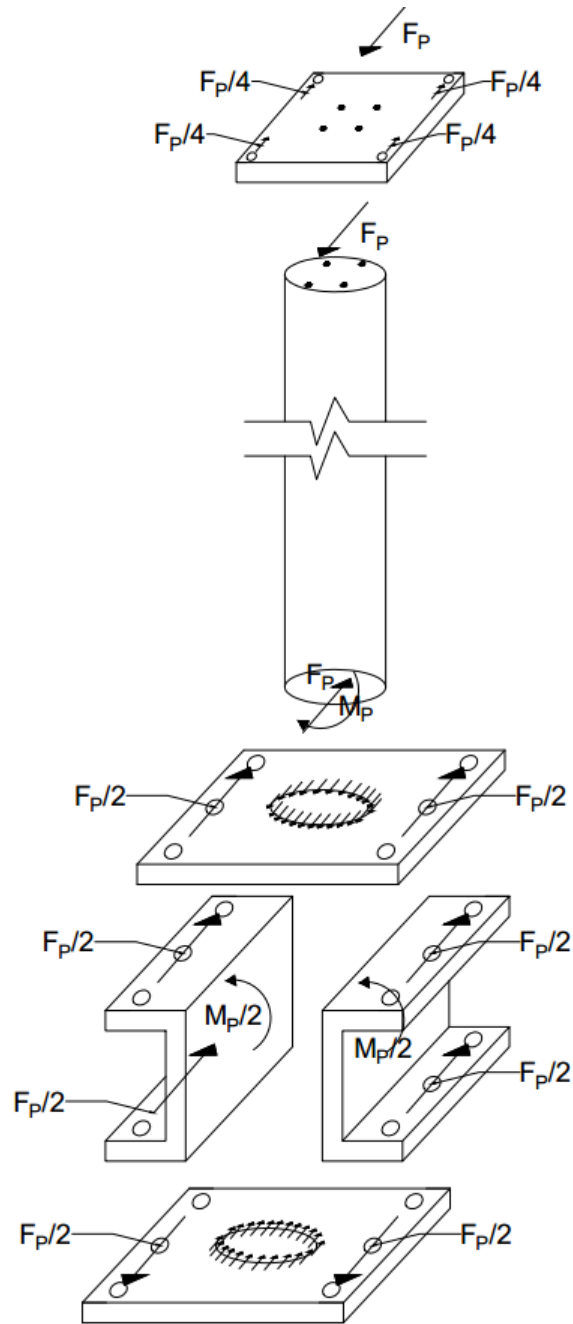


Figure 4- 9 Complete Free Body Diagram of the Specimen

4.3.2.2 Calculation of the Maximum Lateral Load Applied to the Specimen

Maximum lateral load applied to the specimen by the actuator was calculated based on the maximum capacity of the specimen, assuming development of plastic hinging of the column above the plate on top of

the channels. The moment at that position is equal to the sum of the moments caused by the lateral load from the actuator and the axial load applied from the threaded rod since its line of action has a little eccentricity from the center of the plate on top of the channels. The maximum force was calculated using the maximum expected M_p value calculated in the previous section (816 kip.in.). To ensure that all the transfer elements worked safely during the experiments, and for expediency, the whole setup was designed for a maximum lateral load of 10kips, which was about 20% more than the calculated force.

4.3.2.3 Transfer Element (Connecting the Actuator to the Specimen)

The transfer element was designed to carry the load from the actuator to the specimen. It was also used as a bearing plate for the axial load coming from the threaded rod. Considering that this piece was intended to be reusable for different tests, it was designed to be practically rigid, by selecting oversized plates. As shown in Fig. 4.10, the transfer element consisted of a 0.5” thick vertical plate welded to a horizontal plate to form an L-shaped element. The vertical plate was supported by two triangular 0.25” plates, which were welded to both sides of the L-shaped element.

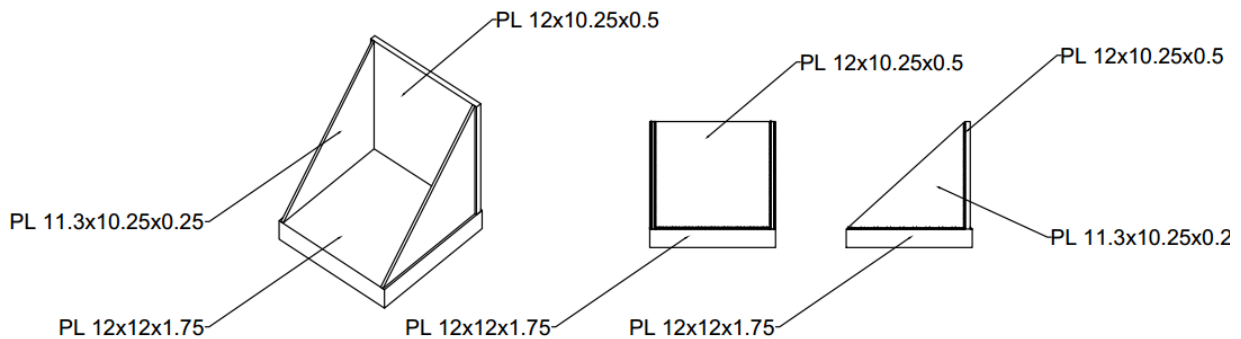


Figure 4- 10 Built-up Transfer Element

The horizontal plate of the transfer element was designed for bearing the axial force coming from the post-tensioning rod. The plate was checked for bearing stresses, punching shear, and yield line analysis capacity for the selection of a proper thickness. The manufacturer suggested thickness for the bearing plates of 1 3/8” threaded rods was finally selected. This thickness of 1 3/4” was larger than the maximum value calculated in the design process.

The transfer element is connected to the specimen with four 1/2” ASTM A193 grade B7 threaded rods. This type of steel has nominal yield and tensile strength of 105ksi (723.9 MPa) and 125ksi (861.8 MPa), respectively. Minimum elongation at failure for this type of steel is expected to be about 16%, but all rods

were designed to remain elastic. The rods were designed to work in combined tension and shear loading based on the anchorage design procedures presented in the Appendix D of ACI 318-11 code (ACI 2011).

The rods are in tension because of the pretensioning and the pulling from the actuator (when pretensioning forces are exceeded). Shear forces are also caused by the lateral force coming from the actuator. It was assumed that the shear force was divided equally between the four rods. The tensile strength of the rods was calculated based on their minimum capacity considering different failure mechanisms: Tensile failure of steel, concrete breakout, anchor pull out and side face blow out. Failure mechanisms considered in the calculation of the shear strength include steel failure, concrete break out and concrete pryout. These mechanisms are shown for tensile and shear failures in Fig. 4.11 and Fig. 4.12, respectively.

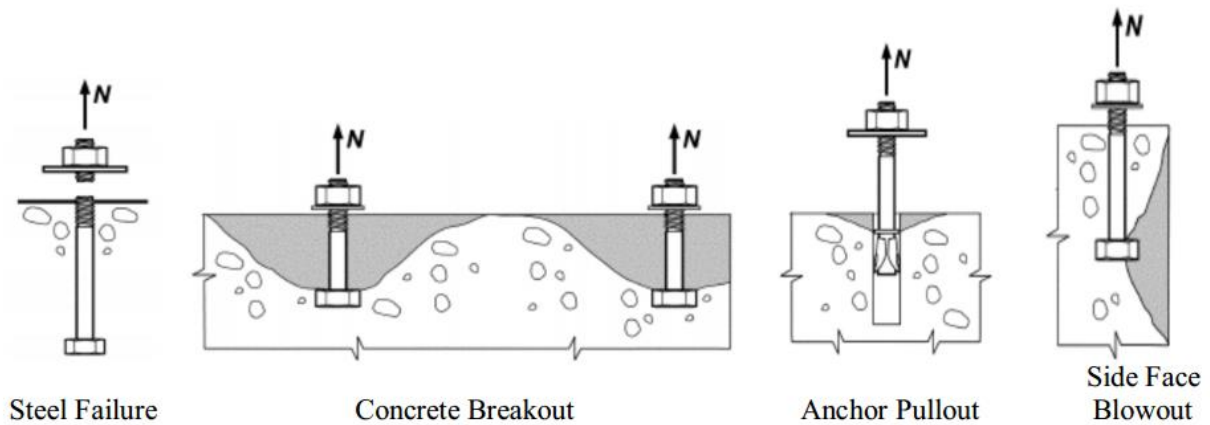


Figure 4- 11 Failure Modes for Anchor Bolts in Tension (ACI 318-11)

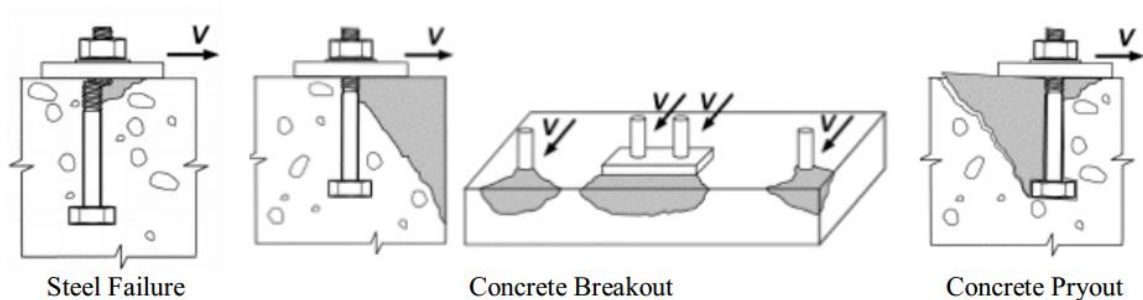


Figure 4- 12 Failure Modes for Anchor Bolts in Shear (ACI 318-11)

Tensile strength (ϕN_n) and shear strength (ϕV_n) for the 1/2" rods were calculated to be 20.39 kips and 32.16 kips, respectively, and found to be adequate when considering tension-shear interaction. An embedment depth for the threaded rods of 16" was selected based on the ACI regulations.

4.3.2.4 Connection of the Cap Plate to the Specimen

The lateral load from the actuator was assumed to be transferred to the specimen by the threaded rods embedded in the concrete. However, there was a possibility that a part of this load could be transferred to the weld connecting the specimen to the cap plate by bearing of the threaded rods to the holes in the cap plate. To make sure no failure would happen in the process of load transfer from the actuator to the full composite section, it was decided to design the weld connecting the cap plate to the specimen to also be capable of carrying the full expected lateral load.

It was assumed that the lateral load was distributed uniformly over the full length of the circular weld. Using the design procedures for welded connections recommended in AISC J2.4 section (AISC 2010a), a minimum weld thickness of 1/8" was found adequate for the connection to carry the maximum lateral load from the actuator. Note that for the cap plate to resist the bearing loads from the threaded rods carrying the actuator force, calculations showed that a 3/16" thick cap plate would be sufficient (and this didn't govern its sizing).

4.3.2.5 Design of the Box Section at the Base of the Specimen

The channels of the box section were designed to carry the full expected plastic moment of the specimen while remaining elastic. Therefore, the required combined section modulus of the channels was calculated based on their yield strength ($F_y=36\text{ksi}$). The channels needed to be checked for flange local buckling, web yielding, web crippling and web compression buckling. As mentioned before, six tube studs were placed tightly between the top and bottom flanges of the channels to ensure stability. Based on the design calculations, two MC12x31 channels were selected to be used for the box section.

It should be mentioned that some of the dimensions of the elements used for the additional part were forced to be within limits imposed by the existing conditions of the testing facility. The width of the top and bottom plates of the box section were selected to be equal to the width of the top flange of the foundation beam (16"). Therefore, square 16"x16" plates were selected to be checked for design requirements. The thickness of the plate was calculated based on the state of the stress in its plane. The governing equations for this analysis were adapted from a study by Fujikura et al. (2007) that presents a similar analysis case. Considering that the load transfers from the outer tube of the specimen to the plate through a bearing mechanism, the thickness of the plate should be adequate to carry the bearing load which is given by:

$$F_{bearing} = \frac{M_P}{d} \quad (4.14)$$

in which M_p is the full plastic moment of the specimen and d is the distance between the top and bottom plates of the box section. This distance is determined by the depth of the channels that are placed between the plates. This calculation determines the minimum required thickness for the top and bottom plates (5/16").

In addition, assuming simply supported conditions for the plates at their welded edges, they were checked for shear loading in beam action. Assuming the bearing load calculated above was applied as a distributed load to the beam, the thickness and length of the plates were found adequate for this load. Another conservative design check was done by assuming the bearing load applied as a concentrated force to a simply supported beam. This time the plates were checked to be adequate for the bending moment caused by this concentrated force.

Since the plates were not embedded in concrete in this project contrary to the design in the study by Fujikura et al. (2007), they were checked for out-of-plane buckling assuming simply supported conditions at the edges. The calculations showed that the critical buckling stress for the selected thickness and width values was larger than the yield stress. Based on the design checks done in this section, two MC 12x31 channels were finalized to be used in the box section. A 5/16" plate was selected for the bottom side of the box. Although this plate size was shown to be also adequate for the top side, due to some concerns about having a limited amount of yielding in some areas of the top plate based on finite element analyses, it was decided to use a 3/8" plate at the top. The welds connecting the channels along all the edges of their flanges to the top and bottom plates were designed to be strong enough for the necessary loads.

4.3.2.6 Welds Connecting Top and Bottom Plates of the Box Section to the Outer Tube

A complete joint penetration groove weld was decided to be used for the connection of the outer tube to top plate of the box section. Filling the gap between the outer tube and the 3/8" plate makes the strength of the connection to be the same as the base metal. Therefore, the capacity of the connection will be equal to the capacity of its elements. This configuration will transfer the force coming from the tube during the cyclic test to the plate as an in plane force for which it was designed to be adequately resistant. The weld of the bottom plate to the outer tube was designed based on the tensile strength of the tube. Calculations showed that a minimum fillet weld size of 1/8" was enough for this connection.

4.3.2.7 Effects of Axial Load on the Specimen and the Box Section

The amount of axial load to be applied to the specimen was based on two limitations. First, it had to be in the range of loads that are applied to columns in typical buildings (gravity load) which is usually close to 30% of the axial strength of the column. The second limitation was imposed by the specific method used for applying the axial load in this project. The available equipment in the cyclic testing lab allowed the maximum axial load of 70-80kip to be applied to the specimen by post-tensioning the threaded rod. The fire testing facility also had the maximum limit of 120kips for the axial load. Since the maximum possible axial load limit in the cyclic testing lab for this particular experimental setup was about 30-40% of the column's axial strength calculated by the measured material properties (208 kips), it was decided to keep the axial load in the range of 70-80kips.

A 1 3/8" ASTM A193 grade B7 threaded rod was used for applying the axial load. The applied load at its upper bound (80 kips) creates a tensile stress which is about 51% of the yield strength of the rod (105ksi). This satisfies the safety requirements and ensures that the same rod can be used for all of the specimens. Along with the threaded rod, two 1 3/4" thick plates were used at top and bottom of the specimen as bearing plates for the axial loads. The sizes of these plates were selected based on manufacturer recommendations and design procedures that were mentioned earlier. These elements were also used multiple times for all of the specimens.

The experimental setup was conservatively checked for an axial load of 120kip to be sure no problems would occur in case the axial load was increased to the limit values of the fire lab. A portion of this load will transfer into the channels added to the base of the column for which the capacity of the connection and the channels should be checked. Since the connection is made of a full joint penetration weld, the total shear capacity of a 3/8" plate is available to be used for the load transfer. This shear capacity is larger than the total axial load applied to the specimen. When the load is transferred to the channels, it will be resisted by the tube studs placed between the top and bottom flanges. The design of the tube studs are presented later in this section.

4.3.2.8 Threaded Rods at the Base and the Supporting Tubes

Six 1.25" ASTM A193 grade B7 threaded rods were used to connect of the specimen to the foundation beam. The diameter size was dictated by the holes already present on the foundation beam and checked to

be adequate for the forces. The rods were designed to run through tube stubs for two time along their way to the base beam. First, the rods go through the tubes that are about 12” long and placed between the top and bottom flanges of the channels (to prevent buckling or instabilities) and second, through the pipes placed between the bottom plate of the specimen and top flange of the foundation beam to keep the specimen about 7” above it. The tubes used for both locations were 2 ½” xx strong pipes that according to AISC specifications have the yield stress and tensile stress of 35ksi and 60ksi, respectively (ASTM A53 Gr. B). The pipes had a nominal wall thickness of 0.552” that satisfied the geometric constraints of the setup. The threaded rods had to be pretensioned to keep the specimen fixed in place during the cyclic loading. Considering the lab safety and the fact that the rods were going to be used for all of the specimens, it was decided to pretension the rods only up to 50% of their yield strength. This pretensioning force is directly transferred to the pipes as an axial load.

The tensile and compressive forces applied the threaded rods and the pipes were calculated by adding up the effects from the lateral and axial loads applied to the specimen plus the pretentioning force applied to the rods. The threaded rods were checked for combined effects of tension and shear according to the AISC J.3 provisions for bolted connections (AISC 2010a). The two sets of pipes were checked to remain below the critical axial load level during the tests.

Results showed that on the compression side, the axial force on the pipes were below the critical buckling load for both the 12” and 7” elements. On the tension side, the pipes lost some of the axial load because of the tension coming from the applied moment, but they were still in compression meaning that the specimen would remain fixed in place during the cyclic loading.

4.3.2.9 Effects of Out of Plane Deformations

The experimental setup for cyclic loading was designed assuming that the top of the specimens would be displaced in a direction parallel to the bottom beam. However, since no lateral bracing was provided for the specimen, there was a possibility of accidental eccentricity and displacements out of that plane, which would cause eccentric shear in the rods and undesirable bending in the weak direction of the box assembly at the base of the specimen. Since all of the elements of the setup were conservatively oversized, the effects of accidental eccentricity on the stresses were expected to be insignificant, but out-of-plane displacements of the specimen were monitored during the experiment in case these became excessive and a cause for concern.

4.4 Construction

Assembly of the specimens started by welding the inner and outer tubes to the base plates of their box sections. Next, the channels were added to both sides of the outer tube and finally the top plate of the base was slid over the outer tube to rest on the two channels. It should be mentioned that the top plate for each specimen had a circular hole in its center with a diameter oversized by 1/8" with respect to the diameter of the outer tube. After checking the alignment of the holes, straightness of the column and equal distribution of the gap around the circular hole, the top plate was fillet welded to the flange of the channels along all edges. Finally, the gap between the top plate of the box section and the outer tube was filled with a full penetration weld (Fig. 4.13).

Since the specimens were to be used in fire tests after the cyclic loading tests, thermocouples were installed inside the specimen before pouring the concrete. Two thermocouples were attached to the outer and inner tube surfaces from inside the specimens. A third thermocouple was positioned approximately at the center of the gap between the inner and outer tubes. The wires attached to these thermocouples were led out of the specimens through one of the four small diameter (1/4") vent holes (Fig. 4.14), which were drilled on the outer tube to provide an escape route for the pressurized vapor during the fire tests (two holes at each end of the column).



Figure 4- 13 Circular Welding of the Additional Elements to the Column's Base



Figure 4- 14 Thermocouple Wires Coming out of the Specimens

In order to keep a uniform gap distance between the inner and outer tubes of the specimens along the length of the column, small diameter rebars with length equal to the projected thickness of the concrete annular region were used as spacers welded between the inner and outer tubes at the top of the specimens.

Along with the three main specimens, three short stub columns were also built to be used in the fire tests. Using a base plate and the same inner and outer tubes, these columns had the same cross-section as the main ones. The only difference was that the stub columns were just 12” high, as opposed to 106.5” for the specimen columns. The same thermocouple instrumentation was also installed on the stub columns before pouring the concrete. The number of vent holes for the stub columns were reduced to two (one at each end) because of their much shorter length, except for the stub column SC2 that was fabricated with three holes in an attempt to study the effects of the number of ventilation holes on the heat transfer process in columns.

Self-compacting concrete was poured between the tubes for all specimen and stub columns. The concrete was poured gradually from the top without using any vibrator devices. A total of nine concrete cylinders were cast from the same batch of concrete to be used for compression tests at different stages of testing. The last step was to hold the threaded rods that were designed to stick out of concrete at the top of the specimens in the right position. This was done by fixing the four rods by nuts to the cap plates and embedding them in concrete while using the cap plate as an aligning tool.

Fig. 4.15 shows the preparation of the cap plates with the threaded rods. The specimens and the cast cylinders were then set aside for concrete curing. After a few days, the nuts connecting the cap plates to the threaded rods were taken out and the cap plates were temporarily removed so that, during the curing period, the top of the specimens was left open. Construction of the specimens was completed by reinstalling the cap plates and welding them to the outer tube of the column.



Figure 4- 15 Threaded Rods fixed on the Cap Plate to Be Embedded in Concrete

4.5 Instrumentation

4.5.1 General

The instrumentation for the cyclic tests was designed to capture the essential structural response parameters that can describe the column's behavior and characteristics under lateral cyclic loading. The parameters of interest include displacement response, forces, and strain distribution at specific locations. Displacement response was recorded at different points of the specimens by different methods to get a complete record of the deformations during the cyclic loading. These recordings can be useful in characterizing the ductility and hysteretic behavior of the specimens.

Displacement response was recorded by two different methods. First, a number of string pots were used to record the displacements relative to a fixed reference point. Second, a Krypton Dynamic Measurement

Machine was used to track the movements of certain points on the specimens where target Light Emitting Diodes (LED) devices were installed. Together, and in addition to the displacement transducer internal to the actuator, these were intended to provide sufficient data to quantify the overall deformation response of the specimens.

Strain distributions were recorded mainly for sake of detecting the occurrence and location of first yielding on the specimen. They also provide some measurement of plastic strain excursions in the specimens. Load cell devices were used to record the applied or resisting forces both in the lateral and axial directions. All instrumentation devices were connected to the input channels of two data acquisition (DAQ) systems: one was used for the strain gauges, linear potentiometers (string pots) and load cells both attached to the specimen and the actuator; the second one was dedicated to the Krypton LED sensors. A detailed description of the equipment used in the instrumentation of the experimental setup for the cyclic tests is presented in the following paragraphs. Fig. 4.16 shows a close view of the experimental setup with instrumentation.

4.5.2 Strain Gauges

Strain gauges were attached to the surface of the specimen in the longitudinal and circumferential directions to capture some aspects of the strain distribution on the outer steel tube. All of the gauges were close to the base of the specimen since it was expected that first yielding and plastic moment would develop in that area. Strain recordings from the gauges installed on the outer tube at locations both above and below the top plate of the box section were planned to be used for calculation of the moment diagram of the specimen at that region.



**Figure 4- 16 Specimen S1 after
Instrumentation**

All of the strain gauges used were from the type CAE-06-125-UW-120 provided by Vishay Precision Group. Each of the specimens used for the cyclic testing was equipped with a total of 16 strain gauges (front and back). Fig. 4.17 shows the strain gauge layout for a typical specimen, with gauges labeled from 1 to 16.

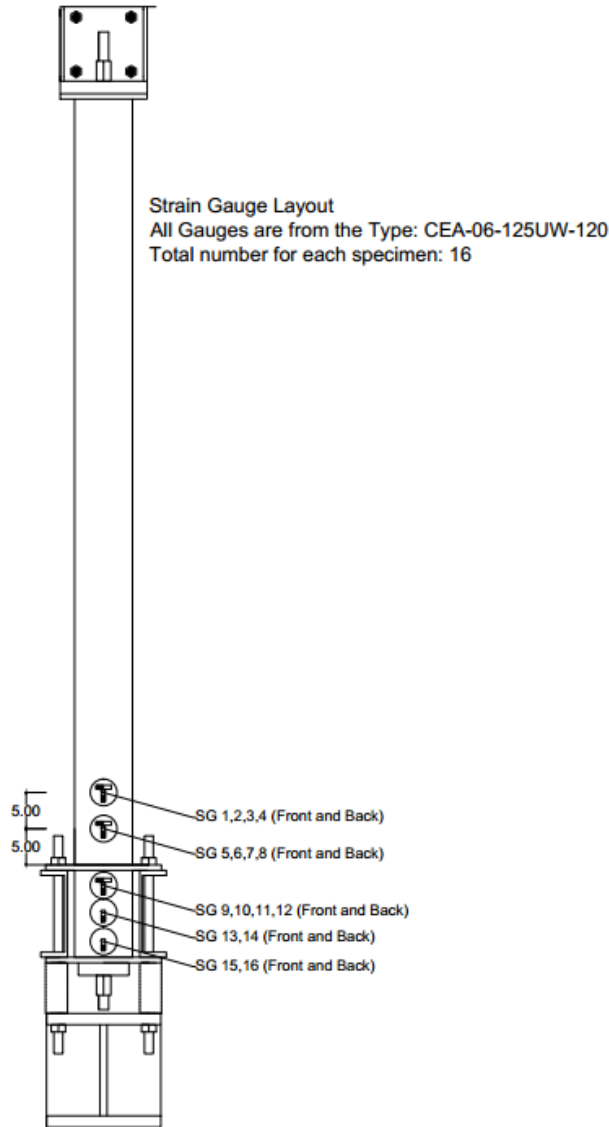


Figure 4- 17 Strain Gauge Layout

4.5.3 String Potentiometers

The displacement at the top of the specimen was recorded by a linear transducer mounted in the MTS 244.31 50 kips actuator, which has a stroke of $\pm 12''$. However, this transducer also recorded displacement of the reaction frame on which the actuator reacted during the test. To get a more reliable set of displacement recordings, seven linear displacement potentiometers (i.e., string pots) were used for each specimen (shown and labeled as SP1 to SP7 in Fig. 4.18), recording specimen displacement relative to a non-reactive post connected to the foundation beam. The string pot wires were attached to the outer tube of the specimen

using a magnetic mount. Note that SP 7 was oriented to record the vertical displacements of the top plate of the box section to capture possible rotations of the base.

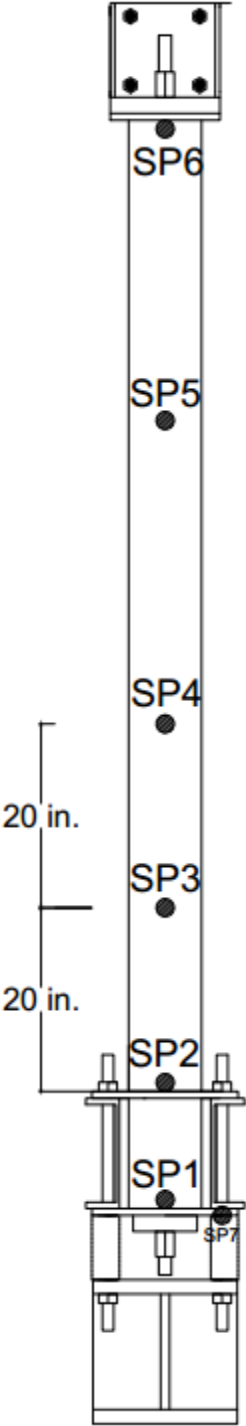


Figure 4- 18 String Pot Layout

4.5.4 Krypton Dynamic Measurement Machine

In addition to the linear potentiometers, displacement response of the specimens was recorded using a Krypton machine. Each specimen was equipped with 22 LEDs to record displacements in three orthogonal directions at each of the selected locations. This allows to monitor possible out-of-plane displacements (given that there was no bracing system to keep the specimen in plane, as mentioned earlier). Fig. 4.19 shows the layout of LEDs used for the specimens.

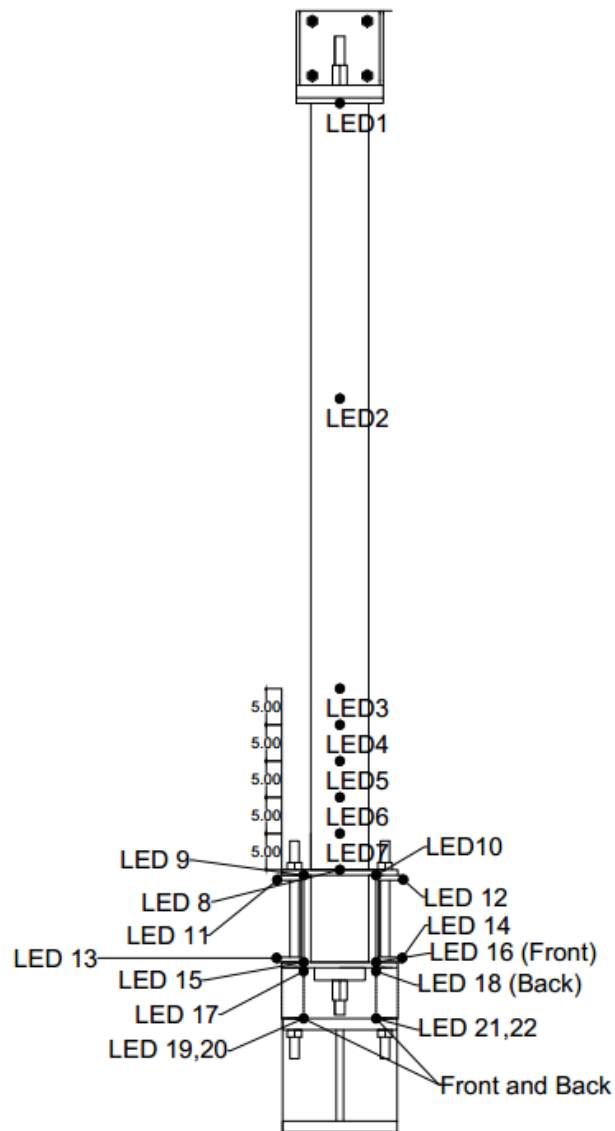


Figure 4- 19 LED Layout

The Krypton device uses three linear CCD cameras to calculate the position of LEDs with respect to a user defined coordinate system by triangulation method. Accuracy is in the range of 0.05mm to 0.5mm depending on the field of the view of the camera system. The field of view is a pyramidal volume that is defined based on the overlap area of the three linear CCD cameras. The camera was located about 12 ft from the specimen to enclose all of the LEDs in its field of view.

4.5.5 Load Cells

Two load cells were used in this experimental setup. One was the built-in load cell for the actuator to read the force applied to the specimen during the cyclic tests. The other load cell monitored the tensile force in the post-tensioning rod used for applying axial load to the specimen. The load cell was tubular with a hole in its center from which the 1 3/8" rod could go through. It was placed between the bearing plate and the nut at the bottom end of the threaded rod, taking the whole axial load in compression. The load cell was calibrated to measure loads up to 100kips. Fig. 4.20 shows the load cell used for the threaded rod.



Figure 4- 20 Load Cell Used to Monitor the Tensile Load of the Threaded Rod

4.6 Experimental Protocol

Two of the three main specimens were subjected to the cyclic testing program. The third one was kept undamaged prior to the fire test. The specimens were tested in displacement controlled mode using the protocol shown in Fig. 4.21 which is based on ATC-24 recommendations (ATC 1992). Each specimen was subjected to three cycles for each predetermined maximum displacement at the initial stages of the test. The first few cycles ended in relatively small displacement amplitudes to capture each specimen's yielding point. Numerical analyses were conducted prior to the tests to get an estimate of the yield displacement.

Maximum displacements for different cycles of the test were defined as multiples of the estimated yield displacement.

Amplitude of displacement for the cycles was increased up to the point when the desired damage level for the specimen could be visually identified. The target damage level was different for the two specimens. The first specimen (S1) was subjected to cyclic displacements until the first visual signs of local buckling appeared on the outer tube. This level was considered a low damage state that created a minimal inelastic history for the specimen. The second specimen was pushed further (with additional cycles) to reach a higher damage level, but testing stopped before any fracture developed. Residual drift of the specimens was used as a damage index to distinguish between the damage levels of the two specimens. The constant axial load was applied to the specimens during the tests.

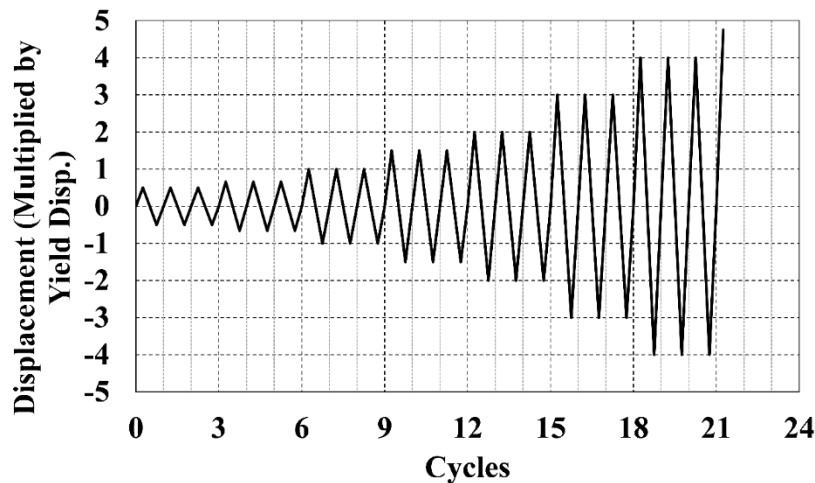


Figure 4- 21 Cyclic Displacement Controlled Test Protocol (ATC-24)

4.7 Cyclic Test Results

4.7.1 Test 1: Specimen S1

Testing on specimen S1 started by applying an axial load of 71 kip by post-tensioning the threaded rod along its longitudinal axis. The axial load was kept constant during the whole cyclic loading period. Cyclic testing started with low amplitude displacement cycles of 0.75". This amplitude was equal to 50% of the estimated yield displacement of 1.5" for this specimen (which was estimated using nominal material properties). The following cycles had target displacement amplitude values equal to

$1/2 \delta_y^*$, $2/3 \delta_y^*$, δ_y^* , $1.5\delta_y^*$, $2\delta_y^*$, $3\delta_y^*$, $4\delta_y^*$, ... where δ_y^* refers to the estimated yield displacement. Monitoring the force-displacement plot of the specimen during the test showed slight inelastic action during the 1.5" displacement cycle followed by clear inelastic hysteretic behavior for the cycles at an amplitude of 2.25". Therefore, the experimentally determined yield displacement and yield force for this specimen were $\delta_y = 2.25"$ and $P_y = 5.13$ kips.

Going through the following cycles, the specimen reached a maximum lateral load of 8.06 kips. The maximum strength was reached during the cycle of amplitude equal to $4\delta_y^* \cong 2.66\delta_y = 6"$. Because slight bulging of the outer tube could be felt by touching the specimen at the end of the $4\delta_y^*$ cycles, the next set of cycles were applied with smaller increments of amplitude. The following cycle was applied to the specimen with a maximum displacement of 7" (just 1" more than the one for the previous cycle). Local buckling could be visually observed at this stage and the test was stopped with an observable residual drift of about 1.5% for the specimen.

Fig. 4.22 shows the resulting lateral force versus drift curve recorded for specimen S1. Drift was calculated based on the relative displacement of the top of the specimen with respect to the top plate of the box section at the base. It should be mentioned that a slight correction was applied to the displacement values before plotting the curve. The correction was done because of the minor rotations that happened to the top plate of the box section at the base of the specimen. These rotations at the base which mainly occurred during the last cycles were considered to be rigid body motions and the corresponding displacement was subtracted from the measured displacement at the top of the specimen.

Results in Fig. 4.22 show that the specimen did not lose significant strength until the last cycle of loading when a strength degradation of approximately 5% occurred. This is logical, as the last cycle is the only one during which local buckling could be seen to develop at the base of the outer tube. Minor strength degradations were also observed in the second and third cycles at displacement amplitudes of 3.6" and 5".

Fig. 4.23 shows local buckling of the outer tube from different angles. Grid lines were painted on the specimen to provide better visualization of plastic behavior. Fig. 4.24 shows a full view of the specimen at the end of the testing. The residual drift of the specimen may not be easily detected because of its relatively low value. Based on the corrected values for the top displacement, the maximum and residual drifts for specimen S1 was calculated to be about 6.2% and 1.4%, respectively.

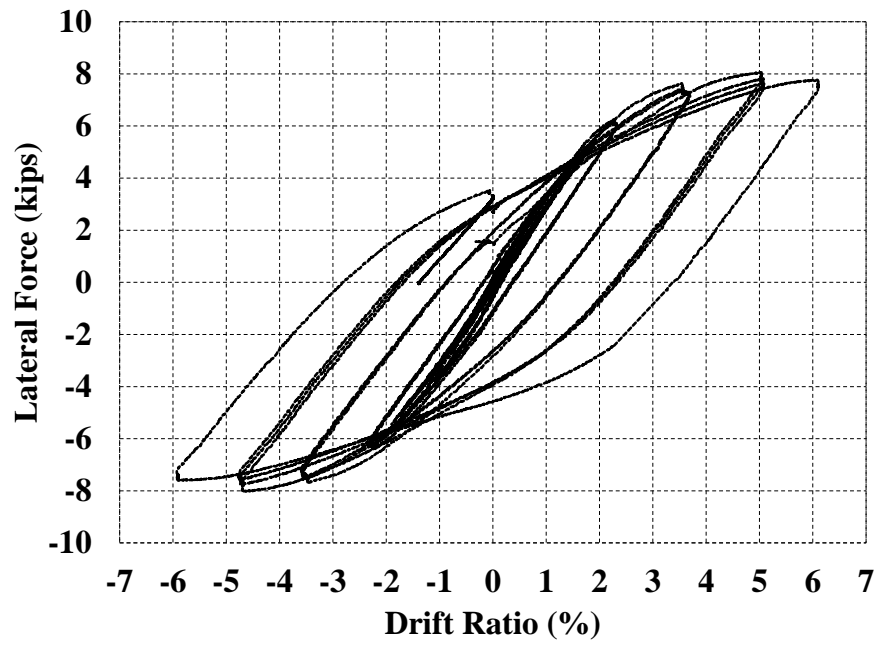


Figure 4- 22 Lateral Force vs. Drift Ratio Results– Specimen S1

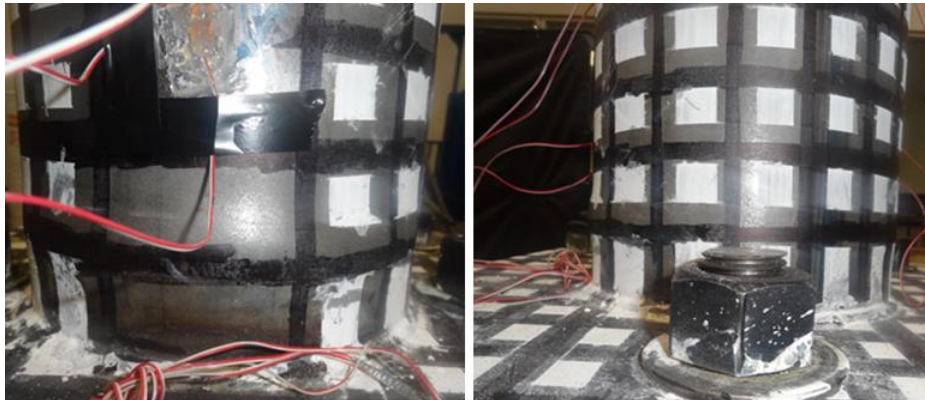


Figure 4- 23 Local Buckling at the Base of Specimen S1



**Figure 4- 24 Specimen S1 at the End of the
Cyclic Test**

4.7.2 Test 2: Specimen S2

The test procedure was similar to that of specimen S1, except for the amount of axial load, which was higher for S2 because of minor developments in the loading equipment. A constant axial load of 80kip was applied to specimen S2 throughout the cyclic testing. Cyclic displacements were applied to specimen S2 based on the same protocol used for the previous specimen. In terms of the yield displacement, specimen S2 started showing inelastic behavior at the 2.25” displacement cycle with the maximum force of 5.07kips. The similarity between the results of the two specimens was expected because both of them were built using materials coming from the same batches.

Specimen S2 was planned to be prepared for the fire test with a higher residual drift as an index of seismic damage. Maximum displacement of the last cycle was kept at the same level with the previous test to avoid possible fractures in the outer tube of the specimen that could be caused by higher displacement cycles. The 7" displacement was applied for another half cycle to make it possible for the specimen to stop at a larger residual displacement upon returning to the zero force position.

The test ended with maximum and residual drifts of 6.3% and 3.9%, respectively. The residual drift for S2 was considerably higher than the previous case (S1). Fig. 4.25 shows the corrected lateral force versus drift curve for specimen S2. Maximum lateral load taken by specimen S2 was 7.86 kips which is about 2.5% less than S1. Strength degradation was more significant for specimen S2 compared to S1. The maximum force reached at the end of the last half cycle was about 14% less than the maximum recorded force. Fig. 4.26 shows local buckling of the specimen S2 which is more severe compared to S1 mostly because of the additional half cycle loading that was applied to S2. Final state of the specimen with the residual drift can be seen in Fig. 4.27. Both of the specimens (S1 and S2) were kept with the residual drift to be tested under fire.

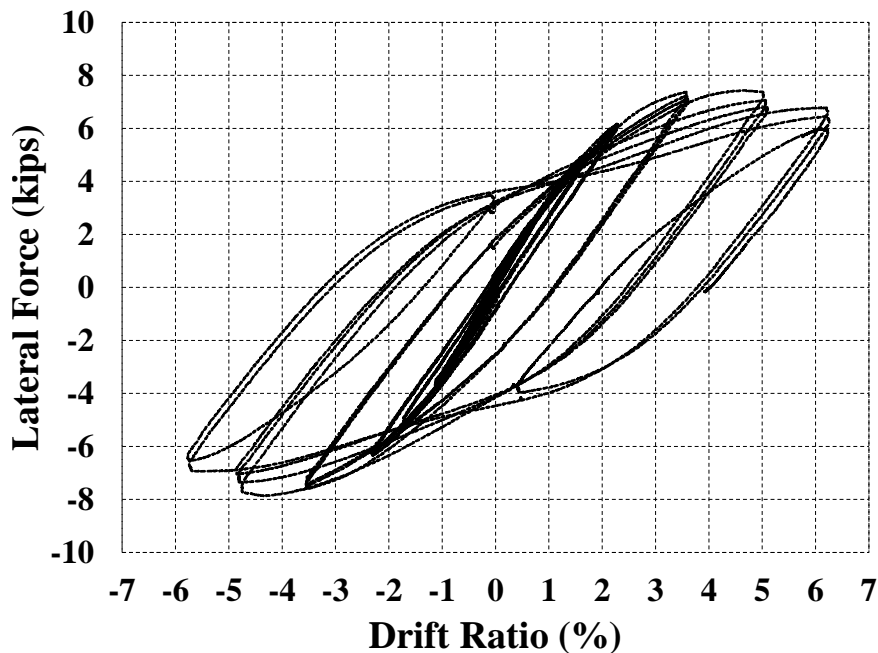


Figure 4- 25 Lateral Force vs. Drift Ratio Results– Specimen S2



Figure 4- 26 Local Buckling at the Base of Specimen S2



Figure 4- 27 Specimen S2 at the End of the Cyclic Test

SECTION 5

FIRE TESTS ON DAMAGED AND UNDAMAGED CFDST COLUMNS

5.1 General

This section presents the second part of the experimental program, which consists of fire tests conducted on CFDST specimens with different initial conditions corresponding to various levels of simulated seismic damage. The fire tests were conducted at the fire lab of NGC Testing Services, an external testing facility with the capability of performing controlled fire tests on structural members. The facility has a number of furnaces in different shapes and sizes available for testing different kinds of building elements. All the furnaces use natural gas as their energy source for fire and have temperature control systems to follow specific fire protocols and standards. Facilities for the type of tests conducted here are not available on the University at Buffalo campus.

Three scaled column specimens built and tested under simulated seismic loading as discussed in the previous section were prepared for testing in the fire lab. In addition to the specimen columns, three short stub columns, which had sections similar to the specimen columns, were also tested under fire for different observational purposes that are discussed later in this report. A total of three fire tests were conducted for this project, one for each of the specimen columns. To limit the number of fire tests, the stub columns were tested together with one of the specimen columns. Section 5.2 describes the experimental setup and specimen preparation for the fire tests. Section 5.3 presents the instrumentation process for recording both thermal and structural response of the specimens. Section 5.4 describes the experimental protocol implemented in this project and finally, section 5.5 presents the complete results of the fire tests.

5.2 Experimental Setup for Fire Tests

5.2.1 Description of the Setup

Based on the geometry of the specimens and test requirements, a vertical 10'x10' furnace available at the NGC lab was selected to conduct the fire tests in this project. This furnace was primarily designed for testing vertical building members (i.e., walls, doors, windows, etc.). The furnace is capable of accommodating 10' tall members, a requirement that was considered during the design of the specimens.

The main features of the experimental setup for the three conducted fire tests are presented in the following paragraphs.

The boundaries of the furnace were defined by two concrete beams at the top and bottom, framing between two concrete columns, a moving wall on one side of the plane delimited by these beams and columns, and a fixed wall on the other side of the furnace. The top and bottom beams were 16" and 12" wide, respectively. The top beam was fixed in place, working as a reacting member to the vertical loads applied to it by the top of the column specimen (in compression, as described later). The bottom beam was attached to a railing that could move up or down over a total travel distance of 4" (± 2 "). The railing was supported from below by eight hydraulic actuators used for applying vertical compression loads to the tested specimens. Maximum load was limited to 120 kips (i.e., 15 kips per actuator) due to the equipment specifications.

Each specimen was installed between the top and bottom beams, and subjected to a constant axial load applied from the bottom beam. Total axial displacement of the column, including thermal expansion and deformation under axial load, was limited to the ± 2 " travel distance of the bottom beam. The walls on both sides of the furnace were designed to keep the heat inside the test chamber for up to a four-hour period which was considered to be sufficient for the fire tests based on numerical estimations (note that these walls are typically designed and built with just enough fire-proofing material to fit the requirements of any particular test).

Natural gas is injected into the furnace and burned to create flames surrounding the specimen. A few observation windows are built on both sides of the furnace, making it possible for the lab technicians to visually inspect the inside of the furnace at any time. Note that the width of the furnace is approximately equal to the width of the top beam (16"). Since the walls on the sides are only built to provide insulation and cannot resist loads from structural members, possible out-of-plane deformations of the structure had to be monitored to ensure that the specimen remained within the available enclosure space. Fig. 5.1 shows a photo of the vertical furnace, with the specimen between the top and bottom beams.



Figure 5- 1 Specimen S3 in the Vertical Furnace

5.2.2 Preparation of the Specimens for the Fire Tests

The three main specimens were prepared for the fire tests with a few modifications at both ends. The only available way to connect any member to the top or bottom beams of the described vertical furnace was to bolt the ends using Unistrut bolts (Unistrut 2013) that could be positioned on a thin track at the center of the top and bottom beam surfaces along their total length. Since the end plates of the specimens could not be drilled for holes in their center, built up members were added to both ends. These added members were designed to push against the end plates of the specimens and were tied down to the top and bottom beams by the bolts along their center lines. Fig. 5.2 shows the details of these built-up members.

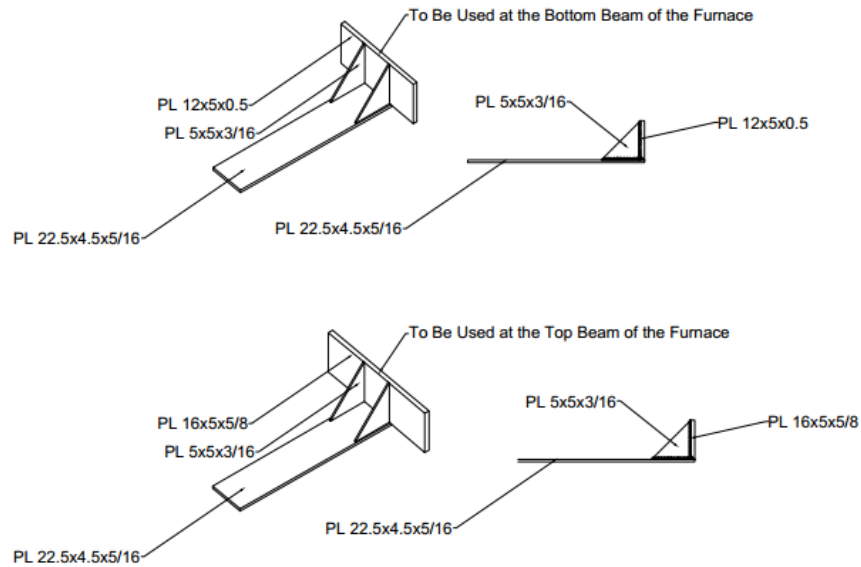


Figure 5- 2 Built-up Elements for Connection of Column Ends to the Top and Bottom Beams of the furnace

In addition to the side members, two built-up channels were designed and added to both ends of the column (Fig. 5.3). The webs of these channels were positioned parallel to the end plate with their flanges aligned such as to allow the top and bottom beams of the furnace to socket into the added channels. This configuration ensured that the specimens would remain in place during the fire tests. Note that a last minute modification was required to adjust the length of the specimens. Initially the columns were designed about 1' shorter than the maximum height of the furnace (10') to provide additional clearance should it be needed. However, it was learned later in the project (much after the specimen had been fabricated) that the fire test specimens had to be exactly 10' since the initial position of the furnace's bottom beam was not adjustable.

To make up for the shortness of the specimens, two extension plates were welded to the top plate of the columns. The built-up channel was welded to the end of extension plates, creating in the process a void between the web of the built-up channel and the top plate. This volume was filled with concrete to avoid any early instability that could happen for the steel elements at that location under the axial load applied during the fire test. This extension was only added to one end of the column. The other end was directly welded to the built up channel.

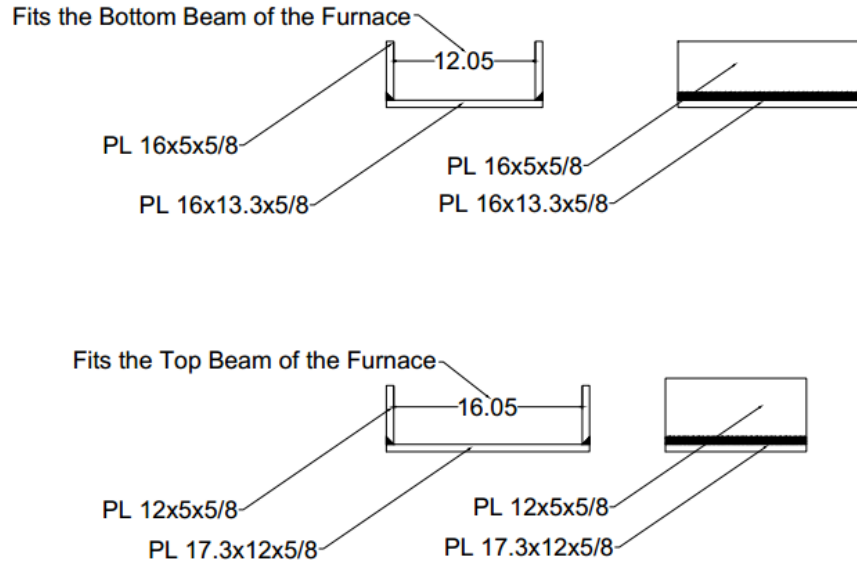


Figure 5- 3 Built-up Channels Added to the Ends of the Specimens for the Fire Test

The lengths of the extension plates were adjusted to bring the specimen length to the 10' requirement of the furnace. Fig. 5.3 shows the details for the additional elements welded to the top and bottom ends of the columns. In addition to these modifications, four 1/4" holes were drilled on the outer tube of the specimens to allow for vapor ventilation during the fire test. The line of the two holes at the top was at a 90° angle relative to that of the holes at the bottom according to the AISC design guide for fire resistance of steel structural framing (AISC 2003). Fig. 5.4 shows the top end of one of the specimens fixed in place using the built-up angles. Note that a new set of these angles was used for each specimen to ensure that the members used had not been damaged or weakened by the previous fire tests.



Figure 5- 4 Built-up Member Used at the Top End Connection

5.3 Instrumentation

5.3.1 Thermal Instrumentation

Two sets of thermocouples were used to record the temperature distribution response around and within the specimens. A first group of thermocouples (that are part of the furnace equipment) were set to monitor the air temperature in the furnace. Recordings from these thermocouples were used as feedback to the control system that was keeping the air temperature in the test chamber within the desired range. Most fire tests are designed to follow a predetermined temperature curve (i.e., fire loading protocol) and use data from these thermocouples during the test to control the fire intensity. Nine thermocouples served for this purpose, installed at different locations in the furnace. The control system was designed to keep the average temperature of these nine sensors as close as possible to the predetermined target temperature curve. Test operators were able to monitor progress of the average furnace temperature over time and its closeness to the predetermined target curve in a single digital graph plotted in real-time during the test. This arrangement provided for the possibility of manual corrections in case the control system did not operate as intended, for any reason. Fig. 5.5 shows the locations of the nine thermocouples used in the furnace.

The second sets of thermocouples were used to record the temperature distribution within the specimen. As mentioned in Section 4, the thermocouples were placed in the specimens during the construction process and embedded in concrete. Heat resistant wires connected to the thermocouples and coming out of a hole drilled in the outer tube were used for connection to the Data Acquisition (DAQ) system. Each specimen was equipped with three thermocouples. Two of them were used to record the temperature time history at the surfaces of the inner and outer tubes. The third one was used to monitor temperature in the middle of the concrete region. The thermocouples were installed at a height close to the top end of the specimens (about 1' from the top plate). The same set of three thermocouples were installed on the stub columns. Fig. 5.6 shows the locations of the three thermocouples in the cross-section of the both specimen and stub columns. All of the thermocouples were connected to the panel on the wall of the furnace (Fig. 5.7) and from there to the DAQ system (Fig. 5.8).

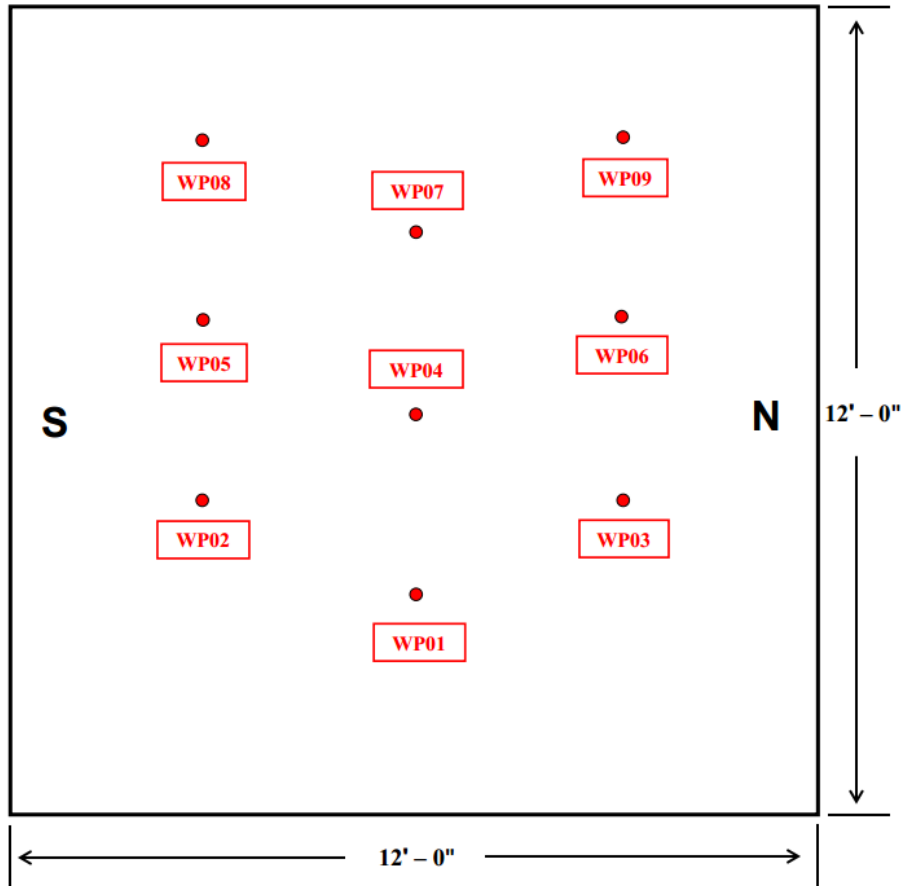


Figure 5- 5 Vertical Furnace Thermocouple Layout
 (view looking into the furnace, S: south side, N: north side)

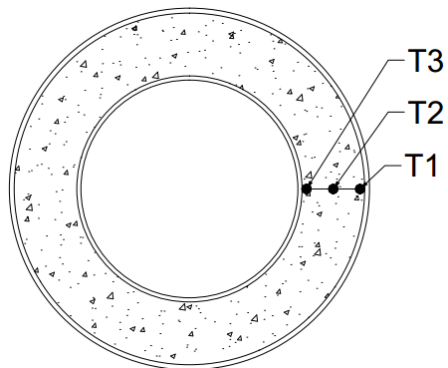


Figure 5- 6 Locations of Thermocouples in the Cross-section of the Specimen and Stub Columns



Figure 5- 7 Wires Carrying Temperature Data Connected to the Channels at the Back of the Furnace Wall



Figure 5- 8 Temperature Data Acquisition System

5.3.2 Structural Instrumentation

The specimens were subjected to a constant axial loading from their bottom side using a set of eight hydraulic actuators, as mentioned earlier. Since the fire testing facility had some limitations regarding the availability of instrumentation devices for structural tests, no load cells were used in the test. The axial load was applied by calculating the equivalent pressure needed to for the pumps to exert the load up to the desired level, knowing the internal area on which pressure acted in the actuator cylinder rams. The load was also monitored during the test by reading the pressure gauges frequently.

Axial displacement of the columns had to be measured according to the movements of the bottom beam. Since the testing facility didn't have a DAQ system for linear potentiometers (the available DAQ system was dedicated to the thermocouples), two mechanical dial gauges were used for measuring the axial displacement. The gauges were read manually at intervals by a technician during the fire tests and had an accuracy of 0.001". Fig. 5.9 shows the mechanical dial gauges placed below the bottom beam of the furnace. Displacement readings were recorded as a function of time since beginning of test using a dedicated timer located next to the technician.



Figure 5- 9 Mechanical Dial Gauges Placed under the Bottom Beam

Although the accuracy of the structural response parameters recorded in the fire lab were considered to be lower than the ones recorded for the cyclic tests, they were considered acceptable for the purposes of this project.

5.4 Experimental Protocol

The tests began with applying the axial load to the columns. While the axial load was kept constant by maintaining the pressure in the pumps, the fire was started in the furnace along with a timer. The specimens

were exposed to the standard ASTM E119 fire which is controlled to reach specific temperature levels within a specified time period (ASTM 2012). Fig. 5.10 shows the temperature-time curve for the adopted fire standard. The curve gets to the temperature of 537°C (1000°F) in 5 minutes and increases up to the temperature of 1050°C (1925°F) at the end of 180 minutes.

The fire test was planned to continue up to the point when the column could no longer resist the axial load. This failure criterion could be confirmed by observation of the global buckling of the specimen or by detecting a suddenly developing relatively fast movement of the bottom beam under the axial load (close to 1"/min.). For safety reasons and due to the possibility of out-of-plane buckling of the column damaging the enclosure walls and the furnace, the tests were stopped as soon as the bottom beam had traveled about 2" towards the top beam.

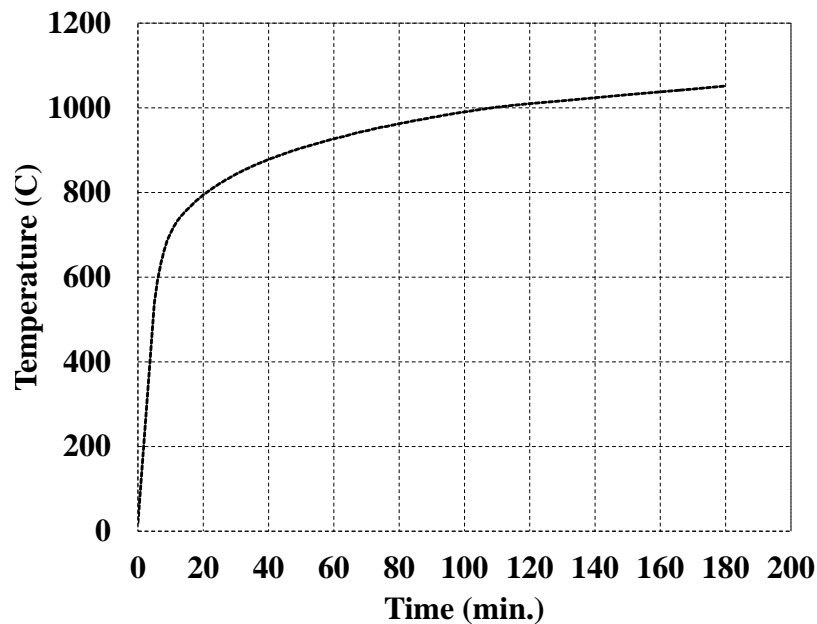


Figure 5- 10 Standard ASTM E119 Fire (ASTM 2012)

Assuming that the undamaged column would probably have the maximum fire resistance time, and to acquire knowledge on the behavior of the undamaged specimen under fire as a benchmark prior to fire testing the earthquake-damaged columns, specimen S3 (which was not subjected to cyclic loading earlier) was selected for the first fire test, keeping the damaged specimens, S1 and S2, for the second and third ones.

5.5 Fire Test Results

5.5.1 Test 1: Specimen S3 (Undamaged specimen)

The furnace wall was conservatively built to keep the heat for a four-hour long fire, even though the initial finite element simulations showed a resistance time of less than two hours. An axial load of 70 kips (the same amount that was applied in the cyclic tests) was applied to the column and kept constant for the rest of the test. The fire test was started in a controlled mode to follow the ASTM E119 temperature curve.

Fig. 5.11 shows the history of the average furnace temperature along with the temperature data recorded by the thermocouples embedded in the specimen. The average furnace temperature closely matches the ASTM E119 curve, as intended. The difference between the temperature of the inner and outer tubes throughout the test shows the effects of concrete as a material with relatively low thermal conductivity. It is speculated that the sudden fluctuations in the recorded temperature data can be related to water content of the concrete traveling within the specimen and corresponding pressure changes inside the specimen. Vaporization of the moisture content of concrete builds up pressure between the inner and outer tubes during the fire test. Sometimes, if this pressure is relieved in some part of the concrete, the heat may travel faster locally to other parts of the concrete, and at specific times and locations, this may have affected readings of the thermocouple installed on the inner tube. This phenomena may also be sensitive to the specific positioning of aggregates in the vicinity of a thermocouple. At times, this could lead to higher temperatures on inner tube compared to the concrete part, where the thermal energy is still partially used to vaporize the water content. Note that these fluctuations appeared to be temporary, allowing the temperature curves to follow the expected trend after a while.

The total fire resistance time was recorded to be about 65min for specimen S3. Fig. 5.12 shows the results for axial displacements of the bottom beam measured during the test. Two curves are plotted based on the data from the mechanical gauges placed on the north and south sides of the beam. Note that since the eight hydraulic pumps were working separately underneath the bottom beam, which was only supported by the actuators and consequently allowed small rotations of the beam to develop, the gauges north and south of the center line of the beams didn't record the same displacements. Assuming that the base of the column was at the center of an imaginary line connecting the two gauges to each other (which is how it was attempted to install the gauges), the average of the two readings was plotted as the assumed axial displacement for the column in Fig. 5.12.

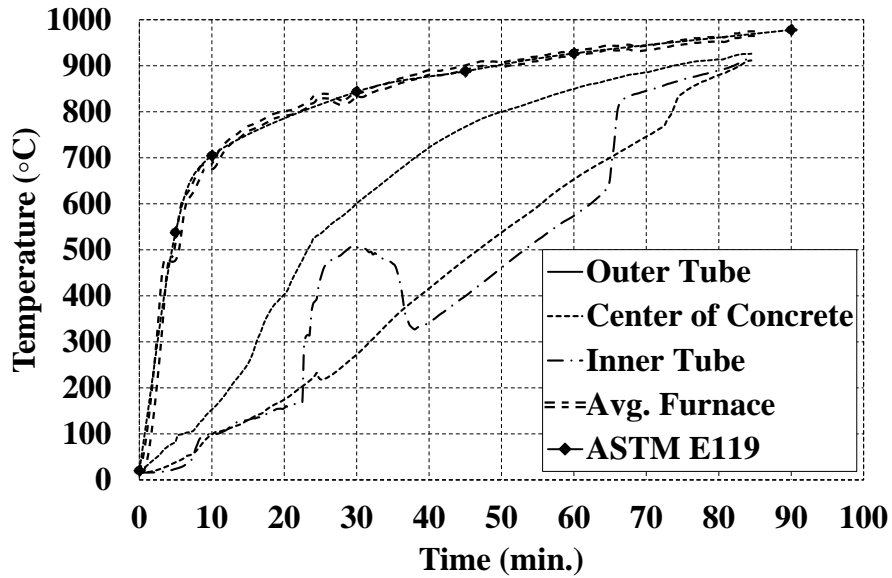


Figure 5- 11 Temperature Data Measured in the Fire Test of Specimen S3

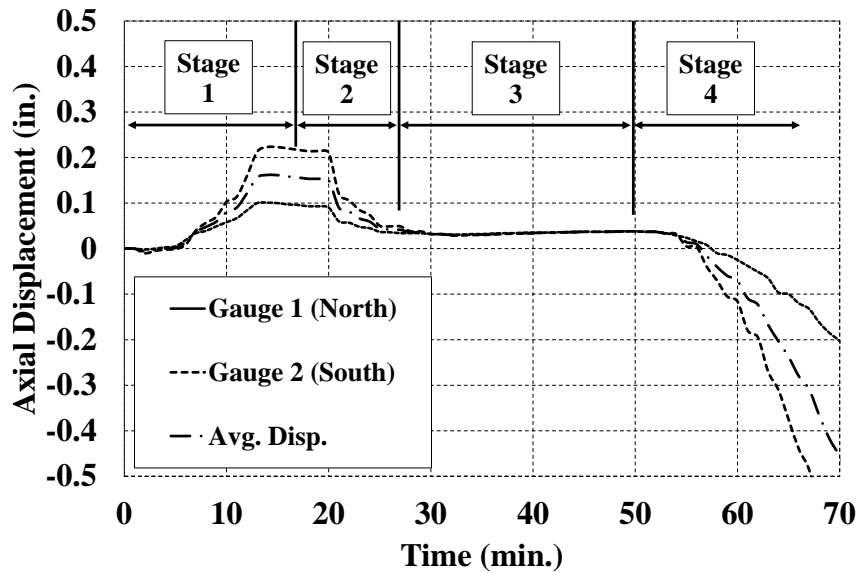


Figure 5- 12 Axial Displacement Results from Fire Test of Specimen S3

Looking at Fig. 5.12, the specimen goes through four stages during the fire test. These are similar to the four stages of the mechanical behavior of the conventional concrete filled tubes presented in a numerical study by Espinos et al. (2010). The first stage lasts about 12min and consists of an expansion process in which the outer steel tube expands faster than the concrete core and inner tube. As a result, the outer steel

tube carries the entire axial load. The second stage occurs a few minutes later when the outer tube reaches higher temperatures, weakening the steel, and can no longer sustain the load. This stage is accelerated by local buckling of the outer tube under the 70 kip load, creating the sudden drop in the axial displacement plots shown in Fig. 5.12, which continues until the concrete is engaged anew in carrying the axial load.

The third stage starts after the drop, when the tubes and the concrete are working together until about 55 minutes from the start of the test. During this period, the specimen is either expanding very slightly or just maintaining its position resisting the axial load. The last stage starts when the specimen can no longer resist the axial load and the displacement begins to increase at a significantly higher rate. The test ends a few minutes later when global buckling is visually confirmed and the bottom beam is moving with a rate close to 1 in./min.

Fig. 5.13 shows the local buckling of the outer tube close to the top beam of the furnace. Although the movement is happening at the bottom beam, no local buckling action is seen around that location. The reason for this difference is expected to be the weight of the concrete core. Although this will be investigated and verified analytically in Section 6, it can be explained for the time being as follows: As the outer tube, which is welded to both top and bottom plates, is heated faster and expands longitudinally more than the concrete core, this excessive expansion can cause the separation of the top or bottom plates from the concrete. Since the weight of the concrete core doesn't let this separation to occur at the bottom, it happens at the top, leading to the local buckling of the outer tube in that area.



Figure 5- 13 Local Buckling of Specimen S3 Close to the Top Beam of the Furnace

Fig. 5.14 shows the final state of the specimen at the end of the test. The specimen failed with an out-of-plane global buckling mechanism. The connection at the top worked as a fixed connection, creating an inflection point in the upper part of the specimen. Close observation of the bottom end of the specimen revealed that this connection had functioned as a semi-rigid joint allowing a limited out-of-plane rotation for the bottom end of the specimen. This limited rotational freedom was considered as a possible reason for the out-of-plane orientation of the global buckling. The other possible reason was the fact that the specimen had more bending strength in the in-plane direction because of the greater in-plane fixity provided by the channels at the bottom.

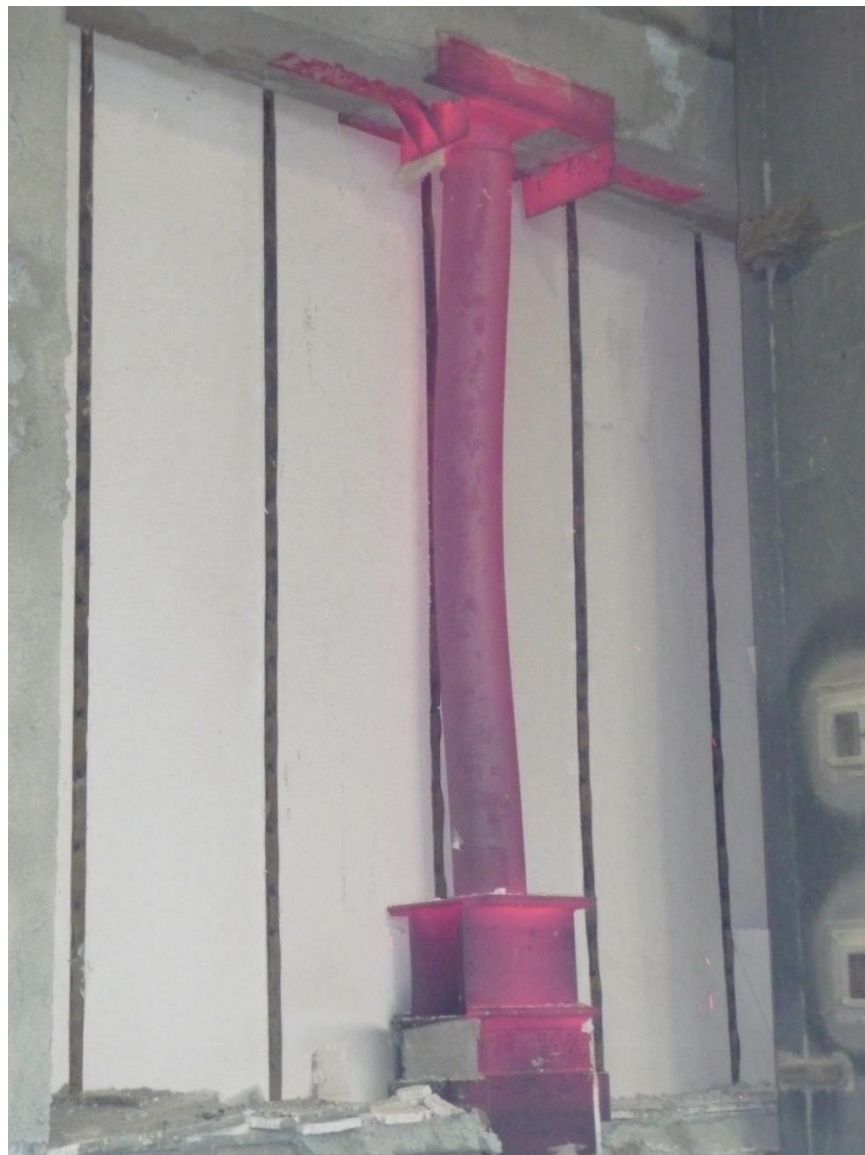


Figure 5- 14 Out of Plane Global Buckling of Specimen S3

5.5.2 Test 2: Specimen S1 (Damage Level 1)

Specimen S1 with a residual cyclic testing drift of 1.8% was selected for the second fire test. This column was considered to be representative of a structural element having a moderate level of seismic damage. The column was modified to fit in the boundaries of the vertical furnace in the same manner as specimen S3. The only difference was that considering the lack of straightness of specimen S1, the built-up channels were welded to both ends of the column with a slightly inclined orientation. This modification was needed in order to get two flat and parallel surfaces at the top and bottom of the specimen. Steel shims were used to fill the space between the straight and inclined plates. Fig. 5.15 shows the details of the inclined connection.

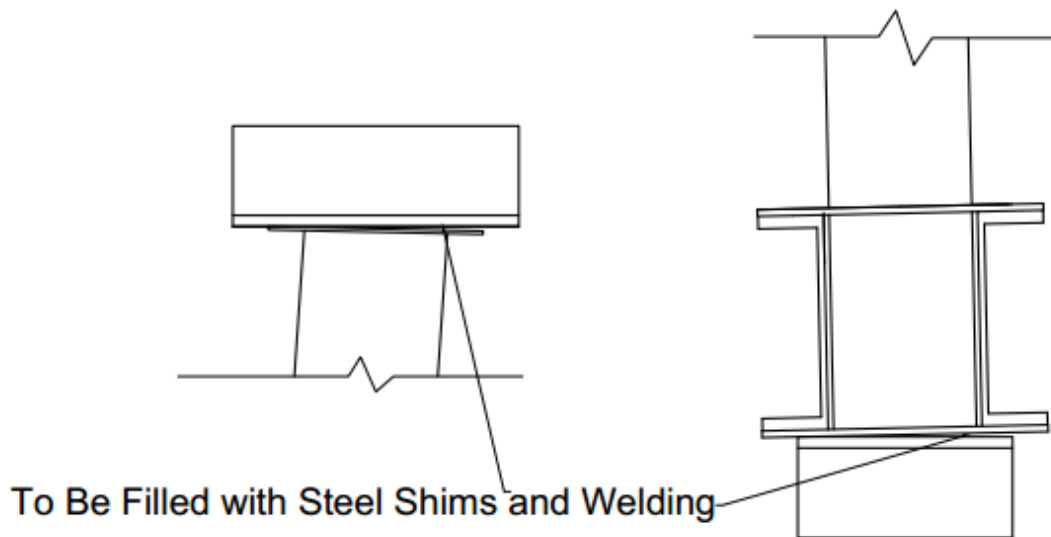


Figure 5- 15 Inclined Connection of the Column with Residual Displacement to the Built-up Channels

Fig. 5.16 shows specimen S1 installed in the fire furnace and ready for the test, just before closing the enclosure. Note that the end of the column with the seismic damage was positioned close to the bottom beam of the furnace. Although the first fire test lasted for only 65 minutes, the insulation wall was conservatively built to keep the heat for at least two hours. The actuators were set up to apply the 70 kip axial load and the fire test started in a controlled mode to follow the standard ASTM E119 temperature curve. The test was terminated due to global buckling of the specimen with a recorded fire resistance time of 60-65 minutes. The resistance time showed that the seismic damage hadn't significantly affected the general performance of the column under fire loading.



Figure 5- 16 Specimen S1 Installed in the Furnace in Preparation for the Fire Test

Fig. 5.17 shows the data recorded by the thermocouples inside the furnace and within the specimen. The results are similar to the data reported from the first fire test. This was predictable because the two specimens have the same geometry and materials. This data also shows that the moderate seismic damage induced at the base of the column did not affect the heat transfer process in the specimen. Note that two of the stub columns were also tested in the furnace along with specimen S1, and their results are presented later in this report (Section 5.5.4).

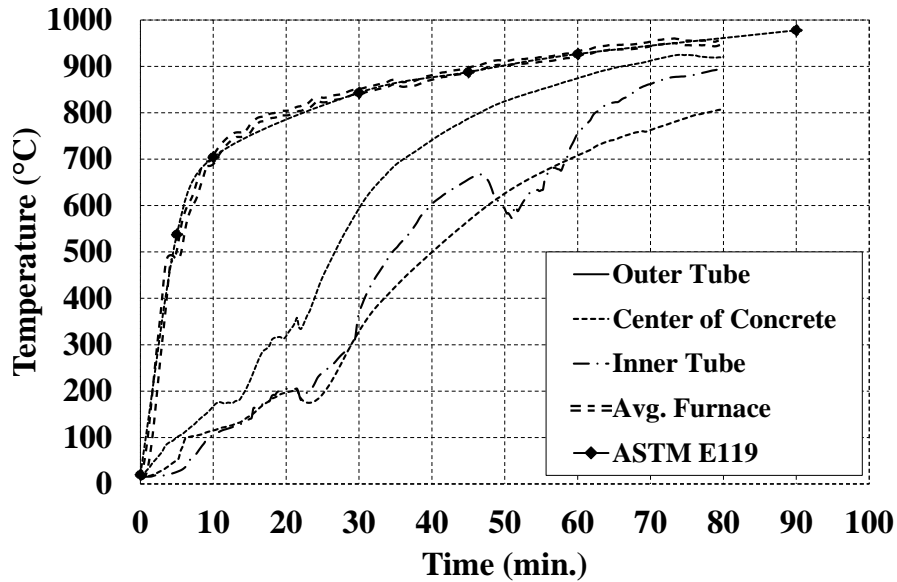


Figure 5- 17 Temperature Data Measured in the Fire Test of Specimen S1

The axial displacement curves recorded by the mechanical gauges are plotted in Fig. 5.18. The data recorded by the gauge at the southern side of the bottom beam show that the beam did not move in the expected direction (away from the specimen) during the expanding stage of the outer column. This is likely due to an unintended jam of the sliding mechanism at the south end of the bottom beam. The other side of the beam was pushed away by the expanding column, causing the bottom beam to rotate slightly more compared to the first fire test. The average of the two readings is also plotted as the best estimate of column axial displacement.

The column went through the same four stages of behavior described for the previous test specimen. Although initial imperfections were imposed at the bottom end of the outer tube because of the damage from cyclic testing, local buckling occurred at the top of the column just like the previous test. This confirmed the effect of gravity forces on the concrete part which leads to the separation of the concrete and top plate of the column. Different locations of the seismic damage (at the bottom end of the column) and fire damage (local buckling of the outer tube at the top end) prevented the occurrence of combined fire-seismic damage to the column. The fact that global buckling still occurred in the out-of-plane direction, even though the in-plane moment resistance of the column was subjected to cyclic loading (resulting in some stiffness reduction), supported the idea that the bottom end connection allowed for a limited out-of-plane rotation facilitating the out-of-plane oriented buckling. These observations were considered in planning of the third fire test, as explained in the subsequent section. Figures 5.19 and 5.20 show the local and global buckling of specimen S1, respectively.

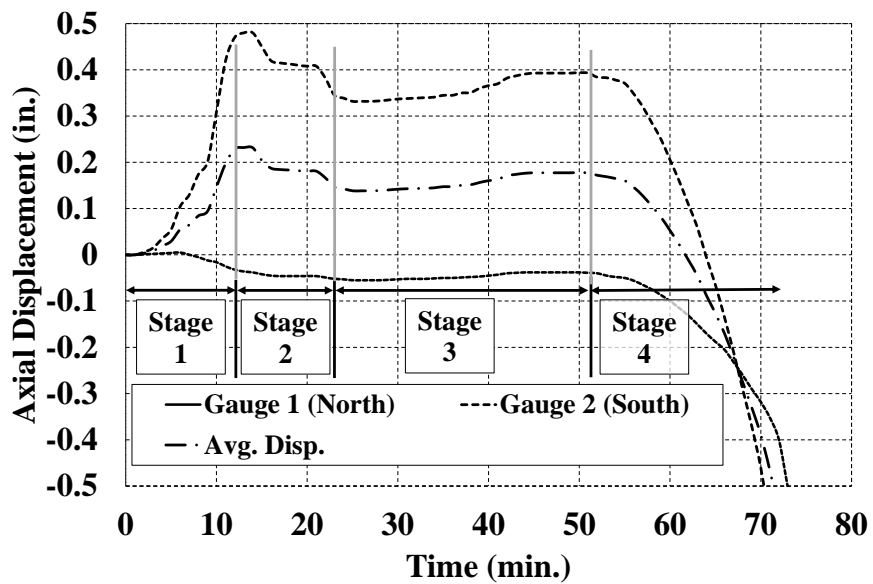


Figure 5- 18 Axial Displacement Results from Fire Test of Specimen S1



Figure 5- 19 Local Buckling of Specimen S1 Close to the Top Beam of the Furnace



Figure 5- 20 Out of Plane Global Buckling of Specimen S1

5.5.3 Test 3: Specimen S2 (High-damage specimen)

Specimen S2 was prepared for the third and last fire test with a residual drift of 3.9% from the lateral cyclic loading. Using the residual drift as a damage index for structures, a ratio of 3.9% can be considered representative of a relatively high damage level. Considering the results from the first two fire tests, the effects of the moderate seismic damage on the overall performance of the specimen were insignificant. Therefore, the setup for the third fire test was modified in two specific ways in an attempt to better capture the potential effects of cyclic loading on performance of the specimen under fire.

First, based on results from the previous tests, because it was expected that local buckling of the outer tube under fire loading will occur close to the top of the column for the reasons mentioned before, the third specimen was inverted such that its seismically damaged end was connected to the top beam of the furnace. The intention was to combine the existing local buckling from the cyclic loading with the potential local buckling from the fire test in the same region.

Second, the specimen was installed in the furnace such that it was rotated 90° with respect to the previous two columns. This orientation was selected to ensure that the out-of-plane buckling of the specimen (predictable given by the partially fixed boundary condition at the bottom end) would occur in the same direction that had already been weakened during the cyclic test. These two modifications, along with the fact that the specimen had deformations corresponding to a relatively high residual drift from the cyclic test, were considered in the third fire test to examine the probable effects of seismic damage on the fire resistance of the particular type of concrete-filled columns studied in this project.

The axial load for specimen S2 was increased to 80kips to match the axial load applied in the cyclic test. The load was kept constant by maintaining the required hydraulic pressure while the specimen was subjected to the standard ASTM E119 fire. Although the column was considerably damaged due to cyclic loading prior to the fire test and was installed with particular conditions in the fire furnace to amplify the effects of the damage, the total fire resistance time was recorded to be about 60 minutes. Therefore, the effects of the seismic damage on the global behavior of this type of column under fire (for the type of boundary conditions considered here) could be considered marginal. In terms of local behavior, a few differences were seen compared to the previous tests, and these are outlined in the following paragraphs.

Fig. 5.21 shows the time history of temperature changes recorded by the thermocouples installed both within and out of specimen S2 in the furnace area. The recordings show a similar trend compared to the previous tests. The only difference is that the temperature values measured for specimen S2 are about, on average, 100°C lower than the temperatures recorded from S1 and S3 at the same points in time. The average furnace air temperature on the other hand is the same for all of the specimens. The 100°C difference seems to be due to some unexpected changes in the heat transfer process. One observed incident occurred at about 25 minutes into the test, when a sustained noise similar to a pressure relief was heard. This was speculated to be related to vaporization of the water content of concrete and its attempt to escape from the steel case. The sound faded out after about 5 minutes.

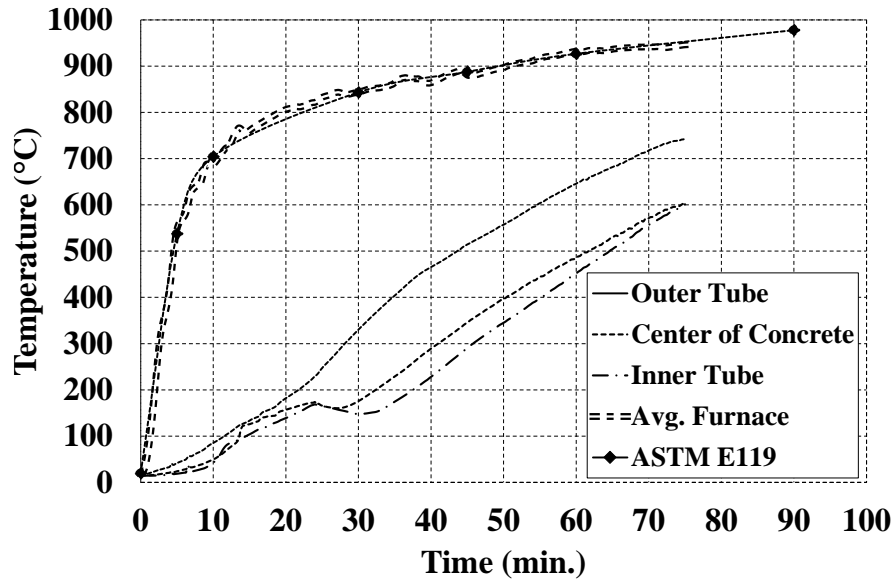


Figure 5- 21 Temperature Data Measured in the Fire Test of Specimen S2

The time history of axial displacement measured by the mechanical gauges for specimen S2 are plotted in Fig. 5.22. The marginal difference between the two readings showed that the bottom beam of the furnace moved uniformly along its length. The fire resistance time was similar to the previous tests, showing that for the fire tests conducted with the aforementioned conditions on the particular columns built in this project, a certain amount of burning time was needed to reach failure, regardless of the amount of simulated seismic damage. Longer burning time simply leads to more degradation in the material properties, causing the specimen's failure.

Apart from the fire resistance time which is controlled by global buckling in these tests, a few differences were observed in the behavior of specimen S2 in comparison with the previous tests. The average maximum axial displacement in the expansion period was measured to be about 1.68mm which was about 30% of the measured values for the other two specimens (4-5mm). Two factors may have contributed to this difference. The first one was the specific orientation of specimen S2 in the furnace. Similar to the previous tests, the expansion of the outer tube was followed by its local buckling close to the top beam of the furnace. Specimen S2 already had initial local buckling in that area acting as an initial imperfection. Therefore, from the beginning of the test, expansion of the outer tube contributed to enlarge the existing local-buckling ring at that location, rather than first contributing to axial displacement of the column. The second factor possibly contributing to the lesser expansion of specimen S2 is based on the fact that S2 had lower temperature values compared to the other two specimens (maximum temperature for the outer tube of S2

was about 720 °C as opposed to 920 °C for S1 and S3). Lower temperature levels lead to lesser expansion of the material.

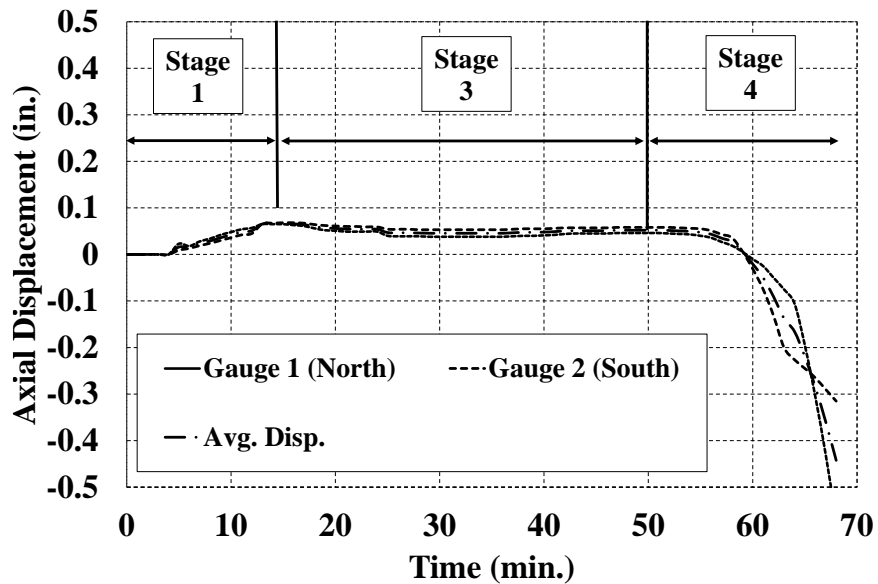


Figure 5- 22 Axial Displacement Results from Fire Test of Specimen S2

Local buckling of the outer tube is shown in Fig. 5.23. Compared to similar photos from the other two specimens, the excessive severity of the local buckling for specimen S2 is visible, and provides an example of combined damage from the seismic and fire loads on the structure. Fig. 5.24 shows the final state of the specimen after the termination of the test. Higher residual drift and impaired moment resistance of the specimen led to a slightly shorter fire resistance time (less than 10 min in difference) in comparison with the other two specimens. The difference in the resistance time is mainly due to the fact that one of the four stages mentioned above for the time history of axial displacement for columns S1 and S3 was eliminated for S2; as explained above, the stage during which the outer tube expands faster than concrete, resisting the axial load alone, could not be achieved for specimen S2 because the outer tube had already buckled.



Figure 5- 23 Local Buckling of Specimen S2 Close to the Top Beam of the Furnace



Figure 5- 24 Out of Plane Global Buckling of Specimen S2

5.5.4 Results from Stub Columns

Two of the three stub columns (SC1, SC2), built to be used as additional references for temperature distribution analyses, were tested in the same furnace with specimen S1. The third one (SC3) was kept intact to be used as a reference model. No structural loads were applied to the two stub columns while being tested under fire. Note that the building materials, geometric properties of the section and the positioning of the thermocouples were similar to those of the column specimens.

Considering that no structural loads were applied to the short columns during the fire test, the temperature measurements recorded on the stub columns could be used to check the dependency of the results of heat transfer analysis on the structural analysis. Fig. 5.25 shows the history of temperature distribution in SC1 and SC2 measured during the fire test. The results showed a similar trend compared to the temperature data from the specimen columns. The maximum temperature reached by the outer tube of stub columns is about 100°C less than the similar records for the main columns. This minor difference was considered to be due to the lower air temperature at the bottom of the furnace where the short columns were located, as opposed to the upper part of the furnace (thermocouples for the full-length specimens were located close to the top of the columns). Note that temperature measurements from the thermocouples installed in different parts of the furnace showed a maximum difference of about 150°C, while the average of their readings closely followed the ASTM E119 fire curve. Fig. 5.26 shows the time history of temperature recorded by the nine thermocouples installed at different parts of the furnace.

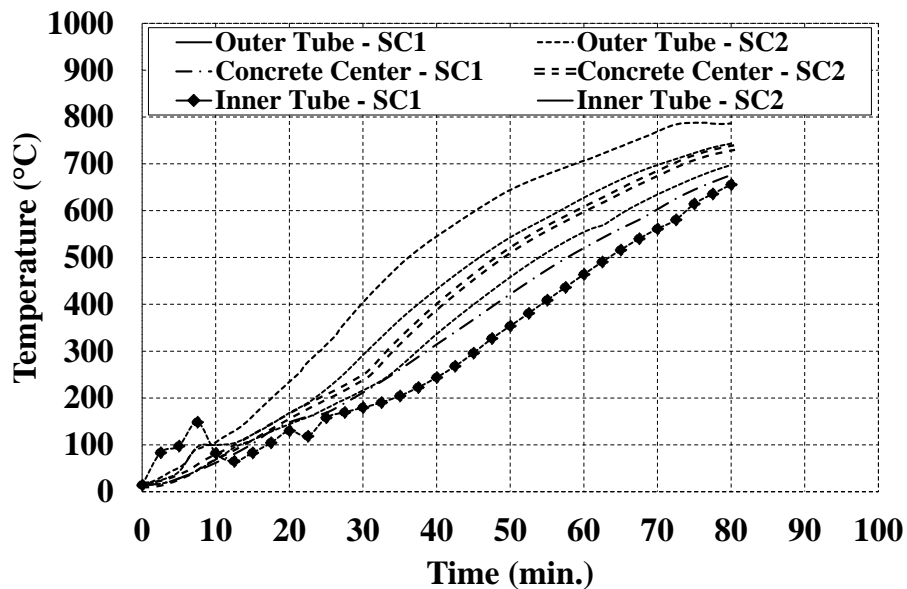


Figure 5- 25 Temperature Data Measured from the Two Short Columns (SC1, SC2)

The recorded temperature curves from the thermocouples installed in the concrete and on the surface of the inner tube for SC1 shows a smoother trend as opposed to recordings from the specimen columns. The temperature response recorded on the surface of the inner tube for SC2 shows sudden fluctuations similar to what was seen for the main columns. Since all of the tested columns had similar section properties with steel plates welded to their both ends (the only difference was length of the tubes for the specimen and stub columns), it is speculated that these fluctuations may be due to the random arrangement of aggregates in concrete part of specimens, causing moisture and pressure relief at certain times and affecting the thermocouple readings. Considering the similarity of heat transfer results from specimen and stub columns, it is speculated that effects of applying structural loads on the heat transfer process of the specific structures used in this study are insignificant (several complimentary numerical studies are needed to verify this speculation).

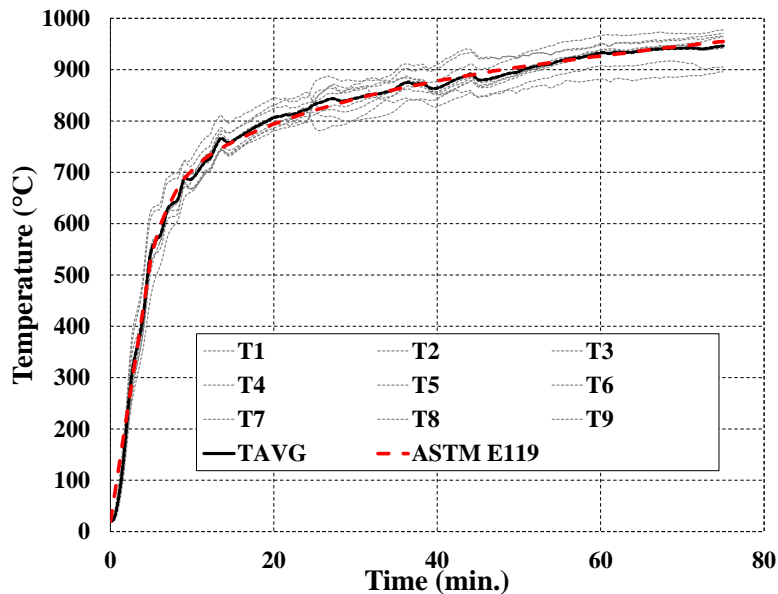


Figure 5- 26 Time history of Temperature Recorded by Nine Thermocouples Installed in Different Parts of the Furnace during Fire Test 2

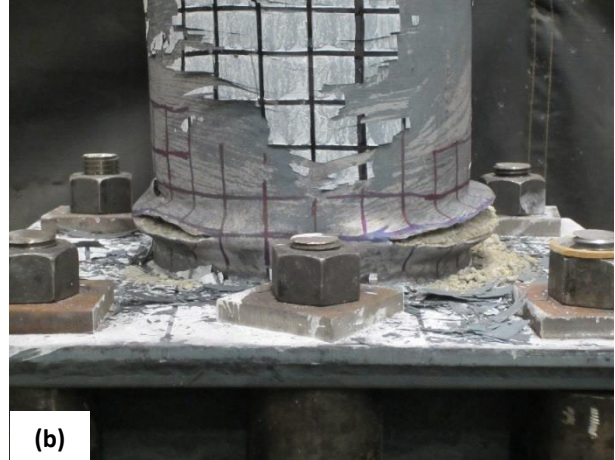
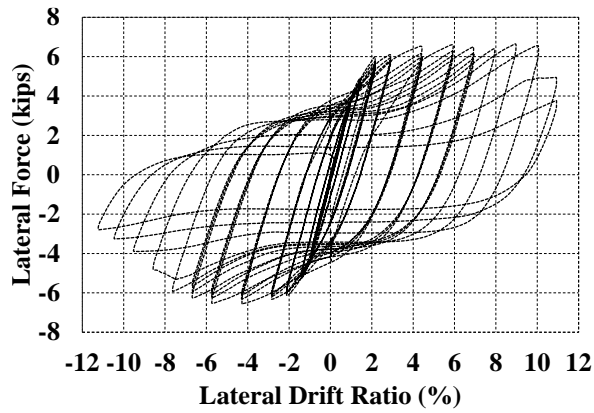
To study the effects of ventilation holes on the heat transfer process in columns, SC2 was built with one additional vent hole compared to SC1 (3 holes instead of 2). The comparison shows that the temperature values for all of the three thermocouples installed in SC2 are about 50°C higher than the values for SC1. Since this difference in temperature values is noticeable from the very beginning of the test, it is inferred that the main reason for this minor difference is more likely to be related to the different location of the stub columns in the furnace than the number of vent holes used. Note that SC1 and SC2 were sitting on the south and north sides of the bottom beam surface, respectively.

Stub columns were also used to study the effects of fire tests on the moisture content of concrete by comparing the measured Relative Humidity (RH) of the two stub columns tested in fire with that of the third one, SC3, which was kept intact in the lab. Relative humidity is the amount of water vapor present in a volume of air at a given temperature to the maximum amount that the air could hold at that temperature, expressed as a percentage. Relative humidity of the three stub columns were measured based on the standard ASTM F2170 (ASTM 2011). An electronic probe was inserted into holes drilled into the concrete (after running through the steel) to measure the RH values. Measurements gave post-fire RH values of 29% and 20% for SC1 and SC2, respectively. These values were about half of the RH value of 59% for SC3 which wasn't tested in fire. The effect of the additional vent hole is seen in the difference of RH values for SC1 and SC2. Note that the holes were drilled after the fire tests at points which were not close to the vent holes of stub columns.

To investigate the permanent effects of an approximate 1-hour long fire (ASTM E119) exposure on the squash load of CFDST columns, an axial loading test was conducted on SC1, SC2 and SC3 stub columns. SC1 and SC2, which were both tested in fire, had squash load values of 334 kips and 339 kips, respectively. These values show a 28% reduction compared to the 471 kip squash load measured for the reference case (SC3). Note that according to the Eurocode 4 specifications for the post-fire structural properties of steel and concrete, a 40% decrease was expected for the squash loads of SC1 and SC2. Test results reveal that the strength reduction factors specified in Eurocode 4 might be slightly conservative but can provide a reasonable estimate of the post-fire conditions.

5.5.5 Post-Fire Lateral Cyclic Testing of Specimen S3

Given that Specimen S3 was only subjected the fire test, a post-fire cyclic loading test was performed in an attempt to investigate the effects of prior fire loading on the flexural behavior of the column under cyclic loading. Note that the column was not loaded axially in this test due to the difficulties caused by its deformed shape. Fig. 27a shows the lateral force vs. drift ratio curve from the post-fire cyclic testing. The test was continued up to the point that a strength degradation of about 50%, which occurred at a drift ratio of 11%, was recorded in the hysteretic curves and substantial fractures occurred in the lower part of the outer tube on both sides. Fig. 27b shows a photo of the fractured column, with cracks over lengths of 11" and 5" on the right and left sides of the column, respectively.



(a)

(b)

Figure 5- 27 Post-fire cyclic testing of specimen S3: a) lateral force vs. lateral drift ratio results and b) fractures at the end of the test

From Fig. 27a, it is observed that specimen S3 retained its ductile behavior after being subjected to fire loading (after cooling down to room temperature). The maximum lateral strength value for the cyclic testing of specimen S3 was about 6.6 kips. According to the theoretical P-M interaction diagram for the specimen cross-section considered, the absence of axial load in this test (compared to the columns tested previously) would result in a 12% reduction in moment capacity. Therefore, considering that specimens S1 and S2 would have reached a maximum lateral strength of about 7 kips in absence of axial load (i.e., a 12% reduction of the experimentally recorded value of 8 kips), this leaves a 5.7% reduction in maximum lateral strength of specimen S3 (compared to S1 and S2) that can be attributed to permanent changes in material strength caused by fire.

Considering the temperature distribution results presented above, the outer and inner steel tubes along with the concrete core reached maximum temperatures above 800°C (except for the third fire test in which the temperatures were on average 100°C lower), and cooled down to the ambient temperature of about 20°C. According to the Eurocode 4 general rules for structural fire design (CEN 2005), this temperature history is expected to cause a 10% permanent loss in the yield and tensile strength of steel, along with an 85% permanent loss in the compressive strength of the concrete core. Calculation of the moment capacity of the cross-section based on these modified strength values shows that the column would have been expected to resist a maximum lateral load of about 6.4 kips. This calculated strength is in good agreement with the recorded value of 6.6 kips from the post-fire cyclic testing of specimen S3.

SECTION 6

FINITE ELEMENT SIMULATION OF EXPERIMENTAL RESULTS

6.1 General

This section investigates the adequacy of the finite element models to numerically replicate the experimental results obtained in this project. In Section 3, these models were initially developed based on recommendations from past numerical studies, and compared to results from past experimental simulations performed on structures with similar characteristics to the ones studied in this project. Here, the selected models using the recommended analysis procedures and material models from these previous studies are further examined by simulating the results of the experiments conducted in this study as described in Sections 4 and 5. Different modeling strategies are then investigated in attempts to improve the match between analytical and experimental results.

Analyses are initiated with the models developed in Section 3, but updated to account for the materials properties obtained for the specimens used in this study. The objective was to see if the models could replicate the experimental results using only measured material properties and geometry as inputs. The goal was to minimize the need for calibration, as it would limit the applicability of the models to other cases. In cases where the accuracy of the simulation results was deemed to be insufficient, the objective then shifted to investigating which material models and analysis procedures could better replicate the physics of the problem, rather than trying to calibrate the existing models (although a limited calibration was performed to investigate to what extent calibration would be needed to best match results for the specific columns tested in this study). The general finite element analysis software ABAQUS was used for the majority of the analyses, except for a few cases in which LS-DYNA was used to address a few modeling problems that were encountered and are discussed later in this report.

Section 6.2 presents the simulation of the two cyclic loading tests described in Section 4. Section 6.3 describes the finite element analyses conducted to replicate the three fire tests on columns with different levels of simulated seismic damage (the tests were presented in Section 5). In each of these sections, the simulation process starts using the models built in Section 3 and modifications are made as necessary to better replicate the test results.

6.2 Simulation of the Cyclic Tests

6.2.1 Finite Element Models

This section presents the finite element simulation of the two cyclic loading tests conducted on Specimens S1 and S2 in order to impose two different levels of simulated seismic damage on the columns (as described in Section 4). The steel material was modeled based on the stress-strain data measured from uniaxial tension tests conducted on various coupons extracted from the same tubes used to construct the inner and outer tubes of the specimens. Two coupons were extracted from the inner and outer tubes used in the construction of each of the three specimens for a total of 12 coupons. Fig. 6.1 shows the results from tensile tests conducted on different coupons for the inner and outer tubes. Different coupons from the inner tubes of different specimens showed almost identical results, as expected, since they were built from the same batch of material. The outer tube coupons also show no significant variation amongst each other, but there is a noticeable difference in strength between the inner tube and outer tube.

A bilinear elastic-plastic model with linear kinematic hardening was fitted to the data with different values for the inner and outer tubes. The yield strength, maximum tensile strength, and corresponding strain parameters were chosen to be equal to the average of the measured values from the coupon tests. The yield and maximum tensile strength values were selected to be 50 ksi (341 MPa) and 58 ksi (401 MPa) for the outer tube, and 44 ksi (304 MPa) and 53 ksi (364 MPa) for the inner tube, respectively (Fig. 6.1). These values were used in the cyclic testing simulations for all of the specimens. Elastic modulus and Poisson's ratio were assumed have values of 29000 ksi (200000 MPa) and 0.3, respectively.

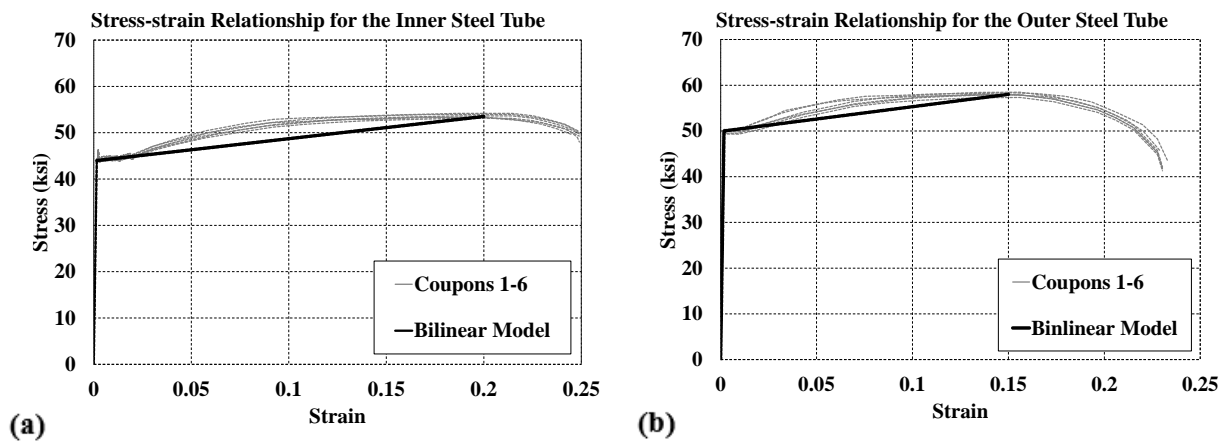


Figure 6- 1 Uniaxial stress-strain relationship used for the modeling of steel material:

a) inner tube b) outer tube

The concrete within the columns was modeled using the Damage Plasticity material with compressive strength, f'_c , measured from the cylinder tests conducted on the day of each cyclic test. Cylinders casted on the construction day showed average compression strength values of 8.0 ksi (55.2 MPa) and 8.7 ksi (60.0 MPa) on the cyclic testing days for specimens S1 (first cyclic test) and S2 (second cyclic test), respectively (complete list of cylinder test results are reported in Table 4.3). The tensile strength of concrete, f_t , was assumed to be about 10% of the compressive strength. The initial stiffness for the linear elastic portion of the uniaxial compressive stress-strain curve was calculated based on the equation given in ACI 318-11, namely: $E_c = 57000\sqrt{f'_c}$ (*psi*), which gives values of 5098 ksi (35,149 MPa) and 5317 ksi (36,659 MPa) for specimens S1 and S2 (ACI 2011). Poisson's ratio for concrete was assumed to be 0.2 in this model. Fig. 6.2 shows the uniaxial compressive and tensile stress-strain curves used for the model of Specimen S1. As explained in Section 3, ABAQUS only accounts for the increase in the concrete compressive strength (but not ductility) caused by the confinement. Therefore, the unconfined stress-strain curve was modified to account for added ductility, using Usami's stress-strain relationship for confined concrete (Usami et al. 2001). The process of obtaining the uniaxial stress-strain relationships in compression (with confinement effects), tension and their corresponding damage parameters was done similarly to the case explained in Section 3 (Section 3.3.4), with modifications to account for the measured material properties for specimens S1 and S2.

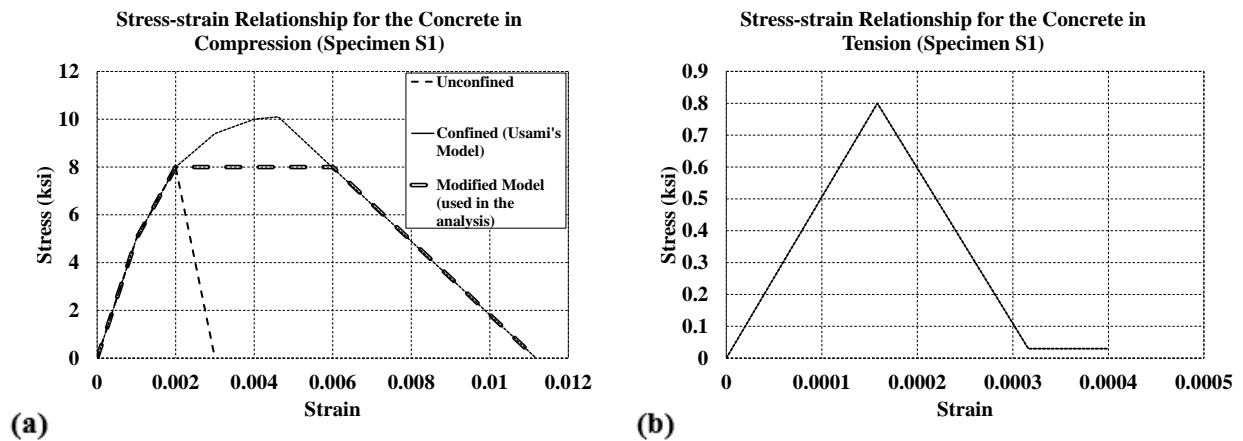


Figure 6- 2 Uniaxial stress-strain relationship used for the modeling of concrete material for specimen S1 in: a) compression (used for FE-CDP and FE-CDP-DS), b) tension (used for FE-CDP)

Fig. 6.3 shows the finite element model built for the cyclic analyses of specimens S1 and S2. A non-uniform mesh pattern was used for the model, with smaller element sizes in the area close to the fixed end of the

column, where local buckling of the outer tube is expected. The average size of the concrete (3D solid) elements in the course and fine areas were about 20x20x20 mm and 10x10x10 mm, respectively. For steel (shell) elements, these sizes were about 20x20 mm and 10x10 mm. The concrete core was modeled using 8-node solid (C3D8R) elements while the steel tubes (both inner and outer) were modeled with 4-node shell (S4R) elements. The default hourglass control method in ABAQUS was used for both element types to control the hourglass modes that might occur in the linear elements that use the reduced integration method.

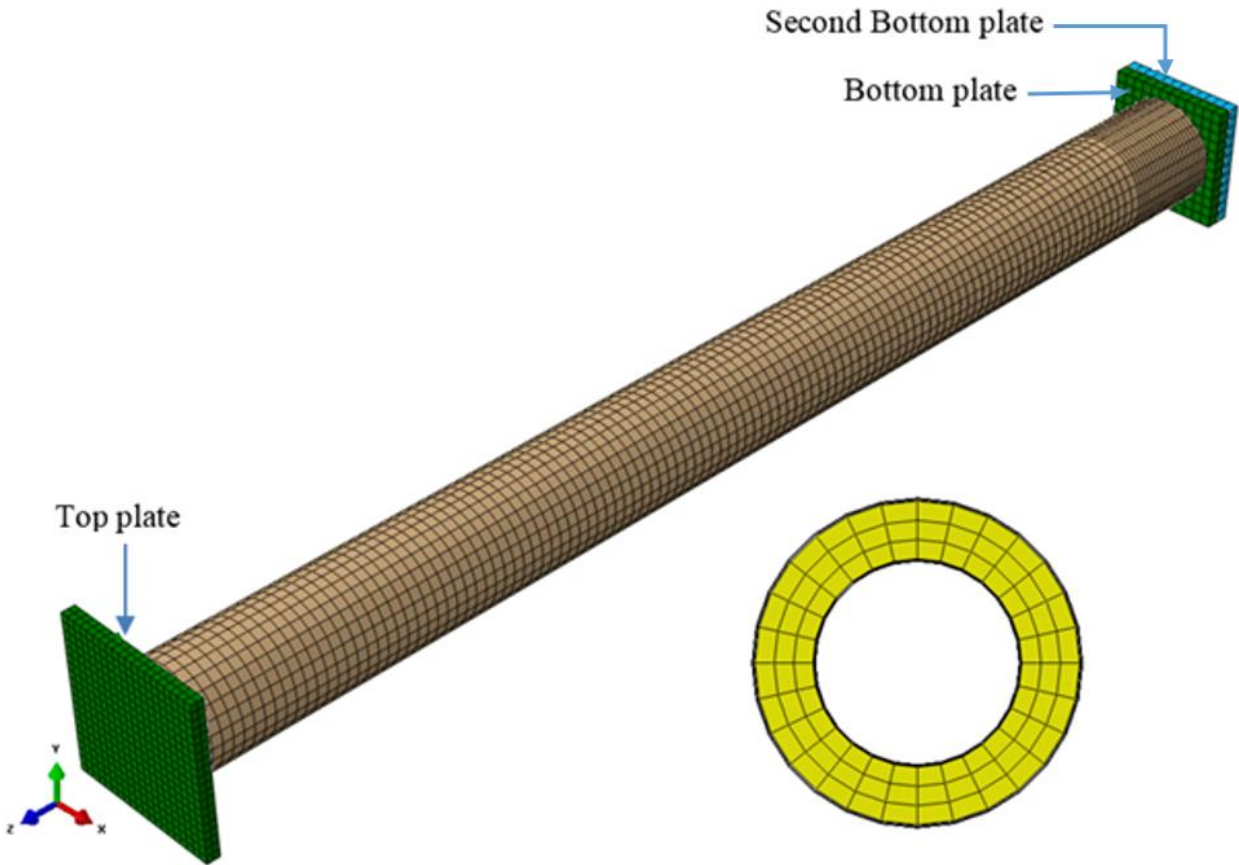


Figure 6- 3 Finite element model built for the numerical simulation of cyclic loading tests

The bottom plate of the column was tied to both the inner and outer tubes in the finite element model, while the top plate was only tied to the outer tube, to replicate the experimental conditions. In the construction of the specimen, the outer tube was welded at both ends while the inner tube was only welded to the bottom plate since there was no access to weld the inner tube to the top plate. The interaction at the steel-concrete interface was defined with a hard contact (allowing separation of the surfaces) in the normal direction, and a coulomb friction model in the tangent direction which a friction coefficient of 0.20.

To avoid adding unnecessary complexities to the numerical model, loads and boundary conditions were defined with some slight differences compared to the test setup. First, the axial load was applied as a pressure to the central part of the top and bottom plates of the column, thus removing the post-tensioning bar from the numerical model. Second, the connection at the base of the column was simplified by removing the additional (built-up) box section, which was used in the experimental setup to protect the base beam. This was done to eliminate the unnecessary stress/deformation complexities and several surface-to-surface tie contact models that would make the analysis computationally expensive.

To account for the flexibility of the base caused by the built-up box section in the cyclic tests, a second plate was modeled just below the bottom plate of the column and was kept elastic to act as the base beam of the experimental setup (Fig. 6.3). A hard contact model (allowing separation of the surfaces) was used for the interaction between the bottom plate of the column and the elastic base plate. The two plates were connected to each other using the Bolt Load feature from the load module of ABAQUS, which was defined using six bolt positions (three on each side of the plates) that could be adjusted for different bolt stiffness and prestress loads. To ensure that this approach was effective to simulate the conditions of the base connection in the experimental setup, while keeping the numerical model simple and efficient, push-over analyses were conducted before the cyclic loading simulation to calibrate the flexibility of the modeled base connection for each specimen based on the results from the cyclic tests. This model is referred to as the FE-CDP model (as it uses the Damaged Plasticity model for concrete) in the following pages and figures of this report.

6.2.2 Push-over Analysis of Specimen S1

The push-over analysis of the FE-CDP model of Specimen S1 was conducted by a three-step loading process as follows: 1) apply the pre-stress load to the bolts; 2) apply an axial load of 71 kips as pressure to the top and bottom plates, and; 3) apply a monotonic displacement to cause a drift ratio of 6.5%. A series of push-over analyses were conducted to calibrate the properties of the bolting system based on initial stiffness of the system recorded at the beginning of the cyclic testing of Specimen S1.

Fig. 6.4 shows the final results from the push-over analysis of Specimen S1 (after calibration for the flexibility of the base) along with the experimental results from the cyclic testing of the column. The two-plate system was able to replicate the effects of the base connection on the initial lateral stiffness of the column with sufficient accuracy. The final calibrated model has an initial lateral stiffness of 3.5 kip/in., which includes combined effects of the specimen column and the base connection with sufficient accuracy.

The initial lateral stiffness for the fixed base model was 3.9 kip/in., which corresponds to a 10.2% difference with the stiffness value for the model with the added flexibility to the base. Note that the difference between the initial stiffness of the fixed-base and calibrated models was attributed to the flexibility of the bolted base connection in the test setup, assuming that the elastic modulus of concrete was equal to the value calculated using the ACI 318 formula based on the measured compressive strength.

The lateral force versus drift curve obtained from push-over analysis follows a path that encloses the experimental cycles and predicts acceptable lateral resisting force values for the increasing drift ratio. Note that the push-over curve gives lateral force values slightly larger than the ones recorded in the experiment for the cycles at the highest displacement amplitudes (i.e., at 5% and 6% drift ratio). The difference is attributed to the minor strength degradation that occurred in the specimen going through repeated cycles of relatively large displacements that caused a slight local buckling to develop at the base of the outer steel tube.

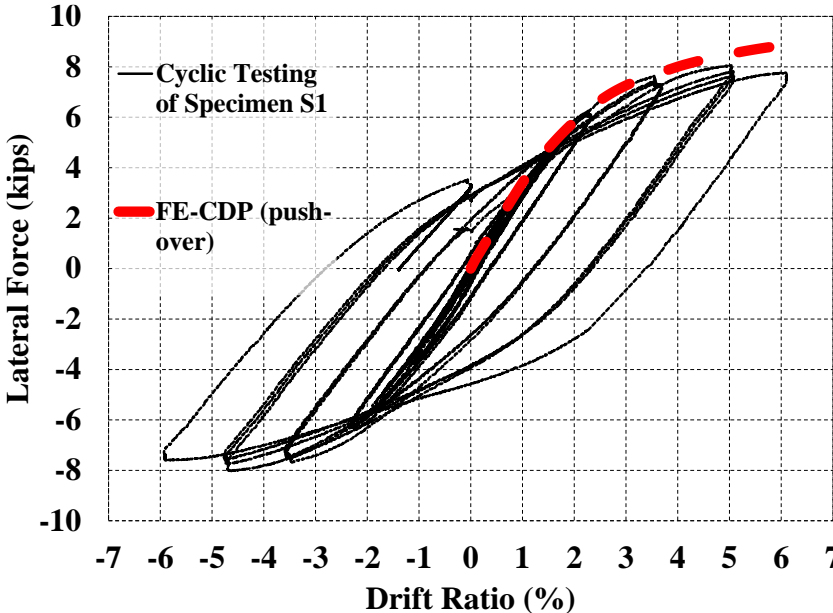


Figure 6- 4 Lateral force vs. drift ratio results from the push-over analysis of specimen S1 using the FE-CDP model (compared with the test results)

6.2.3 Cyclic Analysis of Specimen S1

The FE-CDP model of Specimen S1 with calibrated base flexibility was then subjected to the cyclic displacement protocol recorded from the cyclic testing of the column. Fig. 6.5 shows the lateral force versus

drift ratio results from the finite element analysis. The model provided acceptable stiffness and strength predictions but failed to capture the pinching of the hysteretic curves for the CFDST column under cyclic loading. Note that during the cycles at the maximum drift ratios of 5% and 6%, the model was also not capable of capturing the strength degradation caused by the local buckling of the steel tube.

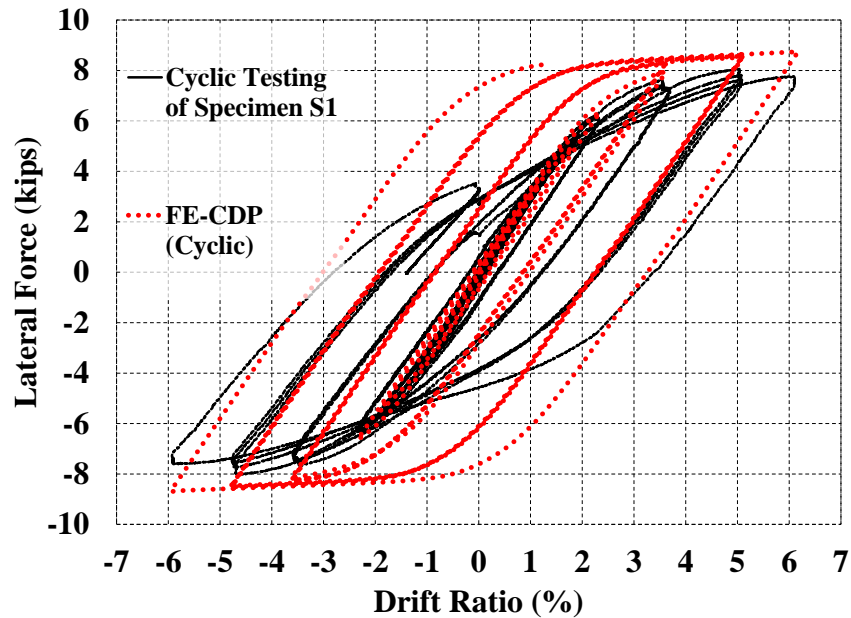


Figure 6- 5 Lateral force vs. drift ratio results from the cyclic loading analysis of specimen S1 (FE-CDP model) compared with the test results

Local buckling of the outer steel tube plays an important role in the formation of pinching in the hysteretic curves of cyclically loaded CFDST columns. It occurs on the compression side of the column, and more easily so when the tube comes under compression after having previously stretched and plastically elongated in tension during loading in the reversed direction. Since the concrete core in CFDST columns provides a bearing support for the tubes (thus delaying the occurrence of local buckling), the formation of tensile cracks and their opening and closing in subsequent cycles can affect the severity of the outer tube's local buckling. As the crack opens on the tension side, the adjacent length of the outer tube is stretched more than the case without the crack opening. More stretching causes more severe buckling in the reverse loading part of the cycle. To account for these effects, the material model for concrete needs to be capable of capturing the initiation and growth of tensile cracks that are expected to form in that region of the concrete core.

As it can be inferred from Fig. 6.5, the Damage Plasticity model used for concrete in the FE-CDP model was not able to accurately simulate tensile cracking in concrete and its subsequent effects (specifically, the opening and closing of the tensile cracks that play an important role in the creation of the pinching behavior in the hysteretic curves). The issue was also reported by Goto et al. (2010) in a similar study on numerical modeling of concrete filled columns, because the Damaged Plasticity model is approximate in terms of its tensile behavior since isotropic plasticity is assumed in tension.

To resolve this problem, Goto et al. proposed a modification to the model by inserting a horizontal discrete crack model (Chen 2007) at the location of the major tensile crack; this location can be identified by a preliminary analysis (in the case of a cantilever column, the major tensile crack occurs in the vicinity of the fixed base). A hard contact was modeled between the two separated surfaces of concrete at the horizontal crack to be able to simulate the opening and closing behavior. In the tangent direction, the friction between the two concrete surfaces was modeled using a friction coefficient of 1.0 based on ACI recommendations (ACI 2011). The effectiveness of the proposed solution was verified by comparison with experimental results of different CFT columns (Goto et al. 2010).

In a similar study, Goto et al. showed that using additional discrete cracks (two or three instead of one) can improve the accuracy of the results for rectangular CFST columns (Goto et al. 2012). The disadvantage of using multiple discrete cracks was the computational difficulties that were added to the problem because of the multiple contact surfaces introduced in that model. To avoid these difficulties, which can be worse for CFDST columns because of their added complexity, and because the studies by Goto et al. showed the sufficiency of using a single discrete crack for circular CFST columns (as opposed to rectangular ones where additional cracks led to better results), the insertion of a single crack was considered for the models used in this study.

In an attempt to better replicate the experimental results of Specimen S1 (specifically the pinching behavior of the hysteretic curves), the FE-CDP model was modified in two ways. First, the stress-strain curve used for the concrete material in tension was replaced with a stress-displacement curve (assumed to be equivalent to the crack opening), which, according to the ABAQUS Documentation, is effective in decreasing the mesh-sensitivity of the results for the elements that reach the softening branch of the concrete material's tensile behavior (SIMULIA 2012). The stress-displacement curve used here was determined using the stress-strain relationship defined earlier in this section and the average element size of the concrete model used in this study. Note that, with this approach, displacement (crack opening, u_{cr}) is related to the equivalent plastic strain by $(\varepsilon^{pl} = \frac{u_{cr}}{l_0})$, where l_0 is the concrete element length. Fig. 6.6 shows the stress-

displacement curve used in the finite element model. The damage parameters for the tension side, previously defined as a function of equivalent plastic strain, were also changed to be a function of displacement.

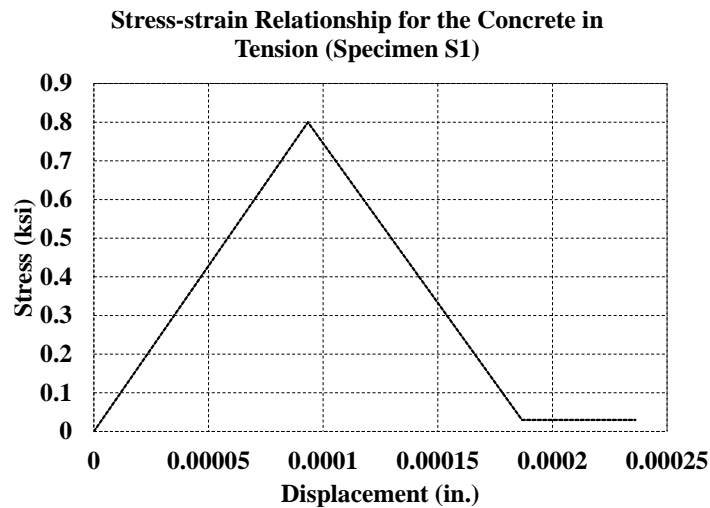


Figure 6- 6 Uniaxial tensile stress-displacement relationship used for modeling the concrete material of specimen S1 (used in FE-CDP-DS model)

Second, considering that the modified concrete model was still incapable of simulating the crack opening and closing behavior, a discrete crack was inserted at the lower end of the concrete core (close to the base), where the stress contour lines showed the maximum tensile stress values (note that, for more complicated systems with less obvious points of maximum tension, locations of the discrete cracks would be determined by additional studies). The crack was modeled by cutting the concrete core along a horizontal plane just above the base and defining an interaction, with the properties mentioned above, between the two concrete surfaces. This model is referred to as the FE-CDP-DS model (DS stands for Discrete Crack) in the following pages and figures of this report.

Fig. 6.7 shows the lateral force vs. drift ratio results for the cyclic loading of the FE-CDP-DS model of Specimen S1. Results show a much closer agreement to the experimental data because of the improved capability of the modified model to capture local buckling of the steel tube, resulting in the pinching of the hysteretic curves of the CFDST column. The hysteresis curves also show small strength degradations in the cycles at drift amplitudes of 5% and 6%. This is also in agreement with the experimental results, supporting the fact that the opening and closing of the tensile cracks in concrete, facilitates the local buckling of the steel tube, which then causes strength degradation.

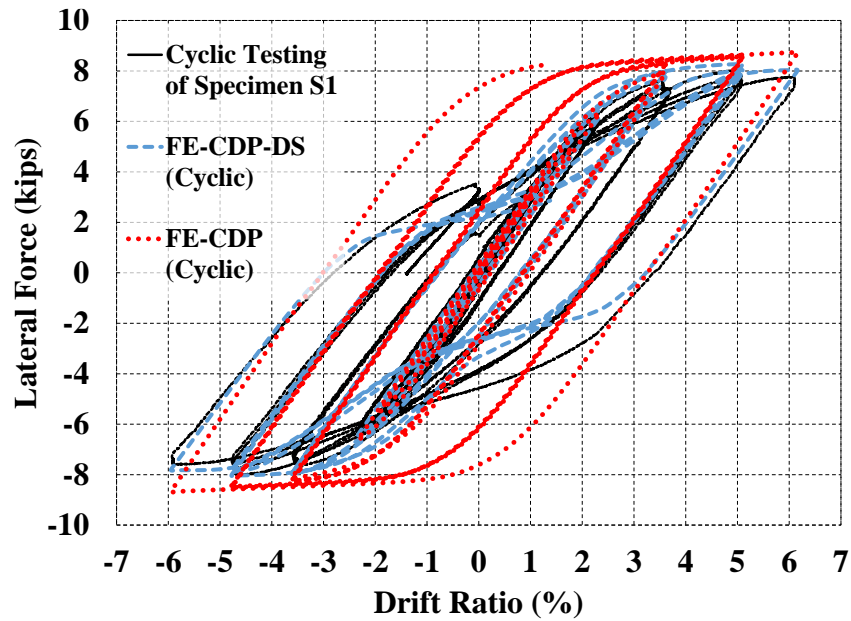


Figure 6- 7 Lateral force vs. drift ratio results from the cyclic loading analysis of specimen S1 (from the FE-CDP-DS model) compared with the test results

Comparing results from the FE-CDP and FE-CDP-DS models, it can be inferred that the model could be improved to create a situation between these two cases. The opening and closing of the tensile cracks help to capture the pinching behavior in the hysteretic curves, but maybe the concrete core should not be completely divided into two separate pieces at the cracked region as was done in the modified model used here. A partial continuity in the cracked region could compensate for the slightly more severe pinching that is seen in the hysteresis curves for the model with the discrete crack, compared to the experimental results.

However, despite the more severe pinching seen in the hysteresis curves, the FE-CDP-DS model with the discrete concrete crack was deemed to provide sufficiently accurate results and was considered acceptable for the finite element analysis simulation of the behavior of CFDST columns under post-earthquake fire scenarios. However, to investigate if the modeling approach could be further improved, additional analyses were conducted using the program LS-DYNA, where instead of inserting discrete cracks at pre-determined locations, a different concrete model capable of simulating the behavior of tensile cracks was used.

As such, the concrete core was modeled using the Winfrith Concrete material available in LS-DYNA, which provides a better simulation of the tensile behavior of concrete by attempting to regularize the strain

softening in tension via parameters accounting for crack opening width, fracture energy and aggregate size. The model is also capable of simulating tensile cracking with up to three orthogonal crack planes per element (Schwer 2011). Additional information about the Winfrith concrete model is presented in Appendix B.

To provide a complete set of needed parameters for the Winfrith model in LS-DYNA, aside from the maximum compressive strength, elastic modulus, and tensile strength (which were assumed to be the same as the values used in the ABAQUS model), the maximum aggregate size was selected to be 0.25” in. (6.35mm), as the concrete mixture used in the specimen construction had small aggregates to facilitate its flow in the 1.5” (38.1 mm) wide space between the two tubes. A new stress-displacement (crack opening width) relationship was defined for the behavior of concrete in tension according to the procedure presented in a study by Schwer (2011) on the performance of the Winfrith concrete model. In this procedure (as shown in Fig. 6.8), the stress-displacement relationship starts with a linear elastic branch, going from zero tensile stress to the tensile strength, f_t , and descends with another linear branch that goes back to zero tensile stress at the crack opening width of w . Defining the area under the stress-displacement curve as the specific fracture energy, G_F , the crack opening width for the zero tensile stress (w) can be calculated from:

$$w = \frac{2G_F}{f_t} \quad (6.1)$$

The Euro-International Committee for Concrete (CEB 1993) provides recommended values for the specific fracture energy of concrete with given maximum compressive strength and maximum aggregate size. For concrete with the maximum compressive strength of 8 ksi (55.2 MPa) and maximum aggregate size of 0.25 in. (6.35 mm), a specific fracture energy of 5.31×10^{-4} kip/in. (95 N/m) is specified, which gives the crack opening width value (w) of 0.0014 in. (0.03 mm) for the zero tensile strength point (f_t was assumed equal to 10% of the compressive strength). Note that the new model, which uses the Winfrith model for concrete, is referred to as the FE-W in the following pages and figures of this paper.

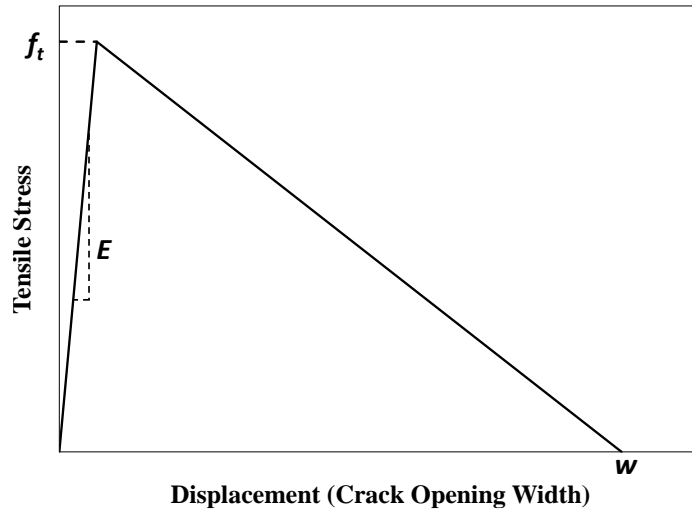


Figure 6- 8 Stress-displacement relationship used for the tensile behavior of concrete in the FE-W model

Fig. 6.9a shows the results from the cyclic loading analysis of the FE-W model of Specimen S1. Note that the steel material was modeled using a bilinear behavior with kinematic hardening (referred to as the Plastic Kinematic material model in LS-DYNA) similarly to the FE-CDP and FE-CDP-DS models (built in ABAQUS). Results from the FE-W model follow the experimental curves with considerable accuracy. The accuracy of the results showed that the crack simulation capabilities of the concrete material were effective in capturing the true behavior of CFDST column. The FE-CDP model required the insertion of a discrete crack (as done in the FE-CDP-DS model) to fully capture the effects of tensile crack opening and closing in concrete structures.

In addition to the mesh sensitivity analyses conducted for both cyclic loading and fire test simulations in Section 3, an LS-DYNA analysis was conducted to check the sensitivity of the results from the Specimen S1 model to the mesh size. Fig. 6.9b shows the results from two similar FE-W models with total number of elements of about 26000 and 58000. The difference between the two sets of hysteresis curves is marginal, confirming the convergence of the finite element analysis (i.e., the mesh size used is sufficiently refined for the current problem).

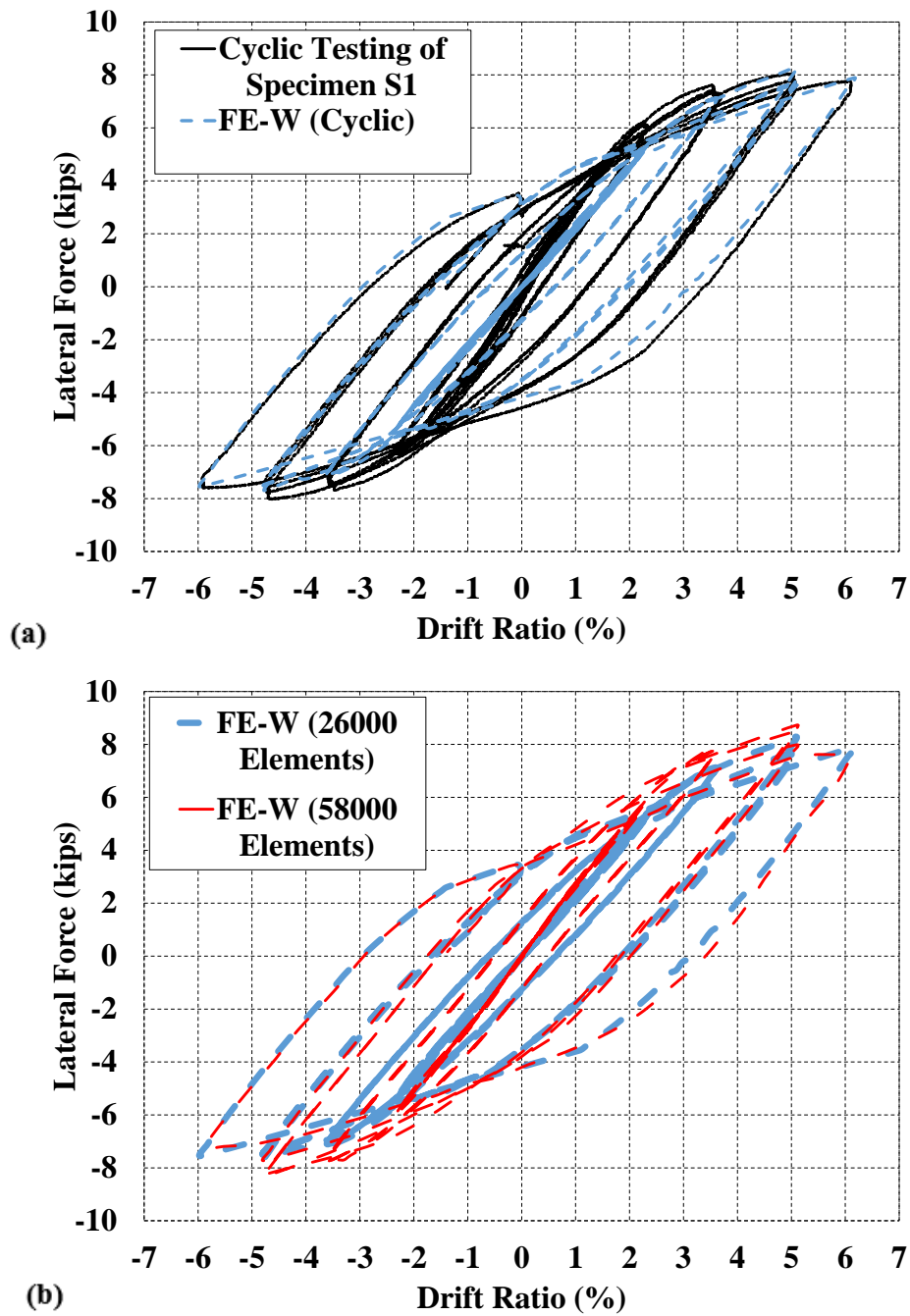
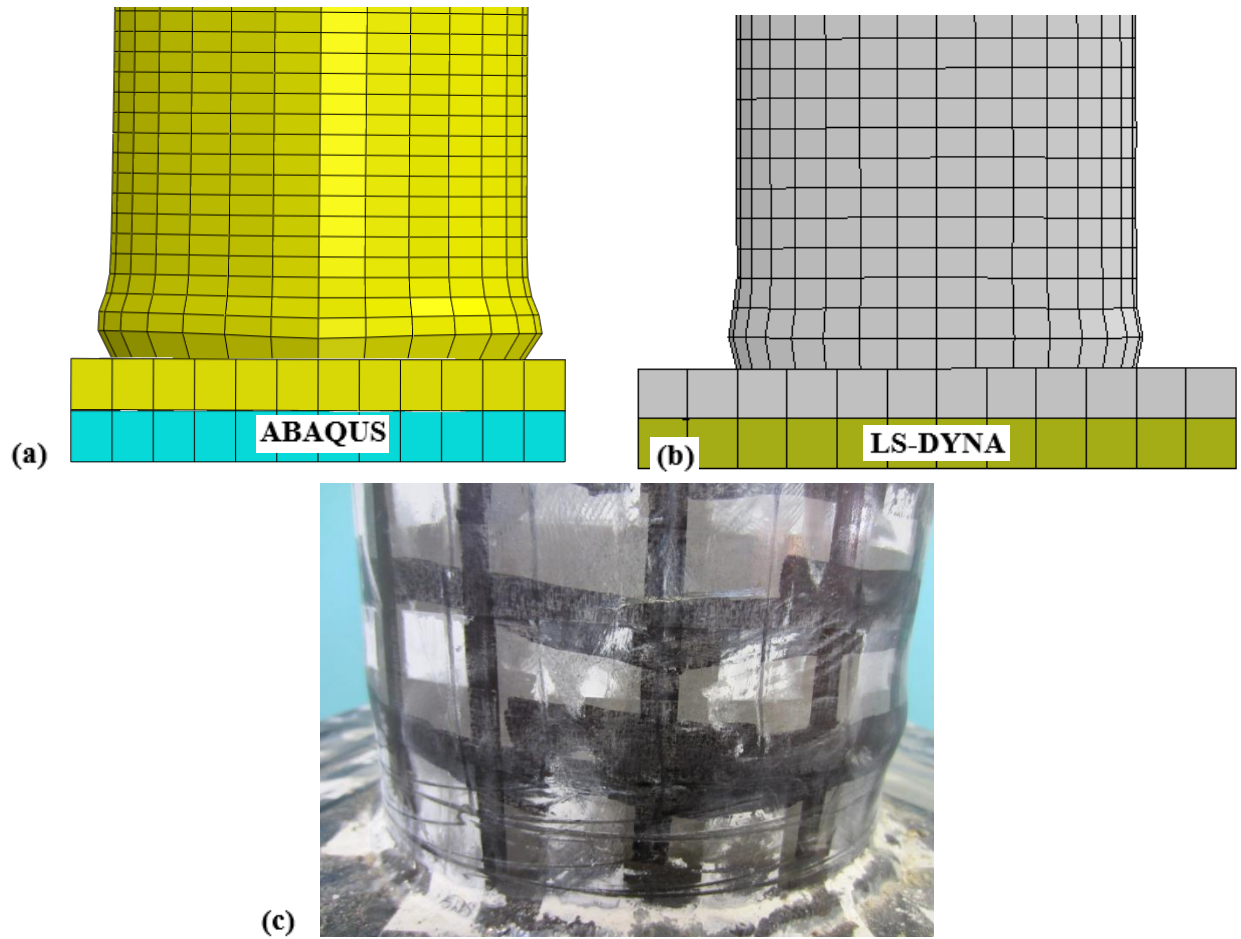


Figure 6- 9 Lateral force vs. drift ratio results from the analysis of the FE-W models of specimen S1: a) comparison with the experimental results b) mesh sensitivity analysis



**Figure 6- 10 Local buckling of specimen S1 at the end of cyclic testing: a) FE-CDP-DS model
b) FE-W model and c) photo from the test**

In terms of deformations, both the ABAQUS and LS-DYNA models were able to capture the local buckling of the outer tube near the fixed base. Fig. 6.10 shows the final deformed shape of the lower end of the column from both analyses, along with a photo from the cyclic testing of Specimen S1. Note that the FE-CDP-DS model (Fig. 6.10a) shows larger deformations in the buckled region, which is in agreement with the more severe pinching, seen in the hysteresis curves of Fig. 6.7.

6.2.4 Push-over Analysis of Specimen S2

Fig. 6.11 shows the results from the push-over analysis of Specimen S2, plotted along with the experimental results from the specimen's cyclic testing. Since specimens S1 and S2 had identical geometries and steel tubes with the same material properties, the model used for the push-over analysis of specimen S1 was just updated to account for the 8% higher compressive strength of concrete measured from the cylinder tests for

Specimen S2. The analysis provided an acceptable replication of the experimental results in terms of the initial stiffness and maximum lateral resisting force.

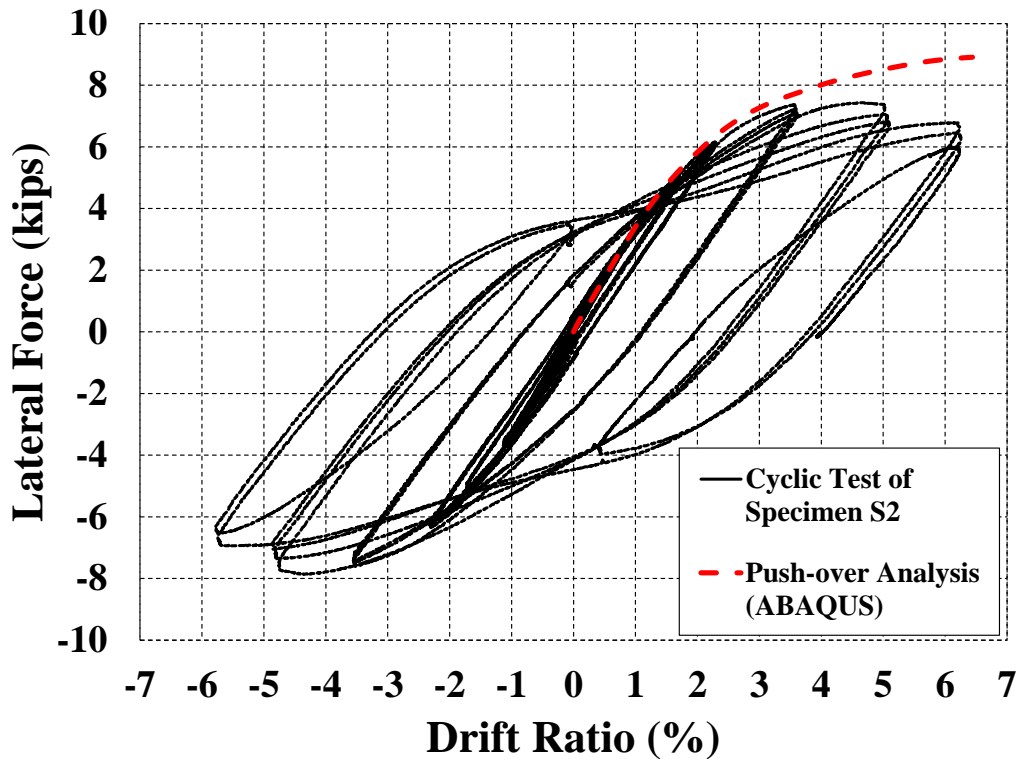


Figure 6- 11 Lateral force vs. drift ratio results from the finite element push-over analysis (compared with results from cyclic testing of specimen S2)

6.2.5 Cyclic Analysis of Specimen S2

Cyclic testing of Specimen S2 was simulated using the FE-CDP-DS model. The applied cyclic displacement time-history was modified to match the corrected values recorded from the second cyclic test. Fig. 6.12 shows results from the analysis along with the experimental hysteresis curves. Similar to what was observed for Specimen S1, the numerical simulation provided acceptable results in terms of predicting strength and stiffness values in agreement with the experimental data through different displacement cycles. The model captured the strength degradation at cycles with drift amplitudes of about 5% and 6.2%. The only notable problem (again, similar to the case of Specimen S1) was the relatively more severe pinching of the numerical hysteresis curves compared to test results. Considering that this issue was due to the discontinuity created at the base of the concrete core to account for the opening and closing of the tensile cracks, an LS-

DYNA analysis was conducted using the Winfrith concrete (FE-W) model in an attempt to better replicate the second cyclic test results.

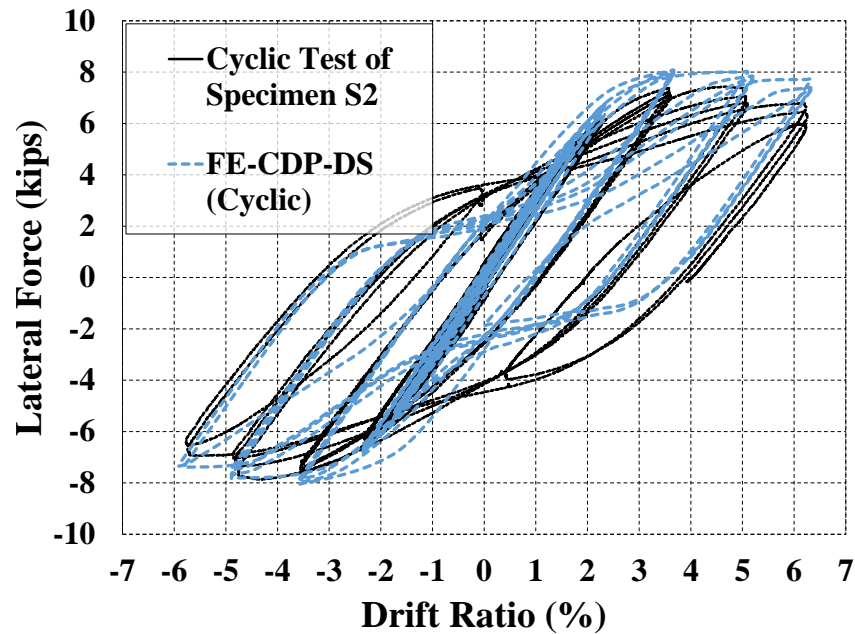


Figure 6- 12 Lateral force vs. drift ratio results from the cyclic loading analysis of specimen S2 (FE-CDP-DS model) compared with the test results

Fig. 6.13a shows the lateral force vs. drift ratio results from the FE-W model, which provided a more accurate match of the experimental data. Fig. 6.13b shows the capability of the FE-W model in simulating the opening and closing of tensile cracks in concrete structures. Appearance and disappearance of the horizontal crack lines at the lower end of the concrete core show the opening and closing of tensile cracks, while the column goes from a 5% drift in one direction to the same amount in the opposite side. Note that the minimum required opening width for a crack to be displayed by the LS-DYNA post-processor was set to 0.002 in. (0.05 mm).

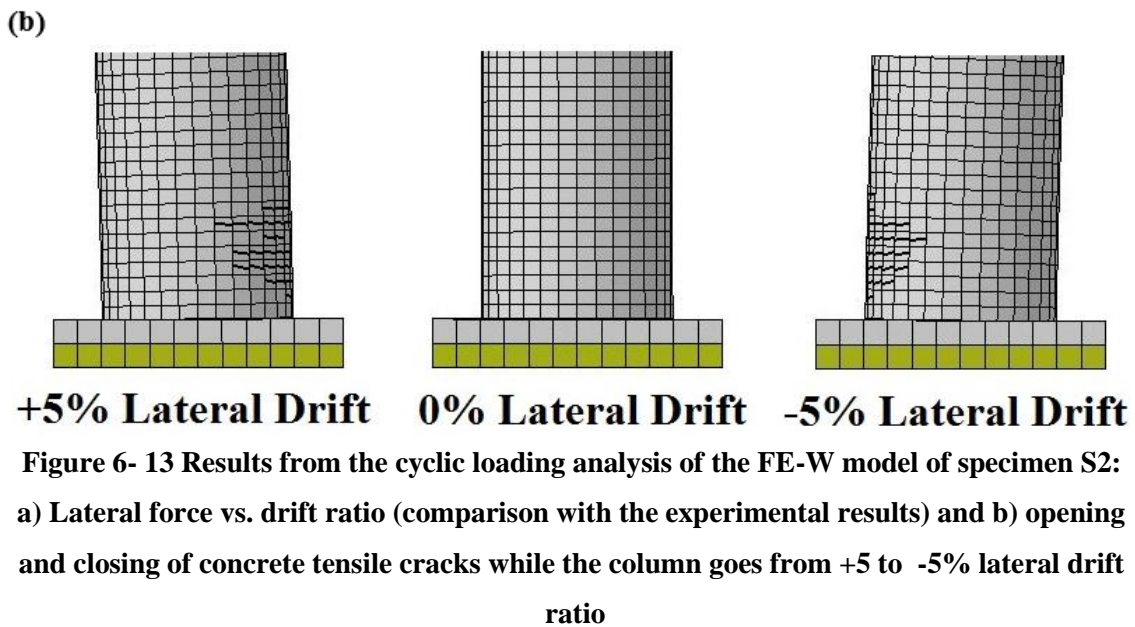
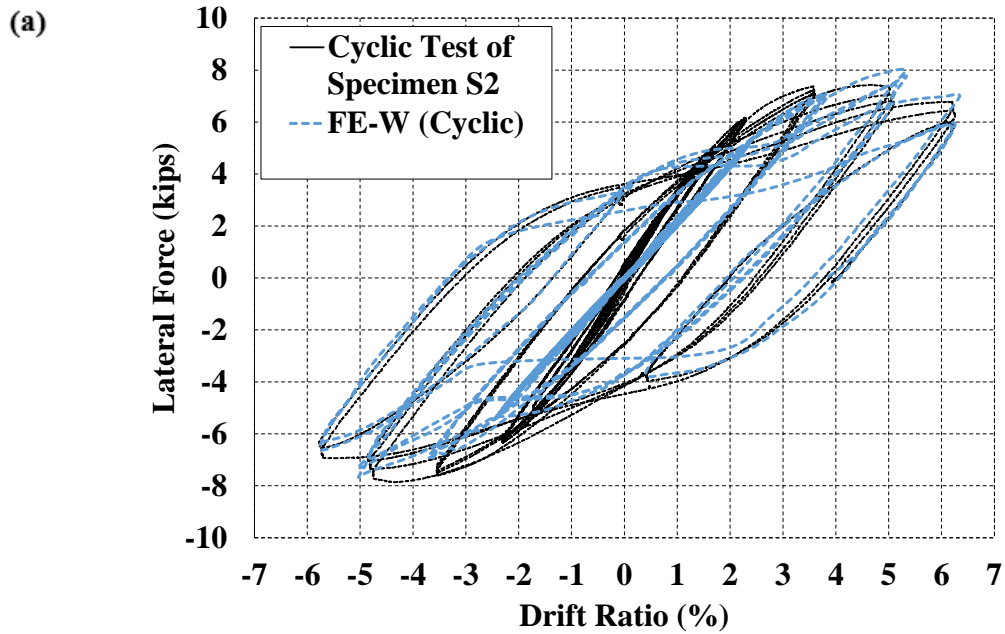


Fig. 6.14 shows the local buckling of the outer tube for Specimen S2, both from numerical simulation (FE-CDP-DS and FE-W) and test results. The figure shows the final state of the column, when the cyclic loading stops at zero lateral load, leaving the specimen at a 3.9% residual drift (considered as a relatively high simulated seismic damage). Results from both simulation analyses are in good agreement with the photo taken at the end of the cyclic testing.

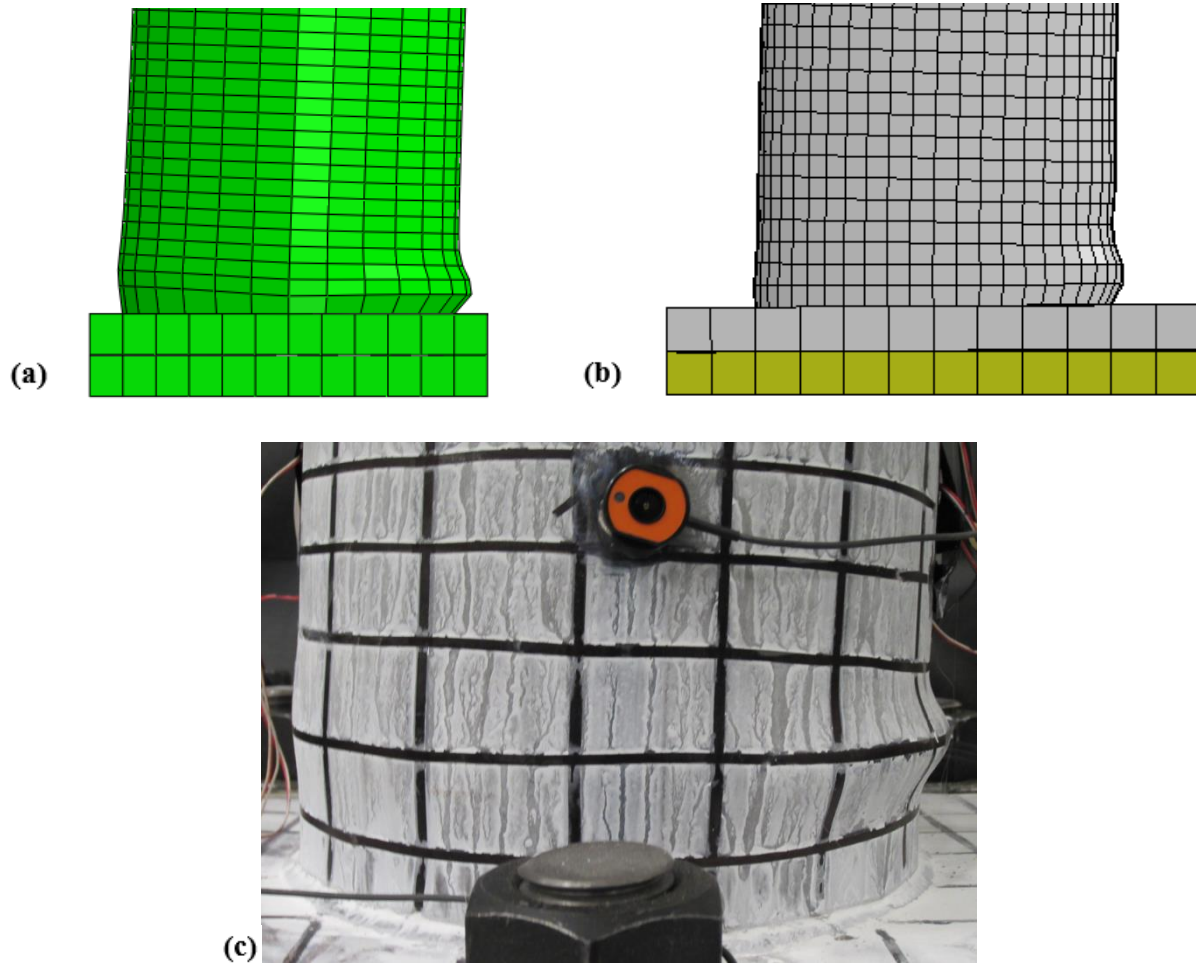


Figure 6- 14 Local buckling of specimen S2 at the end of cyclic testing: a) FE-CDP-DS model, b) FE-W model and c) photo from the test

Note that final results from the ABAQUS analyses of specimens S1 and S2 under cyclic loading are used as initial conditions for the numerical simulation of fire tests of these specimens (presented in Section 6.3) to complete the simulation of the post-earthquake fire scenario

6.3 Simulation of the Fire Tests

6.3.1 General

This section presents results of the series of thermal-stress analyses performed to simulate the three standard ASTM E119 fire tests conducted on specimens S1, S2, and S3. As discussed in Section 3, the full thermal-stress analysis was divided into two sequentially coupled parts, referred to as the heat transfer and

stress/deformation analyses. The alteration from a fully coupled analysis to a sequentially coupled analysis was mainly done to avoid unnecessary complexities in the numerical simulations, thus making the models computationally efficient (the effects of this alteration were discussed in detail in section 3).

The simulation process starts with a heat transfer analysis for each column to obtain the time-history of nodal temperatures to be used as input (for fire loading) in the subsequent stress/deformation analysis. Experimental data from the thermocouples embedded within the columns were used for validation of the numerical models. The stress/deformation analysis was conducted on the models using a multi-step analysis approach that included the axial loading, the cyclic loading (for specimens S1 and S2), and the fire loading. The last phase used the results from heat transfer analysis to simulate the effects of fire on the axially loaded and damaged columns.

Considering the results from thermal-stress analyses conducted in Section 3, the thermal and structural temperature-dependent material properties for both steel and concrete were adopted from the Eurocode specifications (CEN 2005). The concrete core was modeled using 8-node solid elements in both heat transfer and stress/deformation analyses. The steel tube was modeled with different types of elements (8-node solid and 4-node shell) in different occasions for reasons that are mentioned later in this report. The simulations are presented in the same order as the experimental program described in Section 4, starting with the fire testing of the undamaged specimen (S3) and moving on to the fire testing of the moderately and highly damaged columns (specimens S1 and S2).

6.3.2 Fire Testing of the Undamaged Specimen (S3)

6.3.2.1 Heat Transfer Analysis of Specimen S3

A transient heat transfer analysis was conducted on Specimen S3 (the undamaged specimen) to simulate the effects of the ASTM E119 standard fire applied to the column during the first fire test. The recorded time-history of temperature for the outer tube was provided as input for the heat transfer analysis by setting a boundary condition on the outer surfaces of the model. This eliminates possible errors that might affect the results if the furnace air temperature data is used to predict the temperature on the surface of the outer tube. The preliminary finite element analysis of the heat transfer process presented in Section 3.5 showed that the temperature distribution on the outer surfaces of the model can be calculated with an acceptable accuracy by using the furnace air temperature as input for the analysis. Note that although the time-history of temperature was recorded by a thermocouple attached to the inner surface of the outer tube, it was

assumed that the outer surface followed the same temperature curve. The difference in temperature of the inner and outer surfaces of a 0.11” (2.8mm) steel tube can be considered insignificant because of the relatively high thermal conductivity of steel.

Similarly to the model used in Section 3, two heat transfer mechanisms (conduction and radiation) were defined for the steel-concrete interface. The conduction mechanism was defined based on an average conduction factor, selected to account for the possible gaps between the steel and concrete surfaces (discussed in more detail in Section 3). The complete list of the parameters and constants used for the heat transfer mechanism are presented in Table 3.1 (Section 3).

Fig. 6.15 shows the finite element model built for Specimen S3 and the results of the heat transfer analysis for a section chosen at mid-height of the column. The colors of the contour lines show the difference in temperature levels going from the outer tube towards the inner tube of the column. Note that this model contains the additional built-up box at the base of the specimen as it was designed and built in the experimental setup. This was done because the way the bottom end of the inner tube was connected with the bottom plate of the additional built-up box section can affect the results, providing an “all steel” heat-transfer load path at that location. In other words, this connection detail can cause a “short circuit” for the direct transfer of the thermal energy from the outer surfaces of the structure to the inner tube, rather than going through the cross-section of the column with its considerably less conductive concrete part.

Note that a similar “short circuit” exists at the top end of the column, where the thermal energy can find a direct path from the top plate of the specimen to the top end of the inner tube (even though the top plate was not welded to the inner tube, it was most likely in contact with it during the test). In order to investigate the significance of those effects on the heat transfer analysis results, an additional analysis was conducted on the same model in which the thermal connectivity of the built-up box section and the top plate to the bottom and top ends of the inner tube was eliminated (no thermal connectivity was defined between the corresponding surfaces).

Fig. 6.16 shows the results of these heat transfer analyses for two different nodes, located at mid-height and close to the top end of the inner tube, for two different cases (with and without the thermal connectivity of the top and bottom plates to the inner tube). Temperature time-history recorded for the inner tube of Specimen S3 during the first fire test is also plotted for comparison (Fig. 6.16). Note that the test data was recorded by a thermocouple that was located on the outer surface of the inner tube and close to its top end. Results indicate that the thermal connectivity of the inner tube to the plates at its top and bottom ends does

not significantly affect the nodal temperature values at locations close to the mid-height of the inner tube (Fig. 6.16a). However, for the nodes located about 6-12” from the top plate of the specimen (which is approximately the same location where the thermocouple was installed in the test), the connectivity of the top end of the inner tube to the top plate does significantly affect the temperature results (Fig. 6.16b). Note that accounting for the special conditions at the top end of the inner tube leads to a more accurate calculation of the temperature time-history for the inner tube (the obtained curve is closer to the experimental results on average).

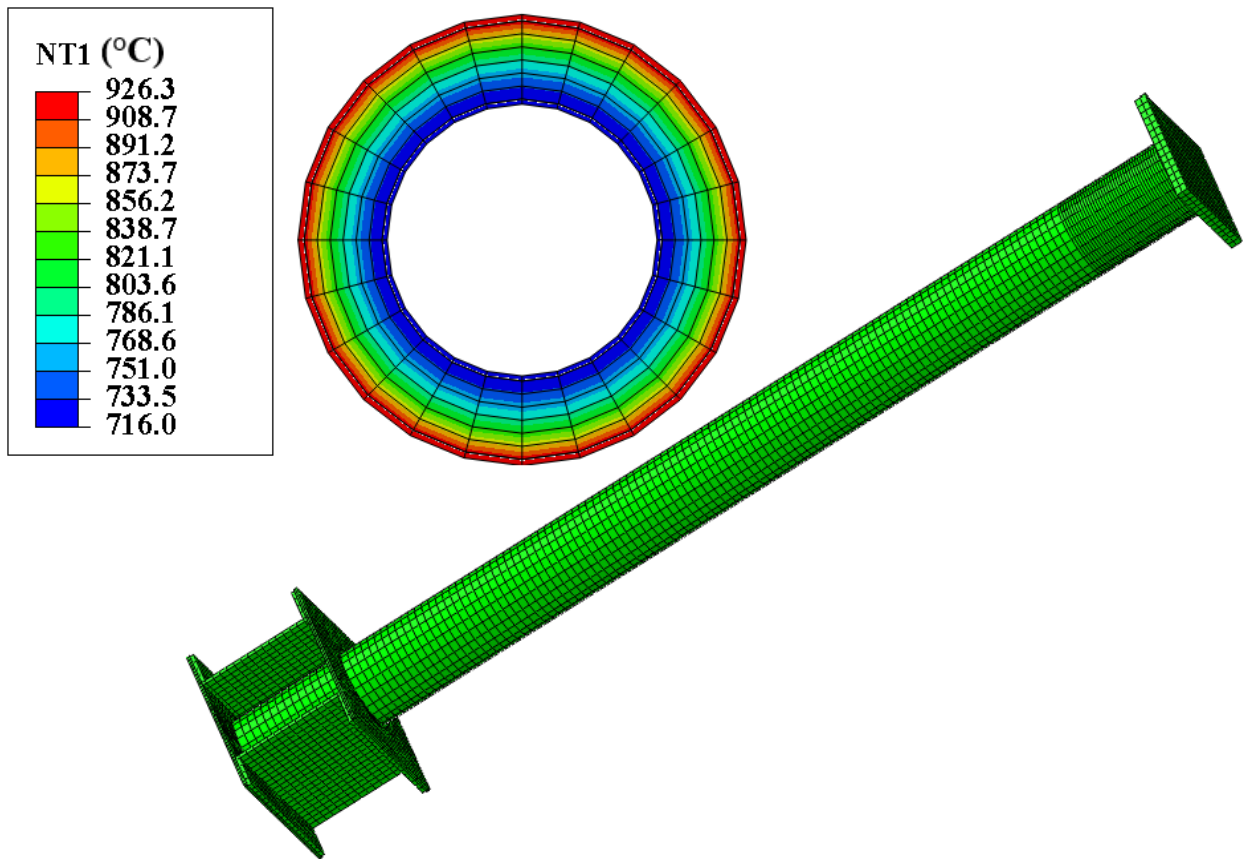
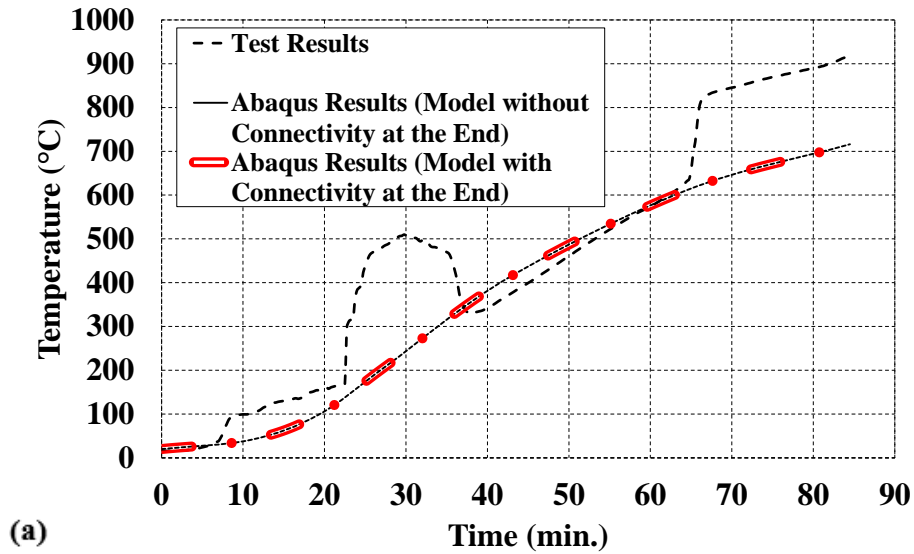


Figure 6- 15 Finite element model built for the thermal stress analysis of specimen S3 along with the final visualized results of the heat transfer analysis for a section chosen at mid-height of the column (from ABAQUS)

Simulation Results for a Point at Mid-Height of the Column



Simulation Results for a Point Close to the Top End of the Column

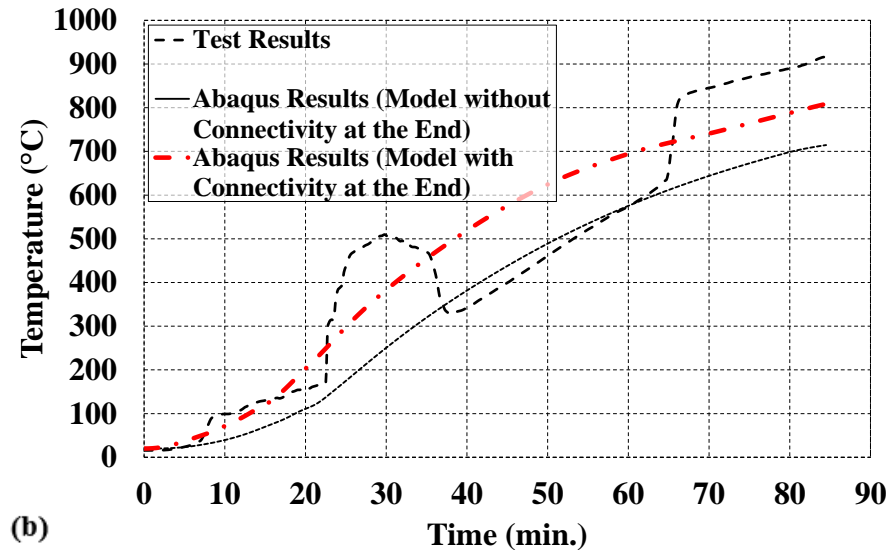


Figure 6- 16 Analysis results for the temperature time-history of the inner tube for cases without and with its connectivity to the end plates for a point at: a) mid-height and b) close to the top end of specimen S3

However, comparison of nodal temperature values at different locations along the specimen, for the two different cases defined above, also revealed that variation in results created by the connection of top and bottom plates to the whole section of the column are limited to relatively short portions of the specimen close to its top and bottom ends. It is expected that this difference in the temperature levels for the nodes

located close to the ends or mid-height of the column due to the presence of steel end-plates would be bigger for sections having thicker concrete fills; in the presence of a relatively thicker concrete, the low conductivity of concrete would keep the temperature of the inner tube at considerably lower temperature levels, thus resulting in a significant difference with the temperatures in the inner tube at its top and bottom ends (where thermal energy has an easier path to get to the inner tube compared to the path going through the concrete).

To simulate the test conditions, the case with steel end-plates (“short circuit”) was used in all of the following analyses. Note that the removal of these plates, which are experimental artifacts, would generally improve the fire resistance of the column.

Figures 6.17 and 6.18 show results of the recorded time-history of temperature from the thermocouples installed in the middle of the concrete layer and on the outer surface of the inner tube, along with the results from heat transfer analysis for two selected nodes located approximately at the same positions. The temperature time-history of the outer tube (applied as a boundary condition to the model) is also included in both figures for comparison purposes. The figures indicate that the numerical simulations have reasonably predicted the temperature time-histories for nodes both in the mid-width of the concrete section and on the inner steel tube.

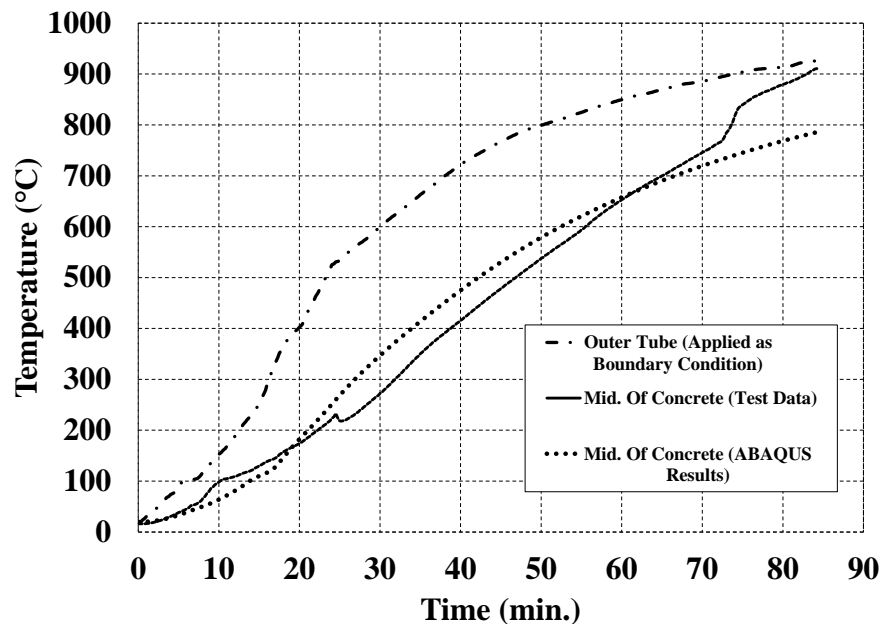


Figure 6- 17 Analysis results for the temperature time-history for a point in mid-width of the concrete core of specimen S3 (compared with test results)

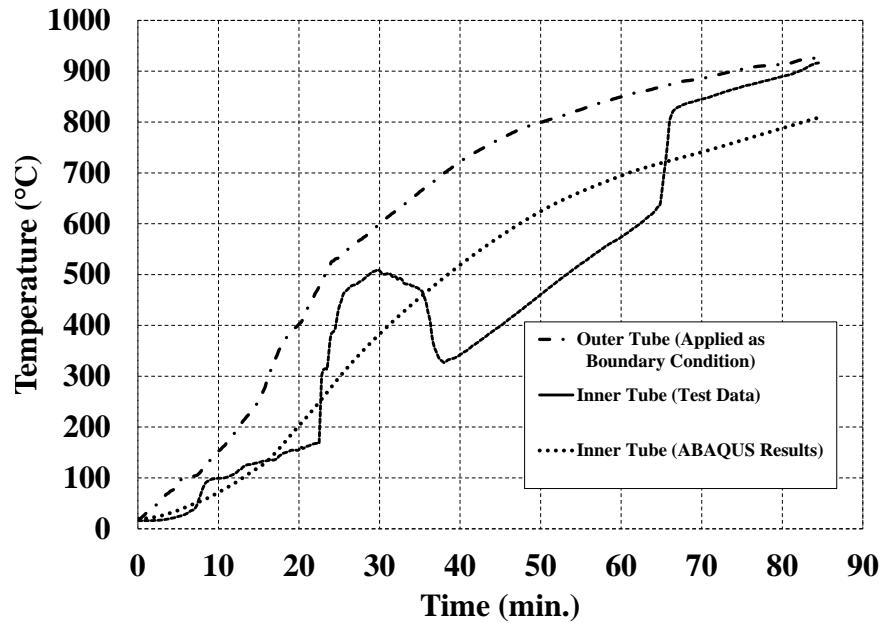


Figure 6- 18 Analysis results of the temperature time-history for a point on the inner tube of specimen S3 (compared with test results)

Note that the fluctuations in temperature values recorded by the thermocouples (especially on the inner tube) do not appear in the numerical results. Analytically, since the temperature values for the concrete and the inner tube increase over time because of the gradual transfer of thermal energy through the defined heat transfer mechanisms over homogenously defined materials, a smooth increase in temperature values is expected. However, no specific mechanism was modeled to replicate the recorded fluctuations that are suspected to be due to localized changes in pressures inside the tube (pressure build-up and release around concrete aggregates), which can create non-linear paths for the heat and alter the trend of temperature distribution. This may also result in non-linear travel of water vapor to the specimen's release holes, and allow temperatures of the inner tube to fluctuate and reach temperature values exceeding that of the concrete part for short periods during the fire test.

Another difference seen between the numerical results and the experimental recordings occurs during the last 15 minutes of the fire test. The experimental data show that temperature of both the inner tube and the concrete increase more rapidly (to reach the temperature of the outer tube) in the last quarter hour of the test, while the analysis results indicate temperature increasing at the same rate throughout the test and maintaining a proportional difference with the temperature of the outer tube until the end of the test. The sharp increase in the temperature values of the thermocouples in the concrete core and on the inner tube

seems to have occurred because of the excessive deformations during the final minutes of the test, which have probably opened a path for the heat to reach both of the mentioned thermocouples, increasing their temperature values up to that of the outer tube.

6.3.2.2 Stress/deformation Analysis of Specimen S3

The finite element model used for the heat transfer analysis of Specimen S3 was modified for the stress/deformation analysis, while keeping the geometric features (specifically the mesh size) fixed. The element types (which were 8-node heat transfer elements) were changed to 8-node 3D stress solid elements (C3D8R) for both the steel and concrete parts. Note that the mesh size was defined considering both heat transfer and stress/deformation analyses (e.g. Fig. 6.15 shows that a smaller mesh size was selected for the top end of the column, where local buckling of the outer tube was expected to occur). A Static General analysis was defined with two steps: first, applying the axial load and maintaining it for the rest of the analysis, and second, simulating the fire test by applying the results of the heat transfer analysis (time-history of temperature distribution during the fire exposure for all of the nodes) to the model.

Temperature dependent thermal and structural properties of steel and concrete materials were adopted from the specifications in the Eurocode (CEN 2005). These properties were presented in Section 3. The analysis was defined to account for geometric nonlinearities to capture the probable buckling in the model. An initial imperfection consisting of the first buckling mode shape of the column (global buckling) with a displacement amplitude of $L/1000$ was imposed on the model to duly trigger global buckling when the degradation in material properties reach the critical level. Note that as discussed in Section 3, no initial imperfection was imposed on the model to initiate local buckling, since the model was shown to be capable of triggering local buckling based on the conditions that are imposed to the elements throughout the analysis (e.g. boundary conditions, constraints, high plastic strains).

In terms of boundary conditions, the top plate of the column was defined to be fixed. The bottom end was free to move in the axial direction and rotate in the weak direction (one of the directions had more flexural strength because of the added channels). Note that the bottom end connection in the test furnace was not completely free to rotate (due to its partial rigidity). An attempt to simulate the effects of the partially fixed connection at the bottom end of the furnace, which had unknown properties, was contemplated, but not done because it was considered that the additional analysis complexities were not necessary to be able to interpret the results in the current context. Modeling with a pinned end results in a reduction of the critical buckling load, thus slightly reducing the fire resistance, and allows for slightly larger rotations as opposed

to the experimental results. These changes are considered in the interpretation of the simulation results throughout the rest of this section. The axial loads consisted of the 71 kips external gravity load that was applied as a pressure to the bottom plate of the column and the weight of the concrete core, which was applied as a force pushing the concrete part towards the bottom plate.

Fig. 6.19 shows the ABAQUS analysis results for the axial displacement time-history of the bottom plate of the column (equivalent to the axial extension or contraction of the column) for Specimen S3 during its exposure to the ASTM E119 fire. Results from the finite element analysis are plotted along with the two curves recorded by manual gauges (which were placed at the north and south sides of the furnace bottom beam) and their calculated average. Numerical results follow the same four-stage pattern explained in Section 5 for the fire tests conducted in this study (consisting of: expansion of the outer tube; local buckling of the outer tube; expansion of the whole column, or maintaining the axial displacement; global buckling).

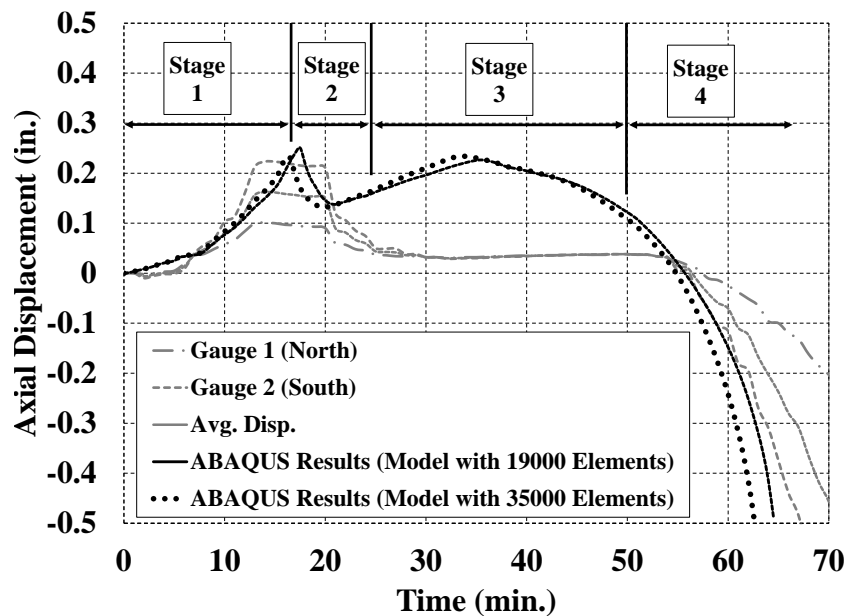


**Figure 6- 19 Analysis results of the axial displacement of the bottom plate of specimen S3
(compared with test results)**

Fig. 6.19 shows that experimental and numerical results are in good agreement in terms of the maximum axial displacement and the total fire resisting time (about 60 minutes). A noticeable difference between the test and analysis results is the trend in the increase and decrease of the axial displacement, especially during Stage 2 while the outer tube expands and contracts. The sudden drop in the total axial displacement values due to the local buckling of the outer tube was more severe in the tested column compared to the finite

element model. The analysis captures the local buckling at the right place and time, but the elements go through a slightly less severe buckling deformation compared to the test results. Also in Stage 3, when the steel tubes and concrete core are sustaining the axial load together (after a short period during which the whole load was on the outer steel tube), the simulation results show more expansion than the test results, in which the tubes and concrete had only a slight expansion and maintained the same level of axial displacement until the last stage of the test. The second phase of expansion, seen in the numerical results, is considered to be logical because the temperature continues to rise and even though further expansion of the outer tube may only contribute to making the local buckling more severe, there is no mechanism to prevent the concrete core from expanding. Considering the fact that displacement measurements during the tests were based on the manual readings from two mechanical gauges (and the limited instrumentation used during the experiment), the match between the recorded values and numerical simulation results was deemed to be sufficiently accurate for the purposes of this study.

An additional analysis was conducted on a similar model with a refined mesh size in order to check mesh-sensitivity issue. Results shown in Fig. 6.19 verify the convergence of the finite element analysis for the initial mesh size. The simulation results could be improved to provide a better match to the experiment by calibrating a few modeling parameters (e.g. the temperature dependent coefficient of thermal expansion for both steel and concrete materials) in a way similar to the case discussed in Section 3. Nevertheless, since the model was shown to be capable of simulating the four stages defined for the experimental results and provided an acceptable prediction of the fire resisting time, it was considered sufficiently accurate for the purposes of this project.

Fig. 6.20 compares the final state of the numerical model after the termination of the analysis due to the global buckling of the column, with a photo taken at the end of the fire testing of Specimen S3. Note that global buckling was triggered by the initial imperfection in the numerical model, but the column could not go through large buckling deformations because the analysis was defined as a force-controlled process during that step. The constant axial load was applied to the column at the beginning of the analysis and maintained during the fire simulation. As the column reached the point when it could no longer sustain the axial load, the force-controlled analysis terminated.



(a)



(b)

Figure 6- 20 Final deformed shape of specimen S3 from: a) finite element analysis (ABAQUS) in the force-controlled mode and b) experimental results

As shown in Fig. 6.19, despite being incapable of simulating the post-buckling phase of the test (after the initiation of global buckling), the analysis was able to replicate the axial displacement of the moving end-plate of the column, which was the main issue in the prediction of the fire resisting time. However, to study the behavior of the numerical model in the post-buckling phase, an additional analysis was conducted on the same column in two steps: first, the model of Specimen S3 was subjected to the same fire curve up to the point that the global buckling was initiated in the previous analysis (about 65 min. after the start of the test, when the column could no longer sustain the load); Second, the moving (bottom) end-plate was pushed to apply compressive load to the column in a displacement-controlled mode, allowing it to go through large buckling deformations.

Fig. 6.21 shows the buckled shape of Specimen S3. The analysis was able to simulate the global buckling in the displacement-controlled mode. Recall that the bottom end of the column was modeled as a pinned-pinned connection (as opposed to the semi-rigid connection in the test setup) and shows a larger rotation compared to the experimental results (Fig. 6.20b). Fig. 6.22 shows the axial force versus axial displacement of the moving (bottom) end-plate of the column obtained when performing the above displacement-controlled analysis after the column was exposed to the first 50, 65, and 80 minutes of the standard ASTM E119 fire curve. The case with the 65 min. fire exposure buckled under an axial load of 69 kips, which is close to the 71 kips load applied during the experiment. Note that for longer periods of fire exposure, the column buckles under lower axial load levels.

Fig. 6.20 also shows the local buckling of the outer tube close to the top end of the column for Specimen S3 (from both test and analysis). Results indicated that applying the weight of the concrete as a constant force pushing it towards the bottom plate was effective in keeping the bottom end surface of the concrete core in contact with the bottom plate throughout the analysis. Considering this configuration, the expansion of the outer tube could only cause the separation of the top end surface of the concrete core from the top plate of the column. This forced the local buckling to occur only at the top end of the specimen, similarly to what occurred in the test. Note that based on calculations, the weight of the concrete core was enough to overcome the friction resistance between the steel tubes and concrete core.

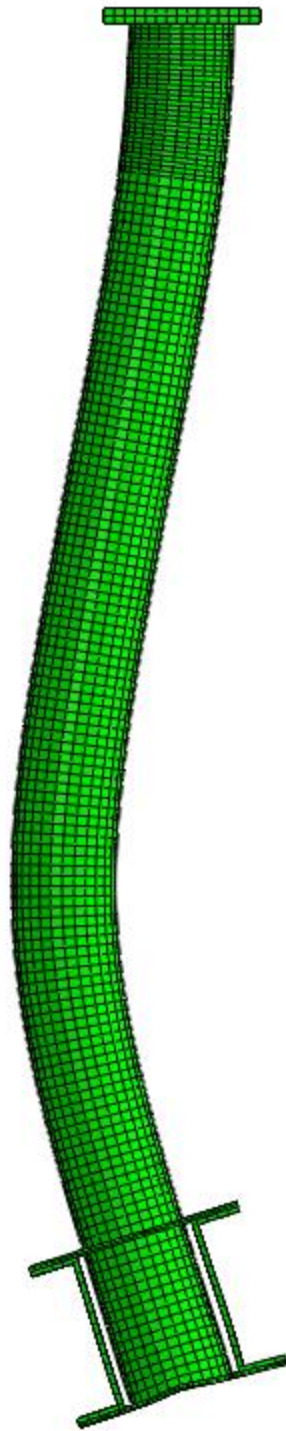


Figure 6- 21 Global buckling of specimen S3 from the displacement-controlled ABAQUS analysis

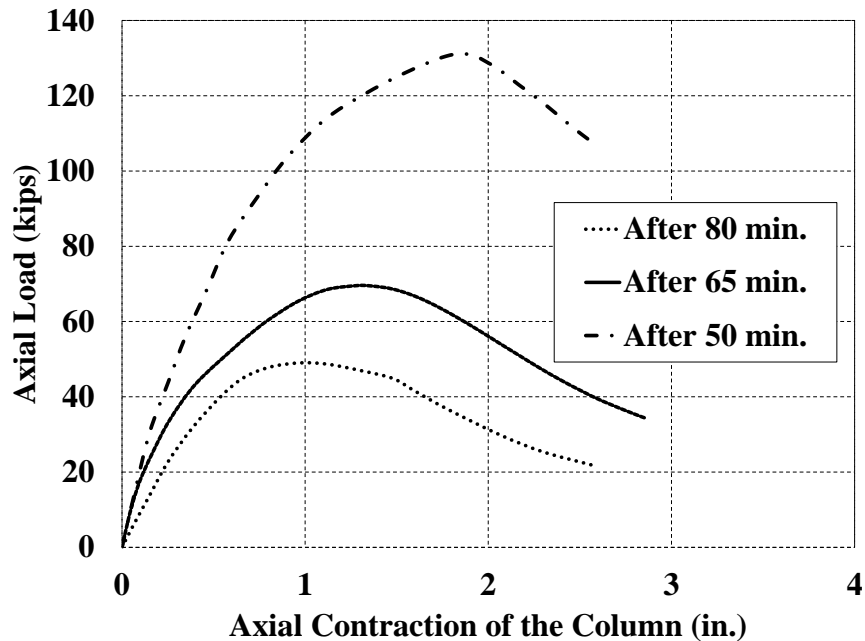


Figure 6- 22 Axial load versus axial contraction results from the displacement controlled analysis of specimen S3 after being exposed to different durations of the standard ASTM E119 fire

Fig. 6.23 provides a closer view of the locally buckled region. It shows that, during the test, local buckling of the outer tube occurs at a lower position than predicted by the simulation results. This difference may be due to the fact that the top steel plate of the column was anchored into the concrete using four ½” threaded rods (16” long) during construction. Note that no threaded rods were used at the bottom end of the column. Cutting open the steel outer tube after the tests revealed that a short segment of concrete (about 8” long) remained tied to the top plate. This indicates that the top end surface of the concrete core did not lose its contact with the top plate of the column. Fig. 6.23c shows the locally damaged end of the column where the outer steel tube was cut to expose the concrete core. A thin crack line is seen in this figure on the concrete surface (and in a closer view in Fig. 6.23d) at the same location where local buckling of the outer tube occurred. It is inferred that while the top end of the concrete core was tied to the steel top plate, the outer steel lost its contact with the concrete core at the location of the mentioned crack line (shown in Fig. 6.23d), leading to the outward buckling of the outer tube around the same location under the applied load and temperature. After the initiation of local buckling, further thermal expansion amplified the amplitude of the local buckle. In the numerical simulation, the threaded rods were not modeled, which may explain why, in that case, the separation occurs at the interface of the top end of the concrete and the top plate. Models including the threaded rods were not attempted, as this slight difference in local buckling location was deemed to be of no significance on the specimen behavior.

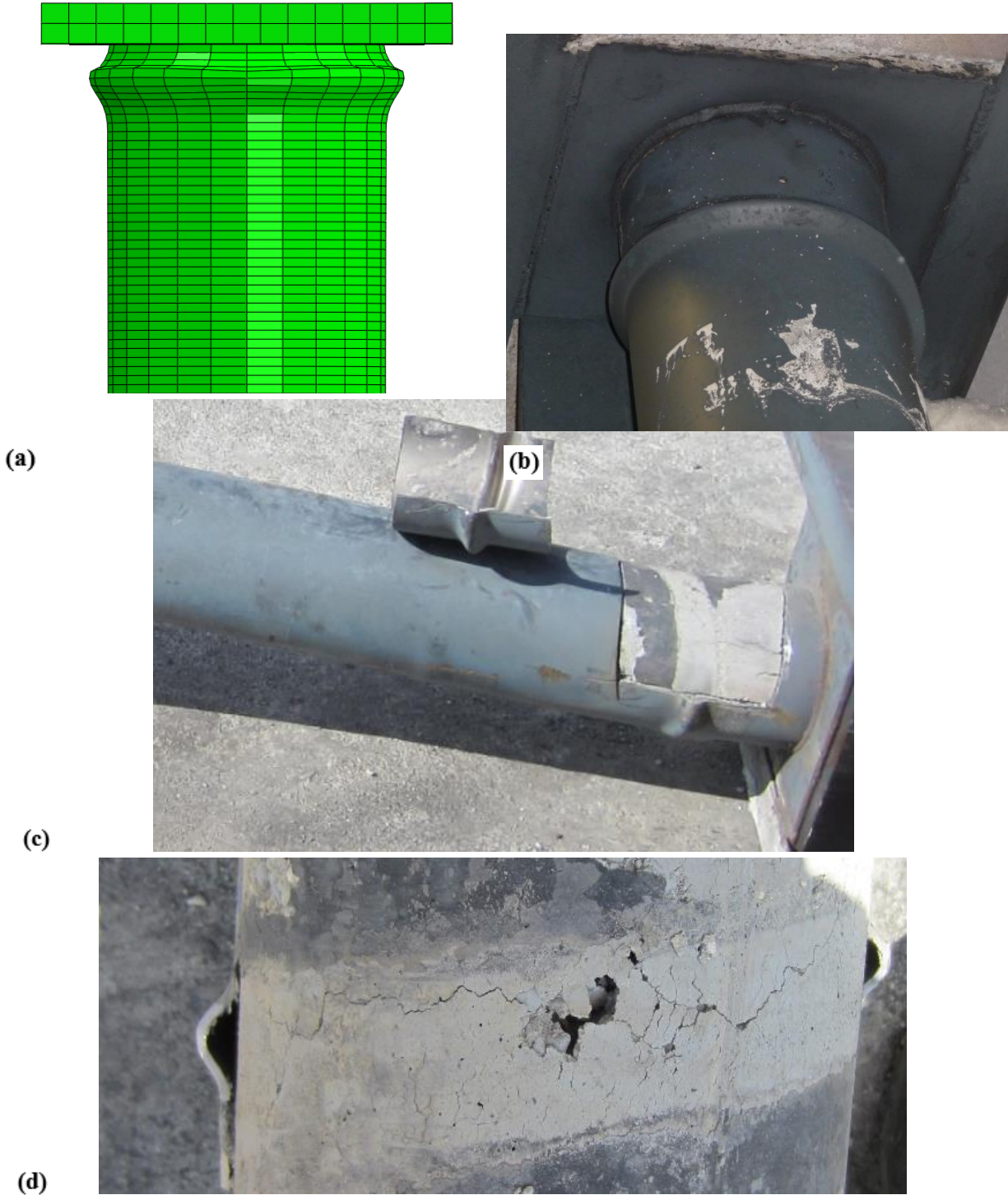


Figure 6- 23 Local buckling of the top end of the outer tube from: a) finite element analysis (ABAQUS) and b,c,d) test results o Specimen S3

6.3.3 Fire Testing of the Moderately Damaged Specimen (S1)

6.3.3.1 Heat Transfer Analysis of Specimen S1

The same model (built for Specimen S3) was used to conduct the heat transfer analysis of Specimen S1. The boundary condition defined for the surface of the outer tube was modified to follow the recorded time-history of the temperature for the exposed surface of Specimen S1 during the second fire test. Figures 6.24 and 6.25 show the results of the recorded time-history of temperature from the thermocouples installed in the middle of the concrete layer and on the outer surface of the inner tube, along with the results from heat transfer analysis for nodes at the corresponding locations. The temperature time-history of the outer tube (applied as a boundary condition to the model) is also included in both figures for comparison purposes. The figures indicate that numerical analysis provided acceptable predictions of the time-history of temperature at both of the selected locations. Note that similarly to Specimen S3, fluctuations in the time-history of temperature values recorded by the thermocouples do not appear in the numerical results (again, no particular mechanism was defined in the model to capture this kind of irregular behavior).

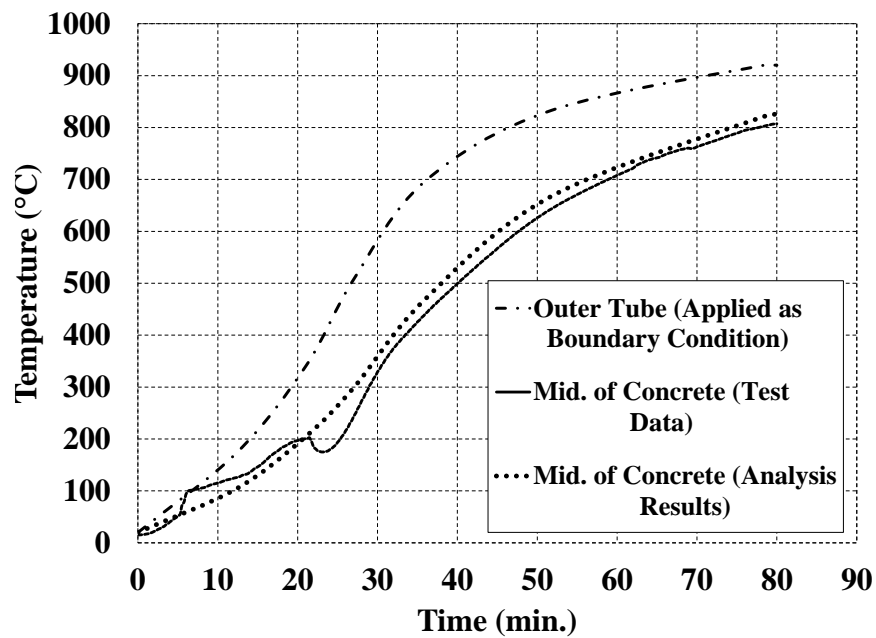


Figure 6- 24 Analysis results of the temperature time-history for a point in mid-width of the concrete core of specimen S1 (compared with test results)

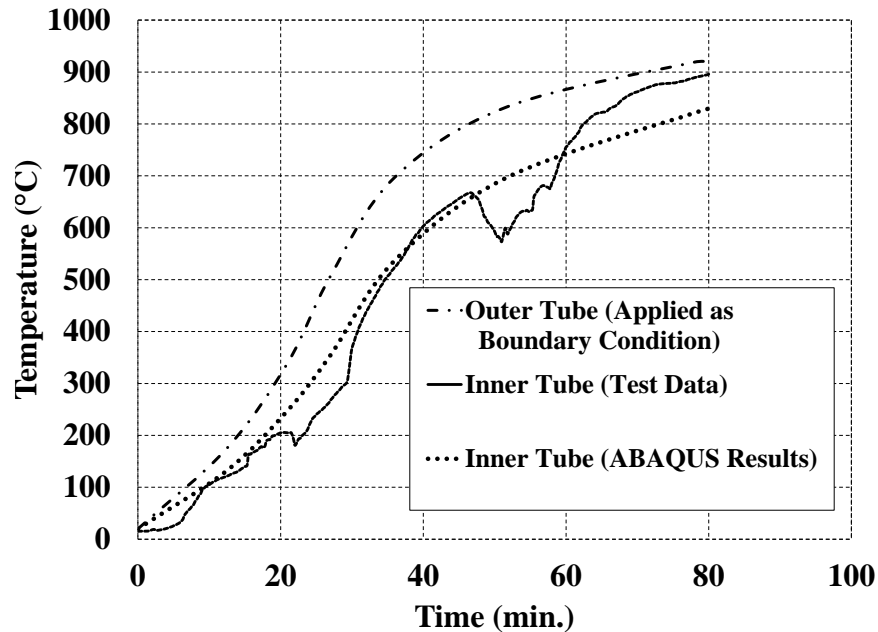


Figure 6- 25 Analysis results of the temperature time-history for a point on the inner tube of specimen S1 (compared with test results)

6.3.3.2 Stress/deformation Analysis of Specimen S1

The finite element model of Specimen S1 was subjected to the 2-step thermal stress analysis (force-controlled axial loading and fire simulation) with an initial imperfection that was created by cyclic lateral loading (ending with a 1.4% residual drift), to simulate the scenario that had occurred for the fire testing of the moderately damaged specimen. The applied initial condition consisted of a stress-free model which had only the residual deformations of the cyclic loading from the previous analysis. Note that although there likely were residual stresses in internal equilibrium in the specimen before the start of the fire test, those were ignored to avoid complexities at this stage of simulations for the moderately damaged specimen. A more sophisticated approach will be used for the highly damaged column.

Fig. 6.26 shows the time-history of axial displacement for Specimen S1 obtained from the ABAQUS analysis, along with the experimental results (corresponding to measurements from the north and south gauges, and their average). Analysis results are in good agreement with test data in terms of the general pattern (following the 4-stage process), the axial peak displacement, and the fire resisting time. Note that the analysis predicted a fire resistance time that was slightly shorter than recorded during the test. Considering that the final failure of the column is controlled by global buckling, modeling the connection of the column to the bottom beam as a pinned end in the out-of-plane direction (as opposed to the partially

fixed condition observed in the test) might have played a role in the prediction of a shorter resistance time by the analysis.

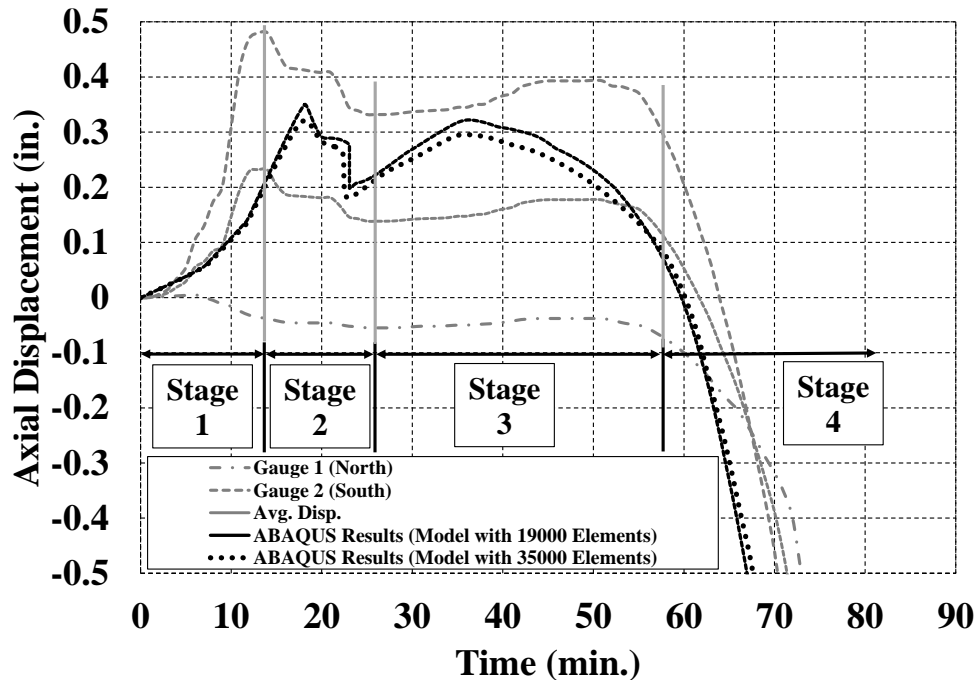


Figure 6- 26 Analysis results of the axial displacement of the bottom plate of specimen S1 (compared with test results)

Fig. 6.26 also shows an additional curve derived from an analysis on a similar model with a refined mesh size, which was conducted to check the mesh-sensitivity of the results. The marginal difference between the curves indicates the convergence of the finite element analysis results. Fig. 6.27 shows the resulting deformed shape of the Specimen S1 model, which includes the initiation of global buckling of the column, local buckling of the outer tube at the top end (caused by the fire test) and local buckling of the outer tube at the bottom end (cause by cyclic loading of the column). Simulation results are in good agreement with photos from experiment. Note that similarly to Fig. 6.20 of Specimen S3, Fig. 6.27 merely shows the initiation of the global buckling for Specimen S1, because the force-controlled analysis could not continue to larger deformations. Repetition of the deformation-controlled buckling analysis conducted for Specimen S3 (Figures. 6.21 and 6.22) was considered to be unnecessary, since global buckling of Specimen S1 occurred under the same load and approximately at the same time (60-65 min.) as those of Specimen S3. Local buckling at the top end of the column occurs at a lower height for the test (compared to the numerical simulation) for the same reason mentioned above for Specimen S3.

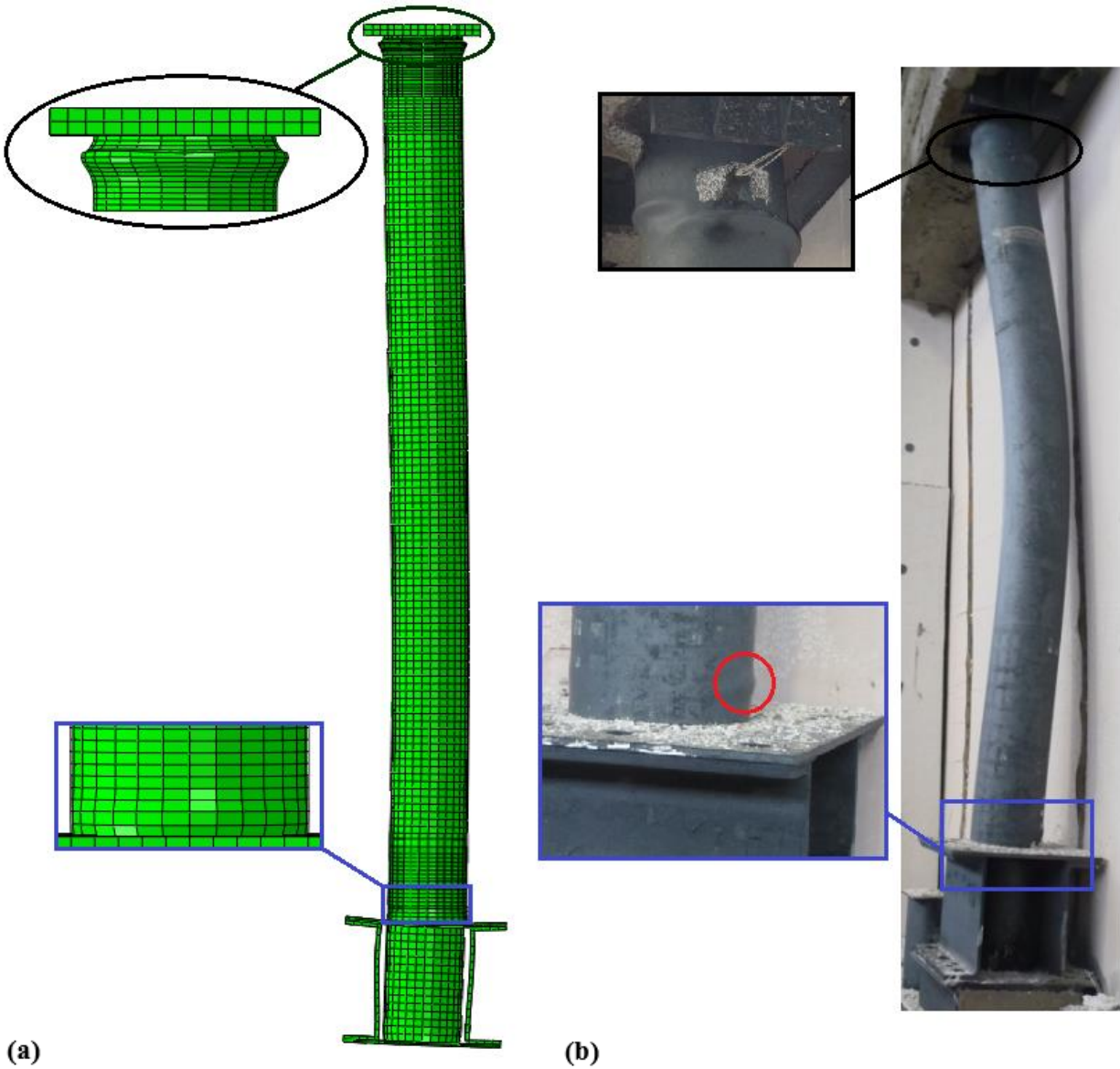


Figure 6- 27 Final deformed shape of specimen S1 from: a) finite element analysis (ABAQUS) and b) experimental results

6.3.4 Fire Testing of the Highly Damaged Specimen (S2)

6.3.4.1 Modification of the Finite Element Model

Considering the higher severity of seismic damage in Specimen S2 prior to the fire test, and in an attempt to better simulate the effects of the cyclic loading history on the performance of S2 under fire, the finite element model for this specimen was modified as follows. To include all the effects of the cyclic loading

history (e.g. residual stresses, strains, deformation, degradations, etc.), an additional analysis step was added to the thermal-stress problem. Note that this configuration was significantly more computationally expensive than the case for the moderately damaged specimen (S2), where the axial loading and fire simulation parts were started after just imposing the stress-free final resulting deformations (from a previously conducted cyclic loading analysis) as initial imperfection to the finite element model.

In order to reduce computational difficulties, the built-up box section was removed from the finite element model, reducing it to the configuration that was used in the simulation of cyclic loading tests in Section 3.2. Flexibility of the base was accounted for using an additional base plate connected by the Bolt Load option in ABAQUS as presented in the same section. The model was also enhanced by inserting a horizontal discrete crack into the concrete core just above the bottom plate of the column (the FE-CDP-DS model was used). The mesh size was refined at the bottom end to better capture the expected local buckling of the outer tube caused by both cyclic and fire loading (results from the simulations conducted on specimens S3 and S1 and their mesh-sensitivity analyses were used as guidance in the mesh size selection for the Specimen S2 model).

Two separate models, using the same geometry and mesh size but different element types, were built for the heat transfer and stress/deformation analyses. To better replicate the effects of the cyclic loading part, the element type for the steel tube sections were changed from 8-node solid, C38DR (as it was for the fire test simulations of specimens S3 and S1), to 4-node shell elements, S4R. Note that although the solid element was shown to provide reasonably accurate results for the fire testing simulations of specimens S3 and S1, the shell element was preferred here for Specimen S2 because of the importance of the cyclic loading history in the approach taken here, and because of the shell element's ability to provide sufficiently accurate replications of local buckling (and subsequent strength and stiffness degradation), as shown in the simulation of the cyclic tests presented in Section 6.2. As such, the finalized model looked the same as the one built for the cyclic testing simulations (Fig. 6.3).

6.3.4.2 Heat Transfer Analysis of Specimen S2

Figures 6.28 and 6.29 show the results from the heat transfer analysis of Specimen S2, conducted by applying the measured temperature time-history of the outer tube as a boundary condition, for nodes in the middle of the concrete part and on the inner tube along with the measured data at the corresponding locations. Analysis results are relatively accurate for both locations. Temperature records from the fire

testing of Specimen S2 show less fluctuations compared to the past two tests, thus making a better match with the smooth numerical results.

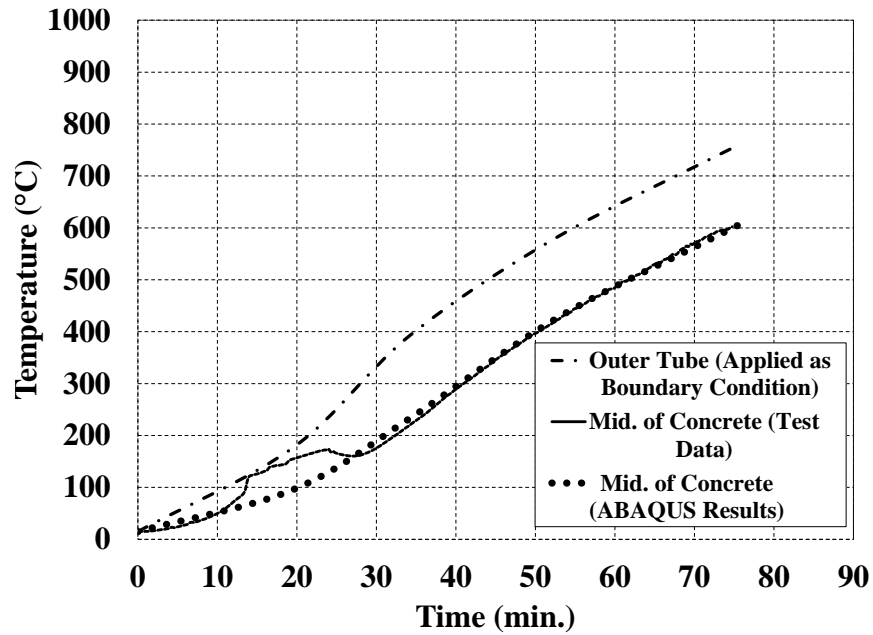


Figure 6- 28 Analysis results for the temperature time-history of a point at mid-width of the concrete core of specimen S3 (compared with test results)

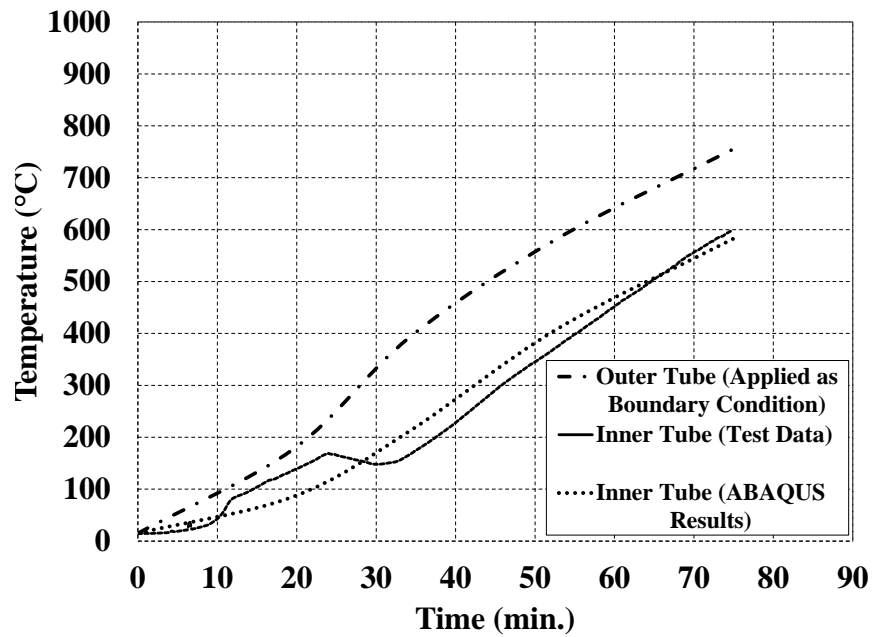


Figure 6- 29 Analysis results for the temperature time-history of a point on the inner tube of specimen S3 (compared with test results)

6.3.4.3 Stress/deformation Analysis of Specimen S2

To keep the multi-step finite element analysis computationally efficient, the cyclic loading step applied only a few displacement cycles (not the full protocol used in the test). The applied displacement cycles were selected to include a few of the drift ratio amplitudes identified in the test protocol, namely cycles at drift ratios of about 3.5%, 5% and the maximum recorded value of 6.2%. Each of these cycles was applied once to create the local buckling effect at the bottom end of the column. An additional cycle at a drift ratio of 6% was applied to the model in the end, making it possible to unload while keeping a residual drift close to the value recorded in the test (3.9%).

The output from the above cyclic analysis was then subjected to a 2-step thermal stress analysis (axial loading and fire test) to simulate the effects of the ASTM E119 fire on the highly damaged specimen. To replicate the test conditions, a fixed boundary condition was imposed at the end of the column close to the locally buckled side, and a pin boundary condition able to translate vertically was modeled at the other end, leaving it free to move in the axial direction and rotate in the direction in which cyclic loading had been applied to the column in the previous step.

Fig. 6.30 shows the time-history of axial displacement for the moving end plate of Specimen S2 (equivalent to the extension and contraction of the column). The numerical model was found to give reasonable predictions of both maximum axial displacement and fire resisting time for the specimen. Note that similarly to the results for specimens S3 and S1, the numerical simulation showed a relatively longer expansion period for the outer tube. In terms of the stages defined for the variation of axial displacement versus time, the analysis results seem to more closely match the experimental ones than was the case for the previous specimens, as the sharp expansion and drop from the curve typically corresponding to stage 2 was not observed in Specimen S2 (contrary to the previous specimens).

Fig. 6.31 shows the damaged end of the column (caused by cyclic loading) before and after the fire test from both analysis and experimental results. Results show that the analysis successfully simulated the effects of fire testing on increasing the severity of the local buckling, which had been initiated in the cyclic loading step and deliberately positioned at the top end of the furnace in an attempt to combine the damaging effects of seismic and fire loads.

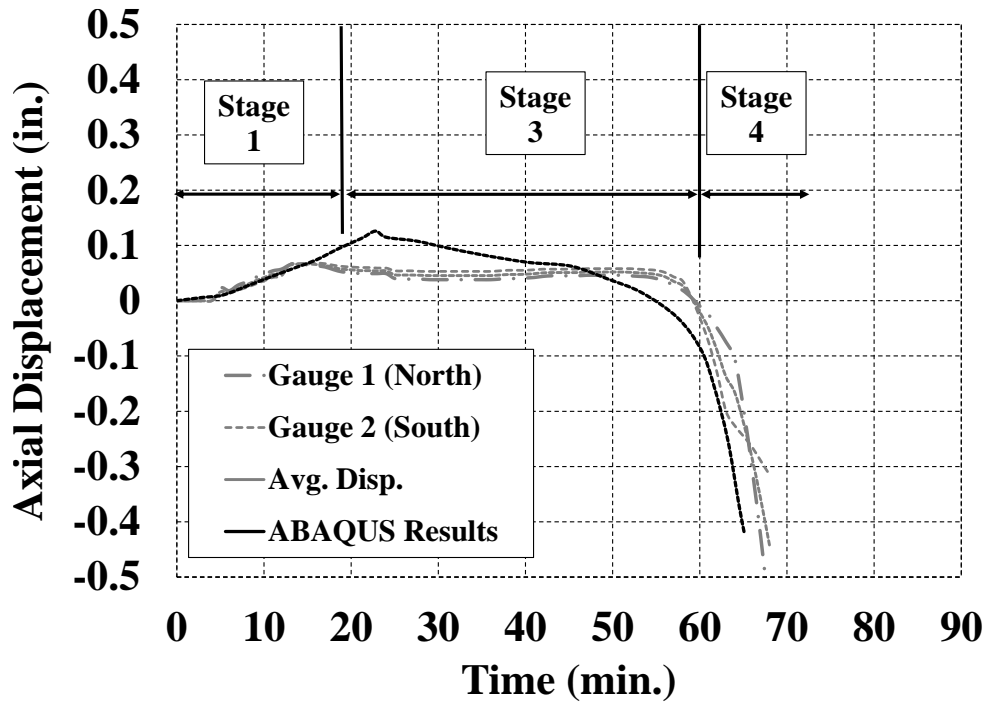


Figure 6- 30 Analysis results of the axial displacement of the bottom plate of specimen S2 (compared with test results)

6.3.5 Fully Coupled Approach versus Sequentially Coupled Approach

Even though the acceptable performance of the sequentially coupled analysis was demonstrated by other researchers (as mentioned in Section 3.4.1), and even though results presented in past sections have shown that the sequentially coupled analysis was adequate to replicate the experimental results obtained as part of the current research, an additional fire simulation analysis was conducted using the fully coupled method to investigate the significance of possible differences between the results of the two methods. Results from the fully coupled analysis, which is presented in detail in Appendix C, did not demonstrate a meaningful difference compared to the ones from the sequentially coupled analyses. It was inferred that for the problem at hand (i.e. behavior of CFDST columns with capped top and bottom ends subjected to axial loading and fire), the sequentially coupled approach was capable of replicating the experimental results with sufficient accuracy.

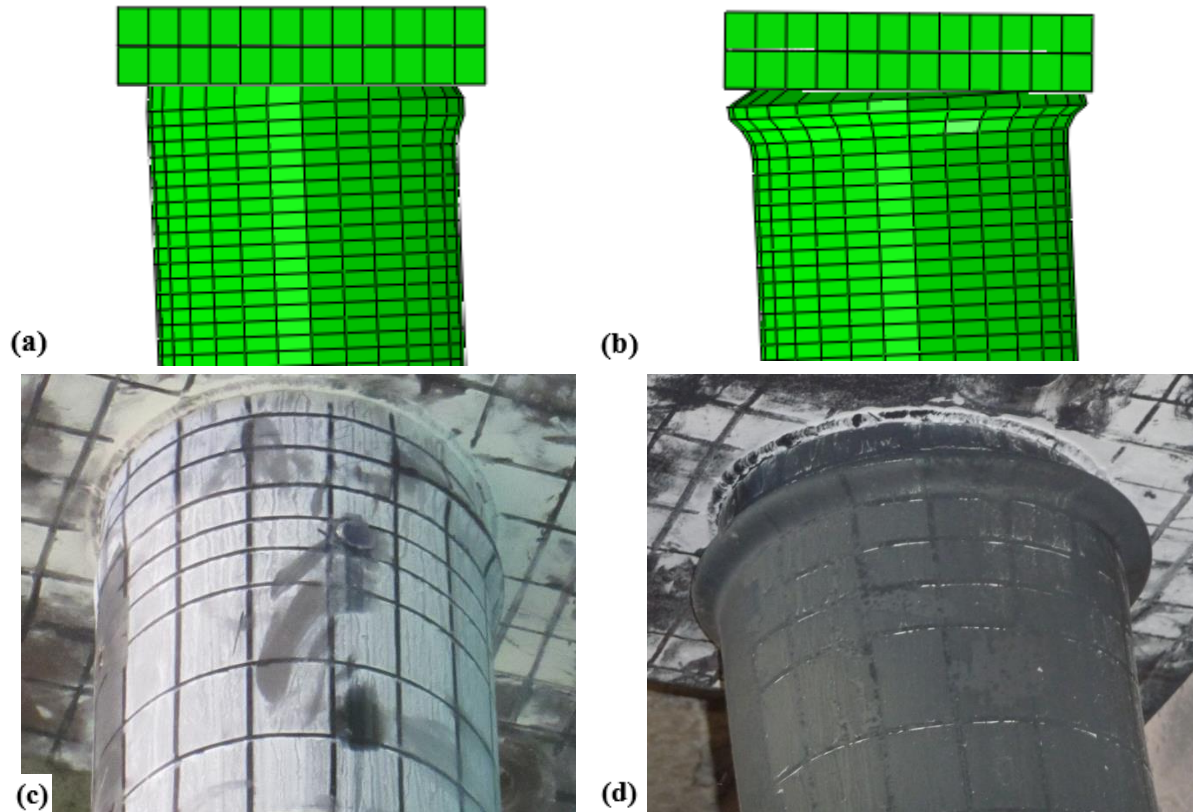


Figure 6- 31 Local buckling of specimen S2 before and after fire testing: a) ABAQUS result before fire test b) ABAQUS result after fire test c) photo of the highly damaged specimen (S2) before fire test d) photo of the highly damaged specimen after fire test

6.4 Simulation of the Post-Fire Cyclic Test

The numerical models built for simulation of the cyclic loading tests were further examined in an attempt to replicate the post-fire cyclic testing of Specimen S3. Note that the first two cyclic loading tests were conducted to impose a limited amount of damage to specimens S1 and S2, thus avoiding large deformations and subsequent fractures. Simulating the post-fire cyclic testing of Specimen S3, which continued until fracture of the outer steel tube and an approximate lateral force resistance decrease of 50%, was used as an additional step in the validation of the finite element models.

Both of the FE-CDP-DS and LS-DYNA models were modified to comply with the conditions of the post-fire cyclic loading test. Since the test was continued up to the fracture of the outer tube, going through severe pinching in hysteretic curves and concrete cracking, the models from both finite element analysis

programs were used in the simulation process to investigate their ability to follow hysteretic behavior up to the large measured displacements.

Material properties for steel and concrete were changed to account for their possible variation during the fire test. Tensile tests were conducted on coupons extracted from the outer tube of Specimen S3 (after test) to measure the post-fire yield and tensile strength of the steel material. The tests showed a 5% decrease in strength compared to the average values measured from the coupons prepared before the construction. According to the Eurocode general rules for structural fire design (CEN 2005), reaching the temperature of 800°C and cooling down to the ambient temperature of 20°C could cause a 10% permanent decrease in the yield and tensile strength of the steel material (although these are values recommended for design, and possibly conservative). Since actual measured values were obtained here, the 5% reduction was applied to the original strength values mentioned in Section 6.2.1 for both the inner and outer tubes and used in the modified finite element models.

The Eurocode also specifies an 85% permanent reduction in the compressive strength of concrete after going through a similar temperature increase history. A compression test conducted on a single concrete cylinder, which was burned in a similar fire test, showed almost no compressive strength. The burned cylinder had a visible crack at one end after the completion of the fire test for unknown reasons. Since the result of a single compression test could not be relied on, the 85% reduction specified in the Eurocode was applied to the finite element models to simulate the effect of the fire test on concrete compression strength.

Steel was modeled using a bilinear elastic-plastic behavior with linear kinematic hardening in both of the FE-CDP-DS and FE-W models. Note that similar to the previous cases, no softening branch was modeled for the steel material at this stage. This made the models capable of capturing the degradations and softening due to the geometric nonlinearities (e.g. local buckling) and large deformations, but not the ones caused by fracture. The concrete material was modeled using the Damaged Plasticity model plus the insertion of a horizontal discrete crack at the lower end of the column in the ABAQUS analysis, while the Winfrith model was used in the analysis conducted using LS-DYNA.

Fig. 6.32 shows the lateral force versus drift ratio results obtained from the FE-CDP-DS and FE-W models, along with the experimental curves from the post-fire cyclic testing of Specimen S3. Observation of the results from the FE-CDP-DS model (Fig. 6.32a) suggests that the model successfully captured the concrete tensile crack opening and closing, which led to the softening of the column stiffness when it went past the zero drift position. The model captured the increase in stiffness and lateral force resisting strength, seen in

the experimental results when the column reached the extreme left or right displacements during an inelastic cycle (i.e., when the buckled tube was straightened and started to work in tension again).

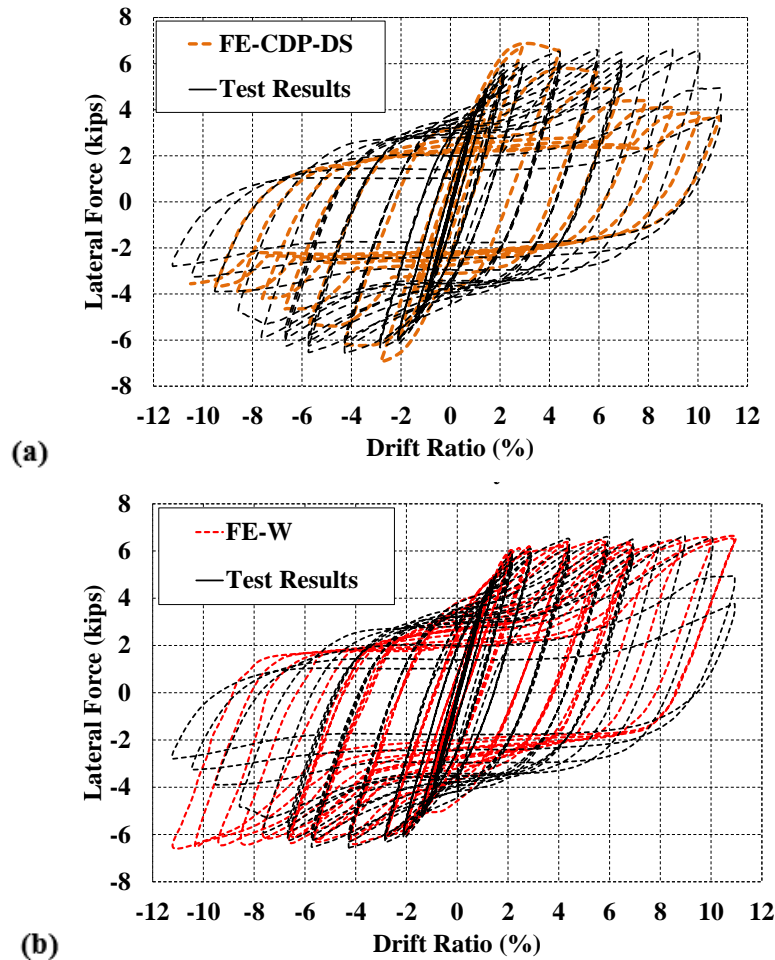


Figure 6- 32 Lateral force vs. drift ratio results from the finite element analyses of post-fire cyclic loading of specimen S3 from: a) FE-CDP-DS model and b) FE-W model (compared with experimental results)

As the column went through cycles with larger displacement amplitudes (above 5% drift), large deformations in the shell elements used for the modeling of the steel tubes lead to continuous strength degradation in the results from the FE-CDP-DS model, a behavior that was not seen in the experimental hysteresis curves (the lateral force increased to the same maximum value at the maximum displacement of each cycle, until the first fracture occurred on one side of the column). Even though the steel tube went through sequential buckling and straightening phases, both in the test and simulation, the straightening

(recovery) phase was less effective in the in the FE-CDP-DS model, leading to a continuous strength degradation in the results.

On the other hand, analysis on the FE-W model provided a better match of the experimental hysteresis curves (Fig. 6.32b). The model captured the softening and strength degradation when the column went through continuous cycles at a certain displacement amplitude (e.g., 4.4%, 6%, and 7% drift), and recovered the maximum lateral force resistance of 6.5 kips upon going to the next cycle at a higher displacement amplitude. Results from the FE-W model almost exactly followed the experimental curves until the point when first fracture occurred on one side of the outer steel tube, which resulted in a sharp strength degradation in the test results (that was not modeled analytically).

The above discrepancy in the results after fracture of the specimen was deemed acceptable, and understood to be a consequence of not introducing a damage criteria in the steel material (i.e., nothing was defined after the strain hardening branch). The definition of cyclic damage initiation and evolution for the steel material was considered to be beyond the scope of this study. However, short of a rigorous damage progression and fracture analysis, in an attempt to enhance the match in that region of the hysteretic curve, an additional analysis was conducted using an arbitrary fracture limit for the accumulative effective plastic strain parameter (defined for the Plastic Kinematic material in LS-DYNA), calibrated to initiate element deletion in the steel tube at a certain point that would result in the best fit with the test results.

Fig. 6.33 shows the results from the modified FE-W model. The fracture (element deletion) started during the cycle at 7% drift ratio, in the reverse loading direction (with respect to the first loading direction), causing a strength degradation that followed the experimental results with acceptable accuracy. Note that this result is based on an arbitrary chosen fracture limit, which was tailored to the specific test conducted here. More sophisticated cyclic damage models are needed to rigorously capture the fracture initiation and evolution in steel, based on a set of measured properties.

6.5 Summary

Finite element models originally built for CFDST columns (in Section 3) using the general finite element software ABAQUS were re-used in attempts to analytically replicate the experimental results obtained for specimens S1, S2 and S3 under both cyclic and fire loads. Initial simulation of the cyclic lateral loading (using the FE-CDP models) provided acceptable predictions of the maximum lateral resisting force, but failed to capture the pinching phenomena observed in the hysteresis behavior of CFDST columns.

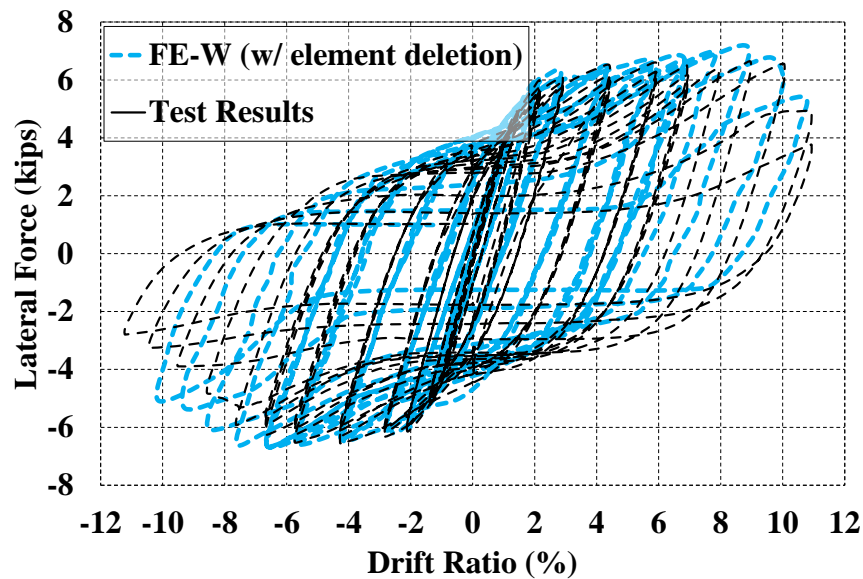


Figure 6- 33 Lateral force vs. drift ratio results from the simulation of the post-fire cyclic loading of specimen S3 (FE-W model with element deletion compared with experimental results)

Considering the short-comings of the Damaged Plasticity model (used in FE-CDP model) in simulating the formation of tensile cracks and the effects of their subsequent opening and closing in concrete structures, the model was modified by inserting a discrete horizontal crack at the location with the maximum tensile stress. The modified model (FE-CDP-DS) provided a much better replication of the experimental hysteresis curves, and underscored how results can be affected by different strategies adopted for modeling the behavior of concrete in tension when investigating inelastic cyclic behavior.

To further investigate the effects of concrete tensile cracking on the flexural behavior of CFDST columns, an additional finite element model was built using the software LS-DYNA and the Winfrith concrete model to account for tensile cracks and the effect of their opening and closing (referred to as the FE-W model). Simulation results showed significant improvements in replicating the experimentally obtained hysteretic results. To validate the models for tests with larger lateral displacements, both of the FE-CDP-DS and FE-W models were used for the simulation of the post-fire cyclic testing of Specimen S3. These results again showed the advantages of the FE-W model in reproducing strength degradation, with the FE-CDP-DS model being less effective in simulating the effects of consecutive cycles of buckling and straightening of the steel tube.

As for the fire testing simulation, the finite element models provided acceptable predictions of the total fire resistance time, and of the specimen deformations for different cases of fire tests conducted on damaged and undamaged specimens. The thermal and structural material properties adopted from the Eurocode general rules for structural fire design for steel and concrete (in both during and post-fire situations) were shown to be sufficiently accurate to be used for the numerical simulation of the behavior of CFDST columns under fire.

SECTION 7

SIMPLIFIED ANALYTICAL SOLUTION FOR FIRE RESISTANCE OF CFDST COLUMNS

7.1 General

When the fire resisting capability of a structural element is to be explicitly considered in the design process (i.e., to determine the minimum dimensions of an element to fulfill a certain fire resistance requirement), robust calculation methods that can provide an acceptable estimate of the fire resistance time in a simple but sufficiently accurate way are crucial. With respect to the performance of CFDST columns under fire conditions, several methods have been developed (based on both experimental and numerical studies) in an attempt to provide such a calculation of their fire resistance time.

Han et al. (2003) proposed an equation for the fire resisting time of unprotected CFDST columns based on regression analyses conducted on experimental results. Another method (more popular in North America) was provided by Kodur and MacKinnon (1998), which uses a single empirical equation to calculate the fire resistance of axially loaded CFDST columns.

Eurocode 4 provides three calculation methods for the design of CFDST columns under fire: a first approach relies on the use of tabulated data (limited for a few cases); the second and third ones are called to be simple and advanced calculation models, respectively (CEN 2005). Due to the limitations of the tabulated data, and the computationally demanding features of the advanced method (which requires the use of finite element models for simulation), the simple calculation method can be considered as the most practical option.

Although the Eurocode simplified method provides a step by step guide to calculate the fire resisting time by incrementally increasing the uniformly distributed strain of the section to satisfy the axial equilibrium using the material properties modified for elevated temperatures, it assumes that the designer knows the temperature distribution within the cross-section at any particular time during the fire exposure (no simplified method is given in the Eurocode for the calculation of the temperature field).

Espinos et al. (2012) proposed a method for calculating a uniform equivalent temperature for the whole concrete core (and similarly another one for the steel tube), which if used in the Eurocode method, will provide the same fire resisting time as the one obtained considering the actual non-uniform temperature

distribution. The uniform temperature value was conservatively determined to be the maximum of two values, which were calculated such as to produce the same plastic resistance and flexural stiffness for the cross-section as for the case with true non-uniform temperature distribution. After conducting fire resistance time analyses using this procedure for several different CFST columns, two equations were proposed, obtained from regression analyses, for calculating of the equivalent uniform temperature for the steel tube and concrete core, namely:

$$T_{s,eq} = 342.1 + 10.77R - 0.044R^2 + 3.922A_m/V - 0.025R A_m/V \quad (7.1)$$

$$T_{c,eq} = -186.44 + 5.764R - 0.026R^2 + 22.577A_m/V - 0.32(A_m/V)^2 + 0.14R A_m/V \quad (7.2)$$

In these equations, $T_{s,eq}$, $T_{c,eq}$ are the equivalent uniform temperature values for the steel and concrete sections, and A_m/V , which is defined as the section factor, is the ratio of the surface area of the steel tube to its volume. The expression for the section factor can be simplified to $4/D$, in which D is the outer diameter of the steel tube. The parameter R , in both equations, refers to the standard fire resistance class, which is given as 30, 60, 90, and 120 for standard resistance times of 30, 60, 90 and 120 minutes. Although Eqs. 7.1 and 7.2 were shown to provide acceptable results for CFST columns with different cross-sections, they were limited to the case of exposure to the standard ASTM E119 fire, and there were no CFDST columns in the database used to develop the regression analysis.

This section presents a simplified two-step procedure developed for the calculation of the fire resistance of the axially load CFDST columns. The first step provides an analytical based solution for the heat transfer problem, which calculates the temperature distribution for the CFDST column cross-section based on a given fire (time-temperature) curve. The second step uses selected results from the first step to calculate the design axial load capacity of the CFDST column at any particular time during the given time-temperature curve. Note that the procedure is defined for CFDST columns, but can also be used for the traditional CFST cases, with slight modifications.

7.2 Analytical Solution for the Heat Transfer Problem

7.2.1 General Solution for Heat Conduction Differential Equation

The objective of this section is to analytically solve the heat conduction partial differential equation for the cross-section of any given CFDST column. The cross-section is initially at room temperature, T_0 , and its

outer edge is subjected to a predetermined time-temperature curve, $f(t)$, where t is time. Fig. 7.1a shows the cross section of a CFDST column. Considering the relatively higher heat conductivity of steel compared to the concrete material (about 10 times larger), it is assumed that both the outer and inner tube sections have a uniform temperature distribution. Based on this assumption, the problem can be reduced to a single material model, that consists of a cylindrical concrete section, initially at room temperature, and subjected to a predetermined time-temperature curve, $f(t)$ (Fig. 7.1b).

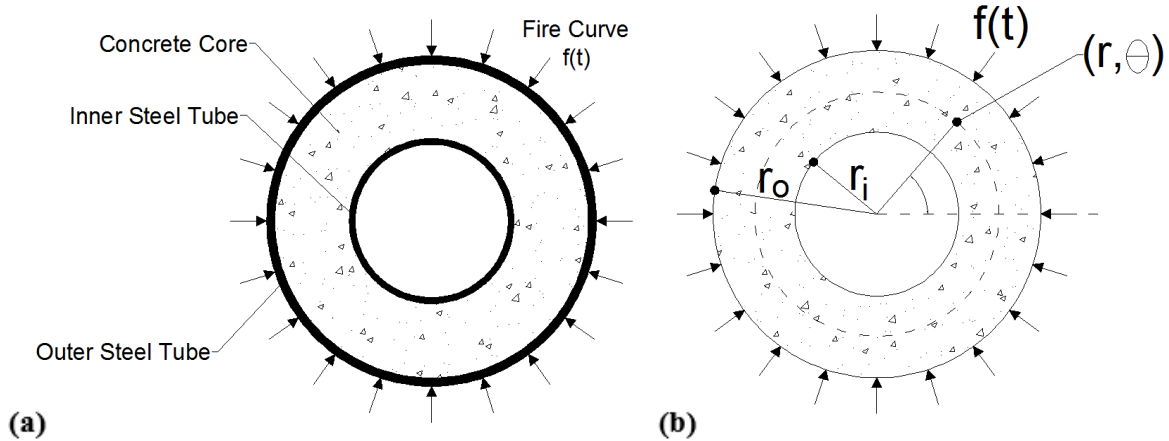


Figure 7- 1 Cross-section of a CFDST column for the heat transfer problem: a) with steel tubes and b) without steel tubes (assuming uniform temperature for steel sections)

Considering a polar coordinate system for the problem, the boundaries of the section are defined by r_o (radius of the outer tube) and r_i (radius of the inner tube). Each point in the cross section can be referred by a specific pair (r, θ) . The differential equation of heat conduction for the cylindrical section can be written as (Greenberg 1998):

$$\alpha^2 \left(u_{,rr} + \frac{1}{r} u_{,r} + \frac{1}{r^2} u_{,\theta\theta} \right) = u_{,t} \quad r_i \leq r \leq r_o, 0 \leq \theta \leq 2\pi, 0 \leq t < \infty \quad (7.3)$$

$$u(r, \theta, 0) = T_0, u(r_o, \theta, t) = f(t)$$

where $u(r, \theta, t)$ is the temperature field in the section, $u_{,r} = \frac{\partial u}{\partial r}$, $u_{,rr} = \frac{\partial^2 u}{\partial r^2}$, $u_{,\theta\theta} = \frac{\partial^2 u}{\partial \theta^2}$ and $u_{,t} = \frac{\partial u}{\partial t}$. The initial condition is defined using the term $u(r, \theta, 0) = T_0$ and the boundary condition corresponding to exposure of the outer edge to the predetermined fire curve, is shown by $u(r_o, \theta, t) = f(t)$. Furthermore, α^2 is the thermal diffusivity of the material (assumed to be a constant in Eq. 7.3), which is given by:

$$\alpha^2 = \frac{k}{\rho c_p} \quad (7.4)$$

in which k is the thermal conductivity, ρ is material density, and c_p is the specific heat capacity of the material. Although all of these parameter can change to some extent with temperature, the differential equation here is solved based on the assumption that α^2 is constant (i.e., calculated using constant values recommended in Eurocode for the parameters shown in Eq. 7.4). Note that possible effects of this simplification on the accuracy of the solution is checked in the verification study presented in Section 7.2.3.

Since the domain is cylindrical and the initial conditions and boundary conditions are both independent of θ , the resulting temperature field, u , is therefore also independent of θ , and only a function only of r and t . Note that if the equation is solved for values of r in the region, $r_i = 0 \leq r \leq r_o$, it can be used for all the other cases that have the configuration $0 < r_i \leq r \leq r_o$. Therefore, the differential equation will be solved for a circular section, providing a general solution that can be used for both CFST and CDFST columns (in case of a CFST section, the temperature at the radius, r_i , is taken as the temperature of the inner tube, and all temperature values for radius values below r_i are irrelevant). Applying these modifications to Eq. 7.3, the new governing differential equation is:

$$\begin{aligned} \alpha^2 \left(u_{,rr} + \frac{1}{r} u_{,r} \right) &= u_{,t} \quad 0 = r_i \leq r \leq r_o, 0 \leq t < \infty \\ u(r, 0) &= T_0, u(r_o, t) = f(t) \end{aligned} \quad (7.5)$$

Note that the term $u_{\theta\theta}$ is eliminated. Since the partial differential equation has a non-homogeneous boundary condition ($u(r_o, t) = f(t)$ instead of zero), its solution, according to a procedure given in various advanced engineering mathematics textbooks (e.g. Greenberg 1998), can be written as the summation of functions u_0 and v :

$$u(r, t) = u_0(r, t) + v(r, t) \quad (7.6)$$

in which $u_0(r, t)$ is a function satisfying only the non-homogeneous boundary condition, $u_0(r_o, t) = f(t)$. To fulfil this requirement, it is assumed that $u_0(r, t) = f(t)$. As a result:

$$u_{,r} = v_{,r} \quad (7.7)$$

$$u_{,rr} = v_{,rr} \quad (7.8)$$

$$u_{,t} = v_{,t} + f'(t) \quad (7.9)$$

$$u(r, 0) = f(0) + v(r, 0) = T_0 \quad (7.10)$$

$$u(r_o, t) = f(t) + v(r_o, t) = f(t) \quad (7.11)$$

Knowing that $f(t)$ is defined as the specified time-temperature curve for fire and assuming that any fire starts from the room temperature, it is inferred that $f(0) = T_0$. Adding this information to Eq. 7.10 gives:

$$v(r, 0) = 0 \quad (7.12)$$

Also from Eq. 7.11:

$$v(r_o, t) = 0 \quad (7.13)$$

Using Eqs. 7.8 to 7.13, a new problem can be defined for the function $v(r, t)$ as:

$$\begin{aligned} \alpha^2 \left(v_{,rr} + \frac{1}{r} v_{,r} \right) &= v_{,t} + f'(t) \quad 0 = r_i \leq r \leq r_o, 0 \leq t < \infty \\ v(r, 0) &= 0, v(r_o, t) = 0 \end{aligned} \quad (7.14)$$

Note that the new problem has a homogeneous boundary condition, but the differential equation itself has changed to a non-homogeneous one because of the addition of the term, $f'(t)$. Assuming the function, v , as a summation of its homogeneous and particular parts ($v = v_h + v_p$), and using the method of Separation of Variables, the homogeneous part of the solution for the differential equation can be written in the product form:

$$v_h(r, t) = R(r)T(t) \quad (7.15)$$

Note that in Eq. 7.15, v_h is assumed to be the product of two separate functions, $R(r)$ and $T(t)$, which are functions of only r and only t , respectively. Substituting Eq. 7.15 into the homogeneous part of Eq. 7.14 and dividing both sides by RT gives:

$$\frac{R_{,rr} + \frac{1}{r} R_{,r}}{R} = \frac{1}{\alpha^2} \frac{T_{,t}}{T} = \text{constant} = -\kappa^2 \quad (7.16)$$

The right hand side of the equation is specified to have a non-positive value, since using a positive value will not provide a proper solution. Now the original partial differential equation is converted to a set of two ordinary differential equations, as:

$$R_{,rr} + \frac{1}{r}R_{,r} + \kappa^2 R = 0 \quad (7.17)$$

$$T_{,t} + \kappa^2 \alpha^2 T = 0 \quad (7.18)$$

Eq. 7.17, for nonzero values of κ , results in a solution that is a summation of first and second types of Bessel functions, J_0 and Y_0 . For $\kappa = 0$, the solution is in the logarithmic form. The two types of solutions can be written as:

$$R(r) = \begin{cases} C_1 J_0(\kappa r) + C_2 Y_0(\kappa r), & \kappa \neq 0 \\ C_3 + C_4 \ln(r), & \kappa = 0 \end{cases} \quad (7.19)$$

Similarly, $T(t)$ has different solutions for different values of κ :

$$T(t) = \begin{cases} C_5 e^{-\kappa^2 \alpha^2 t}, & \kappa \neq 0 \\ C_6, & \kappa = 0 \end{cases} \quad (7.20)$$

Note that C_i 's are constants. Substituting Equations 7.19 and 7.20 into Eq. 7.15 and combining the two different solutions with a linear summation gives:

$$\begin{aligned} v_h(r, t) &= [C_3 + C_4 \ln(r)]C_6 + [C_1 J_0(\kappa r) + C_2 Y_0(\kappa r)]C_5 e^{-\kappa^2 \alpha^2 t} \\ &= C'_1 + C'_2 \ln(r) + [C'_3 J_0(\kappa r) + C'_4 Y_0(\kappa r)]e^{-\kappa^2 \alpha^2 t} \end{aligned} \quad (7.21)$$

where C'_1, C'_2 and C'_3 are a new set of constants. Note that Eq. 7.17 is a second order differential equation and needs two boundary conditions to be solved, but only one boundary condition is given in the problem (Eq. 7.14). As a second boundary condition, it is appropriate to require that v_h must be bounded at $r = 0$. This is a reasonable requirement, since the temperature at r_i starts from the room condition and will increase to some extent according to the given fire curve. Considering the nature of the fire curves, the final temperature value at $r = 0$ will eventually reach a limit (which will be less than the maximum outer tube temperature). Applying this limit condition (as a boundary) at $r = 0$ requires that:

$$v_h(0, t) = C'_1 + C'_2 \ln(r) + [C'_3 J_0(\kappa r) + C'_4 Y_0(\kappa r)] e^{-\kappa^2 \alpha^2 t} \rightarrow \text{bounded} \quad (7.22)$$

Since both $\ln(r)$ and $Y_0(\kappa r)$ are unbounded at $r = 0$, in order to satisfy Eq. 7.22, the constants C'_2 and C'_4 must be equal to zero. Eq. 7.21 simplifies to:

$$v_h(r, t) = C'_1 + C'_3 J_0(\kappa r) e^{-\kappa^2 \alpha^2 t} \quad (7.23)$$

Applying the second boundary condition, $v_h(r_o, t) = 0$ to Eq. 7.23 gives:

$$v_h(r_o, t) = C'_1 + C'_3 J_0(\kappa r_o) e^{-\kappa^2 \alpha^2 t} = 0 \quad \text{for } 0 \leq t < \infty \quad (7.24)$$

Since C'_1 (as a constant) and $C'_3 J_0(\kappa r_o) e^{-\kappa^2 \alpha^2 t}$ are linearly independent in the t interval, it follows from Eq. 7.24 that $C'_1 = 0$ and $C'_3 J_0(\kappa r_o) = 0$. The latter gives $C'_3 = 0$ or $J_0(\kappa r_o) = 0$. Since the elimination of the $C'_3 J_0(\kappa r_o) e^{-\kappa^2 \alpha^2 t}$ term would lead to a trivial solution, it is inferred that:

$$J_0(\kappa r_o) = 0 \quad (7.25)$$

The solution for Eq. 7.25 consists of positive roots of the J_0 function that are referred to as $z_n = \kappa_n r_o$ (these roots are known and will be used later). Using superposition and substituting C for C'_3 for simplicity, the homogenous part of the solution for the differential equation becomes:

$$v_h = \sum_{n=1}^{\infty} C_n J_0\left(z_n \frac{r}{r_o}\right) e^{-\left(\frac{z_n \alpha}{r_o}\right)^2 t} \quad (7.26)$$

where the C_n 's are constants. Now the particular solution, v_p , needs to be added to v_h . Taking v_p as:

$$v_p = \sum_{n=1}^{\infty} D_n(t) J_0\left(z_n \frac{r}{r_o}\right) e^{-\left(\frac{z_n \alpha}{r_o}\right)^2 t} \quad (7.27)$$

where $D_n(t)$ is a function of only t and Substituting it into Eq. 7.14 gives:

$$\alpha^2 \left(v_{prr} + \frac{1}{r} v_{pr} \right) = v_{pt} + f'(t) \quad (7.28)$$

Simplifying Eq.7.28 and removing the terms that satisfy the homogeneous part gives:

$$\sum_{n=1}^{\infty} D'_n(t) J_0\left(z_n \frac{r}{r_o}\right) e^{-\left(\frac{z_n \alpha}{r_o}\right)^2 t} = -f'(t) \quad (7.29)$$

which is in the Bessel-Fourier series form. Multiplying both sides of Eq. 7.29 by the term $\frac{r}{r_o} J_0\left(z_m \frac{r}{r_o}\right)$ and integrating in the domain $0 = r_i < r < r_o$ gives:

$$\int_0^{r_o} \frac{r}{r_o} J_0\left(z_m \frac{r}{r_o}\right) \sum_{n=1}^{\infty} D'_n(t) J_0\left(z_n \frac{r}{r_o}\right) e^{-\left(\frac{z_n \alpha}{r_o}\right)^2 t} dr = \int_0^{r_o} (-f'(t)) \frac{r}{r_o} J_0\left(z_m \frac{r}{r_o}\right) dr \quad (7.30)$$

Using the orthogonality of Bessel functions, Eq. 7.30 is simplified to:

$$\int_0^{r_o} \frac{r}{r_o} D'_n(t) J_0^2\left(z_n \frac{r}{r_o}\right) e^{-\left(\frac{z_n \alpha}{r_o}\right)^2 t} dr = \int_0^{r_o} (-f'(t)) \frac{r}{r_o} J_0\left(z_n \frac{r}{r_o}\right) dr \quad (7.31)$$

Eqs. 7.32 and 7.33 show two relations that can be used for the integration of Bessel functions:

$$\int s J_0(s) ds = s J_1(s) + C \quad (7.32)$$

$$\int_0^a s [J_v^2(z_n s)] ds = \frac{a^2}{2} [J_{v+1}^2(z_n a)] \quad (7.33)$$

Using Eqs. 7.32 and 7.33 to simplify Eq. 7.31 and solving for $D'_n(t)$ results in:

$$D'_n(t) = \frac{2(-f'(t))}{z_n J_1(z_n)} e^{\left(\frac{z_n \alpha}{r_o}\right)^2 t} \quad (7.34)$$

Now $D_n(t)$ can be calculated by integrating Eq. 7.34 in the time domain as:

$$D_n(t) = \int_0^t D'_n(\tau) d\tau = \int_0^t \frac{2(-f'(\tau))}{z_n J_1(z_n)} e^{\left(\frac{z_n \alpha}{r_o}\right)^2 \tau} d\tau \quad (7.35)$$

in which $f'(t)$ is the derivative of the predetermined time-temperature (fire) curve, which is applied to the outer edge of the section. Now summing up the homogeneous and particular solutions ($v = v_h + v_p$) and using Eqs. 7.26, 7.27 and 7.35, gives:

$$\begin{aligned}
 v &= v_h + v_p = \\
 &= \sum_{n=1}^{\infty} [C_n + D_n(t)] J_0 \left(z_n \frac{r}{r_o} \right) e^{-\left(\frac{z_n \alpha}{r_o} \right)^2 t} = \\
 &= \sum_{n=1}^{\infty} \left[C_n + \int_0^t \frac{2(-f'(\tau))}{z_n J_1(z_n)} e^{\left(\frac{z_n \alpha}{r_o} \right)^2 \tau} d\tau \right] J_0 \left(z_n \frac{r}{r_o} \right) e^{-\left(\frac{z_n \alpha}{r_o} \right)^2 t}
 \end{aligned} \tag{7.36}$$

Eq. 7.36 must satisfy the initial boundary condition mentioned in Eq. 7.12 ($v(r, 0) = 0$). Rewriting Eq. 7.36 for $t = 0$ gives:

$$\begin{aligned}
 v(r, 0) &= \sum_{n=1}^{\infty} [C_n + D_n(0)] J_0 \left(z_n \frac{r}{r_o} \right) e^{-\left(\frac{z_n \alpha}{r_o} \right)^2 (0)} = \\
 &= \sum_{n=1}^{\infty} \left[C_n + \int_0^0 \frac{2(-f'(\tau))}{z_n J_1(z_n)} e^{\left(\frac{z_n \alpha}{r_o} \right)^2 \tau} d\tau \right] J_0 \left(z_n \frac{r}{r_o} \right) = \\
 &= \sum_{n=1}^{\infty} C_n J_0 \left(z_n \frac{r}{r_o} \right) = 0
 \end{aligned} \tag{7.37}$$

from which it is inferred that $C_n = 0$ (since $J_0(z_n \frac{r}{r_o}) \neq 0$). Finally, using Eq. 7.6, the solution for the temperature field in the circular section, $u(r, t)$, can be written as:

$$\begin{aligned}
 u(r, t) &= v(r, t) + u_0(r, t) \\
 u(r, t) &= \left[\underbrace{\sum_{n=1}^{\infty} \left[\int_0^t \frac{2(-f'(\tau))}{z_n J_1(z_n)} e^{\left(\frac{z_n \alpha}{r_o} \right)^2 \tau} d\tau \right] J_0 \left(z_n \frac{r}{r_o} \right) e^{-\left(\frac{z_n \alpha}{r_o} \right)^2 t}}_{I^*} \right] + f(t)
 \end{aligned} \tag{7.38}$$

Eq. 7.38 can be used to calculate the temperature of a point, located at the radial distance of r from the center of a circular region, which is subjected to a temperature-time (fire) curve of $f(t)$ along its outer edge. Note that z_n 's are the n first positive roots of the first kind of Bessel function $J_0(z)$. Although Eq. 7.38

provides the exact solution for the heat transfer problem, its implementation requires the use of advanced mathematical tools. A number of simplifications are presented in the following section to make Eq. 7.38 more suitable for simple hand calculations.

7.2.2 Simplification of the Solution for Heat Transfer Problem for Practical Purposes

The first step in the simplification of Eq. 7.38 is to limit the number of terms that are needed to be included in the summation that is part of the equation, provided that the results remain sufficiently accurate for the purposes of this study. Comparison of results obtained considering various number of terms in the summation revealed that the equation can provide acceptable results when the first four terms are included in the summation. Including four terms requires the use of the first four positive roots of $J_0(z)$, namely z_1, z_2, z_3 and z_4 that are equal to:

$$z_1 = 2.405 \quad (7.39)$$

$$z_2 = 5.520 \quad (7.40)$$

$$z_3 = 8.654 \quad (7.41)$$

$$z_4 = 11.792 \quad (7.42)$$

Knowing the values of z_1 to z_4 , it is possible to calculate the numerical values of the first four terms of $J_1(z_n)$, and include them as constants in the final formula. The term, $J_0\left(z_n \frac{r}{r_0}\right)$ must be calculated specifically for a given column's dimensions and cannot be turned into a set of constants. The function, $J_0(z)$, is defined by the infinite series:

$$J_0(z) = 1 - \frac{z^2}{(1!)^2 2^2} + \frac{z^4}{(2!)^2 2^4} - \frac{z^6}{(3!)^2 2^6} + \dots \quad (7.43)$$

For values of $z > 1$, the function $J_0(z)$ can be approximated using the formula:

$$J_0(z) \cong \left(\sqrt{\frac{2}{\pi z}}\right) \cos\left(z - \frac{\pi}{4}\right) \quad (7.44)$$

Fig. 7.2 shows the comparison between the results of the two formulas (Eqs. 7.43 and 7.44) for positive value of z :

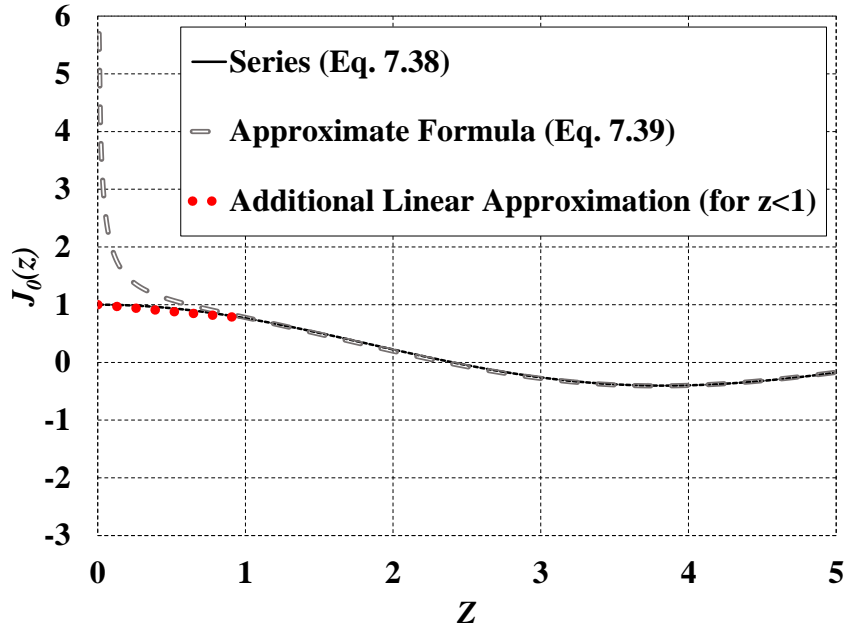


Figure 7- 2 Comparison of the exact and approximated values calculated for the function, $J_0(z)$

Since the approximate formula (Eq. 7.41) diverges from exact results for the values of $z < 1$, an additional linear approximation was defined for that region, which is shown by the dotted line in Fig. 7.2. Combining the two approximate formulas, numerical values of $J_0(z)$ can be obtained from:

$$J_0(z) \cong \begin{cases} 1 - 0.2349z, & z \leq 1 \\ \left(\sqrt{\frac{2}{\pi z}}\right) \cos\left(z - \frac{\pi}{4}\right), & z \geq 1 \end{cases} \quad (7.45)$$

The next step in the simplification of Eq. 7.38 is to calculate the integral term I^* (defined in Eq. 7.38), which needs the first derivative of the applied fire curve. Assuming that any given fire curve, $f(t)$, can be approximated by a piecewise linear function, its first derivative would have constant values over different regions of t . This will allow the term $(-f'(t))$ to be extracted from the integral as a constant, thus simplifying the calculations.

For the purposes of this study, the function $f(t)$ is defined as a bilinear approximation of the given fire curve expressed as:

$$f(t) = \begin{cases} a_1 t + T_0, & t \leq t_1 \\ a_2 t + b_2, & t \geq t_1 \end{cases} \quad (7.46)$$

in which a_1, a_2 , and b_2 are constants defined to provide the best fit for the fire curve. Recall that T_0 is the room temperature. Note that for more sophisticated cases, where a bilinear approximation might be insufficient, multiple linear segments can be defined to follow the given fire curve with more accuracy. Using Eq. 7.46, the first derivative of the function is given by:

$$f'(t) = \begin{cases} a_1, & t \leq t_1 \\ a_2, & t \geq t_1 \end{cases} \quad (7.47)$$

As an example for this approximation, a bilinear function can be defined to represent the standard ASTM E119 fire curve as:

$$f_{ASTM\ E119}(t) = \begin{cases} 78t + 20, & t \leq 10\ min. \\ 1.8t + 783.2, & t \geq 10\ min. \end{cases} \quad (7.48)$$

Fig. 7.3 shows the ASTM E119 Standard fire curve along with the approximate bilinear function. Since this fire curve has an initial sharp increasing branch followed by a second part over which temperature increases at a much slower rate, the bilinear function provides a reasonable approximation.

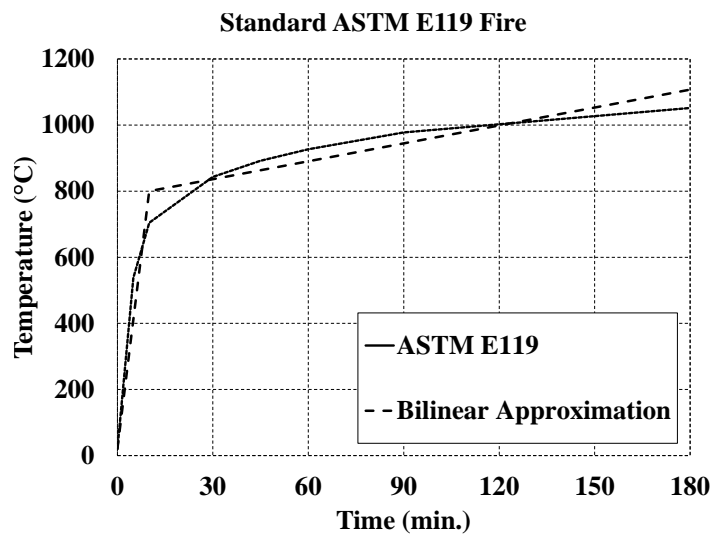


Figure 7- 3 ASTM E119 Standard fire curve compared with its bilinear approximation

The proposed bilinear approximation for the ASTM E119 standard fire curve gives the following values for the first derivative:

$$f'_{ASTM E119}(t) = \begin{cases} a_1 = 78, & t < 10 \text{ min.} \\ a_2 = 1.8, & t > 10 \text{ min.} \end{cases} \quad (7.49)$$

Assuming that the function, $f(t)$, is bilinear, the integral term in Eq. 7.38 can be computed as:

$$\begin{aligned} \int_0^t \frac{2(-f'(\tau))}{z_n J_1(z_n)} e^{\left(\frac{z_n \alpha}{r_0}\right) \tau} d\tau = \\ = \frac{-2}{z_n J_1(z_n)} \begin{cases} \left[a_1 \int_0^t e^{\left(\frac{z_n \alpha}{r_0}\right)^2 \tau} d\tau \right], & t \leq t_1 \\ \left[a_1 \int_0^{t_1} e^{\left(\frac{z_n \alpha}{r_0}\right)^2 \tau} d\tau + a_2 \int_{t_1}^t e^{\left(\frac{z_n \alpha}{r_0}\right)^2 \tau} d\tau \right], & t > t_1 \end{cases} \end{aligned} \quad (7.50)$$

After computing the integral terms, Eq. 7.50 can be written as:

$$\begin{aligned} \int_0^t \frac{2(-f'(\tau))}{z_n J_1(z_n)} e^{\left(\frac{z_n \alpha}{r_0}\right) \tau} d\tau = \\ \frac{-2r_0^2}{\alpha^2 z_n^3 J_1(z_n)} \begin{cases} a_1 \left[e^{\left(\frac{z_n \alpha}{r_0}\right)^2 t} - 1 \right], & t \leq t_1 \\ a_1 \left[e^{\left(\frac{z_n \alpha}{r_0}\right)^2 t_1} - 1 \right] + a_2 \left[e^{\left(\frac{z_n \alpha}{r_0}\right)^2 t} - e^{\left(\frac{z_n \alpha}{r_0}\right)^2 t_1} \right], & t > t_1 \end{cases} \end{aligned} \quad (7.51)$$

according to which, the function $A_n(t)$ can be defined as:

$$A_n(t) = \begin{cases} a_1 \left[e^{\left(\frac{z_n \alpha}{r_o}\right)^2 t} - 1 \right], & t \leq t_1 \\ a_1 \left[e^{\left(\frac{z_n \alpha}{r_o}\right)^2 t_1} - 1 \right] + a_2 \left[e^{\left(\frac{z_n \alpha}{r_o}\right)^2 t} - e^{\left(\frac{z_n \alpha}{r_o}\right)^2 t_1} \right], & t > t_1 \end{cases} \quad (7.52)$$

Note that as mentioned above, only the first four terms of $A_n(t)$ are needed (using the constants z_1 to z_4) for a sufficiently accurate result. Using Eqs. 7.51 and 7.52 and limiting the number of terms used in the summation part of Eq. 7.38 to the first four terms, the solution of the temperature field for a circular section subjected to a bilinear fire curve can be calculated from:

$$u_{bilinear\ fire}(r, t) = \left[\sum_{n=1}^4 \frac{-2r_o^2 A_n(t)}{\alpha^2 z_n^3 J_1(z_n)} J_0\left(z_n \frac{r}{r_o}\right) e^{-\left(\frac{z_n \alpha}{r_o}\right)^2 t} \right] + f(t) \quad (7.53)$$

Using the numerical values of $J_1(z_n)$ for the first four terms, the approximate formula for the calculation of $J_0(z)$ (Eq. 7.45) and the information provided above, the resulting equation is:

$$u_{bilinear\ fire}(r, t) = \frac{r_o^2}{\alpha^2} [-0.2770A_1(t)B_1(t) + 0.0349A_2(t)B_2(t) - 0.0114A_3(t)B_3(t) + 0.0052A_4(t)B_4(t)] + f(t) \quad (7.54)$$

All of the parameters used in Eq. 7.54 (including the newly introduced $B_i(t)$'s) are summarized in Table 7.1. In this equation, r_o is the radius of a circular section (or the outer radius of a cylindrical section), r is the radial distance of any selected point in the section and t is the amount of time (in minutes) past from the start of the exposure of the circular section's outer edge to the bilinear fire curve, $f(t)$. Using these parameters, $u_{bilinear\ fire}(r, t)$ can be calculated as the temperature of the selected point at the selected time. Note that, from here on, the equation defining the temperature distribution in a cross-section of a CFDST column exposed to a bilinear fire curve will be referred to as $u(r, t)$ for simplicity (instead of $u_{bilinear\ fire}(r, t)$).

7.2.3 Verification of the Heat Transfer Solution

The analytical approach described in the previous section was applied to one of the tested columns, namely the undamaged specimen used in the first fire test (Specimen S3), to be verified against the experimental and finite element simulation results. Results from Eq. 7.54 needed to be checked against data from both

experiment and finite element analysis, because the differential equation was solved using a bilinear approximation of the true applied fire curve along with the assumption of a constant diffusivity (α), which is a temperature dependent quantity.

Table 7- 1 Summary of the parameters needed for the calculation of the temperature field using Eq. 7.54

Parameter/Function	Expression
$A_n(t), n = 1 \text{ to } 4$	$A(t) = \begin{cases} a_1 \left[e^{\left(\frac{z_n \alpha}{r_o}\right)^2 t} - 1 \right], & t \leq t_1 \\ a_1 \left[e^{\left(\frac{z_n \alpha}{r_o}\right)^2 t_1} - 1 \right] + a_2 \left[e^{\left(\frac{z_n \alpha}{r_o}\right)^2 t} - e^{\left(\frac{z_n \alpha}{r_o}\right)^2 t_1} \right], & t > t_1 \end{cases}$
$B_n(t), n = 1 \text{ to } 4$	$B_n(t) = \left[e^{-\left(\frac{z_n \alpha}{r_o}\right)^2 t} \right] \left[\begin{cases} 1 - 0.2349 z_n^*, & z_n^* = z_n \frac{r}{r_o} \leq 1 \\ \sqrt{\frac{2}{\pi z_n^*}} \text{Cos}\left(z_n^* - \frac{\pi}{4}\right), & z_n^* = z_n \frac{r}{r_o} \geq 1 \end{cases} \right]$
$f(t)$	$f(t) = \begin{cases} a_1 t + T_0, & t \leq t_1 \\ a_2 t + b_2, & t \geq t_1 \end{cases} \quad T_0: \text{Room temperature}$ <p style="text-align: center;">For ASTM-E119 Standard fire:</p>
Bilinear fire curve applied to the outer edge	$a_1 = 78, a_2 = 1.8 \text{ } ^\circ\text{C}/\text{min.} \quad b_2 = 783.2^\circ\text{C} \quad t_1 = 10 \text{ min.}$
α^2	
Thermal Diffusivity of the section's material	$\alpha^2 = \frac{k}{\rho c_p}$
$z_n, n = 1 \text{ to } 4$	
First four positive roots of the Bessel function, $J_0(z)$	$z_1 = 2.405, \quad z_2 = 5.520, \quad z_3 = 8.654, \quad z_4 = 11.792$

Since the time-temperature curve applied to the outer tube of specimen S3 was different than the standard ASTM E119 curve, a new bilinear function ($f(t)$) needed to be fitted to the recorded curve. Note that although the furnace air temperature followed the ASTM E119 curve accurately, a slightly different curve

with lower temperature values was recorded on the surface of the outer tube. Using the recorded temperature-time curve for the outer tube of specimen S3, the fitted function was determined as:

$$f_{S_3}(t) = \begin{cases} 17.03t + 20, & t \leq 42.75 \text{ min.} \\ 4.27t + 565.49, & t \geq 42.75 \text{ min.} \end{cases} \quad (7.55)$$

in which t is time in minutes. Fig. 7.4 shows the plots of the recorded values versus the fitted function.

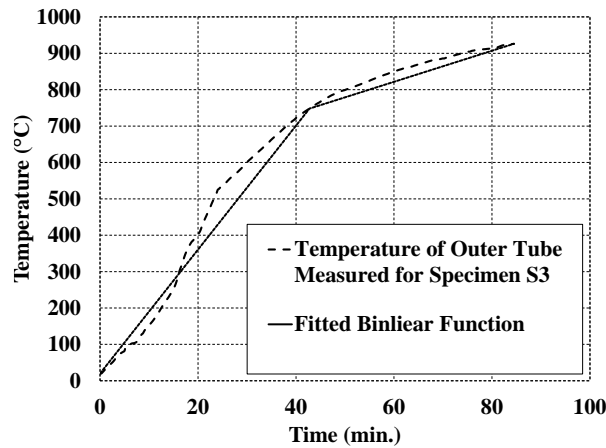


Figure 7- 4 Time-temperature curve measured for the outer tube of specimen S3 along with the curve from the fitted bilinear function

The proposed bilinear approximation gives the following values for the first derivative:

$$f'_{S_3}(t) = \begin{cases} a_1 = 17.03, & t \leq 42.75 \text{ min.} \\ a_2 = 4.27, & t \geq 42.75 \text{ min.} \end{cases} \quad (7.56)$$

Substituting Equations. 7.55 and 7.56 into Eq. 7.54, the temperature distribution in the cross-section of specimen S3 can be calculated using the set of parameters: $r_o = 4 \text{ in.}$, $r_i = 2.5 \text{ in.}$ and α^2 , which must be specified as a constant for concrete. According to Eq. 7.4, α is dependent on thermal conductivity (k), specific heat capacity (c_p) and density (ρ) of the material. Eurocode 4 general rules for structural fire design specify temperature independent values for the specific heat and thermal conductivity of concrete to be used in simplified calculation procedures.

The specified constant values of 1000 J/kg °C for the specific heat and 1.6 W/m °C for the thermal conductivity of concrete were used here. Fig. 7.5 shows the temperature dependent versus constant values

for both of the mentioned parameters. Note that the specific heat parameter shows little variation as a function of temperature. Thermal conductivity, on the other hand, changes significantly at higher temperature levels. Therefore, using the recommended constant value consequently increases the rate of heat transfer through the concrete material, leading to slightly conservative predictions of the axial load capacity of the column at the end of the process. Recall that constant values for these parameters must be used here because the governing partial differential equation was solved with the assumption of a constant α .

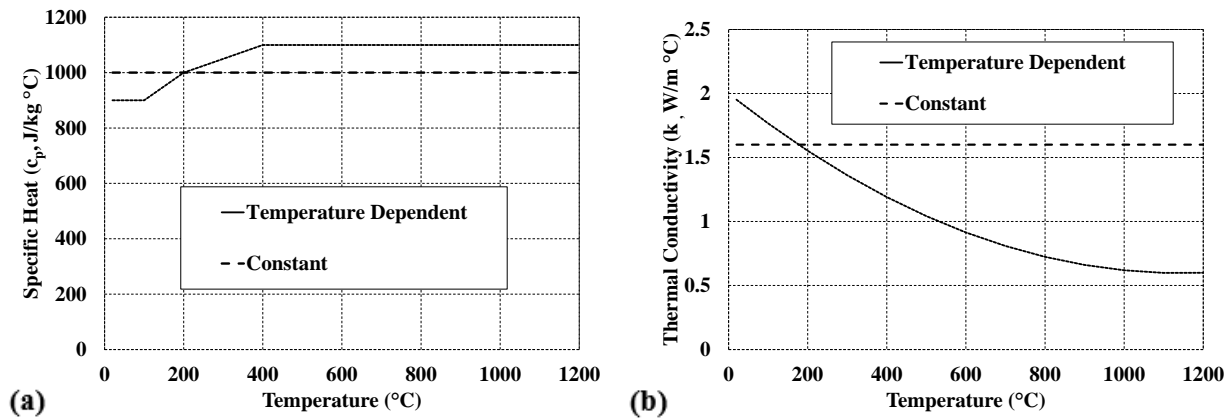


Figure 7- 5 Temperature dependent vs. constant values of: a) specific heat and b) thermal conductivity for concrete (Eurocode 2005)

Assuming a density of 140 lb/in³ (2242 kg/m³) for concrete (normal weight), α^2 can be calculated as:

$$\alpha^2 = \frac{k}{\rho c_p} \cong 0.07 \text{ in}^2/\text{min.} \cong 7.13 \times 10^{-7} \text{ m}^2/\text{s} \quad (7.57)$$

For verification with the available experimental and finite element analysis results for temperature values of points at mid-width of the concrete section and on the inner tube surface, Eq. 7.54 was used to calculate temperature values for points with $r_1 = 3.25 \text{ in.}$ (corresponding to a point at mid-width of concrete) and $r_2 = r_i = 2.5 \text{ in.}$ (corresponding to a point on the outer surface of the inner tube) as a function of time.

Fig. 7.6 shows the variation of temperature through time for a point at mid-width of the concrete section, as obtained from test recordings, finite element heat transfer analysis (presented in Section 6.3.2.1) and the analytical solution proposed for the heat transfer equation in this section (Eq. 7.54). The analytical solution is in good agreement with the experimental and finite element analysis results. Note that, especially in the

last 40 minutes of the fire time, temperature values obtained from Eq. 7.54 are slightly higher than the ones from finite element analyses. This is contradictory to the fact that the bilinear approximation used for the temperature curve (which was applied as a boundary condition to the outer tube) had lower temperatures than the ones from the recorded data (also used in the finite element model). This discrepancy was caused by using a constant diffusivity parameter (α) for concrete in the analytical solution (Eq. 7.54) instead of the temperature dependent variable used in the finite element analyses. Using the constant value, which was calculated based on Eurocode 4 general rules for structural fire design, leads to slightly conservative results (i.e. higher temperature values for a certain point at a certain time) as shown in Fig. 7.6.

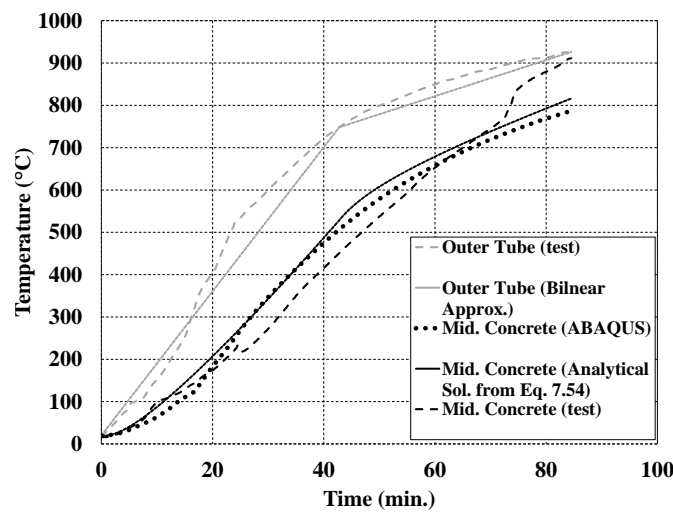


Figure 7- 6 Time-temperature curves for a point at mid-width of the concrete section for specimen S3 from the test, finite element analysis and analytical (Eq. 7.54) results

Fig. 7.7 shows the time-temperature curves for a point on the surface of the inner tube, as obtained from the test, finite element analysis and, analytical (Eq. 7.54) results for specimen S3 subjected to the standard ASTM E119 fire. Results from the finite element heat transfer analysis and the analytical solution (Eq. 7.54) are in good agreement. The test results, however, show significantly higher temperatures than those of the other two curves during certain periods of the fire test. The difference, as discussed in Section 6, is attributed to two main causes: first, sudden fluctuations of the recorded temperature possibly due to pressure built-ups and releases in the CFDST columns; and second, the fact that the temperature of the inner tube was recorded by a thermocouple that was installed close to the top end of the specimen, and therefore affected by the thermal “short circuit” that was created because of the contact between the surface of the top plate with the top end of inner tube.

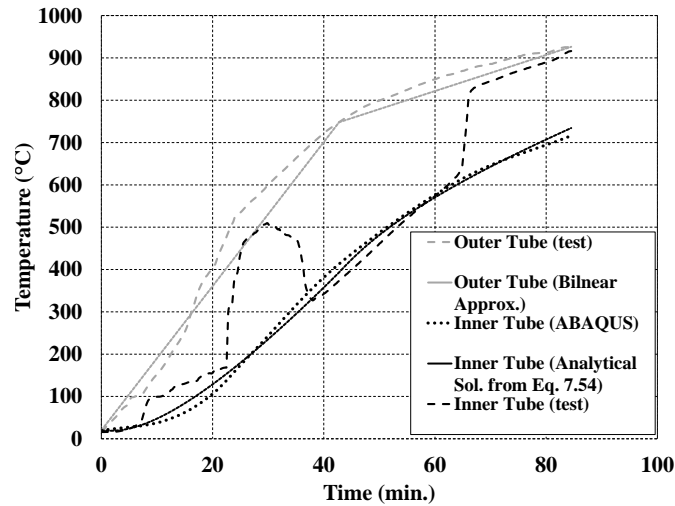


Figure 7- 7 Time-temperature curves for a point on the surface of inner tube for specimen S3 from the test, finite element analysis and analytical (Eq. 7.54) results

The first issue was not accounted for in either of the finite element or analytical (Eq. 7.54) approaches, but the finite element model was capable of simulating the effects of the second issue (i.e., the “short circuit”). Note that the analytical solution (Eq. 7.54) was derived based on the assumption of heat transfer inside an infinitely long cylindrical section; therefore, it cannot account for the boundary condition imposed by the connectivity of a heated top plate to the inner tube. To make the comparison in Fig. 7.7 more relevant, the curve from the finite element analysis results was derived from a node located in the central portion of the specimen S3 model, which was not affected by the mentioned “short circuit”.

To further investigate the accuracy of Eq. 7.54 in calculating the distribution of temperature in the cross-section of a CFDST column, results of the variation of temperature going through the thickness of the concrete layer from the finite element analysis of specimen S3 (the undamaged specimen) were plotted in Fig. 7.8 for a number of points in time (i.e., $t = 0, t = 20, t = 40, t = 60$ and $t = 80 \text{ min.}$) along with the curves resulted from using Eq. 7.54. Fig. 7.8 shows a good agreement between the two set of results.

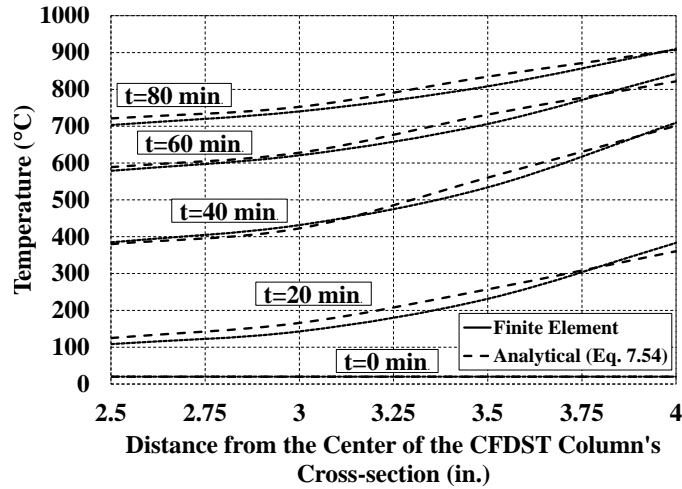


Figure 7- 8 Variation of temperature through the thickness of the Specimen S3’s cross-section for different points in time (finite element results compared with the analytical solution)

Assuming that the “short circuit” effects are limited to a short portion of the column near its top or bottom ends (as was demonstrated to be the case in Section 6), or avoided in cases where no heated end plates are connected to the ends of the column, the analytical solution (Eq. 7.54) was shown to be capable of providing accurate results for the distribution of temperature in the cross-section of CFDST columns.

7.3 Calculation of the Axial Load Capacity of CFDST Columns Subjected to Fire

7.3.1 Development of the Analytical Procedure

Knowing the temperature distribution through the cross-section of a CFDST column, its axial load capacity can then be calculated by using the modified material properties at a given time during the column’s exposure to the ASTM E119 (or any other defined) fire curve. Uniform temperature values for the outer and inner steel tubes with radii r_o and r_i (Fig. 7.9) at time t^* measured from the start of the outer tube’s exposure to the bilinear fire curve, $f(t)$, is given by (T is used for temperature):

Temperature of the outer steel tube (uniform):

$$T_{ost,t^*} = f(t^*) \tag{7.58}$$

Temperature of the inner steel tube (uniform):

$$T_{ist,t^*} = u(r_i, t^*) \text{ (using Eq. 7.54)} \tag{7.59}$$

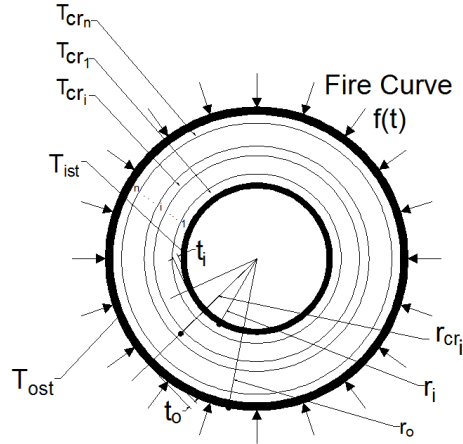


Figure 7- 9 Steel and concrete regions with uniform temperature distribution

Calculations then proceed by dividing the concrete into n concentric layers set to have different uniform temperature (Fig. 7.9). This discretization can account for the non-uniform temperature distribution in the concrete section, with its accuracy dependent on the selected number of layers (i.e., a larger n leads to better accuracy). The uniform temperature for each layer is selected to be equal to the temperature of the point located on a circle going along the mid-width of the layer.

Uniform temperature values for concrete layer i (shown in Fig. 7.9) at time t^* measured from the start of the outer tube's exposure to the fire curve, $f(t)$, is given by:

$$\begin{aligned} &\text{Temperature of concrete layer } i \text{ (uniform):} \\ &T_{cr_i,t^*} = u\left(\frac{(2n-1)(r_o-t_o-r_i)}{2n}, t^*\right) \quad \text{(using Eq. 7.54)} \end{aligned} \quad (7.60)$$

where t_o is the thickness of the outer tube and n is the number of concrete layers.

In this study, as discussed in Section 3, the temperature dependent structural properties for steel were adapted from the Eurocode general rules for structural fire design (Eurocode 2005). Repeating from Section 3.4.3.1, the complete stress-strain relationship for steel at a given temperature can be constructed using these four parameters: elastic modulus ($E_c(T)$), proportional limit stress (stress at the end of the linear elastic part, $f_p(T)$), effective yield stress ($f_y(T)$) and tensile strength ($f_u(T)$). The curve constructed using these parameters is shown in Fig. 7.10. The equations needed for construction of stress-strain relationships using the mentioned parameters were presented in Table 3.3.

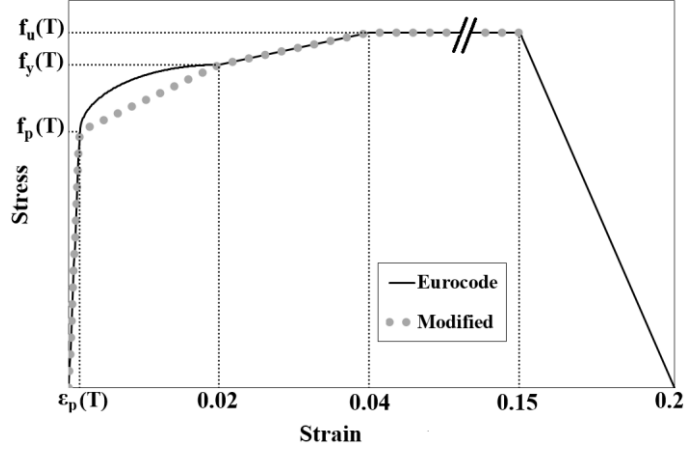


Figure 7- 10 Stress-strain curve of steel in uniaxial tension at temperature T : Eurocode curve compared with the simplified function (Eq. 7.73)

Eurocode provides tabulated data for the determination of the four parameters at different temperatures. To provide an easier approach for the calculation of these parameters at any given temperature, approximate fitted curves were developed as follows:

The reduction factor for elastic modulus of steel, R_{E_s} , at temperature T is given by:

$$R_{E_s,T} = \frac{E_s(T)}{E_s} = \frac{1}{1 + \left(\frac{T}{523}\right)^4} - 0.04 \quad (7.61)$$

in which T is in $^{\circ}\text{C}$ and E_s is the elastic modulus at room temperature. Similarly for the yield stress, the reduction factor, R_{f_y} , is given by:

$$R_{f_y,T} = \frac{f_y(T)}{f_y} = \begin{cases} 1, & T \leq 400 \\ \frac{1.10}{1 + \left(\frac{T}{572}\right)^{6.54}}, & T > 400 \end{cases} \quad (7.62)$$

in which T is in $^{\circ}\text{C}$ and f_y is the yield stress at room temperature. The reduction factor for the proportional limit stress, R_{f_p} , can be calculated as:

$$R_{f_p,T} = \frac{f_p(T)}{f_p} = \begin{cases} 1, & T \leq 100 \\ 1.27 - 2.71 \times 10^{-3}T + 1.71 \times 10^{-6}T^2 - 2.69 \times 10^{-10}T^3, & T > 100 \end{cases} \quad (7.63)$$

in which f_p is the proportional limit stress at room temperature. Note that $f_p = f_y$ for room temperature ($T = 20^\circ\text{C}$). Finally, tensile stress of steel at temperature T is given as:

$$f_u(T) = \begin{cases} 1.25f_y(T), & T \leq 400 \\ f_y(T), & T > 400 \end{cases} \quad (7.64)$$

Figures 7.11 to 7.13 show plots of the tabulated data from Eurocode for the reduction factors mentioned above (R_{E_s} , R_{f_y} and R_{f_p}) along with the values calculated from the proposed fitted functions. The functions are shown to be sufficiently accurate.

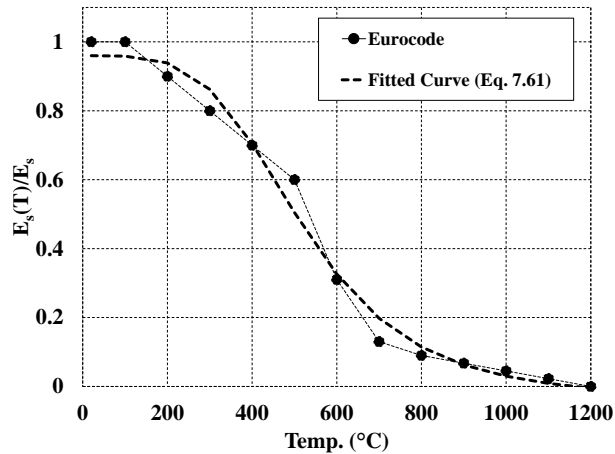


Figure 7- 11 Reduction factor for the elastic modulus of steel at high temperatures (tabulated data from Eurocode compared with calculated values from the proposed fitted function)

According to the Eurocode specifications for concrete at high temperatures (presented in Section 3.4.3.1), the ascending branch of the stress-strain curve for concrete in compression at temperature, T , can be constructed using two parameters, namely the compressive strength (f'_c) and the strain at maximum stress ($\epsilon_{cu}(T)$). Note that after this point, the curve continues with a descending branch, down to a zero stress at the strain of $\epsilon_{ce}(T)$.

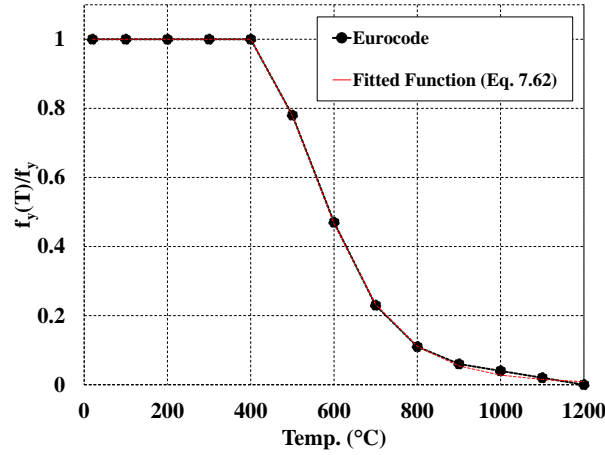


Figure 7- 12 Reduction factor for the yield stress of steel at high temperatures (tabulated data from Eurocode compared with calculated values from the proposed fitted function)

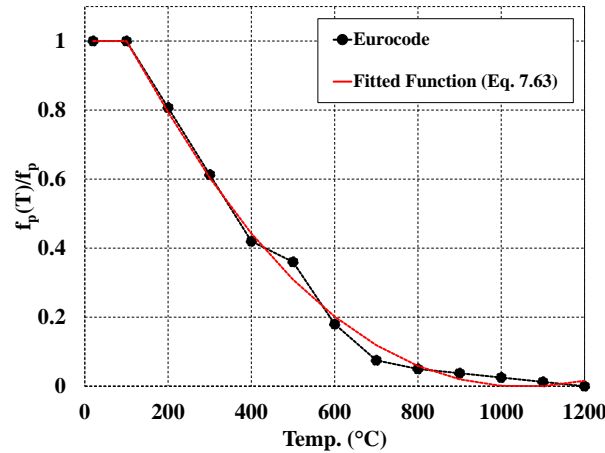


Figure 7- 13 Reduction factor for the proportional limit stress of steel at high temperatures (tabulated data from Eurocode compared with calculated values from the proposed fitted function)

A fitted function was also developed here for the reduction factor to adjust the maximum compressive strength of concrete at high temperatures, $R_{f'_c}$, based on the tabulated data provided in Eurocode 4. The resulting equation for $R_{f'_c}$ is given by:

$$R_{f'_c,T} = \frac{f'_c(T)}{f'_c} = \frac{1.12}{1 + \left(\frac{T}{597}\right)^{3.27}} - 0.13 \quad (7.65)$$

in which T is in $^{\circ}\text{C}$ and f'_c is the maximum compressive stress of concrete at room temperature. Using two additional fitted functions, $\varepsilon_{cu}(T)$ and $\varepsilon_{ce}(T)$ can be calculated as:

$$\varepsilon_{cu}(T) = \begin{cases} 1.75 \times 10^{-3} + 3.45 \times 10^{-5}T - 1.22 \times 10^{-7}T^2 + 2.14 \times 10^{-10}T^3, & x < 600 \\ 0.025, & x \geq 600 \end{cases} \quad (7.66)$$

$$\varepsilon_{ce}(T) = 1.99 \times 10^{-2} + 2.50 \times 10^{-5}T \quad (7.67)$$

Figures 7.14 to 7.16 show plots of the values of $R_{f'_c,T}$, $\varepsilon_{cu}(T)$ and $\varepsilon_{ce}(T)$ extracted from tabulated data in Eurocode, along with the ones calculated using Equations 7.65 to 7.67. The fitted functions are shown to follow the Eurocode's specifications accurately.

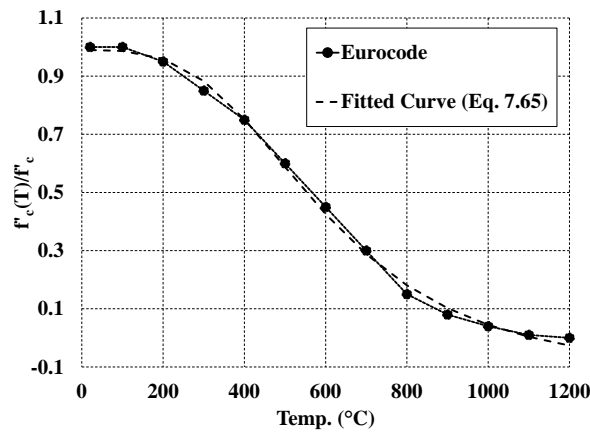


Figure 7- 14 Reduction factor for the maximum compressive strength of concrete (tabulated data from Eurocode compared with calculated values from the proposed fitted function)

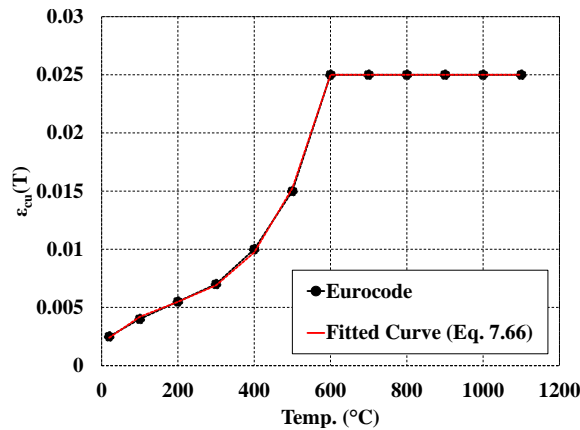


Figure 7- 15 Strain at maximum compressive stress for concrete at high temperatures (tabulated data from Eurocode compared with calculated values from the proposed fitted function)

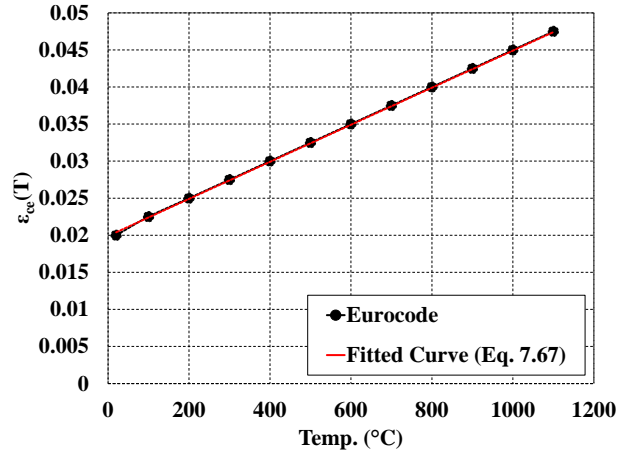


Figure 7- 16 Strain at zero compressive stress (ultimate strain) for concrete at high temperatures (tabulated data from Eurocode compared with calculated values from the proposed fitted function)

The equations needed to determine the complete stress-strain curve of concrete in compression using the three parameters mentioned above were presented in Section 3.4.3.1. Now that the stress at both steel and concrete sections can be calculated as a function of strain and temperature ($\sigma(\varepsilon, T)$), the total applied axial load on a CFDST column, $P_{axial}(\varepsilon, T)$, can be calculated as:

$$P_{axial}(\varepsilon, T) = A_{ost}\sigma_{ost}(\varepsilon, T) + A_{ist}\sigma_{sti}(\varepsilon, T) + \sum_{i=1}^n A_{cr_i}\sigma_{cr_i}(\varepsilon, T) \quad (7.68)$$

in which $A_{ost/ist/cr_i}$ refers to the area of the outer steel tube, inner steel tube, and i 'th concrete layer, respectively. Likewise, $\sigma_{ost/ist/cr_i}(\varepsilon, T)$ refers to the value of uniform stress in the same components as a function of strain and temperature, which can be calculated using the stress-strain relationships mentioned above. Note that the formula is written for a concrete region divided into n layers and assumes a compressive strain uniformly distributed over the cross-section. In each of the terms on the right hand side of Eq. 7.68, T refers to the temperature of one specific layer (inner tube, outer tube, or concrete) at a certain time (the ost, ist and cr_i indices for T have been removed for simplification). At a certain temperature, when going from zero to higher values of strain, $P_{axial}(\varepsilon, T)$ increases to its maximum value, attained when the steel and concrete layers reach a uniform stress distribution at their maximum strength values ($f_u(T)$ and $f'_c(T)$).

The critical buckling load as a function of strain and temperature, $P_{critical}(\varepsilon, T)$, can be written as:

$$P_{critical}(\varepsilon, T) = \frac{\pi^2}{(KL)^2} \left[I_{ost} E_{t_{ost}}(\varepsilon, T) + I_{ist} E_{t_{sti}}(\varepsilon, T) + \sum_{i=1}^n I_{cr_i} E_{t_{cr_i}}(\varepsilon, T) \right] \quad (7.69)$$

in which, $I_{ost/ist/cr_i}$ and $E_{t_{ost/ist/cr_i}}(\varepsilon, T)$ refer to the moment of inertia and tangent modulus values for the different sections, and KL is the effective length of the column. Note that using the tangent modulus in Eq. 7.69 makes it capable of calculating the elastic and inelastic critical buckling loads as the materials go through the increasing values of strain. At any given temperature level, the tangent moduli of steel and concrete decrease while going towards higher strain values. Therefore, Eq. 7.69 returns the maximum value for $P_{critical}(\varepsilon, T)$ at $(\varepsilon = 0)$ (calculated $P_{critical}(\varepsilon, T)$ remains constant or decreases as ε increases). According to the Eurocode specifications, the tangent modulus of steel heated to the temperature of T , $E_{s_t}(\varepsilon, T)$, can be calculated as:

$$E_{s_t}(\varepsilon, T) = \begin{cases} E_s(T), & \varepsilon < \varepsilon_p(T) \\ \frac{b(0.02 - \varepsilon)}{a\sqrt{a^2 - (0.02 - \varepsilon)^2}}, & \varepsilon_p(T) < \varepsilon < 0.02 \\ \frac{f_u(T) - f_y(T)}{0.02}, & 0.02 < \varepsilon < 0.04 \\ 0, & 0.04 < \varepsilon < 0.15 \end{cases} \quad (7.70)$$

Note that Eq. 7.70 is given for strains up to the start of the descending branch of the uniaxial tensile behavior and must be used separately for the inner and outer steel tubes, as they would be at different temperature levels. Similarly for concrete, the tangent modulus for strains up to the limit of compressive strength can be calculated as:

$$E_{c_t}(\varepsilon, T) = f_c(T) \left[\frac{3}{2 + \left(\frac{\varepsilon}{\varepsilon_{cu}(T)}\right)^3} - \frac{9}{\varepsilon_{cu}(T) \left[\frac{\varepsilon}{\varepsilon_{cu}(T)}\right]^3} \right]^2 \quad (7.71)$$

Eq. 7.71 can be used separately for each of the n layers of concrete at their respective calculated uniform temperature. Fig. 7.17 shows generic plots from the $P_{axial}(\varepsilon, T)$ and $P_{critical}(\varepsilon, T)$ functions for a fixed (current) T for each of the steel and concrete layers and a varying ε . Finally, the axial load capacity of the column after a certain duration of exposure to a given fire curve can be determined from the intersection of

the two functions $P_{axial}(\varepsilon, T)$ and $P_{critical}(\varepsilon, T)$ (Equations 7.68 and 7.69), as shown in Fig. 7.17. Defining ε_{int} as the strain value of the intersection point gives:

$$P_{axial\ capacity}(T) = P_{axial}(\varepsilon_{int}, T) = P_{critical}(\varepsilon_{int}, T) \quad (7.72)$$

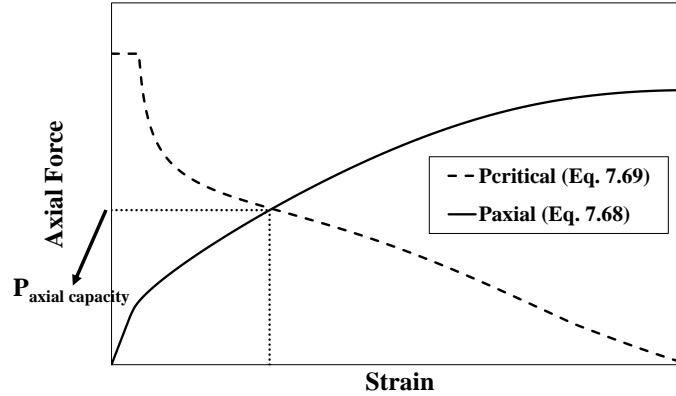


Figure 7- 17 Generic plots of the $P_{axial}(\varepsilon, T)$ and $P_{critical}(\varepsilon, T)$ functions for a fixed T and varying ε (the axial load capacity is determined by the load at the intersection of the two curves)

Assuming a uniform temperature distribution in each of the inner tube, outer tube, and the defined concrete sections, Eq. 7.72 can be solved by incrementally increasing the strain value up to the point when the two load functions ($P_{axial}(\varepsilon, T)$ and $P_{critical}(\varepsilon, T)$) return the same load, which is then the axial capacity of the column. This part of the procedure (i.e., solving Eq. 7.72 by incrementally increasing the strain value) is similar to what is presented in the simple calculation method described in Annex H of the Eurocode 4 general rules for structural fire design. Alternatively, the equation can be solved graphically by plotting the two curves as functions of strain and finding their intersecting point.

Although the solution procedure is straight forward, it needs a few lines of programming or spreadsheets to find the intersection point while accounting for the strain- and temperature-dependency of the material properties. Therefore, a further simplified procedure was developed to provide an acceptable approximation of the axial load capacity of CFDST columns by calculating the values of $P_{axial}(\varepsilon, T)$ and $P_{critical}(\varepsilon, T)$ at a few selected key points. The procedure is presented in the following section.

7.3.2 Simplified Step by Step Procedure to Calculate the Axial Load Capacity for CFDST Columns under Fire

To reduce the complexity of the analytical approach described above for the calculation of the axial load capacity of CFDST columns subjected to fire, an alternative set of simplified equations were selected to calculate the uniform stress and tangent modulus to be used in the different parts of the cross-sections, as functions of strain and temperature. For steel, as shown in Fig. 7.10, the elliptical part of the Eurocode stress-strain curve (for strains in the range $\varepsilon_p < \varepsilon < 0.02$), which has a varying tangent modulus as specified in Eq. 7.70, was replaced by a multi-linear curve, turning the reference curve into four linear segments. The new stress-strain relationship for different strain ranges with their corresponding tangent modulus is given as:

$$\sigma_{steel}^*(\varepsilon, T) = \begin{cases} E_{s_1}(T)\varepsilon, & \varepsilon < \varepsilon_p(T) \\ f_p(T) + E_{s_2}(\varepsilon - \varepsilon_p(T)), & \varepsilon_p(T) < \varepsilon < 0.02 \\ f_y(T) + E_{s_3}(\varepsilon - 0.02), & 0.02 < \varepsilon < 0.04 \\ f_u(t), & 0.04 < \varepsilon < 0.15 \end{cases} \quad (7.73)$$

in which $\sigma_{steel}^*(\varepsilon, T)$ is the simplified function for the stress-strain relationship of steel at temperature T . Note that $E_{s_1}, E_{s_2}, E_{s_3}, E_{s_4}$ refer to the tangent modulus of steel over different strain ranges and are given as:

$$E_{st}^*(\varepsilon, T) = \begin{cases} E_{s_1}(T) = E_s(T), & \varepsilon < \varepsilon_p(T) \\ E_{s_2}(T) = \frac{f_y(T) - f_p(T)}{0.02 - \varepsilon_p(T)}, & \varepsilon_p(T) < \varepsilon < 0.02 \\ E_{s_3} = \frac{f_u(T) - f_y(T)}{0.02}, & 0.02 < \varepsilon < 0.04 \\ E_{s_4} = 0, & 0.04 < \varepsilon < 0.15 \end{cases} \quad (7.74)$$

Similarly for concrete, since the stress-strain relationship given in the Eurocode leads to a complicated nonlinear equation for the tangent modulus (Eq. 7.71), Hognestad's equation (1951), which is a polynomial of degree two, was used to express the stress-strain relationship for concrete as follows:

$$\sigma_{concrete}^*(\varepsilon, T) = f_c'(T) \left[\frac{2\varepsilon}{\varepsilon_{cu}(T)} - \left(\frac{\varepsilon}{\varepsilon_{cu}(T)} \right)^2 \right] \quad (7.75)$$

in which $f'_c(T)$ and $\varepsilon_{cu}(T)$ are calculated based on the Eurocode specifications (using the fitted functions presented above in Equations 7.65 and 7.66). Note that Eq. 7.75 gives the stress-strain relationship up to the point of maximum compressive stress, $f'_c(T)$, which occurs at the strain of $\varepsilon_{cu}(T)$ for concrete at the specific temperature, T . Taking the first derivative of Eq. 7.75 with respect to ε , the tangent modulus for concrete can then be calculated as:

$$E_{ct}^*(\varepsilon, T) = \frac{2f'_c(T)}{\varepsilon_{cu}(T)} \left[1 - \frac{\varepsilon}{\varepsilon_{cu}(T)} \right] \quad (7.76)$$

which is a simple linear equation in terms of ε . Note that the ‘*’ used in the equations above is used to distinguish the new simple equations from the previously presented Eurocode equations for the same parameters. Using the new set of equations for the stress and tangent modulus calculation, Equations 7.68 and 7.69 are rewritten as:

$$P_{axial}^*(\varepsilon, T) = A_{ost}\sigma_{ost}^*(\varepsilon, T) + A_{ist}\sigma_{sti}^*(\varepsilon, T) + \sum_{i=1}^n A_{cr_i}\sigma_{cr_i}^*(\varepsilon, T) \quad (7.77)$$

$$P_{critical}^*(\varepsilon, T) = \frac{\pi^2}{(KL)^2} \left[I_{ost}E_{t_{ost}}^*(\varepsilon, T) + I_{ist}E_{t_{sti}}^*(\varepsilon, T) + \sum_{i=1}^n I_{cr_i}E_{t_{cr_i}}^*(\varepsilon, T) \right] \quad (7.78)$$

Now redrawing the curve for the critical buckling load from Fig. 7.17, this time with more details, according to the changes of the tangent moduli of steel and concrete over different strain ranges, a number of discontinuity points occur in the curve as shown in Fig. 7.18. The discontinuities are caused by the sudden changes in the tangent modulus of steel when the strain in each of the inner or outer tubes gets past the limits of $\varepsilon_p(T)$ (which is different for the outer and inner steel tubes) and 0.02. Note that changes in the tangent modulus of concrete do not create discontinuities because it is defined as the first derivative of a continuous function.

The curve in Fig. 7.18 needs to be continued up to the point when the uniform strain in the section reaches to the limit of $\varepsilon_{cu}(T)$ for one of the concrete layers, which will be the limit of $\varepsilon = \min_{i=1-n}\{\varepsilon_{cu_i}(T)\}$. The behavior of concrete in compression enters the descending branch at this point and Eq. 7.76 can no longer be used for the calculation of the tangent modulus. However, when the strain level in the section reaches this limit, the total critical buckling load has dropped more than needed to create

an intersection with the applied axial load $P_{axial}(\varepsilon, T)$, making the rest of the curve irrelevant. Note that the strain limits in Fig. 7.18 are based on the assumption that $\min_{i=1-n}\{\varepsilon_{cu_i}(T)\} > 0.02$.

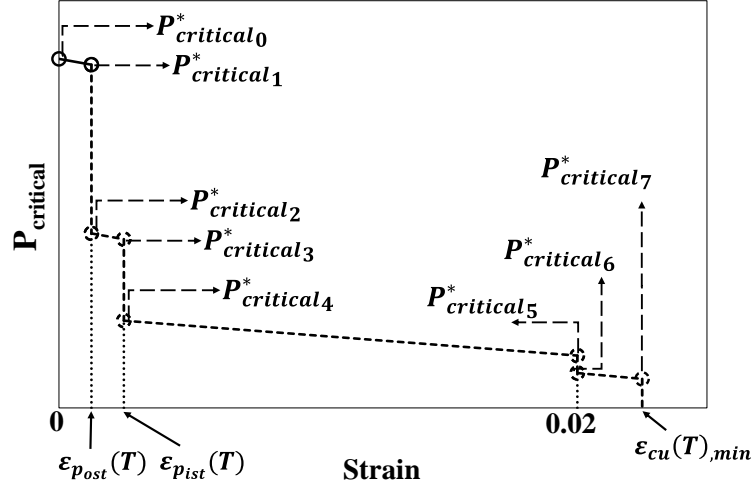


Figure 7- 18 Generic plot of the $P^*_{critical}(\varepsilon, T)$ functions for a fixed T and varying ε (Eq. 7.78)

Considering the possible range of values for $\varepsilon_{cu}(T)$ according to the Eurocode specifications ($0.0025 \leq \varepsilon_{cu} \leq 0.025$), the strain limits $\varepsilon_1, \varepsilon_2, \varepsilon_3$ and ε_4 can be determined as follows:

$$\begin{aligned}
 \varepsilon_1 &= \varepsilon_{p_{ost}}(T) \\
 \varepsilon_2 &= \varepsilon_{p_{ist}}(T) \\
 \varepsilon_3 &= \min\{0.02, \min_{i=1-n}\{\varepsilon_{cu_i}(T)\}\} \\
 \varepsilon_4 &= \min_{i=1-n}\{\varepsilon_{cu_i}(T)\} \text{ (applicable only if } \varepsilon_3 = 0.02)
 \end{aligned}
 \tag{7.79}$$

Note that $\varepsilon_{p_{ost}}(T)$ will always be lower than $\varepsilon_{p_{ist}}(T)$ because the outer steel tube is at a higher temperature level (according to Eurocode specifications, for a certain steel, $\varepsilon_p(T)$ decreases as temperature increases). According to the strain limits defined in Eq. 7.79, the tangent moduli for the inner and outer tubes at the temperatures of T_{ost} and T_{ist} are given as:

$$E_{ost_t}(T_{ost}), E_{ist_t}(T_{ist}) = \begin{cases} E_{ost_1}(T), E_{ist_1}(T) & \varepsilon < \varepsilon_1 \\ E_{ost_2}(T), E_{ist_1}(T) & \varepsilon_1 < \varepsilon < \varepsilon_2 \\ E_{ost_2}(T), E_{ist_2}(T) & \varepsilon_2 < \varepsilon < 0.02 \\ E_{ost_3}(T), E_{ist_3}(T) & 0.02 < \varepsilon < 0.04 \end{cases}
 \tag{7.80}$$

in which $E_{ost/ist_{1-3}}$ are calculated using Eq. 7.74. Note that the location of the strain limits ε_3 and ε_4 with respect to the 0.02 and 0.04 limits must be determined specifically for a given problem. At this point, the intersection of the two curve defined by the functions, $P_{axial}^*(\varepsilon, T)$ and $P_{critical}^*(\varepsilon, T)$ (Equations 7.77 and 7.78), which is equal to the axial load capacity of the CFDST column after being exposed to the first t minutes of a given fire curve, $f(t)$, can be determined by following these steps:

Step1. Using the analytical solution derived for the heat transfer problem (using Equations 7.58 to 7.60), determine the uniform temperature values for the outer steel tube, inner steel tube and all of the n concentric concrete layers at time t after the start of the CFDST column's exposure to the given fire curve, $f(t)$.

Step2. Determine $\varepsilon_1, \varepsilon_2, \varepsilon_3$ and ε_4 (if applicable) for the column using Eq. 7.79.

Step3. Calculate the critical buckling load, using the tangent moduli of different steel and concrete regions, for the strain values shown with dots in Fig 7.19a, if $\varepsilon_3 = \min_{i=1-n}\{\varepsilon_{cu_i}(T)\}$, or Fig. 7.19b, if $\varepsilon_3 = 0.02, \varepsilon_4 = \min_{i=1-n}\{\varepsilon_{cu_i}(T)\}$. Note that these critical buckling load values, calculated using Equations 7.78 to 7.80, are referred to as $P_{critical_0}^*, P_{critical_1}^*, \dots, P_{critical_5}^*$ for the first case and $P_{critical_0}^*, P_{critical_1}^*, \dots, P_{critical_7}^*$ for the second case, as shown in Fig. 7.18. Recall that the sudden drops (discontinuities) occur due to the sudden changes in the tangent modulus of steel as the strain value jumps from one of the strain ranges defined in Eq. 7.80 to the other. The infinitesimal value ϵ is used to distinguish between the tangent modulus when the strain is just below or just above one of the strain ranges defined in Eq. 7.78. The slight gradual decreases seen between any two discontinuity points in Fig. 7.18 are caused by the gradual reduction of the concrete tangent modulus as the curve goes to higher strains.

Step4. Assuming $P_{axial_i}^* = P_{axial}^*(\varepsilon_i, T)$ that can be calculated using Eq. 7.77 for the strain values $\varepsilon_0 = 0, \varepsilon_2, \varepsilon_3$ and ε_4 (given by Eq. 7.78), axial load capacity of the column can be determined through the simple iterative process defined in Eq. 7.81. Knowing that $P_{axial_0}^* = 0$ and starting from $i = 1$:

$$P_{axial\ capacity} = \begin{cases} \frac{P_{critical_{2i-2}}^* P_{axial_i}^* - P_{critical_{2i-1}}^* P_{axial_{i-1}}^*}{(P_{axial_i}^* - P_{axial_{i-1}}^*) - (P_{critical_{2i-1}}^* - P_{critical_{2i-2}}^*)}, & P_{critical_{2i-1}}^* < P_{axial_i}^* \\ P_{axial_i}^*, & P_{critical_{2i}}^* \leq P_{axial_i}^* \leq P_{critical_{2i-1}}^* \\ \text{Redo the process for } i = i + 1, & P_{axial_i}^* < P_{critical_{2i}}^* \end{cases} \quad (7.81)$$

in which $P_{critical_i}^*$'s come from the calculation in step 3 and i_{max} is equal to 4 when the strain limit of ϵ_4 is defined according to Eq. 7.79, and to 3 otherwise. Fig. 7.20 visually explains the logic used in the definition of Eq. 7.81. Note that for the cases where $P_{critical_{2i-1}}^* < P_{axial_i}^*$, the equation provides a slightly conservative result for the axial capacity of the column.

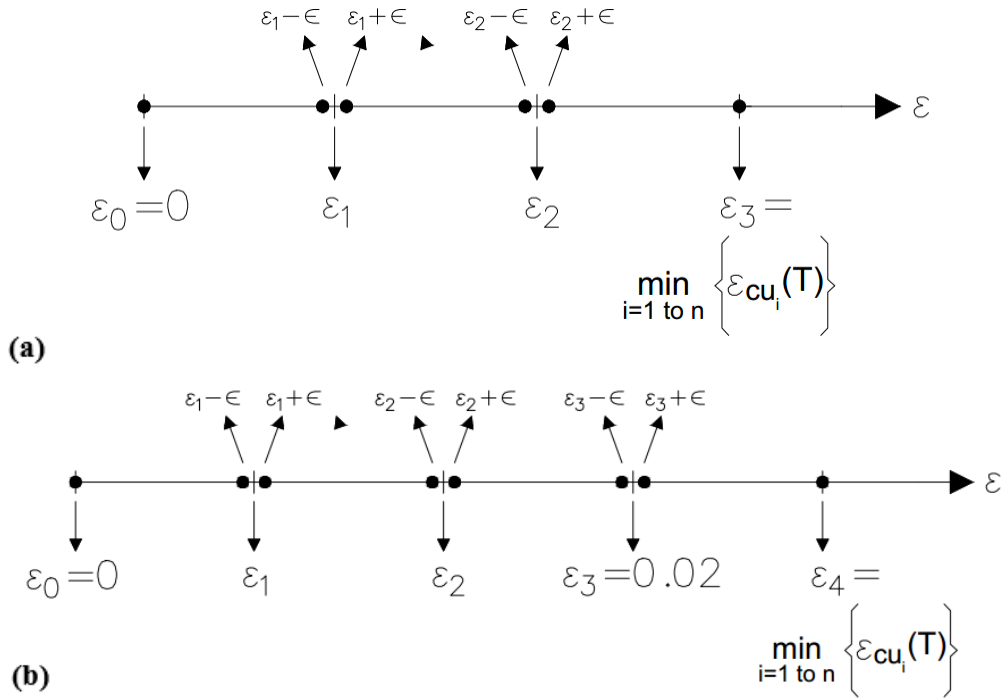


Figure 7- 19 Strain values needed for the calculation of $P_{critical_0}^*$, $P_{critical_1}^*$, ...

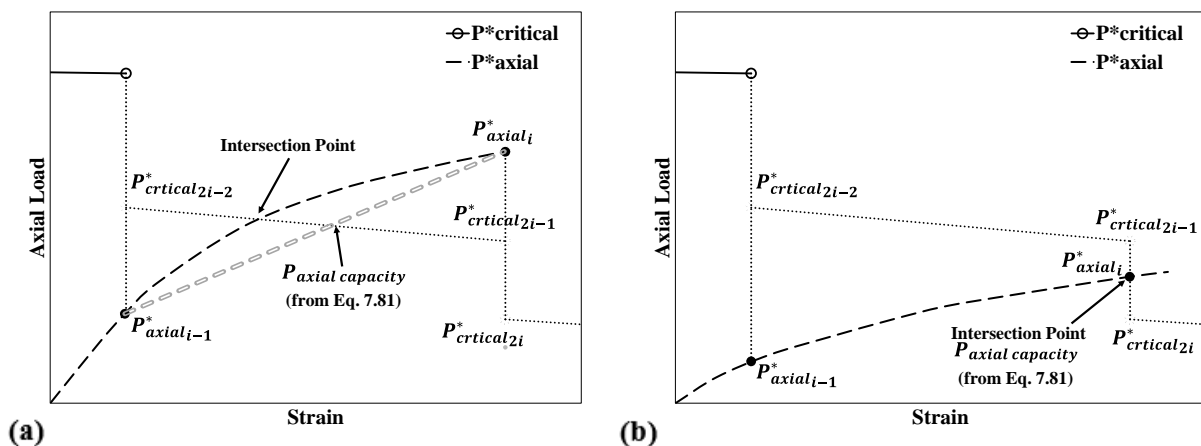


Figure 7- 20 Graphical explanation for calculating the axial load capacity using Eq. 7.81 for the cases where: a) $P_{critical_{2i-1}}^* < P_{axial_i}^*$ and b) $P_{critical_{2i}}^* \leq P_{axial_i}^* \leq P_{critical_{2i-1}}^*$

7.3.3 Verification of the Analytical Approach to Calculate the Axial Load Capacity for CFDST Columns under Fire

The analytical approach described in Section 7.3.1 for calculating the axial load capacity of CFDST columns subjected to fire was applied to one of the tested columns, namely the undamaged specimen used in the first fire test (Specimen S3), to be verified against the experimental and finite element simulation results. Knowing the temperature distribution in the cross-section of specimen S3, which was calculated and verified using the solution described in Section 7.2, the axial load capacity of Specimen S3 can be calculated using Eq. 7.72, which equates two load curves that are determined using the stress distribution in different sections at certain temperature and strain levels, and the current critical buckling load of the column calculated according to the tangent modulus of different sections at certain temperatures. A simple MATLAB code was developed to generate the mentioned load curves and solve for the equation to determine the axial load capacity of any given CFDST column subjected to the first t minutes of a predetermined fire curve. Results from this MATLAB code for Specimen S3 are presented later in this report. In addition to applying the procedure described in Section 7.3.1, the axial load capacity of Specimen S3 subjected to the ASTM E119 fire curve was also determined using the simplified step by step procedure presented in Section 7.3.2 for verification.

According to the first fire test results, specimen S3 had a fire resisting time of about 65 minutes under a constant axial load of 71 kips. As presented in Section 6, the finite element analysis successfully simulated the fire scenario, predicting a similar fire resisting time for the numerical model of specimen S3 subjected to the 71 kips axial load. To check the capability of the proposed simplified analytical method in predicting the axial load bearing capacity of CFDST columns subjected to any given fire curve, the axial load capacity of specimen S3 was calculated using the analytical procedure described in Section 7.3.1 after 50, 65 and 80 minutes from the start of the outer tube's exposure to the bilinear fire curve defined by Eq. 7.55 (which follows the outer tube's recorded temperature curve from the test).

To assess the dependency of accuracy on the assumed number of concrete layers, the procedure was conducted for two cases, namely $n = 2$ and $n = 3$. Using Eqs. 7.57 to 7.67, the uniform temperature values for the sections of inner and outer tube, concrete layer 1, and concrete layer 2 (and 3 for the second case), along with their corresponding material properties (modified for high temperatures) were calculated to be used in Equations 7.68 and 7.69. These parameters are presented in Table 7.2. Initial values of material properties at room temperature were taken from the measured values presented in Section 4 ($E_s = 29000 \text{ ksi}$, $f_{y,inner \text{ tube}} = 44 \text{ ksi}$, $f_{y,outer \text{ tube}} = 50 \text{ ksi}$, $f'_c = 9.7 \text{ ksi}$, $E_c = 5613 \text{ ksi}$).

Table 7- 2 Uniform temperature and material prop. calculated for different parts of the cross-section of specimen S3 after 50, 65 and 80 min. of exposure to the ASTM E119 fire

	Steel Regions	Outer	Inner	Concrete Regions	<i>n</i> = 2		<i>n</i> = 3		
		Tube	Tube		1	2	1	2	3
Conditions	Outer Radius (in.)	4.00	2.50	Outer Radius (in.)	3.89	3.19	3.89	3.43	2.97
	Thickness (in.)	0.11	0.09	Thickness (in.)	0.70	0.70	0.46	0.46	0.46
	<i>E_s</i> (ksi)	29000	29000	<i>E_c</i> (ksi)	5613	5613	5613	5613	5613
Room Temperature	<i>f_p</i> (ksi)	50	44	<i>f'_c</i> (ksi)	9.70	9.70	9.70	9.70	9.70
	<i>f_y</i> (ksi)	50	44	ϵ_{cu}	0.0025	0.0025	0.0025	0.0025	0.0025
	<i>f_u</i> (ksi)	58	53	ϵ_{ce}	0.0200	0.0200	0.0200	0.0200	0.0200
	Temp. (°C)	778.9	440.1	Temp. (°C)	513.5	681.0	488.2	594.3	710.5
After 50 min. of Fire Exposure	<i>E_s(T)</i> (ksi)	3737	18153	<i>f'_c(T)</i> (ksi)	5.48	3.02	5.89	4.21	2.67
	<i>f_p(T)</i> (ksi)	3.49	16.91	$\epsilon_{cu}(T)$	0.0164	0.0250	0.0145	0.0242	0.0250
	<i>f_y(T)</i> (ksi)	6.44	41.01	$\epsilon_{ce}(T)$	0.0353	0.0403	0.0345	0.0377	0.0412
	<i>f_u(T)</i> (ksi)	6.44	41.01	-	-	-	-	-	-
	Temp. (°C)	843.0	573.8	Temp. (°C)	634.1	767.0	613.5	698.8	790.0
After 65 min. of Fire Exposure	<i>E_s(T)</i> (ksi)	2581	10684	<i>f'_c(T)</i> (ksi)	3.64	2.06	3.93	2.80	1.84
	<i>f_p(T)</i> (ksi)	2.01	9.97	$\epsilon_{cu}(T)$	0.0250	0.0250	0.0250	0.0250	0.0250
	<i>f_y(T)</i> (ksi)	4.03	23.96	$\epsilon_{ce}(T)$	0.0389	0.0429	0.0383	0.0409	0.0436
	<i>f_u(T)</i> (ksi)	4.03	23.96	-	-	-	-	-	-
	Temp. (°C)	907.1	678.6	Temp. (°C)	729.1	841.7	711.9	783.7	861.5
After 80 min. of Fire Exposure	<i>E_s(T)</i> (ksi)	1726	6405	<i>f'_c(T)</i> (ksi)	2.46	1.40	2.65	1.90	1.26
	<i>f_p(T)</i> (ksi)	0.95	5.91	$\epsilon_{cu}(T)$	0.0250	0.0250	0.0250	0.0250	0.0250
	<i>f_y(T)</i> (ksi)	2.57	11.93	$\epsilon_{ce}(T)$	0.0418	0.0452	0.0413	0.0434	0.0457
	<i>f_u(T)</i> (ksi)	2.57	11.93	-	-	-	-	-	-

Recall that Specimen S3 was connected with fixed and semi-rigid connections at its top and bottom ends, respectively. Due to the lack of information about the properties of the semi-rigid connection at the bottom end, two different cases, with fixed and pinned connections at the base, were considered in the axial load capacity calculations. Fig. 7.21 shows the buckling deformation of the column under the two mentioned configurations. Note that the bottom portion of the column, which consists of the built-up part (steel box

filled with concrete) that was added as a length extension to make the column fit the 10' high vertical fire furnace, was assumed as a rigid segment with a total length of 14", leaving a length of 106" for the CFDST column. Note that since the out-of-plane buckling of Specimen S3 engaged the added channels (for the other built-up part that was used for the cyclic testing setup) about their weak axes, the portion of the column with the added channels was not included in the rigid segment (it has a larger EI compared to the CFDST section, but so large as to be considered rigid).

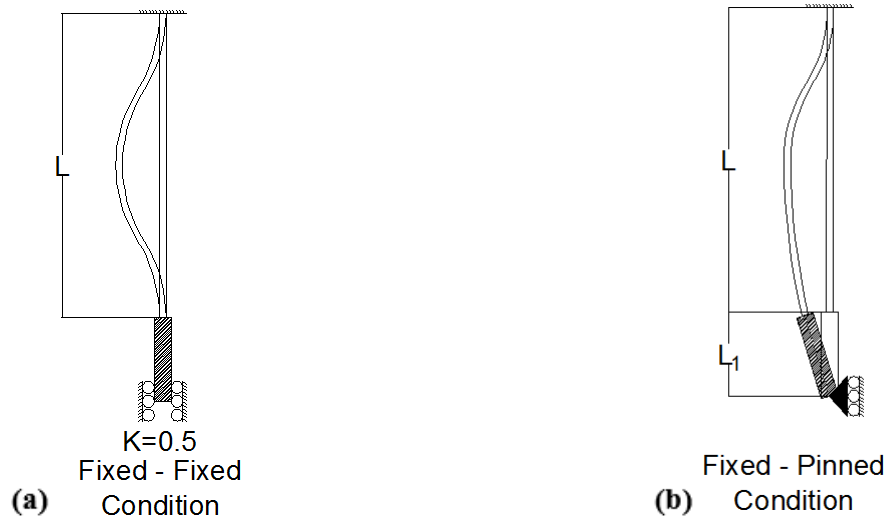


Figure 7- 21 Buckling deformation of Specimen S3 with the rigid part at the bottom end subjected to different boundary conditions: a) fixed-fixed and b) fixed-pinned

For the fixed-fixed configuration (Fig. 7.21a), it was assumed that the rigid part stayed straight and that the upper 106" segment acted as a column with fixed conditions at both ends. The corresponding effective length for this case was calculated as $KL = 53"$ ($K = 0.5$), to be used in Eq. 7.69. The critical buckling load for the fixed-pinned case needs to be calculated as a special case because the rigid part is engaged in the buckling deformation and the problem must be formulated in a different way.

Assuming that the function $w(x)$ returns the deflection of the column at point A, which is located at the distance x from the top end of the column as shown in Fig. 7.22, the governing differential equation and the appropriate boundary conditions can be written as (Hjelmstad 2005):

$$EIw''(x) + Pw(x) + R(x - L - L_1) \quad , 0 \leq x \leq L$$

$$B. C.'s: \begin{cases} (1) & w(0) = 0 \\ (2) & w'(0) = 0 \\ (3) & w(L) = L_1w'(L) \end{cases} \quad (7.82)$$

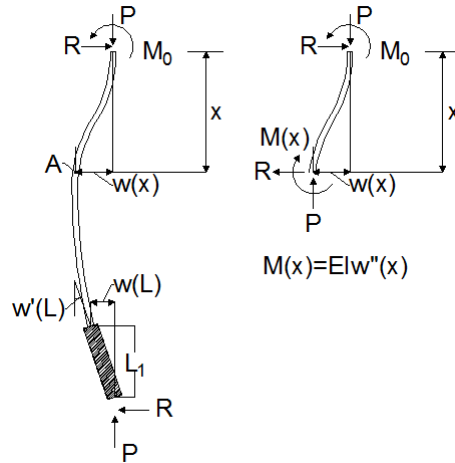


Figure 7- 22 Free body diagram of Specimen S3 with the added rigid part after buckling with the fixed-pinned end conditions

Note that Eq.7.82 is derived by satisfying the moment equilibrium at point A. The General solution for the governing differential equation can be written as:

$$w(x) = a_1 \sin(\mu x) + a_2 \cos(\mu x) - \frac{R}{P}(x - L - L_1) \quad (7.83)$$

in which $\mu = \sqrt{P/EI}$ and the term $(-\frac{R}{P}(x - L - L_1))$ is the particular solution (R is the support reaction at the pinned end). Satisfying the first and second boundary conditions gives:

$$a_1 = \frac{R}{P\mu} \quad (7.84)$$

$$a_2 = -\frac{R(L + L_1)}{P} \quad (7.85)$$

Substituting Equations 7.84 and 7.85 in Eq. 7.83 gives:

$$w(x) = \frac{R}{P\mu} \sin(\mu x) - \frac{R(L + L_1)}{P} \cos(\mu x) - \frac{R}{P}(x - L - L_1) \quad (7.86)$$

Now applying the third boundary condition to Eq. 7.86, one gets:

$$(L + 2L_1) \cos(\mu L) + \left(L_1 \mu (L + L_1) - \frac{1}{\mu} \right) \sin(\mu L) - 2L_1 = 0 \quad (7.87)$$

which must be solved for roots of μ , from which the critical buckling load values for different buckling modes can be calculated ($P_{critical} = \mu^2 EI$). Note that if $L_1 = 0$, which means the column does not have a rigid part, Eq. 7.87 reduces to the equation, $\tan(\mu L) = \mu L$, which has the smallest root of $\mu = \frac{4.493}{L}$ and leads to the familiar critical buckling load of $P_{critical} = \frac{20.19EI}{L^2}$ (equivalent to $K \cong 0.7$ for $P_{critical} = \frac{\pi^2 EI}{(KL)^2}$).

Assuming $L = 106"$ and $L_1 = 16"$, Eq. 7.87 was numerically solved to obtain the smallest root of $\mu \cong 0.05$. The critical buckling load for this value of μ is $P_{critical} = 2.5 \times 10^{-3} EI$. Assuming a column with the length of $L = 106"$, the calculated μ is equivalent to taking $K = 0.593$ in the formula $P_{critical} = \frac{\pi^2 EI}{(KL)^2}$.

To determine the axial load capacity of Specimen S3, the P_{axial} and $P_{critical}$ functions (defined in Equations 7.68 and 7.69) were calculated for different strain values and plotted in Fig. 7.23 for the four cases considered (fixed-fixed and fixed-pinned, each with 2 and 3 concrete layers) after 65 min. of exposure to the ASTM E119 fire. Note that the plots were derived from the results of the MATLAB code written for the procedure that used the varying tangent moduli of steel and concrete (Equations 7.70 and 7.71) for the calculation of $P_{critical}$ at different strain values.

Fig. 7.23 shows that the case with three concrete layers gives the same results as using two concrete layers (the results have converged with respect to the number of concrete layers for the specific problem in hand). The axial load capacity values calculated by solving Eq. 7.72 for different cases (namely, Specimen S3 subjected to the first 50, 65 and 80 minutes of the standard ASTM E119 fire curve) are summarized in Table 7.3. Note that for 65 minutes of fire exposure, the cases with fixed-fixed and fixed-pinned end conditions have axial load capacity of 84.1 kips and 68.4 kips, respectively. Considering that the column buckled under a load of 70 kips in the fire test, it was inferred that the end conditions were closer to the fixed-pinned case rather than the fixed-fixed one.

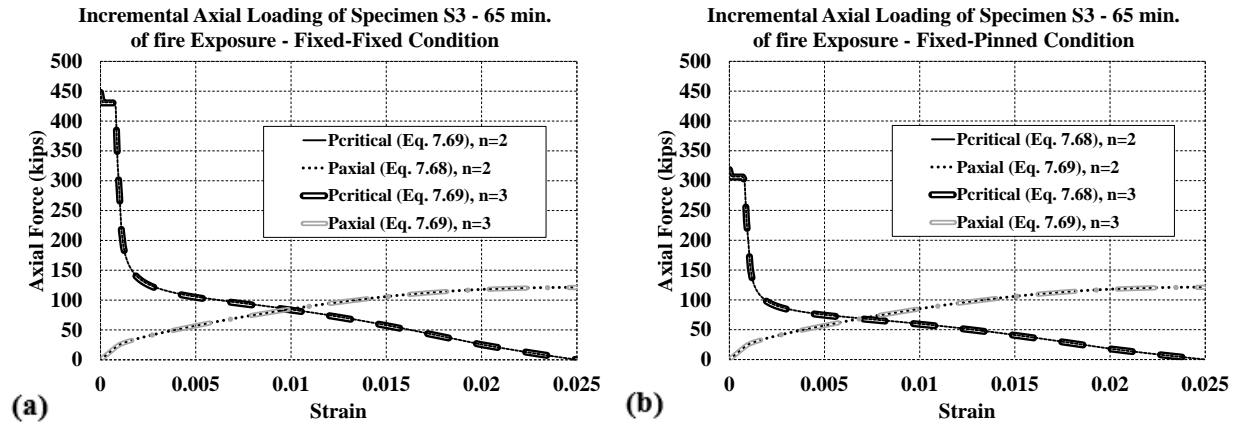


Figure 7- 23 P_{axial} and $P_{critical}$ functions plotted for Specimen S3 after 65 minutes of exposure to the ASTM E119 standard fire curve assuming: a) fixed-fixed and b) fixed-pinned end conditions for cases with different number of defined concrete layers ($n = 2$ and $n = 3$)

Results for the 50, 65 and 80 minutes of fire exposure time were also verified with the buckling forces calculated for Specimen S3 in Section 6.3.2.2 using finite element analysis with ABAQUS. From the results presented in Table 7.3, it is inferred that the results from applying the analytical approach to the case with the fixed-pinned end conditions are again reasonably close to the finite element analysis results, and slightly conservative due to the assumptions made in the heat transfer part of the solution. Recall that the finite element models were built with the assumption of fixed-pinned end conditions.

Table 7- 3 Axial load capacity calculated for Specimen S3 using the analytical approach (Eq. 7.72) compared with finite element analysis and test results for different cases (force unit: kips)

Calculation Method	Analytical Eq. 7.71		Analytical Eq. 7.71		Finite Element Analysis	Test Results	
End Conditions	Fixed-Fixed		Fixed-Pinned		Fixed-Pinned	Fixed-Semi fixed	
No. of Concrete Layers	n=2	n=3	n=2	n=3	-	-	
Exposure Time (min.)	50	143.4	140.2	121.0	118.4	130.8	-
	65	84.1	84.7	68.9	68.4	69.0	70.0
	80	54.0	53.6	44.1	43.7	49.0	-

As the last part of the verifications process, the simplified step by step approach described in Section 7.3.2 was applied to Specimen S3 to calculate the axial load capacity after 65 minutes of exposure to the standard ASTM E119 fire curve. Since the first step of the process (the heat transfer solution) was already completed in the previous verification analysis, the procedure started with the second step, which requires the calculation of the strain limits $\varepsilon_1, \varepsilon_2, \varepsilon_3, \varepsilon_4$ (if applicable) using Eq. 7.79. Using the information provided in Table 7.2, after 65 minutes of fire exposure time, the mentioned strain limits are calculated as:

$$\begin{aligned}\varepsilon_1 &= \varepsilon_{p_{ost}}(T_{ost @ 65min.}) = \frac{f_{p_{ost}}(T_{ost @ 65min.})}{E_{s_{ost}}(T_{ost @ 65min.})} = \frac{2.01}{2581} = 7.79 \times 10^{-4} \\ \varepsilon_2 &= \varepsilon_{p_{ist}}(T_{ist @ 65min.}) = \frac{f_{p_{ist}}(T_{ist @ 65min.})}{E_{s_{ist}}(T_{ist @ 65min.})} = \frac{9.97}{10684} = 9.33 \times 10^{-4} \\ \varepsilon_3 &= \min\{0.02, \min_{i=1-n}\{\varepsilon_{cu_i}(T_{cr_i @ 65min.})\}\} = \min\{0.02, 0.025\} = 0.02 \\ \varepsilon_4 &= \min_{i=1-n}\{\varepsilon_{cu_i}(T_{cr_i @ 65min.})\} = 0.025\end{aligned}\quad (7.88)$$

The next step is dedicated to the calculation of the $P_{critical_i}^*$'s for $i = 1$ to 4 using Equations 7.78 to 7.80. These are the critical buckling loads at different strain levels, which are calculated using the tangent moduli of steel and concrete sections as explained in Section 7.3.2. The load values were calculated for specimen S3 after 65 minutes of exposure to the ASTM E119 fire and are reported in Table 7.4.

Using the load values summarized in Table 7.4, the axial load capacity of the column can be determined for different end conditions according to the iterative method described in step 4 of the simplified procedure proposed in Section 7.3.2. Axial load capacity for the case with fixed-pinned end conditions and two concrete layers can be calculated as (using Eq. 7.77 for calculation of $P_{axial_i}^*$'s):

$$\begin{aligned}P_{axial_0}^* &= 0 \\ i = 1: P_{axial_1}^* &= 21.8 \text{ kips} < P_{critical_2}^* = 192.4 \text{ kips} \rightarrow i = i + 1 = 2 \\ i = 2: P_{axial_2}^* &= 25.0 \text{ kips} < P_{critical_4}^* = 87.9 \text{ kips} \rightarrow i = i + 1 = 3 \\ i = 3: P_{axial_3}^* &= 118.1 \text{ kips} > P_{critical_5}^* = 28.7 \text{ kips} : \\ P_{axial \text{ capacity}}^* &= \frac{P_{critical_4}^* P_{axial_3}^* - P_{critical_5}^* P_{axial_2}^*}{(P_{axial_3}^* - P_{axial_2}^*) - (P_{critical_5}^* - P_{critical_4}^*)} \\ &= \frac{(87.9)(118.1) - (28.7)(25.0)}{(118.1 - 25.0) - (28.7 - 87.9)} = \frac{10380.9}{152.3} = 68.2 \text{ kips}\end{aligned}\quad (7.89)$$

Table 7- 4 $P_{critical}^*$ and P_{axial}^* loads calculated at different strain levels for Specimen S3 after 65 minutes of exposure to the ASTM E119 fire (n: no. of concrete layers)

Strain Level	End Condition	$P_{critical}^*(\epsilon)$ (kips)			
		Fixed - Fixed		Fixed - Pinned	
		n=2	n=3	n=2	n=3
$\epsilon_0 = 0$		458.7	457.2	326.1	325.1
$\epsilon_1 - \epsilon = 7.79 \times 10^{-4} - \epsilon$		455.3	453.9	323.7	322.7
$\epsilon_1 + \epsilon = 7.79 \times 10^{-4} + \epsilon$		270.7	269.3	192.4	191.4
$\epsilon_2 - \epsilon = 9.33 \times 10^{-4} - \epsilon$		269.9	268.6	191.9	190.9
$\epsilon_2 + \epsilon = 9.33 \times 10^{-4} + \epsilon$		123.7	122.3	87.9	86.9
$\epsilon_3 - \epsilon = 2.0 \times 10^{-2} - \epsilon$		40.5	40.2	28.7	26.6
$\epsilon_3 + \epsilon = 2.0 \times 10^{-2} + \epsilon$		21.8	21.5	15.5	15.3
$\epsilon_4 = 2.5 \times 10^{-2}$		≈ 0	≈ 0	≈ 0	≈ 0

Note that the calculated capacity (68.2 kips) is reasonably close to the load values calculated from the analytical solution (following the procedure of Section 7.3.1) and finite element analysis for the case with fixed-pinned end conditions, which were 68.9, 69.0 kips (from Table 7.3), respectively. Recall that Specimen S3, after 65 minutes of exposure to the ASTM E119 fire curve (the same fire loading condition as the one considered for the calculations above), failed under an axial load of 70 kips.

The analytical approaches described in this section for calculation of the axial load capacity of CFDST columns subjected to fire were shown to be sufficiently accurate when compared with results from finite element analyses and test data. Although the more sophisticated procedure described in Section 7.3.1 can provide relatively more accurate results if implemented in a short computer code, the simplified step by step process (presented in Section 7.3.2) was shown to be capable of providing reasonable axial capacity estimations for design purposes.

The analytical approach described in this section for calculation of the axial load capacity of CFDST columns subjected to fire was shown to be sufficiently accurate when compared with results from finite element analyses and test data. Considering the significant assumptions used in the presented simplified analytical approach (i.e. uniform distribution of strain in the total cross-section, full composite action between the steel and concrete regions, negligible differential expansions, and Euler-Bernouli beam behavior), and the fact that each of these assumptions are possibly contentious, it can be arguably surprising that accurate results were obtained from the simplified method. The reasons for such good agreement are not fully known, and future research may eventually establish why satisfactory results are nonetheless obtained. However, it may be that the equations provide acceptable estimates of the axial load capacity during fire due to the specific boundaries of the column considered here. The CFDST columns used in this study are capped with steel plates at their top and bottom ends. Capped ends limit the relative movements at the steel-concrete interfaces and may contribute to develop enough composite action between the steel and concrete region. If that is the case, the proposed equations might not provide conservative results for CFDST columns without such cap plates at their ends (such as in long columns that can go through significant expansion), or for tubes with large D/t ratios that might lose a considerable amount of their flexural resistance (MP) due to the local buckling.

Another possible explanation is that, after significant fire exposure, little global buckling resistance is provided by the outside tube; since the inside tube remains in contact with the concrete (as steel laterally expands more than concrete), most of the initial assumptions remains applicable. Finally, given that the concrete has lost 85% of its strength (and subsequently its tangent modulus has reduced to almost zero) by the time global buckling develops, for the verification case considered, the inside tube has a tangent modulus of about 10684 ksi, indicating that the inside tube alone provides most of the flexural strength developed during buckling. This proportion may change when a thicker concrete layer exists between the tubes, which may affect the accuracy of the approximate methods. This remains to be elucidated in future research.

7.4 Design Recommendations for Fire Resistance of CFDST Columns Subjected to Fire

This section presents general design recommendations to achieve a desired amount of fire resisting time for CFDST columns under axial load. The recommendations are targeted to achieve three levels of fire resistance (under standard ASTM E119 fire), namely 1, 2 and 3 hour limits, which each can be sufficient depending on specific applications. The design recommendations are presented separately for the outer tube, concrete core, and inner tube, using the analytical methods described above for both the heat transfer and axial load capacity calculations as needed.

7.4.1 Inner Steel Tube

According to the Eurocode specifications for the structural properties of steel at high temperatures (Figures 7.11 and 7.12), the temperature of 300 °C can be selected as a critical limit, as the material experiences a decrease of 20% in its elastic modulus and will continue to do so at a significantly higher rate when reaching slightly higher temperatures. Note that the 300 °C limit is also just below the temperature limit for the start of significant reductions in the yield stress of steel (400° C). In a CFDST column, the inner tube can be thermally protected by the concrete layer to remain below the critical temperature limit for a desired amount of fire exposure time.

Assuming that the minimum required thickness of concrete layer is provided to keep the temperature of the inner tube below the critical limit for the desired amount of fire exposure time (discussed later in Section 7.4.2), the diameter and thickness of the inner tube can be selected to be capable of, apart from contributing to the pre-fire seismic and service load resistance, sustaining the permanent gravity loads, which remain acting on the structure in a post-earthquake fire scenario, for the desired fire exposure time. Note that the D/t ratio of the inner tube must be checked to comply with the desired compactness and ductility levels.

7.4.2 Concrete Core

Concrete has a relatively low heat conductance rate and can act as a fire protection layer for the inner steel tube. Considering the 300° C limit as the critical temperature for the inner tube, the thickness of the concrete between the inner and outer tube can be chosen such as to delay the inner tube attainment of the critical limit for the desired amount of fire resistance time.

Using the analytical solution presented in Section 7.2 for the heat transfer problem (specifically Equations 7.59 and 7.54), it is possible to calculate the minimum concrete thickness values required to keep the temperature of inner tubes with diameter sizes ranging from 2” to 30” below the critical limit (i.e., 300° C) for 1, 2 and 3 hours of exposure of the corresponding CFDST column to the standard ASTM E119 fire. Fig. 7.24 shows the results of these analyses for different fire exposure times. Note that as the inner tube diameter increases, the minimum required concrete layer thickness values converge to a constant limit. This might be explained by looking into a relatively simpler situation where the inner and outer surfaces of a cylinder, with radii of r_1 and r_2 , have constant (steady state) temperature values of T_1 and T_2 . In this situation, temperature of a point at the distance of r from the center ($r_1 \leq r \leq r_2$) is proportional to the value $\ln(\frac{r}{r_1})$ (Sukhatme 2005). Assuming r_1 as the radius of the inner tube (equal to the inner radius of the concrete layer), and $r - r_1$ as the thickness of the concrete layer, variation of temperature through the thickness of the concrete layer will be proportional to $\ln(\frac{r}{r_1})$. Fig. 7.25 shows the variation of $\ln(\frac{r}{r_1})$ for different values of inner tube diameter in the range of 2” to 30” ($1 \leq r_1 \leq 15$) and different concrete layer thickness ($r - r_1$) values in the range of 2” to 6”. The figure shows that the rate of change in $\ln(\frac{r}{r_1})$ values decrease as r_1 increases.

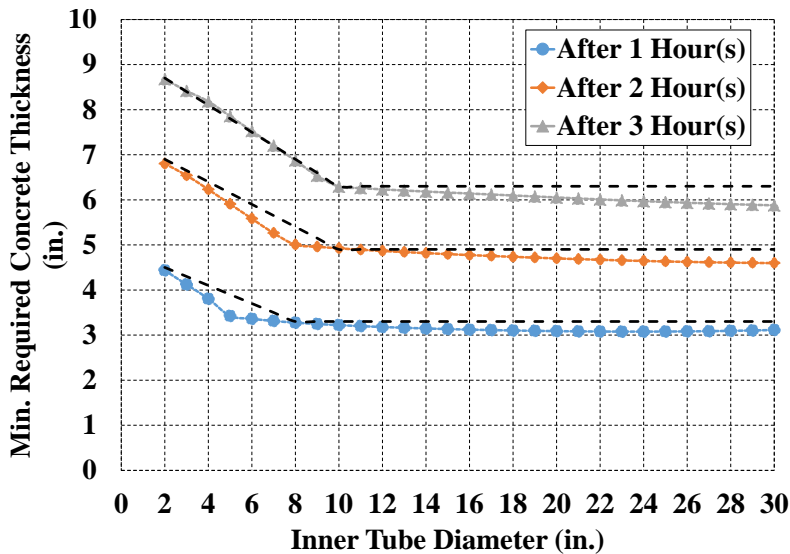


Figure 7- 24 Minimum concrete thickness values required to keep the temperature of inner tubes with different diameter sizes below the critical limit (i.e., 300 C) for 1, 2 and 3 hours of exposure to the standard ASTM E119 fire

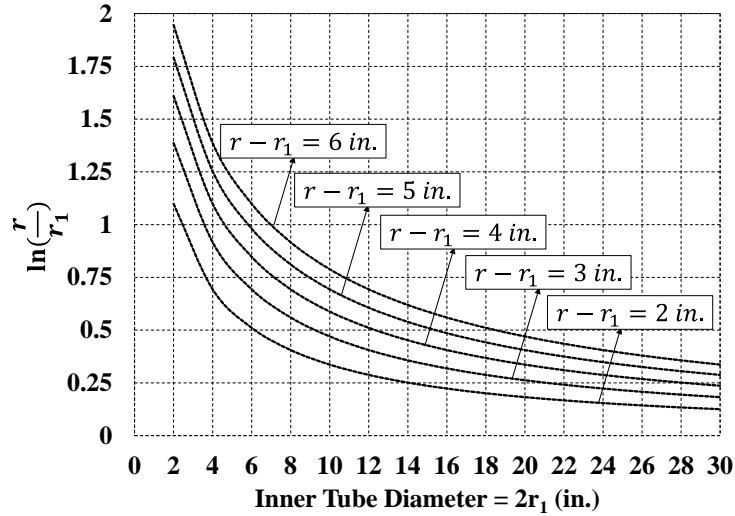


Figure 7- 25 Variation of $\ln\left(\frac{r}{r_1}\right)$ for different values of r_1 and $r - r_1$

(r_1 : inner tube radius, $r - r_1$: concrete layer thickness)

Using the plots shown in Fig. 7.24, simple equations were defined for the calculation of the minimum required concrete layer thickness as a function of inner tube diameter for different amount of fire exposure time. For a 1-hour exposure:

$$t_{min.}^{conc.} = \begin{cases} 4.90 - 0.20d_{ist}, & 2 \leq d_{ist} \leq 8 \\ 3.30, & d_{ist} > 8 \end{cases} \quad (7.90)$$

for a 2-hour exposure:

$$t_{min.}^{conc.} = \begin{cases} 7.40 - 0.25d_{ist}, & 2 \leq d_{ist} \leq 10 \\ 4.90, & d_{ist} > 10 \end{cases} \quad (7.91)$$

and for a 3-hour exposure:

$$t_{min.}^{conc.} = \begin{cases} 9.30 - 0.20d_{ist}, & 2 \leq d_{ist} \leq 10 \\ 6.30, & d_{ist} > 10 \end{cases} \quad (7.92)$$

where $t_{min.}^{conc.}$ is the minimum required concrete layer thickness and d_{ist} is the diameter of the inner tube in inches. The curves resulting from Equations 7.90 to 7.92 are plotted with dashed lines on top of the exiting curves in Fig. 7.24.

7.4.3 Outer Steel Tube

The outer tube of a CFDST column subjected to fire reaches the critical temperature level in a relatively short time due its direct exposure to fire. Note that in the standard ASTM E119 fire curve, the air temperature reaches 300° C in less than 10 minutes. Therefore, the outer steel tube will go through significant elastic modulus and yield strength reductions in the early minutes of its fire exposure.

Considering the situation described above and the fact that the relatively high thermal conductance rate of steel would cause the heat to almost immediately transfer through the thickness of the outer tube, it is inferred that the outer tube has a marginal contribution to the fire resistance of the CFDST columns. Therefore, it is recommended that the minimum required thickness of the outer tube be selected based on the seismic and service load requirements (ignoring the fire performance criteria). Compactness and ductility criteria for round concrete filled composite elements, per the AISC specifications, were presented in Table 4.1 (AISC 2010a,b). For instance, assuming an outer diameter of 15"-20" for a column used in a typical multistory building, the minimum thickness of the outer tube ($f_y = 50 \text{ ksi}$) would need to be 0.29"-0.39" to satisfy both the compactness and moderate ductility requirements.

Note that the above requirements are for cases where no fire-proofing material is applied to the the outer steel, consistently with what has been done throughout this study.

7.4.4 Examples: Investigating the Effect of Different Section Geometry Parameters on the Axial Load Capacity of CFDST Columns Subjected to Fire

Different trial cases with outer tube diameters in the range of 15"-20" (practical sizes for multi-story building columns) were considered to calculate their axial load capacities when subjected to the first 1, 2, and 3 hours of the standard ASTM E119 fire. Note that the goal of these examples was not to design a CFDST column for a specific fire performance, but rather to provide a general sense of the axial load capacity of CFDST columns subjected to the standard ASTM E119 fire and study the effects of geometric properties of the section, while the outer diameter size was limited to the range of 15"-20" and the other remaining parameters (i.e., outer tube thickness, concrete layer thickness, and inner tube thickness) were changing.

In the calculations presented here, the outer steel tube is assumed to exactly follow the standard time-temperature curve throughout the fire exposure time. Therefore, the results from these calculation are

relatively conservative, because the standard fire curve is defined for the air temperature and the temperature on the surface of the outer steel tube is slightly lower (as seen, for example, in the fire tests results reported in Section 5).

Both the outer and inner steel tubes were assumed to have elastic modulus and yield strength values of 29000 ksi and 42 ksi, respectively. These are nominal values for HSS round sections. A maximum compressive strength of 5 ksi was assumed for the concrete. Table 7.5 shows the geometric properties of the different round HSS section selected for the outer steel tubes.

Table 7- 5 Geometric properties of the selected profiles for the outer steel tube

Code	Profile	Outer Diameter (in.)	Thickness (in.)	D/t	Compactness and Ductility level
AA	HSS16x0.375	16	0.349	45.84	Compact and Highly Ductile
AB	HSS16x0.438	16	0.407	39.31	Compact and Highly Ductile
AC	HSS16x0.500	16	0.465	34.41	Compact and Highly Ductile
AD	HSS16x0.625	16	0.581	27.54	Compact and Highly Ductile
B	HSS18x0.500	18	0.465	38.71	Compact and Highly Ductile
C	HSS20x0.500	20	0.465	43.01	Compact and Highly Ductile

To study the effect of concrete thickness, different cases, ranging from a minimum thickness of 2” up to a maximum of 7”, were checked for all of the outer tube sections specified in Table 7.5 using Equations 7.59 and 7.54, with the goal of keeping the inner tube temperature below the critical limit (300° C) at the end of the 1, 2 and 3-hour fire exposures. Fig. 7.26 shows the results of the inner tube temperatures calculated for a CFDST column with the outer tube section AA (from Table 7.5) for different values of concrete thicknesses (ranging from 2” to 7”), after 1, 2 and 3 hours of exposure to the ASTM E119 fire curve.

Looking into Fig. 7.26, there are two cases for the 1-hour fire exposure time in which the inner tube temperature was kept below the critical limit. These cases have concrete thickness values of 4” and 5” for inner tubes with outer diameters of 8” and 6”, respectively. Note both of the mentioned concrete layer thickness values are above the minimum required value calculated using Eq. 7.90 for inner tube with the mentioned diameter sizes (the calculated minimum thickness values were equal to 3.3” and 3.7”). Fig. 7.26 also shows that a CFDST column with the outer tube diameter of 16”, regardless of the geometric properties of the inner tube and concrete layer, will not be able to keep the temperature of its inner tube below the critical limit for a 3-hour period. This is because selection of an inner tube with the smallest available

diameter size ($d_{ist} = 1.66''$) results in the thickness value of 6.82'' for the concrete layer, which is not sufficient.

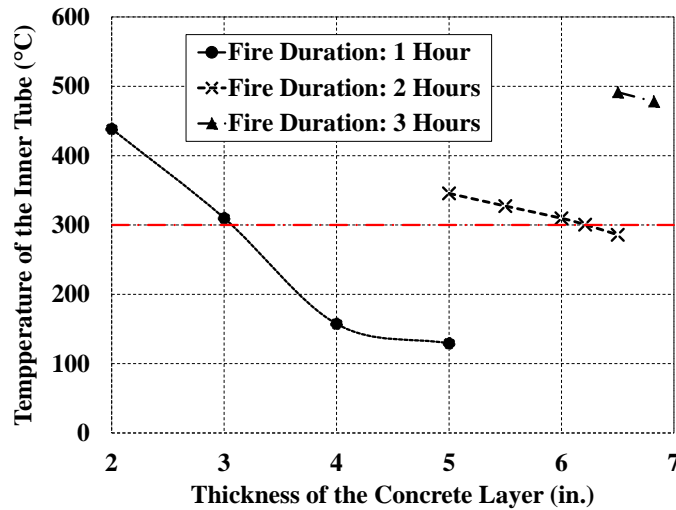


Figure 7- 26 Results of inner tube temperature calculated for a CFDST column with the outer tube section AA for different values of concrete layer thickness after 1,2 and 3 hours of exposure to the ASTM E119 fire curve

Using the outer tube sections shown in Table 7.5, a total of 15 CFDST column cross-sections were defined to be used in the axial load capacity calculation for different fire exposure times. Table 7.6 shows all of the selected cases with their axial load capacity values calculated using the simplified analytical step by step method described in Section 7.3.2. All of the columns are assumed to have a length of 160'' (typical story height) and pinned-pinned boundary conditions. The inner tube sections were selected such as to create cases with different concrete layer thickness and inner tube thickness values. Note that design cases 1.AD.1 to 1.AD. 4 are selected to assess the effects of changes in the inner tube thickness on the axial load capacity of the column when all of the other geometric parameters are kept constant. Also cases 1.AA, 1.AB, 1.AC and 1.AD.4 are selected to perform a similar analysis on the outer tube thickness (with marginal changes in the concrete layer thickness). For cases in which only one thickness is chosen for the inner or outer tube, it was taken to be equal to the maximum available thickness (based on shapes listed in the AISC Steel Construction Manual).

Table 7- 6 CFDST design cases with their calculated axial load capacity

Case ID.	Outer Tube Section	Inner Tube Section	Conc. Layer Thickness (in.)	Fire Exposure Time (hour)	Axial Load Capacity (kips)
1.AA	HSS16.000x0.375	HSS9.625x0.500	2.84	1	391.4
1.AB	HSS16.000x0.438	HSS9.625x0.500	2.78	1	394.1
1.AC	HSS16.000x0.500	HSS9.625x0.500	2.72	1	396.7
1.AD.1	HSS16.000x0.625	HSS9.625x0.250	2.61	1	272.59
1.AD.2	HSS16.000x0.625	HSS9.625x0.312	2.61	1	290.7
1.AD.3	HSS16.000x0.625	HSS9.625x0.375	2.61	1	321.7
1.AD.4	HSS16.000x0.625	HSS9.625x0.500	2.61	1	401.8
1.B	HSS18.000x0.500	HSS10.750x0.500	3.16	1	577.3
1.C	HSS20.000x0.500	HSS12.750x0.500	3.16	1	784.6
2.AD	HSS16.000x0.625	HSS2.875x0.250	5.98	2	187.2
2.B	HSS18.000x0.500	HSS7.625x0.375	4.72	2	342.5
2.C	HSS20.000x0.500	HSS10.000x0.625	4.54	2	590.5
3.AD	HSS16.000x0.625	HSS1.660x0.140	6.59	3	74.5
3.B	HSS18.000x0.500	HSS1.660x0.140	7.71	3	172.9
3.C	HSS20.000x0.500	HSS3.500x0.313	7.79	3	355.3

Fig. 7.27 shows the effect of changes in the thickness of outer and inner tubes on the axial load capacity of CFDST columns subjected to the first hour of the standard ASTM E119 fire. Note that the changes are made to a base model with an axial load capacity of about 400 kips, for which all other geometric parameters are kept constant. The figure shows that changes in the outer tube thickness do not significantly affect the axial load capacity of the column. On the other hand, increasing the thickness of the inner tube has increased the axial load capacity by as much as 32% in the cases considered. The difference is due to the fact that the inner tube temperature remains significantly lower than that of the outer tube and increasing the thickness of the former leads to a significant increase in the column's axial load capacity.

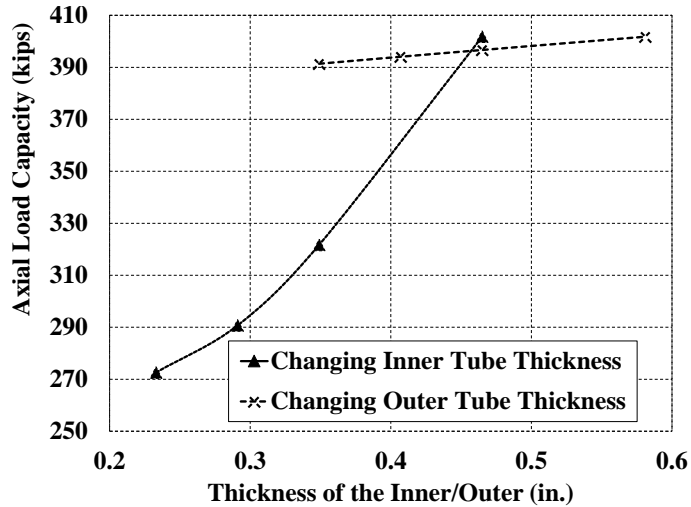


Figure 7- 27 Effects of changes in the thickness of inner and outer tubes on the axial load capacity of CFDST columns subjected to the first hour of ASTM E119 fire curve

Fig. 7.28 shows the effects of changes in the outer tube diameter on the axial load capacity of CFDST columns, assuming that all of the other section geometric properties are selected such as to maximize the axial resistance after the start of fire. The axial load capacity increases for larger outer tube diameters in a similar trend for all of the three fire duration choices. The results were expected, since increasing the diameter of the outer tube allows for the selection of larger concrete layer thickness, which can generally enhance the column's performance under fire.

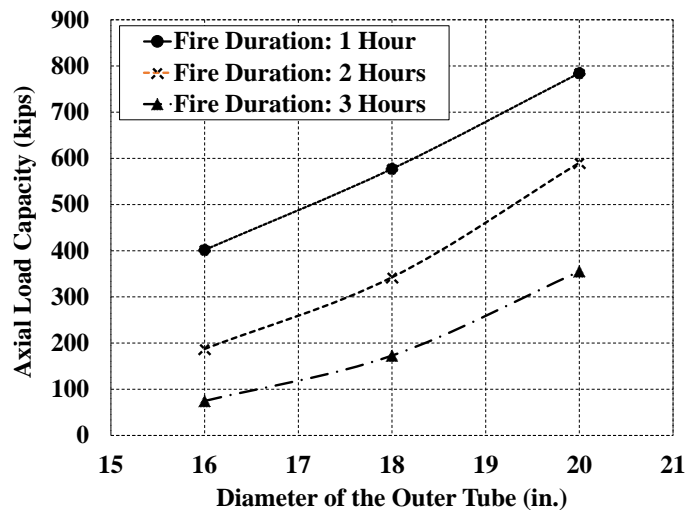


Figure 7- 28 Effects of changes in the outer tube diameter, on the axial load capacity of the CFDST column, assuming that all of the other section geometry properties are selected as such to maximize the axial resistance

SECTION 8

SUMMARY AND CONCLUSIONS

The main goal of this research was to study the behavior of CFDST columns subjected to post-earthquake fire scenarios. CFDST columns with different levels of simulated seismic damage (imposed by lateral cyclic loading) were tested in the standard ASTM E119 fire while sustaining a constant axial load. The key observations from the experiments and the subsequent analytical studies are summarized here.

Two identical CFDST columns were subjected to a constant axial load and increasing cyclic lateral displacements to reach two different levels of simulated seismic damage: a moderate damage level, which had maximum and residual drift ratios of 6.2% and 1.4%, respectively, and a high damage level, which had maximum and residual drift ratios of 6.3% and 3.9%, respectively. A third specimen was kept undamaged as a reference. The hysteretic load-drift curves from cyclic loading tests showed a stable ductile behavior for the CFDST columns.

Results from testing the three CFDST columns subjected to the standard ASTM E119 fire revealed that, for the particular type of columns built and tested under the boundary conditions considered in this study, differences in the initial simulated seismic damage level had insignificant effects on the total fire resistance time of the specimens. The shortest fire resistance time was recorded for the highly damaged specimen (i.e., the one with the residual drift ratio of 3.9%); it was almost 10 minutes shorter than the 65-minute time recorded for the undamaged specimen. This suggests that CFDST columns can be particularly effective in resisting a combination of seismic and fire conditions. However, since the three fire tests were limited to a specific boundary condition (fixed and semi-fixed ends), results should not be indiscriminately expanded to other conditions without further experimental and numerical studies (nor should the trends observed be extrapolated to other types of column constructions). All of the three columns experienced severe local buckling due to the expansion of the outer tube during the fire, and failed due to global buckling under the constant axial load.

Post-fire cyclic testing of a CFDST column, which was not previously subjected to cyclic loading and cooled down to room temperature after being exposed to a 65-minute long ASTM E119 standard fire, showed a permanent loss in lateral strength. The experimentally measured lateral resistance reduction was in good agreement with the strength calculated using the fire-modified material properties defined in the Eurocode 4 (general rules for structural fire design). Results showed a resilient behavior for CFDST

columns in a post-fire cyclic loading scenario, although the conclusion is based on a single test and needs supplemental studies to generalize these findings.

Finite element simulation of the cyclic lateral loading tests revealed that the Damaged Plasticity model implemented in ABAQUS for concrete has acceptable performance under cyclic compression, but is not sufficiently accurate in accounting for the effects of tensile cracks and their opening/closing. Therefore, the FE-CDP model (which used the Damaged Plasticity model for concrete) was not able to replicate the pinching hysteretic load-drift curves recorded in the tests. Local buckling of the outer tube and the concrete tensile crack opening/closing were identified as responsible for the pinching behavior of the hysteretic curves.

The FE-CDP model was modified by inserting a horizontal discrete crack at the base of the concrete section of the column, where the maximum tensile stress values were obtained from the results of the FE-CDP (without the discrete crack). The new model, referred to as FE-CDP-DS, could simulate the crack opening/closing (by separation/hard contact of the two opposite surfaces of concrete at the crack interface) and capture the pinching hysteretic curves for the column. This underscores how numerical results can be affected by different strategies adopted for modeling the behavior of concrete in tension when investigating inelastic cyclic behavior.

The FE-CDP-DS model was also capable of properly capturing the local buckling of the outer tube. However, the simulated hysteretic curves showed more severe pinching than the experimental results. The difference was caused by the fact that the insertion of a discrete crack creates two separate pieces of concrete with absolutely zero strength in tension, whereas in reality there is a partial continuity in part of the concrete cross-section at the location of the cracks.

To further enhance the accuracy of the finite element simulation, a new CFDST model, referred to as FE-W, was developed using the software, LS-DYNA, which includes different material models for concrete. The concrete model used, referred to as the Winfrith Model, can provide a better simulation of the tensile behavior of concrete and account for tensile cracking with up to three orthogonal crack planes per element. Results from this model followed the experimental curves with considerable accuracy, thus validating the desirable performance of the Winfrith model in simulating the tensile behavior of concrete. Modeling the steel material with a simple bilinear behavior and kinematic hardening was shown to be sufficient for the purposes of this research.

A finite element model was built in ABAQUS to simulate the behavior of CFDST columns subjected to the standard ASTM E119 fire. Temperature dependent thermal and structural material properties were selected from the Eurocode 4. Sequentially coupled thermal stress analyses were conducted on CFDST columns with different simulated seismic damage levels subjected to a constant axial load and fire. Damage simulation for the moderately and highly damaged columns was achieved through additional finite element analyses prior to the fire simulation. For the moderate damage case, the residual displacement results (including the residual drift and slight local buckle of the outer tube) were derived from the output of a cyclic lateral loading analysis and used as the initial conditions for the fire simulation analysis. For the high damage case, a more accurate procedure was used by including the cyclic lateral loading part as an additional step to be completed prior to the beginning of the heating in the fire simulation analysis. The new procedure was capable of retaining the complete history of cyclic lateral loading, including the residual deformations, possible strength and stiffness degradations and residual stresses, in a state of internal equilibrium at the end of a cyclic loading protocol that has terminated with a zero lateral force.

The finite element models were shown to be capable of replicating the experimental results with sufficient accuracy. Local buckling of the outer tube and the failure of the columns due to global buckling were both captured for all of the three cases. For the highly damaged column, the model successfully combined the local buckling effects from seismic and fire loading to make the already initial local buckle (due to seismic damage) more severe after the fire simulation. The onset of global buckling was predicted properly by the force-controlled analysis for all of the columns. An additional displacement controlled analysis was conducted on the undamaged specimen to simulate the severe global buckling deformations which occurred in the test.

In terms of the fire resistance time, the simulation results were in good agreement with the records from the experiments, confirming that the CFDST columns could almost retain the same fire resistance for all of the three damage levels. The columns' axial extension/contraction versus time results from the finite element analyses followed the same pattern that was observed in the experiments. However, a difference was observed in the axial extension/contraction values after the local buckling of the outer tube, where the finite element simulation predicted higher column extension values (i.e. expansion of the CFDST column) compared to the test results. Although the accuracy of the simulation results could be enhanced by modifying the thermal expansion rates for the two materials used in these specific columns, such modifications were considered to be unnecessary, since the model built with Eurocode 4 specifications was able to predict the total fire resistance time with an acceptable accuracy.

To validate the models for tests with larger lateral displacements, both of the FE-CDP-DS and FE-W models were used for the simulation of the post-fire cyclic testing of a CFDST column. These results showed a better performance from the FE-W model in reproducing strength degradation and the stiffness loss/recovery during the cyclic loading, with the FE-CDP-DS model being less effective in simulating the effects of consecutive cycles of buckling and straightening of the steel tube. Overall, the thermal and structural material properties adopted from the Eurocode 4 for steel and concrete (in both during and post-fire situations) were shown to be sufficiently accurate to be used for the numerical simulation of the behavior of CFDST columns subjected to fire.

An analytical procedure was developed for the calculation of the axial load capacity of CFDST columns subjected to fire. The procedure started with a solution for the heat transfer problem, derived analytically by solving the partial differential equation of heat conduction. The solution was simplified to an explicit formula that can provide the temperature of any point in the CFDST column's cross-section, after a given amount of exposure time to any predefined time-temperature curve. The simplification process had a marginal conservative effect on the accuracy of the calculation that resulted in slightly higher temperature values as a consequence of replacing a few temperature dependent factors with constant values recommended in the Eurocode 4. Comparing experimental and finite element results, the temperature values calculated using the simplified analytical formula were shown to be sufficiently accurate.

The second part of the analytical procedure consisted of a simplified step by step method to estimate the axial load capacity of CFDST columns subjected to fire using the temperature modified material properties calculated in the previous part. The method is based on solving for axial equilibrium using simple expressions for the structural material properties at elevated temperatures. Results calculated for the specimen not previously subjected to earthquake damage were in good agreement with the finite element and experimental data.

The analytical procedure defined for the axial load capacity calculation was applied to a few case studies to propose some general design recommendations for axially loaded CFDST columns subjected to fire. It was revealed that to retain a given axial load for a certain amount of time, the most effective solution is to design an inner tube capable of sustaining that load and make the concrete layer thick enough to keep the inner tube's temperature below the critical limit (about 300°C) for the specified amount of fire resistance time.

Moreover, it was found that for a given CFDST column cross-section (i.e., diameters of the inner and outer tube are known), changes in the thickness of the outer tube do not significantly affect the column's axial load capacity after a certain amount of exposure to fire. Changing the thickness of the inner tube, on the other hand, can be significantly effective, because, being at much lower temperatures than the outer tube, its capacity is retained for a longer time. Additional calculations revealed that increasing the diameter of the outer tube, or any other change that results in a thicker concrete layer, generally increases the axial load capacity of CFDST columns subjected to fire.

According to the experimental and numerical studies conducted in this research, CFDST columns were shown to have a desirable behavior when subjected to post-earthquake fires by retaining almost the same fire resistance regardless of the severity of the simulated seismic damage imposed on them prior to the start of the heating. The structural contribution of the inner tube, which is thermally protected by the concrete layer, was seen to have a crucial role in the fire resistance of the CFDST column. Note that the results of this work, especially from the experimental phase, are limited to the specific conditions used here and should not be extrapolated for different conditions. Additional studies are needed to further investigate the behavior of CFDST columns under other boundary conditions and also as parts of single- or multi-story structural frames to better understand their behavior when subjected to post-earthquake fires.

SECTION 9

REFERENCES

ACI (2011). "ACI 318-11: Building code requirements for structural concrete and commentary." American Concrete Institute, Farmington Mills, MI.

AISC (2003). "Design Guide 19: Fire Resistance of Structural Steel Framing." Am. Institute of Steel Const., Chicago, IL.

AISC (2010a). "ANSI/AISC 360-10: Specification for Structural Steel Buildings." American Institute of Steel Construction, Chicago, IL.

AISC (2010b). "ANSI/AISC 341-10: Seismic Provisions for Structural Steel Buildings." American Institute of Steel Construction, Chicago, IL.

ASTM (2011). "F2170-11: Standard Test Method for Determining Relative Humidity in Concrete Floor Slabs Using in situ Probes." ASTM International, West Conshohocken, PA.

ASTM (2012). "E119-12a: Standard Test Methods for Fire Tests of Building Construction and Materials." ASTM International, West Conshohocken, PA.

Baltay, P., and Gjelsvik, A. (1990). "Coefficient of friction for steel on concrete at high normal stress." *J Materials in Civil Eng.*, 2(1), 46-49.

Broadhouse, B.J., and Neilson, A.J. "Modeling reinforced concrete structures in DYNA3D," AEEW – M2465, Safety & Engineering Science Division, AEE, Winfrith, October, 1987.

CEB (1993). "CEB-FIP model code 1990." Comite Euro-International du Beton, *Redwood Books*, Trowbridge, Wiltshire, UK.

CEN (2005). "Eurocode 4: design of composite steel and concrete structures, part 1.2: general rules - structural fire design". Comité Européen de Normalisation, Brussels, Belgium.

Chabot, M., Lie, T. T., and Construction, I. f. R. i. (1992). "Experimental Studies on the Fire Resistance of Hollow Steel Columns Filled with Bar-reinforced Concrete." National Research Council Canada, Institute for Research in Construction.

Chen, W.-F., and Han, D. J. (1988). "Plasticity for structural engineers." J. Ross Pub., Ft. Lauderdale, FL.

Chen, W. F. (2007). "Plasticity in Reinforced Concrete." J. Ross Pub.

Cousins, W.J. and Smith, W.D. (2004). "Estimated losses due to post-earthquake fire in three New Zealand cities." Proc. 2004 NZSEE Conference, Rototua, New Zealand.

CSA (1989). "CAN/ULC-S101-M89: Standard Methods of Fire Endurance Tests of Building Construction and Materials;" Underwriters' Laboratories of Canada, Scarborough, Ontario.

Davidson, R. (2012). "Post-earthquake fires in the March 2011 Japan earthquake and tsunami." Proc. 2012 Japan and New Zealand RAPID and Research Needs Workshop, NSF, Arlington, VA, Feb. 9-10.

Ding, J., and Wang, Y. C. (2008). "Realistic modelling of thermal and structural behavior of unprotected concrete filled tubular columns in fire." J. Constr. Steel Res., 64(10), 1086-1102.

Elchalakani M., Zhao X.L. and Grzebieta R. (2002). "Tests on concrete filled double-skin (CHS outer and SHS inner) composite short columns under axial compression." Thin-walled Struct., 40(5), 415-441.

Espinos, A., Romero, M. L., and Hospitaler, A. (2010). "Advanced model for predicting the fire response of concrete filled tubular columns." J. Constr. Steel Res., 66(8-9), 1030-1046.

Espinos, A., Romero, M. L., and Hospitaler, A. (2012). "Simple calculation model for evaluating the fire resistance of unreinforced concrete filled tubular columns." Engineering Structures, 42, 231-244.

Flügge, W. (1973). "Stresses in shells." Springer-Verlag, New York.

Fouche, P., and Bruneau, M. (2010). "Non-Linear Analysis of Multi-Hazard Performance of Concrete Filled Steel Tubes Bridge Piers." 8th International Conference on Short and Medium Span Bridges, Niagara Falls, Ontario, Canada.

Fujikura, S., Bruneau, M., and Lopez-Garcia, D. (2007). "Experimental Investigation of Blast Performance of Seismically Resistant Concrete-Filled Steel Tube Bridge Piers." Technical Report MCEER-07-0005, MCEER, University at Buffalo, Buffalo, NY.

Ghojel, J. (2004). "Experimental and analytical technique for estimating interface thermal conductance in composite structural elements under simulated fire conditions." *Experimental Thermal and Fluid Science*, 28(4), 347-354.

Goto, Y., Wang, Q., and Obata, M. (1998). "FEM analysis for hysteretic behavior of thin-walled columns." *J. Struct. Eng.*, 124(11), 1290-1301.

Goto, Y., Kumar, G. P., and Kawanishi, N. (2010). "Nonlinear finite-element analysis for hysteretic behavior of thin-walled circular steel columns with in-filled concrete." *J. Struct. Eng.*, 136(11), 1413-1422.

Goto, Y., Mizuno, K., and Prosenjit Kumar, G. (2012). "Nonlinear finite element analysis for cyclic behavior of thin-walled stiffened rectangular steel columns with in-filled concrete." *J. Struct. Eng.*, 138(5), 571-584.

Green, A. E., and Naghdi, P. M. (1965). "A general theory of an elastic-plastic continuum." *Arch. Rational Mech. Anal.*, 18(4), 251-281.

Greenberg, M., D. (1998). "Advanced Engineering Mathematics." Pearson Education.

Hajjar, J. F. (2000). "Concrete-filled steel tube columns under earthquake loads." *Progress in Struct. Eng. and Materials*, 2(1), 72-81.

Hajjar, J. F., Gourley, B. C., Tort, C., Denavit, M. D., and Schiller, P. H. (2013). "Steel-Concrete Composite Structural Systems." Department of Civil and Environmental Engineering, Northeastern University, Boston, Massachusetts, <<http://www.northeastern.edu/compositesystems>>.

Han, L. H. (2001). "Fire performance of concrete filled steel tubular beam-columns." *J. Constr. Steel Res.*, 57(6), 695-709.

- Han, L. H., Zhao, X. L., Yang, Y. F., and Feng, J. B. (2003). "Experimental study and calculation of fire resistance of concrete-filled hollow steel columns." *ACSE J. Struct. Eng.*, 129(3), 346-356
- Han, L. H., Tao, Z., Huang, H., and Zhao, X. L. (2004). "Concrete-filled double skin (SHS outer and CHS inner) steel tubular beam-columns." *Thin Wall Struct.*, 42(9), 1329-1355.
- Han, L. H., and Yang, Y. F. (2005). "Cyclic performance of concrete-filled steel CHS columns under flexural loading." *J. Constr. Steel Res.*, 61(4), 423-452.
- Han L.H., Huang H., Tao Z. and Zhao X.L. (2006). "Concrete-filled double skin steel tubular (CFDST) beam-columns subjected to cyclic bending." *Eng. Struct.*, 28(12), 1698–714
- Harmathy, T. Z., and Allen, L. W. (1973). "THERMAL PROPERTIES OF SELECTED MASONRY UNIT CONCRETES." *J. The American Concrete Institute*, 70(2), 132-142.
- Hjelmstad, K. D. (2005). "Fundamentals of Structural Mechanics." Springer.
- Hognestad, E. (1951). "A study on combined bending and axial load in reinforced concrete members." Univ. of Illinois Engineering Experiment Station, Univ. of Illinois at Urbana-Champaign, IL, 43-46.
- Holman, J. P. (2009). "Heat transfer." New York, McGraw-Hill Book Co.
- Hong, S., and Varma, A. H. (2009). "Analytical modeling of the standard fire behavior of loaded CFT columns." *J. Constr. Steel Res.*, 65(1), 54-69.
- ISO (1980). "ISO-834: Fire resistance tests, elements of building construction." International Standards Organization, Switzerland.
- Johansson, M., and Gylltoft, K. (2001). "Structural behavior of slender circular steel-concrete composite columns under various means of load application." *Steel & Composite Structures*, 1(4), 393-410.
- Kodur, V. K. R. (1998). "Performance of high strength concrete-filled steel columns exposed to fire." *Can. J Civil Eng.*, 25(6), 975-981.

Kodur, V. K. R., and MacKinnon, D. H. (1998). "Simplified design of concrete-filled hollow structural steel columns for fire endurance." *J. Constr. Steel Res.*, 46(1-3), 298.

Kodur, V., Dwaikat, M., and Fike, R. (2010). "High-Temperature Properties of Steel for Fire Resistance Modeling of Structures." *J. Materials in Civil Eng.*, 22(5), 423-434.

Lazarov, L., Cvetkovska, M., and Todorov, K. (2013). "Fire resistance of RC frame in case of post-earthquake fire." *J. Struct. Fire Eng.*, 4(2), 87-94.

Lee, J. H., and Fenves, G. L. (1998). "Plastic-damage model for cyclic loading of concrete structures." *J. Eng. Mech.*, 124(8), 892-900.

Lie T. T. (1994). "Fire resistance of circular steel columns filled with bar-reinforced concrete." *J Struct. Eng.*, 120(5), 1489-509.

Lin M.L., and Tsai K.C. (2001). "Behavior of double-skinned composite steel tubular columns subjected to combined axial and flexural loads." *Proc. of the First International Conference on Steel and Composite Structures*, Pusan, Korea, June 14–16, p. 1145–52.

Lindberg G. M., Olson M. D., and Cowper G. R. (1969). "New developments in the finite element analysis of shells." *Quarterly Bulletin of the Division of Mechanical Engineering and the National Aeronautical Establishment, National Research Council of Canada*, vol. 4.

Lu, H., Han, L. H., and Zhao, X. L. (2010). "Fire performance of self-consolidating concrete filled double skin steel tubular columns: Experiments." *Fire Safety J.*, 45(2), 106-115.

Lu, H., Zhao, X. L., and Han, L. H. (2011). "FE modelling and fire resistance design of concrete filled double skin tubular columns." *J. Constr. Steel Res.*, 67(11), 1733-1748.

Lublinter, J., Oliver, J., Oller, S., and Onate, E. (1989). "Plastic-damage model for concrete." *International Journal of Solids and Structures*, 25(3), 299-326.

Luecke, W. E. (2005). "Federal Building and Fire Safety Investigation of the World Trade Center Disaster: Physical Properties of Structural Steels. NIST NCSTAR 1-3E.", 162p.

Mander, J. B., Priestley, M. J. N., and Park, R. (1988). "Theoretical stress-strain model for confined concrete." *J. Struct. Eng.*, 114(8), 1804-1826.

Marson, J., and Bruneau, M. (2004). "Cyclic testing of concrete-filled circular steel bridge piers having encased fixed-based detail." *J. Bridge. Eng.*, 9(1), 14-23.

Memari, M., Turbert, C., and Mahmoud, H. "Effects of Fire Following Earthquakes on Steel Frames with Reduced Beam Sections." *Proc., Structures Congress 2013, 2-4 May 2013, American Society of Civil Engineers*, 2555-2565.

McCormick, J., Fadden, M., and Buison, J. "Cyclic testing of hollow structural sections for seismic applications in low to mid-rise moment frames." *Proc., 13th International Symposium on Tubular Structures, ISTS13, December 15, 2010 - December 17, 2010, CRC Press*, 175-183.

Moliner, V., Espinos, A., Romero, M. L., and Hospitaler, A. (2013). "Fire behavior of eccentrically loaded slender high strength concrete-filled tubular columns." *J. Constr. Steel Res.*, 83, 137-146.

Mostafaei, H., and Kabeyasawa, T. (2010). "Performance of a six-story reinforced concrete structures in post-earthquake fire." *Proc., 9th US National and 10th Canadian Conference on Earthquake Engineering, Including Papers from the 4th International Tsunami Symposium, July 25, 2010 - July 29, 2010, Earthquake Engineering Research Institute*, 481-490.

NIST (2010). "Technical note 1681: Best Practice Guidelines for Structural Fire Resistance Design of Concrete and Steel Buildings.", 199p.

NOAA (1972). "A Study of Earthquake Losses in the San Francisco Bay Area – Data and Analysis." Report to the Office of Emergency Preparedness: US Department of Commerce, National Oceanic and Atmospheric Administration (NOAA).

Poh, K. W. (2001). "Stress-strain-temperature relationship for structural steel." *J. Materials in Civil Eng.*, 13(5), 371-379.

Popovics, S. (1973). "Numerical approach to the complete stress-strain curve of concrete." *Cement and Concrete Res.*, 3(5), 583-599.

Sakino, K., Nakahara, H., Morino, S., and Nishiyama, A. (2004). "Behavior of centrally loaded concrete-filled steel-tube short columns." *J. Struct Eng.*, 130(2), 180-188.

Scawthorn, C., Eidinger, J. M., and Schiff, A. J. (2005). "Fire Following Earthquake." American Society of Civil Engineers.

Scawthorn, C.R. (2008). "Fire following earthquake - The shake out scenario report." SPA Technical Report, SPA Risk, LLC, Berkeley, CA.

Schwer, L. (2011). "The Winfrith Concrete Model: Beauty or Beast? Insights into the Winfrith Concrete Model." 8th European LS-DYNA Users Conference, 23-24 May 2011, Strasbourg, France.

SIMULIA (2012). "Abaqus Documentation." Dassault Systèmes Simulia Corporation.

Sukhatme, S. P. (2005). "A Textbook on Heat Transfer." Universities Press.

Tao Z., Han L.H. and Zhao X.L. (2004). "Behaviour of concrete-filled double skin (CHS inner and CHS outer) steel tubular stub columns and beam-columns.", *J. Constr. Steel Res.*, 60(8), 1129-1158.

Tao Z. and Han L.H. (2006). "Behaviour of concretefilled double skin rectangular steel tubular beam-columns." *J. of Constr. Steel Res.*, 62(7), 631-646.

Uenaka, K., Kitoh, H., and Sonada, K. (2008). "Concrete filled double skin tubular members subjected to bending (vol 8, pg 297, 2008)." *Steel Comp. Struct.*, 8(5), 439-439.

Uenaka, K., Kitoh, H. and Sonoda, K.(2010). "Concrete Filled Double Skin Circular Stub Columns under Compression.", *Thin-Walled Struct.*, 48(1), 19-24.

Unistrut (2013). <[http:// http://www.unistrut.us/](http://www.unistrut.us/)>.

Usami, T., Susantha, K. A. S., and Ge, H. (2001). "Uniaxial stress-strain relationship of concrete confined by various shaped steel tubes." *Engineering Structures*, 23(10), 1331-1347.

Wittmann, F.H., Rokugo, K., Bruhwiler, E., Mihashi, H. and Simonin, P. (1988) "Fracture Energy and Strain Softening of Concrete as Determined by Means of Compact Tension Specimens," *Materials and Structures*, Volume 21, pages 21-32.

Yang, Y. F., and Han, L. H. (2008). "Concrete-filled double-skin tubular columns under fire." *Mag. Concrete Res.*, 60(3), 211-222.

Yassin, M. H., Bagchi, A., and Kodur, V. K. R. "Mitigation of post-earthquake fire risk to building structures." *Proc., 6th International Conference on Structures in Fire, SiF'10, June 2, 2010 - June 4, 2010, DEStech Publications Inc.*, 943-950.

Yin, J., Zha, X.-X., and Li, L.-Y. (2006). "Fire resistance of axially loaded concrete filled steel tube columns." *J. Constr. Steel Res.*, 62(7), 723-729.

Zhao X. L., Han B., and Grzebieta R. H. (2002). "Plastic mechanism analysis of concrete-filled double-skin (SHS inner and SHS outer) stub columns." *Thin-walled Struct.*, 40(10), 815-833.

Zhao, X. L., and Grzebieta, R. (2002). "Strength and ductility of concrete filled double skin (SHS inner and SHS outer) tubes." *Thin Wall Struct.*, 40(2), 199-213.

APPENDIX A

A COMPARISON BETWEEN SOLID AND SHELL ELEMENTS

A.1 Accuracy Assessment Based on the Simulation of an Experimental Study

Finite element analyses were conducted to simulate the behavior of thin-walled rectangular HSS sections subjected to bending. Different types of shell and solid elements were used in the simulation process. The solutions were compared to the results of an experimental study by McCormick et al. (2010), on the cyclic testing of the hollow structural sections for seismic applications in low to mid-rise moment frames.

A.1.1 Experiment Description

The HSS member was used as a vertical cantilever with a rigid connection at the base, and a top end, which was pinned to the loading frame. Rigid angles and stiffeners were used at the base connection to make sure that the plastic behavior would occur outside of the connection region and in the beam member. A slotted hole at the top of the HSS member was used to prevent the creation of axial forces because of shortening and local buckling. The hydraulic actuator allowed for rotations of up to 0.08 radians to be imparted to the beam. Rotation was calculated by dividing the horizontal displacement of the top of the beam by the length of the beam (i.e. 1537 mm).

Several different specimens were tested at that study, but only one of them was used here for accuracy checking purposes. The member used here is a rectangular HSS section with the properties mentioned in Table A.1.

Table A- 1 Properties of the HSS member used in analyses

HSS Member	t (mm)	d (mm)	b (mm)	A (mm ²)	d/t	b/t
304.8x152.4x6.4	5.91	304.8	152.4	5179	51.57	25.79

The yield stress of the steel was assumed to be 422.7 MPa (obtained from coupon tests). Figures A.1 and A.2 show a schematic of test setup and the displacement controlled load protocol used in this quasi-static test.

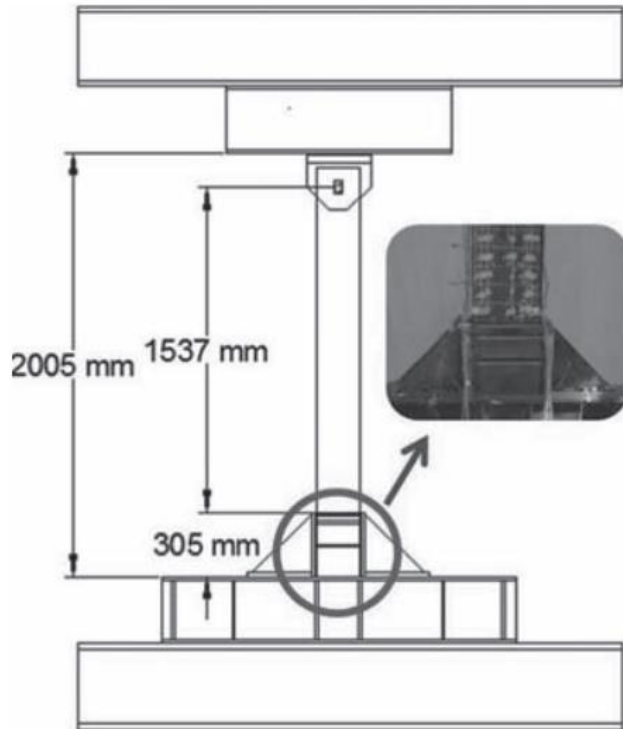


Figure A- 1 Test setup (McCormick et al., 2010)

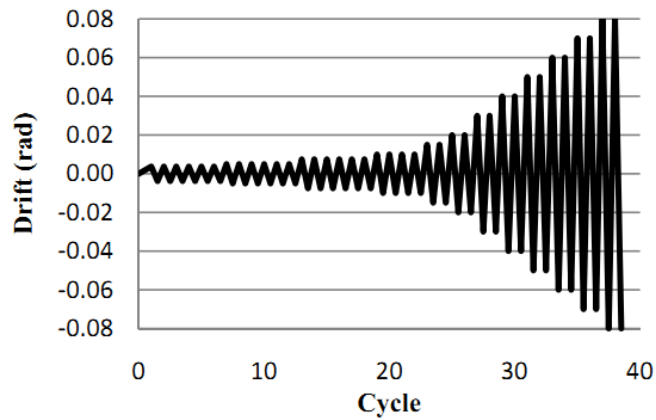


Figure A- 2 Protocol for applied displacement cycles (McCormick et al., 2010)

A.1.2 Experimental Results

Fig. A.3 shows the moment versus rotation results from the lateral cyclic loading of the HSS member.

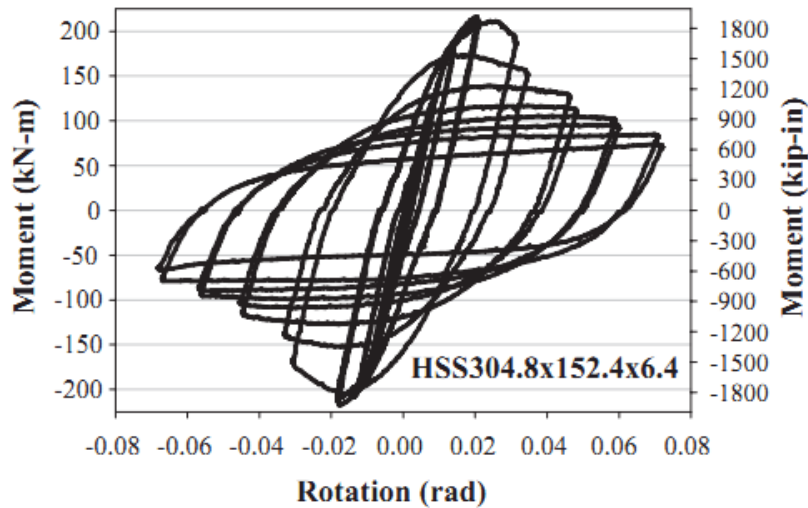


Figure A- 3 Moment vs. rotation results for HSS 304.8x152.4x6.4 (McCormick et al., 2010)

A.1.3 Simulation with 3D Shell Elements

The test was simulated using the commercial software ABAQUS with shell elements to check the accuracy of numerical results. Two different types of shell elements were used:

- S4R: 4-node thick or thin shell element with reduced integration
- S8R: 8-node thick shell reduced integration

The problem with the S8R elements was that they took more time for analysis and also had convergence problems when the model was pushed to large displacements. When the mesh is finer, the problem gets worse, because obviously a lot more work is added for the solver dealing with 8-node elements.

Fig. A.4 shows the results for a uniform 20mm×20mm mesh size with S8R elements, which have produced a behavior very similar to what was seen in Fig. A.3. Strength reduction has started at nearly the same rotation value and has eventually converged to a final value very close to the test result. The only problem was that, the analysis stopped just before the last cycle due to convergence problems.

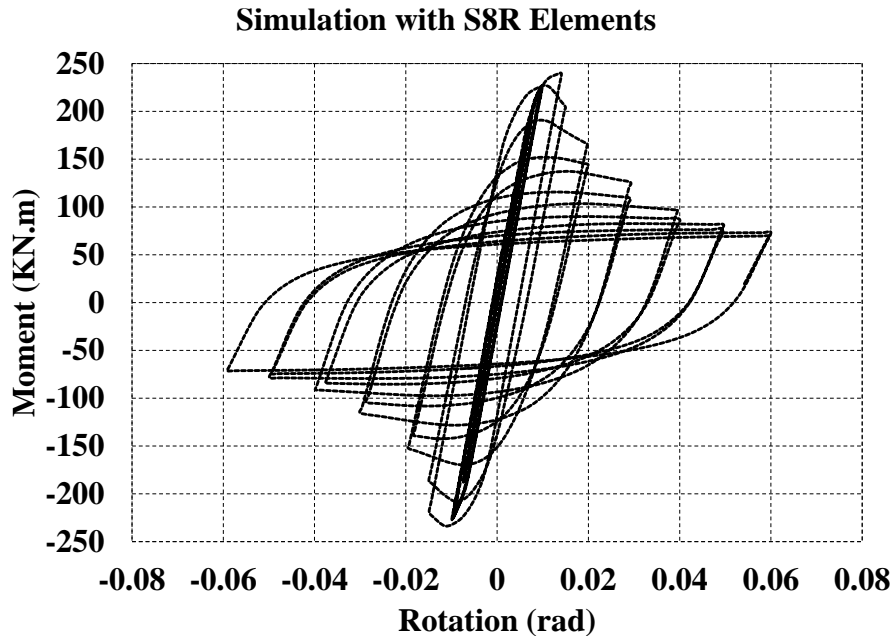


Figure A- 4 Moment vs. rotation results obtained from the model using S8R shell elements

Because the accuracy seemed to be enough, no finer mesh patterns were used with S8R elements. For the S4R elements, the same analysis was conducted with a different mesh pattern, which consisted of 20mm×20mm elements for almost the entire height of the HSS member, but was customized to be finer near the fixed base (10mm×10mm). This was done to somehow compensate for the less integration points of the S4R elements compared to the S8R type.

The moment versus rotation results from the model with S4R elements are shown in Fig. A.5. Results show that the model with S4R elements provided sufficiently accurate results for the purposes of this study. The model was also capable of simulating the last cycle of applied displacements, approving that the S4R elements are less likely to encounter convergence problems compared to the S8R types. Note that the mesh pattern for the model with S4R elements was refined at the critical locations.

A.1.4 Simulation with 3D Solid Elements

The performance of 3D solid elements was checked with results from the experimental study mentioned above to get an idea of their capability in predicting the response of thin structures. Obviously in case they prove to work well if used properly, it would be beneficial to have the options of both solid and shell

elements for these kinds of problems dealing with tubes, so that in any particular model, the one that works faster can be used. Two different types of solid elements were used in the simulation analyses:

- C3D8R: 8-node linear 3D solid element with reduced integration
- C3D20R: 20-node quadratic 3D solid element with reduced integration

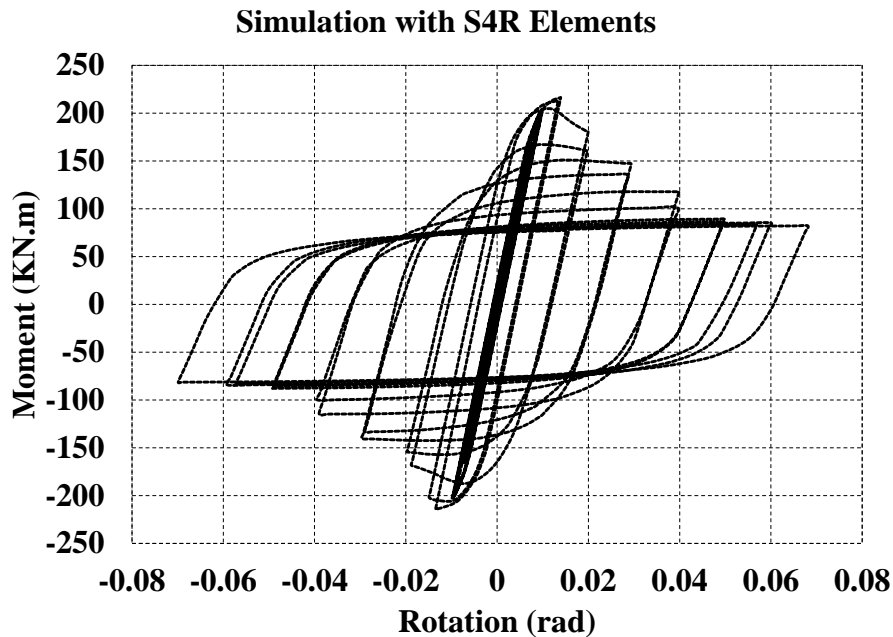


Figure A- 5 Moment vs. rotation results obtained from the model using S4R shell elements

Similarly to the case with S4R elements, a mesh with a combination of 20mm×20mm and 10mm×10mm elements, with the latter used at critical locations (i.e. near to the base of the beam for the problem at hand), was used in the models with both C3D8R and C3D20R elements. Fig. A.6 shows the results from these analyses. Although the model with C3D20R elements showed a faster strength reduction compared to the one with C3D8R elements (the 20-node elements showed generally better results), both of the models were shown to be capable of providing sufficiently accurate results for the behavior of HSS member subjected to cyclic lateral loading.

A.2. Accuracy Assessment Based on the Classical Pinched Cylinder Problem

The accuracy of shell element, which were shown to provide acceptable results for thin structures under bending, was also checked for a classical problem by comparing its results with the available analytical solution. In this example, which is one of the standard test cases used to evaluate the performance of

different element formulations, a finite length circular cylinder shell with rigid diaphragms in its ends is subjected to concentrated pinching loads. This example is especially useful because comparison can be made with known solutions like the one by Lindberg et al. (1969).

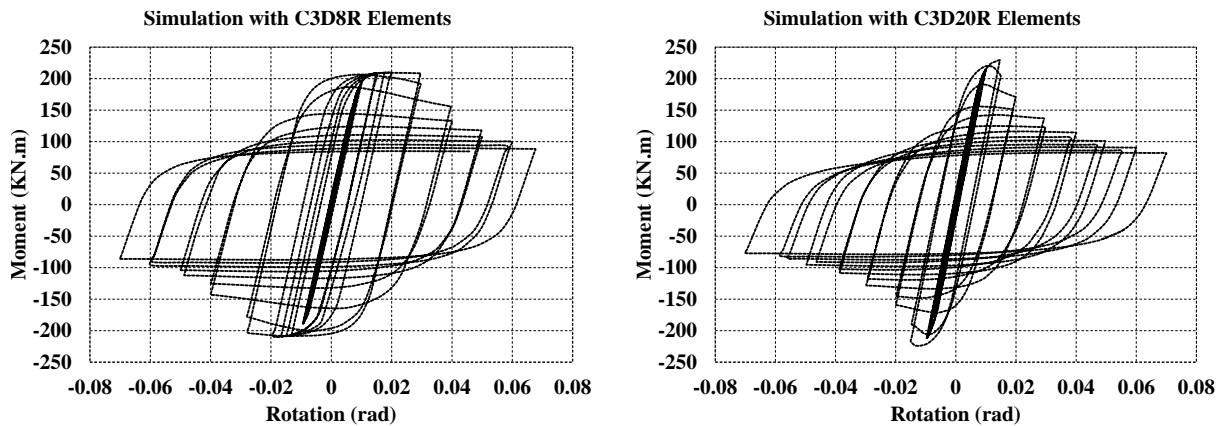


Figure A- 6 Moment vs. rotation results obtained from the models using 3D solid elements:

a) C3D8R; b) C3D20R

A.2.1 Problem Description

The geometry and material properties used for this example are shown in Fig. A.1. No units are specified since the values given are in a self-consistent set of units. The thickness of the cylinder is 1/100 of its radius, so the structure can be considered a thin shell. The mesh covers a symmetric segment of the cylinder, as indicated in the figure, with symmetry boundary conditions imposed on three edges of the mesh, while the fourth edge (the end of the cylinder) is supported by a rigid diaphragm.

The response parameter used for comparison is the radial displacement at the point where the pinching load is applied. The solution given by Lind berg et al. based on Flügge 's (1973) series solution is 1.825×10^{-4} .

A.2.2 Analysis with Shell Elements

Four different types of shell elements were used:

- S4R: 4-node thick or thin shell element with reduced integration
- S4: 4-node general purpose shell
- S8R: 8-node thick shell reduced integration
- S8R5: 8-node thin shell, reduced integration, five degrees of freedom per node

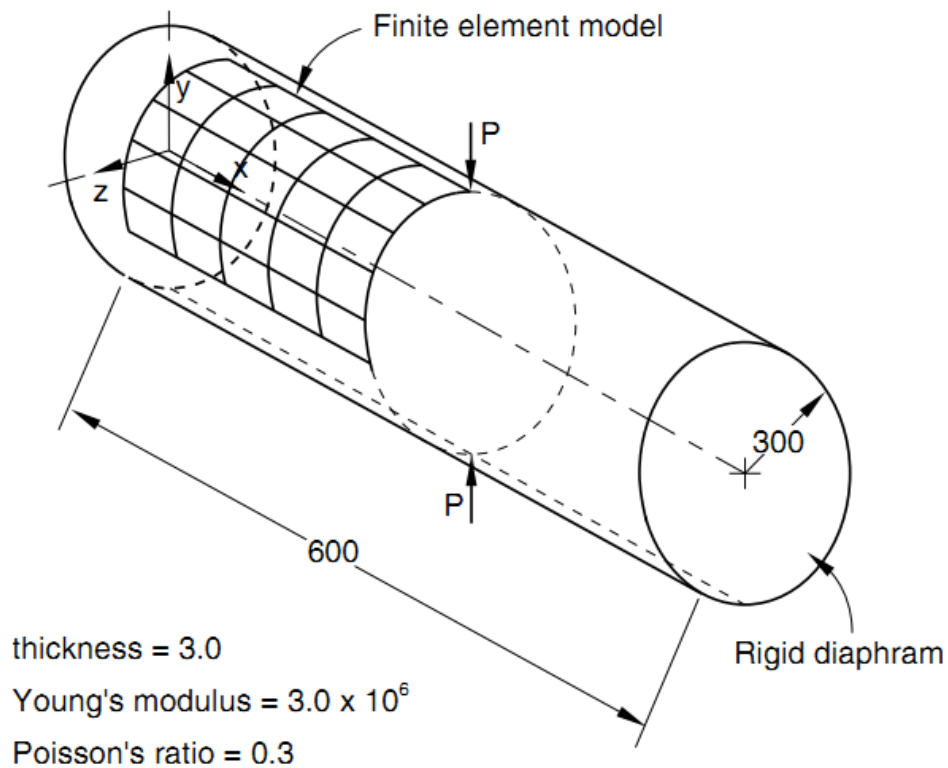


Figure A- 7 The Pinched Cylinder Problem (ABAQUS benchmark examples manual)

Note that element type with full integration formulations were also included in the models for this example. Analysis was conducted using the shell elements listed above with different mesh sizes. In all of the configurations, equal numbers of elements were generated in the both straight and curved boundaries of the model. Results are summarized in Table A.2. The column with the header, $N \times N$, shows the number of elements generated in each side. Looking into the results, it is inferred that:

- The S4R and S4 elements cannot provide acceptable results for relatively coarse mesh patterns, but their accuracy improves significantly with each step of mesh refinement.
- The S8R and S8R5 elements were able to produce relatively accurate results even when a 5×5 mesh size was used.
- Comparing the S8R and S8R5 types while used with different mesh patterns, it was shown that the S8R5 type can provide better results when a coarse mesh is used. As the mesh pattern is refined, results from the S8R element become closer to the accurate solution.

**Table A- 2 Comparison of the displacement results gained by
different types of shell elements**

Element Type	$N \times N$	Disp. (10^{-5})	Error (%)
S4R	5×5	1.086	40.49
S4	5×5	0.951	47.89
S8R	5×5	1.721	5.70
S8R5	5×5	1.804	1.15
S4R	10×10	1.591	12.82
S4	10×10	1.519	16.77
S8R	10×10	1.806	1.04
S8R5	10×10	1.832	0.38
S4R	25×25	1.803	1.21
S4	25×25	1.783	2.30
S8R	25×25	1.842	0.93
S8R5	25×25	1.846	1.15
S4R	50×50	1.838	0.71
S4	50×50	1.831	0.33
S8R	50×50	1.849	1.32
S8R5	50×50	1.851	1.42

A.3 Summary

Comparing the results shown above, it was inferred that both the 4-node shell (S4R) and 8-node solid (CD38R) elements were able to provide acceptable results if used with suitable mesh pattern for the specific problem. Note that this is contingent on identifying the parts of the structural members that will be subject to local buckling and large inelastic deformations and using a finer mesh pattern at those areas (solid elements need to be finer than shell elements at the locally buckling areas). Inability to capture these excessive deformations, stress concentrations and local instabilities will negatively impact the results. Therefore, the 4-node shell element with reduced integration (S4R) was selected as the first choice for the modeling of the steel tube in the following parts of this study, because, compared to the solid element, it

needed less mesh refinements at the locally buckling areas. Note that the 8-node solid elements were also used in a number occasions, where there was a possibility of improvement in the simulation results and also for comparative purposes.

APPENDIX B

THE WINFRITH CONCRETE MODEL

The Winfrith Concrete Model which is implemented in LS-DYNA, was originally developed for the simulation of the behavior of reinforced concrete structures under accidental impact loadings (Broadhouse and Neilson 1987). The model is a smear crack, smear rebar model that has been implemented in the 8-noded single integration point continuum element. The model was referred to and used in Section 6, Section 6.2.3 of this document. A few additional details about the formulation of this model is presented here.

The plasticity of the Winfrith model is based on the Ottosen shear failure surface, which can be defined using a four parameter formulation given as (Schwer 2011):

$$F(I_1, J_2, \cos 3\theta) = a \frac{J_2}{(f'_c)^2} + \lambda \frac{\sqrt{J_2}}{f'_c} + b \frac{I_1}{f'_c} - 1 \quad (\text{B.1})$$

in which the constants a and b define the meridional shape of the shear failure surface, $\lambda = \lambda(\cos 3\theta)$ determines the shape of the failure surface in the π -plane, and f'_c is the maximum compressive strength of concrete. Note that the constants, a and b , also depend on the ratio of the unconfined tensile strength to the unconfined compressive strength (f'_t/f'_c). It should be mentioned that while the Winfrith model uses the Ottosen shear failure surface, it does not allow the user to determine the parameters a and b . These parameters are calculated internally based on undocumented data fitting and the f'_t/f'_c ratio defined by the user. The proposed equations for the calculation of a and b parameters can be found in the study on the Winfrith model by Schwer 2011).

The Winfrith material flows plastically if failure is reached under compression, up to three orthogonal cracks can be formed in the elements according to the tensile principal stresses. When a crack is formed, the crack-normal stress decays as a linear function of the crack-normal extension. The model is capable of accounting for the shear transfer through the cracked regions due to the aggregate interlock (Broadhouse and Neilson 1987).

The formulation of the tensile crack width in the Winfrith model was based on the study by Wittmann et al. (1988), in which different parameter, including the specific fracture energy, crack opening displacement

and maximum load was measured for a large number of concrete samples. These sample tests had different configurations in terms of the aggregate size, compressive strengths, loading rates and water to cement ratios.

The model is capable of simulating the tensile crack formation in the two conditions of with and without strain rate effects. If the strain rate effects are ignored, which was the case in this study for the problem at hand, the softening branch of the behavior of concrete in tension is modeled with a linear declining path from the tensile strength at the crack width of zero to zero tensile stress at the crack width of w . As it was mentioned in Section 6, Section 6.2.3, the crack width for zero tensile stress, w , can be determined based on the CEB (1993) recommendations for the specific fracture energies for concrete material with a given unconfined compressive strength and maximum aggregate size values (Schwer 2011).

APPENDIX C

CASE STUDY: FINITE ELEMENT SIMULATION OF THE FIRST FIRE TEST (CONDUCTED ON SPECIMEN S3) USING A FULLY COUPLED TEMPERATURE-DISPLACEMENT APPROACH

As mentioned in Section 6.3.5, in order to investigate the significance of possible differences between the results of the two methods (i.e. sequentially coupled and fully coupled), which can be used for the solution of a thermal stress problem, an additional fire simulation analysis was conducted using the fully coupled method for the first fire test on Specimen S3. The element types for both steel and concrete parts in the previously used ABAQUS finite element models were changed to S4RT (4-node coupled temperature-displacement shell element) and C3D8T (8-node coupled temperature-displacement 3D brick element), respectively. The heat transfer and stress/deformation analysis steps were combined to form a single coupled step, in which the thermal and displacement equations were solved simultaneously. All of the temperature dependent thermal and structural material properties for steel and concrete were adopted from the Eurocode 4 recommendations. The gap conductance rate at the steel-concrete interface (as explained in Section 3.4.1) was selected based on the results of the sensitivity analysis in a study by Espinos et al. (2010) on finite element simulation of CFST columns subjected to fire. Results of this analysis are presented below.

Fig. C.1a shows the time history of temperature, for a point at mid-width of the concrete region, resulted from the fully coupled thermal stress analysis compared with measured values from the test and simulation results from the sequentially coupled method. Note that the recorded temperature of the outer steel tube (from the test) was applied as a boundary condition to the outer surface of the column. Fig. C.1b shows similar plots for a point on the inner steel tube. Results show a marginal difference between the two methods, thus approving the validity of the assumption, that the sequentially coupled method can be used as a sufficiently accurate alternative for the problem at hand. The almost identical results also demonstrate that the dependency of the temperature field on the stress/deformation field, in this specific problem, is limited to the gap conductance rate at the steel-concrete interface. Therefore, if a proper value is selected for this parameter, which was determined here based on the results of sensitivity analyses conducted in past studies on simulation of similar fire tests), the sequentially coupled approach can provide acceptable results.

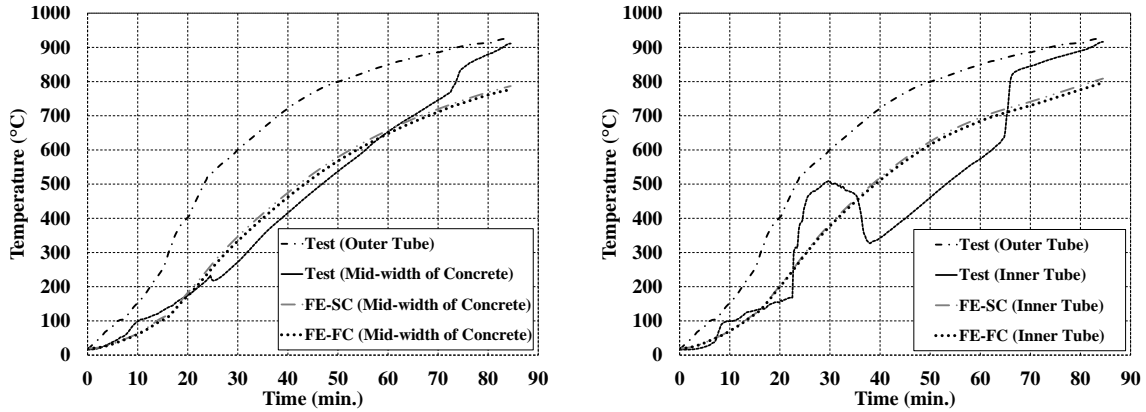


Figure C- 1 Comparison between the heat transfer results from the sequentially coupled (FE-SC) and fully coupled (FE-FC) finite element analyses: a) mid-width of concrete; b) inner tube

Fig. C.2 shows the time history of the axial deformation (extension/contraction) of Specimen S3 when subjected to axial loading and fire from the test, sequentially coupled, and fully coupled analysis results. The difference between the two simulation methods, both of which were successful in providing an acceptable replication of the experimental results, is again, marginal.

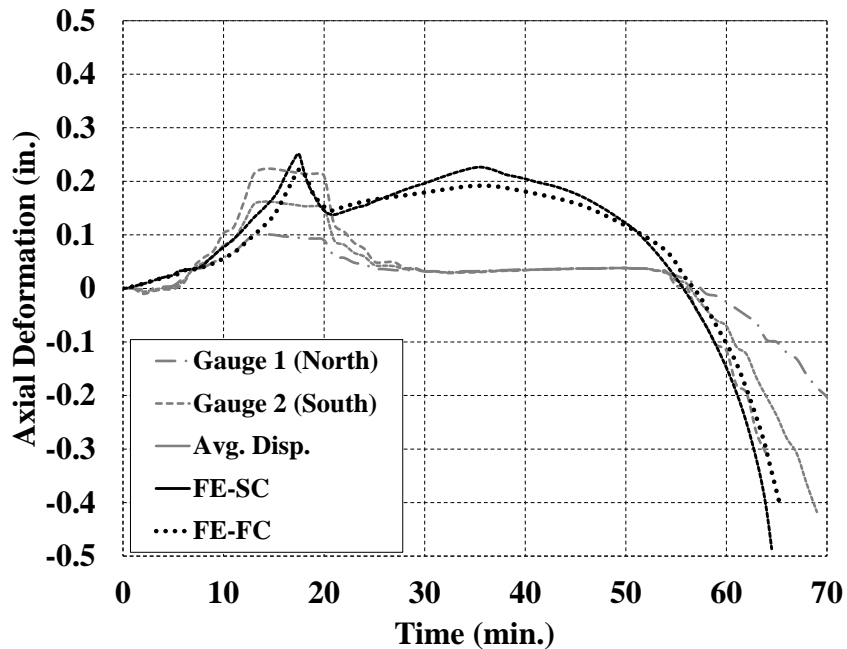


Figure C- 2 Comparison between the axial deformation results from the sequentially coupled (FE-SC) and fully coupled (FE-FC) finite element analyses

Looking at these comparisons, and the fact that the finite element models using the sequentially coupled method were validated based on the experimental results in Section 6, it is inferred that the sequentially coupled method can be used for the simulation of the behavior of CFDST columns when subjected to axial loading and fire.

MCEER Technical Reports

MCEER publishes technical reports on a variety of subjects written by authors funded through MCEER. These reports are available from both MCEER Publications and the National Technical Information Service (NTIS). Requests for reports should be directed to MCEER Publications, MCEER, University at Buffalo, State University of New York, 133A Ketter Hall, Buffalo, New York 14260. Reports can also be requested through NTIS, P.O. Box 1425, Springfield, Virginia 22151. NTIS accession numbers are shown in parenthesis, if available.

- NCEER-87-0001 "First-Year Program in Research, Education and Technology Transfer," 3/5/87, (PB88-134275, A04, MF-A01).
- NCEER-87-0002 "Experimental Evaluation of Instantaneous Optimal Algorithms for Structural Control," by R.C. Lin, T.T. Soong and A.M. Reinhorn, 4/20/87, (PB88-134341, A04, MF-A01).
- NCEER-87-0003 "Experimentation Using the Earthquake Simulation Facilities at University at Buffalo," by A.M. Reinhorn and R.L. Ketter, not available.
- NCEER-87-0004 "The System Characteristics and Performance of a Shaking Table," by J.S. Hwang, K.C. Chang and G.C. Lee, 6/1/87, (PB88-134259, A03, MF-A01). This report is available only through NTIS (see address given above).
- NCEER-87-0005 "A Finite Element Formulation for Nonlinear Viscoplastic Material Using a Q Model," by O. Gyebe and G. Dasgupta, 11/2/87, (PB88-213764, A08, MF-A01).
- NCEER-87-0006 "Symbolic Manipulation Program (SMP) - Algebraic Codes for Two and Three Dimensional Finite Element Formulations," by X. Lee and G. Dasgupta, 11/9/87, (PB88-218522, A05, MF-A01).
- NCEER-87-0007 "Instantaneous Optimal Control Laws for Tall Buildings Under Seismic Excitations," by J.N. Yang, A. Akbarpour and P. Ghaemmaghami, 6/10/87, (PB88-134333, A06, MF-A01). This report is only available through NTIS (see address given above).
- NCEER-87-0008 "IDARC: Inelastic Damage Analysis of Reinforced Concrete Frame - Shear-Wall Structures," by Y.J. Park, A.M. Reinhorn and S.K. Kunnath, 7/20/87, (PB88-134325, A09, MF-A01). This report is only available through NTIS (see address given above).
- NCEER-87-0009 "Liquefaction Potential for New York State: A Preliminary Report on Sites in Manhattan and Buffalo," by M. Budhu, V. Vijayakumar, R.F. Giese and L. Baumgras, 8/31/87, (PB88-163704, A03, MF-A01). This report is available only through NTIS (see address given above).
- NCEER-87-0010 "Vertical and Torsional Vibration of Foundations in Inhomogeneous Media," by A.S. Veletsos and K.W. Dotson, 6/1/87, (PB88-134291, A03, MF-A01). This report is only available through NTIS (see address given above).
- NCEER-87-0011 "Seismic Probabilistic Risk Assessment and Seismic Margins Studies for Nuclear Power Plants," by Howard H.M. Hwang, 6/15/87, (PB88-134267, A03, MF-A01). This report is only available through NTIS (see address given above).
- NCEER-87-0012 "Parametric Studies of Frequency Response of Secondary Systems Under Ground-Acceleration Excitations," by Y. Yong and Y.K. Lin, 6/10/87, (PB88-134309, A03, MF-A01). This report is only available through NTIS (see address given above).
- NCEER-87-0013 "Frequency Response of Secondary Systems Under Seismic Excitation," by J.A. HoLung, J. Cai and Y.K. Lin, 7/31/87, (PB88-134317, A05, MF-A01). This report is only available through NTIS (see address given above).
- NCEER-87-0014 "Modelling Earthquake Ground Motions in Seismically Active Regions Using Parametric Time Series Methods," by G.W. Ellis and A.S. Cakmak, 8/25/87, (PB88-134283, A08, MF-A01). This report is only available through NTIS (see address given above).
- NCEER-87-0015 "Detection and Assessment of Seismic Structural Damage," by E. DiPasquale and A.S. Cakmak, 8/25/87, (PB88-163712, A05, MF-A01). This report is only available through NTIS (see address given above).

- NCEER-87-0016 "Pipeline Experiment at Parkfield, California," by J. Isenberg and E. Richardson, 9/15/87, (PB88-163720, A03, MF-A01). This report is available only through NTIS (see address given above).
- NCEER-87-0017 "Digital Simulation of Seismic Ground Motion," by M. Shinozuka, G. Deodatis and T. Harada, 8/31/87, (PB88-155197, A04, MF-A01). This report is available only through NTIS (see address given above).
- NCEER-87-0018 "Practical Considerations for Structural Control: System Uncertainty, System Time Delay and Truncation of Small Control Forces," J.N. Yang and A. Akbarpour, 8/10/87, (PB88-163738, A08, MF-A01). This report is only available through NTIS (see address given above).
- NCEER-87-0019 "Modal Analysis of Nonclassically Damped Structural Systems Using Canonical Transformation," by J.N. Yang, S. Sarkani and F.X. Long, 9/27/87, (PB88-187851, A04, MF-A01).
- NCEER-87-0020 "A Nonstationary Solution in Random Vibration Theory," by J.R. Red-Horse and P.D. Spanos, 11/3/87, (PB88-163746, A03, MF-A01).
- NCEER-87-0021 "Horizontal Impedances for Radially Inhomogeneous Viscoelastic Soil Layers," by A.S. Veletsos and K.W. Dotson, 10/15/87, (PB88-150859, A04, MF-A01).
- NCEER-87-0022 "Seismic Damage Assessment of Reinforced Concrete Members," by Y.S. Chung, C. Meyer and M. Shinozuka, 10/9/87, (PB88-150867, A05, MF-A01). This report is available only through NTIS (see address given above).
- NCEER-87-0023 "Active Structural Control in Civil Engineering," by T.T. Soong, 11/11/87, (PB88-187778, A03, MF-A01).
- NCEER-87-0024 "Vertical and Torsional Impedances for Radially Inhomogeneous Viscoelastic Soil Layers," by K.W. Dotson and A.S. Veletsos, 12/87, (PB88-187786, A03, MF-A01).
- NCEER-87-0025 "Proceedings from the Symposium on Seismic Hazards, Ground Motions, Soil-Liquefaction and Engineering Practice in Eastern North America," October 20-22, 1987, edited by K.H. Jacob, 12/87, (PB88-188115, A23, MF-A01). This report is available only through NTIS (see address given above).
- NCEER-87-0026 "Report on the Whittier-Narrows, California, Earthquake of October 1, 1987," by J. Pantelic and A. Reinhorn, 11/87, (PB88-187752, A03, MF-A01). This report is available only through NTIS (see address given above).
- NCEER-87-0027 "Design of a Modular Program for Transient Nonlinear Analysis of Large 3-D Building Structures," by S. Srivastav and J.F. Abel, 12/30/87, (PB88-187950, A05, MF-A01). This report is only available through NTIS (see address given above).
- NCEER-87-0028 "Second-Year Program in Research, Education and Technology Transfer," 3/8/88, (PB88-219480, A04, MF-A01).
- NCEER-88-0001 "Workshop on Seismic Computer Analysis and Design of Buildings With Interactive Graphics," by W. McGuire, J.F. Abel and C.H. Conley, 1/18/88, (PB88-187760, A03, MF-A01). This report is only available through NTIS (see address given above).
- NCEER-88-0002 "Optimal Control of Nonlinear Flexible Structures," by J.N. Yang, F.X. Long and D. Wong, 1/22/88, (PB88-213772, A06, MF-A01).
- NCEER-88-0003 "Substructuring Techniques in the Time Domain for Primary-Secondary Structural Systems," by G.D. Manolis and G. Juhn, 2/10/88, (PB88-213780, A04, MF-A01).
- NCEER-88-0004 "Iterative Seismic Analysis of Primary-Secondary Systems," by A. Singhal, L.D. Lutes and P.D. Spanos, 2/23/88, (PB88-213798, A04, MF-A01).
- NCEER-88-0005 "Stochastic Finite Element Expansion for Random Media," by P.D. Spanos and R. Ghanem, 3/14/88, (PB88-213806, A03, MF-A01).

- NCEER-88-0006 "Combining Structural Optimization and Structural Control," by F.Y. Cheng and C.P. Pantelides, 1/10/88, (PB88-213814, A05, MF-A01).
- NCEER-88-0007 "Seismic Performance Assessment of Code-Designed Structures," by H.H-M. Hwang, J-W. Jaw and H-J. Shau, 3/20/88, (PB88-219423, A04, MF-A01). This report is only available through NTIS (see address given above).
- NCEER-88-0008 "Reliability Analysis of Code-Designed Structures Under Natural Hazards," by H.H-M. Hwang, H. Ushiba and M. Shinozuka, 2/29/88, (PB88-229471, A07, MF-A01). This report is only available through NTIS (see address given above).
- NCEER-88-0009 "Seismic Fragility Analysis of Shear Wall Structures," by J-W Jaw and H.H-M. Hwang, 4/30/88, (PB89-102867, A04, MF-A01).
- NCEER-88-0010 "Base Isolation of a Multi-Story Building Under a Harmonic Ground Motion - A Comparison of Performances of Various Systems," by F-G Fan, G. Ahmadi and I.G. Tadjbakhsh, 5/18/88, (PB89-122238, A06, MF-A01). This report is only available through NTIS (see address given above).
- NCEER-88-0011 "Seismic Floor Response Spectra for a Combined System by Green's Functions," by F.M. Lavelle, L.A. Bergman and P.D. Spanos, 5/1/88, (PB89-102875, A03, MF-A01).
- NCEER-88-0012 "A New Solution Technique for Randomly Excited Hysteretic Structures," by G.Q. Cai and Y.K. Lin, 5/16/88, (PB89-102883, A03, MF-A01).
- NCEER-88-0013 "A Study of Radiation Damping and Soil-Structure Interaction Effects in the Centrifuge," by K. Weissman, supervised by J.H. Prevost, 5/24/88, (PB89-144703, A06, MF-A01).
- NCEER-88-0014 "Parameter Identification and Implementation of a Kinematic Plasticity Model for Frictional Soils," by J.H. Prevost and D.V. Griffiths, not available.
- NCEER-88-0015 "Two- and Three- Dimensional Dynamic Finite Element Analyses of the Long Valley Dam," by D.V. Griffiths and J.H. Prevost, 6/17/88, (PB89-144711, A04, MF-A01).
- NCEER-88-0016 "Damage Assessment of Reinforced Concrete Structures in Eastern United States," by A.M. Reinhorn, M.J. Seidel, S.K. Kunnath and Y.J. Park, 6/15/88, (PB89-122220, A04, MF-A01). This report is only available through NTIS (see address given above).
- NCEER-88-0017 "Dynamic Compliance of Vertically Loaded Strip Foundations in Multilayered Viscoelastic Soils," by S. Ahmad and A.S.M. Israil, 6/17/88, (PB89-102891, A04, MF-A01).
- NCEER-88-0018 "An Experimental Study of Seismic Structural Response With Added Viscoelastic Dampers," by R.C. Lin, Z. Liang, T.T. Soong and R.H. Zhang, 6/30/88, (PB89-122212, A05, MF-A01). This report is available only through NTIS (see address given above).
- NCEER-88-0019 "Experimental Investigation of Primary - Secondary System Interaction," by G.D. Manolis, G. Juhn and A.M. Reinhorn, 5/27/88, (PB89-122204, A04, MF-A01).
- NCEER-88-0020 "A Response Spectrum Approach For Analysis of Nonclassically Damped Structures," by J.N. Yang, S. Sarkani and F.X. Long, 4/22/88, (PB89-102909, A04, MF-A01).
- NCEER-88-0021 "Seismic Interaction of Structures and Soils: Stochastic Approach," by A.S. Veletsos and A.M. Prasad, 7/21/88, (PB89-122196, A04, MF-A01). This report is only available through NTIS (see address given above).
- NCEER-88-0022 "Identification of the Serviceability Limit State and Detection of Seismic Structural Damage," by E. DiPasquale and A.S. Cakmak, 6/15/88, (PB89-122188, A05, MF-A01). This report is available only through NTIS (see address given above).
- NCEER-88-0023 "Multi-Hazard Risk Analysis: Case of a Simple Offshore Structure," by B.K. Bhartia and E.H. Vanmarcke, 7/21/88, (PB89-145213, A05, MF-A01).

- NCEER-88-0024 "Automated Seismic Design of Reinforced Concrete Buildings," by Y.S. Chung, C. Meyer and M. Shinozuka, 7/5/88, (PB89-122170, A06, MF-A01). This report is available only through NTIS (see address given above).
- NCEER-88-0025 "Experimental Study of Active Control of MDOF Structures Under Seismic Excitations," by L.L. Chung, R.C. Lin, T.T. Soong and A.M. Reinhorn, 7/10/88, (PB89-122600, A04, MF-A01).
- NCEER-88-0026 "Earthquake Simulation Tests of a Low-Rise Metal Structure," by J.S. Hwang, K.C. Chang, G.C. Lee and R.L. Ketter, 8/1/88, (PB89-102917, A04, MF-A01).
- NCEER-88-0027 "Systems Study of Urban Response and Reconstruction Due to Catastrophic Earthquakes," by F. Kozin and H.K. Zhou, 9/22/88, (PB90-162348, A04, MF-A01).
- NCEER-88-0028 "Seismic Fragility Analysis of Plane Frame Structures," by H.H-M. Hwang and Y.K. Low, 7/31/88, (PB89-131445, A06, MF-A01).
- NCEER-88-0029 "Response Analysis of Stochastic Structures," by A. Kardara, C. Bucher and M. Shinozuka, 9/22/88, (PB89-174429, A04, MF-A01).
- NCEER-88-0030 "Nonnormal Accelerations Due to Yielding in a Primary Structure," by D.C.K. Chen and L.D. Lutes, 9/19/88, (PB89-131437, A04, MF-A01).
- NCEER-88-0031 "Design Approaches for Soil-Structure Interaction," by A.S. Veletsos, A.M. Prasad and Y. Tang, 12/30/88, (PB89-174437, A03, MF-A01). This report is available only through NTIS (see address given above).
- NCEER-88-0032 "A Re-evaluation of Design Spectra for Seismic Damage Control," by C.J. Turkstra and A.G. Tallin, 11/7/88, (PB89-145221, A05, MF-A01).
- NCEER-88-0033 "The Behavior and Design of Noncontact Lap Splices Subjected to Repeated Inelastic Tensile Loading," by V.E. Sagan, P. Gergely and R.N. White, 12/8/88, (PB89-163737, A08, MF-A01).
- NCEER-88-0034 "Seismic Response of Pile Foundations," by S.M. Mamoon, P.K. Banerjee and S. Ahmad, 11/1/88, (PB89-145239, A04, MF-A01).
- NCEER-88-0035 "Modeling of R/C Building Structures With Flexible Floor Diaphragms (IDARC2)," by A.M. Reinhorn, S.K. Kunnath and N. Panahshahi, 9/7/88, (PB89-207153, A07, MF-A01).
- NCEER-88-0036 "Solution of the Dam-Reservoir Interaction Problem Using a Combination of FEM, BEM with Particular Integrals, Modal Analysis, and Substructuring," by C-S. Tsai, G.C. Lee and R.L. Ketter, 12/31/88, (PB89-207146, A04, MF-A01).
- NCEER-88-0037 "Optimal Placement of Actuators for Structural Control," by F.Y. Cheng and C.P. Pantelides, 8/15/88, (PB89-162846, A05, MF-A01).
- NCEER-88-0038 "Teflon Bearings in Aseismic Base Isolation: Experimental Studies and Mathematical Modeling," by A. Mokha, M.C. Constantinou and A.M. Reinhorn, 12/5/88, (PB89-218457, A10, MF-A01). This report is available only through NTIS (see address given above).
- NCEER-88-0039 "Seismic Behavior of Flat Slab High-Rise Buildings in the New York City Area," by P. Weidlinger and M. Ettouney, 10/15/88, (PB90-145681, A04, MF-A01).
- NCEER-88-0040 "Evaluation of the Earthquake Resistance of Existing Buildings in New York City," by P. Weidlinger and M. Ettouney, 10/15/88, not available.
- NCEER-88-0041 "Small-Scale Modeling Techniques for Reinforced Concrete Structures Subjected to Seismic Loads," by W. Kim, A. El-Attar and R.N. White, 11/22/88, (PB89-189625, A05, MF-A01).
- NCEER-88-0042 "Modeling Strong Ground Motion from Multiple Event Earthquakes," by G.W. Ellis and A.S. Cakmak, 10/15/88, (PB89-174445, A03, MF-A01).

- NCEER-88-0043 "Nonstationary Models of Seismic Ground Acceleration," by M. Grigoriu, S.E. Ruiz and E. Rosenblueth, 7/15/88, (PB89-189617, A04, MF-A01).
- NCEER-88-0044 "SARCF User's Guide: Seismic Analysis of Reinforced Concrete Frames," by Y.S. Chung, C. Meyer and M. Shinozuka, 11/9/88, (PB89-174452, A08, MF-A01).
- NCEER-88-0045 "First Expert Panel Meeting on Disaster Research and Planning," edited by J. Pantelic and J. Stoyke, 9/15/88, (PB89-174460, A05, MF-A01).
- NCEER-88-0046 "Preliminary Studies of the Effect of Degrading Infill Walls on the Nonlinear Seismic Response of Steel Frames," by C.Z. Chrysostomou, P. Gergely and J.F. Abel, 12/19/88, (PB89-208383, A05, MF-A01).
- NCEER-88-0047 "Reinforced Concrete Frame Component Testing Facility - Design, Construction, Instrumentation and Operation," by S.P. Pessiki, C. Conley, T. Bond, P. Gergely and R.N. White, 12/16/88, (PB89-174478, A04, MF-A01).
- NCEER-89-0001 "Effects of Protective Cushion and Soil Compliancy on the Response of Equipment Within a Seismically Excited Building," by J.A. HoLung, 2/16/89, (PB89-207179, A04, MF-A01).
- NCEER-89-0002 "Statistical Evaluation of Response Modification Factors for Reinforced Concrete Structures," by H.H-M. Hwang and J-W. Jaw, 2/17/89, (PB89-207187, A05, MF-A01).
- NCEER-89-0003 "Hysteretic Columns Under Random Excitation," by G-Q. Cai and Y.K. Lin, 1/9/89, (PB89-196513, A03, MF-A01).
- NCEER-89-0004 "Experimental Study of 'Elephant Foot Bulge' Instability of Thin-Walled Metal Tanks," by Z-H. Jia and R.L. Ketter, 2/22/89, (PB89-207195, A03, MF-A01).
- NCEER-89-0005 "Experiment on Performance of Buried Pipelines Across San Andreas Fault," by J. Isenberg, E. Richardson and T.D. O'Rourke, 3/10/89, (PB89-218440, A04, MF-A01). This report is available only through NTIS (see address given above).
- NCEER-89-0006 "A Knowledge-Based Approach to Structural Design of Earthquake-Resistant Buildings," by M. Subramani, P. Gergely, C.H. Conley, J.F. Abel and A.H. Zaghaw, 1/15/89, (PB89-218465, A06, MF-A01).
- NCEER-89-0007 "Liquefaction Hazards and Their Effects on Buried Pipelines," by T.D. O'Rourke and P.A. Lane, 2/1/89, (PB89-218481, A09, MF-A01).
- NCEER-89-0008 "Fundamentals of System Identification in Structural Dynamics," by H. Imai, C-B. Yun, O. Maruyama and M. Shinozuka, 1/26/89, (PB89-207211, A04, MF-A01).
- NCEER-89-0009 "Effects of the 1985 Michoacan Earthquake on Water Systems and Other Buried Lifelines in Mexico," by A.G. Ayala and M.J. O'Rourke, 3/8/89, (PB89-207229, A06, MF-A01).
- NCEER-89-R010 "NCEER Bibliography of Earthquake Education Materials," by K.E.K. Ross, Second Revision, 9/1/89, (PB90-125352, A05, MF-A01). This report is replaced by NCEER-92-0018.
- NCEER-89-0011 "Inelastic Three-Dimensional Response Analysis of Reinforced Concrete Building Structures (IDARC-3D), Part I - Modeling," by S.K. Kunnath and A.M. Reinhorn, 4/17/89, (PB90-114612, A07, MF-A01). This report is available only through NTIS (see address given above).
- NCEER-89-0012 "Recommended Modifications to ATC-14," by C.D. Poland and J.O. Malley, 4/12/89, (PB90-108648, A15, MF-A01).
- NCEER-89-0013 "Repair and Strengthening of Beam-to-Column Connections Subjected to Earthquake Loading," by M. Corazao and A.J. Durrani, 2/28/89, (PB90-109885, A06, MF-A01).
- NCEER-89-0014 "Program EXKAL2 for Identification of Structural Dynamic Systems," by O. Maruyama, C-B. Yun, M. Hoshiya and M. Shinozuka, 5/19/89, (PB90-109877, A09, MF-A01).

- NCEER-89-0015 "Response of Frames With Bolted Semi-Rigid Connections, Part I - Experimental Study and Analytical Predictions," by P.J. DiCorso, A.M. Reinhorn, J.R. Dickerson, J.B. Radzimirski and W.L. Harper, 6/1/89, not available.
- NCEER-89-0016 "ARMA Monte Carlo Simulation in Probabilistic Structural Analysis," by P.D. Spanos and M.P. Mignolet, 7/10/89, (PB90-109893, A03, MF-A01).
- NCEER-89-P017 "Preliminary Proceedings from the Conference on Disaster Preparedness - The Place of Earthquake Education in Our Schools," Edited by K.E.K. Ross, 6/23/89, (PB90-108606, A03, MF-A01).
- NCEER-89-0017 "Proceedings from the Conference on Disaster Preparedness - The Place of Earthquake Education in Our Schools," Edited by K.E.K. Ross, 12/31/89, (PB90-207895, A012, MF-A02). This report is available only through NTIS (see address given above).
- NCEER-89-0018 "Multidimensional Models of Hysteretic Material Behavior for Vibration Analysis of Shape Memory Energy Absorbing Devices, by E.J. Graesser and F.A. Cozzarelli, 6/7/89, (PB90-164146, A04, MF-A01).
- NCEER-89-0019 "Nonlinear Dynamic Analysis of Three-Dimensional Base Isolated Structures (3D-BASIS)," by S. Nagarajaiah, A.M. Reinhorn and M.C. Constantinou, 8/3/89, (PB90-161936, A06, MF-A01). This report has been replaced by NCEER-93-0011.
- NCEER-89-0020 "Structural Control Considering Time-Rate of Control Forces and Control Rate Constraints," by F.Y. Cheng and C.P. Pantelides, 8/3/89, (PB90-120445, A04, MF-A01).
- NCEER-89-0021 "Subsurface Conditions of Memphis and Shelby County," by K.W. Ng, T-S. Chang and H-H.M. Hwang, 7/26/89, (PB90-120437, A03, MF-A01).
- NCEER-89-0022 "Seismic Wave Propagation Effects on Straight Jointed Buried Pipelines," by K. Elhmadi and M.J. O'Rourke, 8/24/89, (PB90-162322, A10, MF-A02).
- NCEER-89-0023 "Workshop on Serviceability Analysis of Water Delivery Systems," edited by M. Grigoriu, 3/6/89, (PB90-127424, A03, MF-A01).
- NCEER-89-0024 "Shaking Table Study of a 1/5 Scale Steel Frame Composed of Tapered Members," by K.C. Chang, J.S. Hwang and G.C. Lee, 9/18/89, (PB90-160169, A04, MF-A01).
- NCEER-89-0025 "DYNA1D: A Computer Program for Nonlinear Seismic Site Response Analysis - Technical Documentation," by Jean H. Prevost, 9/14/89, (PB90-161944, A07, MF-A01). This report is available only through NTIS (see address given above).
- NCEER-89-0026 "1:4 Scale Model Studies of Active Tendon Systems and Active Mass Dampers for Aseismic Protection," by A.M. Reinhorn, T.T. Soong, R.C. Lin, Y.P. Yang, Y. Fukao, H. Abe and M. Nakai, 9/15/89, (PB90-173246, A10, MF-A02). This report is available only through NTIS (see address given above).
- NCEER-89-0027 "Scattering of Waves by Inclusions in a Nonhomogeneous Elastic Half Space Solved by Boundary Element Methods," by P.K. Hadley, A. Askar and A.S. Cakmak, 6/15/89, (PB90-145699, A07, MF-A01).
- NCEER-89-0028 "Statistical Evaluation of Deflection Amplification Factors for Reinforced Concrete Structures," by H.H.M. Hwang, J-W. Jaw and A.L. Ch'ng, 8/31/89, (PB90-164633, A05, MF-A01).
- NCEER-89-0029 "Bedrock Accelerations in Memphis Area Due to Large New Madrid Earthquakes," by H.H.M. Hwang, C.H.S. Chen and G. Yu, 11/7/89, (PB90-162330, A04, MF-A01).
- NCEER-89-0030 "Seismic Behavior and Response Sensitivity of Secondary Structural Systems," by Y.Q. Chen and T.T. Soong, 10/23/89, (PB90-164658, A08, MF-A01).
- NCEER-89-0031 "Random Vibration and Reliability Analysis of Primary-Secondary Structural Systems," by Y. Ibrahim, M. Grigoriu and T.T. Soong, 11/10/89, (PB90-161951, A04, MF-A01).

- NCEER-89-0032 "Proceedings from the Second U.S. - Japan Workshop on Liquefaction, Large Ground Deformation and Their Effects on Lifelines, September 26-29, 1989," Edited by T.D. O'Rourke and M. Hamada, 12/1/89, (PB90-209388, A22, MF-A03).
- NCEER-89-0033 "Deterministic Model for Seismic Damage Evaluation of Reinforced Concrete Structures," by J.M. Bracci, A.M. Reinhorn, J.B. Mander and S.K. Kunnath, 9/27/89, (PB91-108803, A06, MF-A01).
- NCEER-89-0034 "On the Relation Between Local and Global Damage Indices," by E. DiPasquale and A.S. Cakmak, 8/15/89, (PB90-173865, A05, MF-A01).
- NCEER-89-0035 "Cyclic Undrained Behavior of Nonplastic and Low Plasticity Silts," by A.J. Walker and H.E. Stewart, 7/26/89, (PB90-183518, A10, MF-A01).
- NCEER-89-0036 "Liquefaction Potential of Surficial Deposits in the City of Buffalo, New York," by M. Budhu, R. Giese and L. Baumgrass, 1/17/89, (PB90-208455, A04, MF-A01).
- NCEER-89-0037 "A Deterministic Assessment of Effects of Ground Motion Incoherence," by A.S. Veletsos and Y. Tang, 7/15/89, (PB90-164294, A03, MF-A01).
- NCEER-89-0038 "Workshop on Ground Motion Parameters for Seismic Hazard Mapping," July 17-18, 1989, edited by R.V. Whitman, 12/1/89, (PB90-173923, A04, MF-A01).
- NCEER-89-0039 "Seismic Effects on Elevated Transit Lines of the New York City Transit Authority," by C.J. Costantino, C.A. Miller and E. Heymsfield, 12/26/89, (PB90-207887, A06, MF-A01).
- NCEER-89-0040 "Centrifugal Modeling of Dynamic Soil-Structure Interaction," by K. Weissman, Supervised by J.H. Prevost, 5/10/89, (PB90-207879, A07, MF-A01).
- NCEER-89-0041 "Linearized Identification of Buildings With Cores for Seismic Vulnerability Assessment," by I-K. Ho and A.E. Aktan, 11/1/89, (PB90-251943, A07, MF-A01).
- NCEER-90-0001 "Geotechnical and Lifeline Aspects of the October 17, 1989 Loma Prieta Earthquake in San Francisco," by T.D. O'Rourke, H.E. Stewart, F.T. Blackburn and T.S. Dickerman, 1/90, (PB90-208596, A05, MF-A01).
- NCEER-90-0002 "Nonnormal Secondary Response Due to Yielding in a Primary Structure," by D.C.K. Chen and L.D. Lutes, 2/28/90, (PB90-251976, A07, MF-A01).
- NCEER-90-0003 "Earthquake Education Materials for Grades K-12," by K.E.K. Ross, 4/16/90, (PB91-251984, A05, MF-A05). This report has been replaced by NCEER-92-0018.
- NCEER-90-0004 "Catalog of Strong Motion Stations in Eastern North America," by R.W. Busby, 4/3/90, (PB90-251984, A05, MF-A01).
- NCEER-90-0005 "NCEER Strong-Motion Data Base: A User Manual for the GeoBase Release (Version 1.0 for the Sun3)," by P. Friberg and K. Jacob, 3/31/90 (PB90-258062, A04, MF-A01).
- NCEER-90-0006 "Seismic Hazard Along a Crude Oil Pipeline in the Event of an 1811-1812 Type New Madrid Earthquake," by H.H.M. Hwang and C-H.S. Chen, 4/16/90, (PB90-258054, A04, MF-A01).
- NCEER-90-0007 "Site-Specific Response Spectra for Memphis Sheahan Pumping Station," by H.H.M. Hwang and C.S. Lee, 5/15/90, (PB91-108811, A05, MF-A01).
- NCEER-90-0008 "Pilot Study on Seismic Vulnerability of Crude Oil Transmission Systems," by T. Ariman, R. Dobry, M. Grigoriu, F. Kozin, M. O'Rourke, T. O'Rourke and M. Shinozuka, 5/25/90, (PB91-108837, A06, MF-A01).
- NCEER-90-0009 "A Program to Generate Site Dependent Time Histories: EQGEN," by G.W. Ellis, M. Srinivasan and A.S. Cakmak, 1/30/90, (PB91-108829, A04, MF-A01).
- NCEER-90-0010 "Active Isolation for Seismic Protection of Operating Rooms," by M.E. Talbott, Supervised by M. Shinozuka, 6/8/9, (PB91-110205, A05, MF-A01).

- NCEER-90-0011 "Program LINEARID for Identification of Linear Structural Dynamic Systems," by C-B. Yun and M. Shinozuka, 6/25/90, (PB91-110312, A08, MF-A01).
- NCEER-90-0012 "Two-Dimensional Two-Phase Elasto-Plastic Seismic Response of Earth Dams," by A.N. Yiagos, Supervised by J.H. Prevost, 6/20/90, (PB91-110197, A13, MF-A02).
- NCEER-90-0013 "Secondary Systems in Base-Isolated Structures: Experimental Investigation, Stochastic Response and Stochastic Sensitivity," by G.D. Manolis, G. Juhn, M.C. Constantinou and A.M. Reinhorn, 7/1/90, (PB91-110320, A08, MF-A01).
- NCEER-90-0014 "Seismic Behavior of Lightly-Reinforced Concrete Column and Beam-Column Joint Details," by S.P. Pessiki, C.H. Conley, P. Gergely and R.N. White, 8/22/90, (PB91-108795, A11, MF-A02).
- NCEER-90-0015 "Two Hybrid Control Systems for Building Structures Under Strong Earthquakes," by J.N. Yang and A. Daniellians, 6/29/90, (PB91-125393, A04, MF-A01).
- NCEER-90-0016 "Instantaneous Optimal Control with Acceleration and Velocity Feedback," by J.N. Yang and Z. Li, 6/29/90, (PB91-125401, A03, MF-A01).
- NCEER-90-0017 "Reconnaissance Report on the Northern Iran Earthquake of June 21, 1990," by M. Mehrain, 10/4/90, (PB91-125377, A03, MF-A01).
- NCEER-90-0018 "Evaluation of Liquefaction Potential in Memphis and Shelby County," by T.S. Chang, P.S. Tang, C.S. Lee and H. Hwang, 8/10/90, (PB91-125427, A09, MF-A01).
- NCEER-90-0019 "Experimental and Analytical Study of a Combined Sliding Disc Bearing and Helical Steel Spring Isolation System," by M.C. Constantinou, A.S. Mokha and A.M. Reinhorn, 10/4/90, (PB91-125385, A06, MF-A01). This report is available only through NTIS (see address given above).
- NCEER-90-0020 "Experimental Study and Analytical Prediction of Earthquake Response of a Sliding Isolation System with a Spherical Surface," by A.S. Mokha, M.C. Constantinou and A.M. Reinhorn, 10/11/90, (PB91-125419, A05, MF-A01).
- NCEER-90-0021 "Dynamic Interaction Factors for Floating Pile Groups," by G. Gazetas, K. Fan, A. Kaynia and E. Kausel, 9/10/90, (PB91-170381, A05, MF-A01).
- NCEER-90-0022 "Evaluation of Seismic Damage Indices for Reinforced Concrete Structures," by S. Rodriguez-Gomez and A.S. Cakmak, 9/30/90, PB91-171322, A06, MF-A01).
- NCEER-90-0023 "Study of Site Response at a Selected Memphis Site," by H. Desai, S. Ahmad, E.S. Gazetas and M.R. Oh, 10/11/90, (PB91-196857, A03, MF-A01).
- NCEER-90-0024 "A User's Guide to Strongmo: Version 1.0 of NCEER's Strong-Motion Data Access Tool for PCs and Terminals," by P.A. Friberg and C.A.T. Susch, 11/15/90, (PB91-171272, A03, MF-A01).
- NCEER-90-0025 "A Three-Dimensional Analytical Study of Spatial Variability of Seismic Ground Motions," by L-L. Hong and A.H.-S. Ang, 10/30/90, (PB91-170399, A09, MF-A01).
- NCEER-90-0026 "MUMOID User's Guide - A Program for the Identification of Modal Parameters," by S. Rodriguez-Gomez and E. DiPasquale, 9/30/90, (PB91-171298, A04, MF-A01).
- NCEER-90-0027 "SARCF-II User's Guide - Seismic Analysis of Reinforced Concrete Frames," by S. Rodriguez-Gomez, Y.S. Chung and C. Meyer, 9/30/90, (PB91-171280, A05, MF-A01).
- NCEER-90-0028 "Viscous Dampers: Testing, Modeling and Application in Vibration and Seismic Isolation," by N. Makris and M.C. Constantinou, 12/20/90 (PB91-190561, A06, MF-A01).
- NCEER-90-0029 "Soil Effects on Earthquake Ground Motions in the Memphis Area," by H. Hwang, C.S. Lee, K.W. Ng and T.S. Chang, 8/2/90, (PB91-190751, A05, MF-A01).

- NCEER-91-0001 "Proceedings from the Third Japan-U.S. Workshop on Earthquake Resistant Design of Lifeline Facilities and Countermeasures for Soil Liquefaction, December 17-19, 1990," edited by T.D. O'Rourke and M. Hamada, 2/1/91, (PB91-179259, A99, MF-A04).
- NCEER-91-0002 "Physical Space Solutions of Non-Proportionally Damped Systems," by M. Tong, Z. Liang and G.C. Lee, 1/15/91, (PB91-179242, A04, MF-A01).
- NCEER-91-0003 "Seismic Response of Single Piles and Pile Groups," by K. Fan and G. Gazetas, 1/10/91, (PB92-174994, A04, MF-A01).
- NCEER-91-0004 "Damping of Structures: Part 1 - Theory of Complex Damping," by Z. Liang and G. Lee, 10/10/91, (PB92-197235, A12, MF-A03).
- NCEER-91-0005 "3D-BASIS - Nonlinear Dynamic Analysis of Three Dimensional Base Isolated Structures: Part II," by S. Nagarajaiah, A.M. Reinhorn and M.C. Constantinou, 2/28/91, (PB91-190553, A07, MF-A01). This report has been replaced by NCEER-93-0011.
- NCEER-91-0006 "A Multidimensional Hysteretic Model for Plasticity Deforming Metals in Energy Absorbing Devices," by E.J. Graesser and F.A. Cozzarelli, 4/9/91, (PB92-108364, A04, MF-A01).
- NCEER-91-0007 "A Framework for Customizable Knowledge-Based Expert Systems with an Application to a KBES for Evaluating the Seismic Resistance of Existing Buildings," by E.G. Ibarra-Anaya and S.J. Fennes, 4/9/91, (PB91-210930, A08, MF-A01).
- NCEER-91-0008 "Nonlinear Analysis of Steel Frames with Semi-Rigid Connections Using the Capacity Spectrum Method," by G.G. Deierlein, S-H. Hsieh, Y-J. Shen and J.F. Abel, 7/2/91, (PB92-113828, A05, MF-A01).
- NCEER-91-0009 "Earthquake Education Materials for Grades K-12," by K.E.K. Ross, 4/30/91, (PB91-212142, A06, MF-A01). This report has been replaced by NCEER-92-0018.
- NCEER-91-0010 "Phase Wave Velocities and Displacement Phase Differences in a Harmonically Oscillating Pile," by N. Makris and G. Gazetas, 7/8/91, (PB92-108356, A04, MF-A01).
- NCEER-91-0011 "Dynamic Characteristics of a Full-Size Five-Story Steel Structure and a 2/5 Scale Model," by K.C. Chang, G.C. Yao, G.C. Lee, D.S. Hao and Y.C. Yeh, 7/2/91, (PB93-116648, A06, MF-A02).
- NCEER-91-0012 "Seismic Response of a 2/5 Scale Steel Structure with Added Viscoelastic Dampers," by K.C. Chang, T.T. Soong, S-T. Oh and M.L. Lai, 5/17/91, (PB92-110816, A05, MF-A01).
- NCEER-91-0013 "Earthquake Response of Retaining Walls; Full-Scale Testing and Computational Modeling," by S. Alampalli and A-W.M. Elgamal, 6/20/91, not available.
- NCEER-91-0014 "3D-BASIS-M: Nonlinear Dynamic Analysis of Multiple Building Base Isolated Structures," by P.C. Tsopelas, S. Nagarajaiah, M.C. Constantinou and A.M. Reinhorn, 5/28/91, (PB92-113885, A09, MF-A02).
- NCEER-91-0015 "Evaluation of SEAOC Design Requirements for Sliding Isolated Structures," by D. Theodossiou and M.C. Constantinou, 6/10/91, (PB92-114602, A11, MF-A03).
- NCEER-91-0016 "Closed-Loop Modal Testing of a 27-Story Reinforced Concrete Flat Plate-Core Building," by H.R. Somaprasad, T. Toksoy, H. Yoshiyuki and A.E. Aktan, 7/15/91, (PB92-129980, A07, MF-A02).
- NCEER-91-0017 "Shake Table Test of a 1/6 Scale Two-Story Lightly Reinforced Concrete Building," by A.G. El-Attar, R.N. White and P. Gergely, 2/28/91, (PB92-222447, A06, MF-A02).
- NCEER-91-0018 "Shake Table Test of a 1/8 Scale Three-Story Lightly Reinforced Concrete Building," by A.G. El-Attar, R.N. White and P. Gergely, 2/28/91, (PB93-116630, A08, MF-A02).
- NCEER-91-0019 "Transfer Functions for Rigid Rectangular Foundations," by A.S. Veletsos, A.M. Prasad and W.H. Wu, 7/31/91, not available.

- NCEER-91-0020 "Hybrid Control of Seismic-Excited Nonlinear and Inelastic Structural Systems," by J.N. Yang, Z. Li and A. Daniellians, 8/1/91, (PB92-143171, A06, MF-A02).
- NCEER-91-0021 "The NCEER-91 Earthquake Catalog: Improved Intensity-Based Magnitudes and Recurrence Relations for U.S. Earthquakes East of New Madrid," by L. Seeber and J.G. Armbruster, 8/28/91, (PB92-176742, A06, MF-A02).
- NCEER-91-0022 "Proceedings from the Implementation of Earthquake Planning and Education in Schools: The Need for Change - The Roles of the Changemakers," by K.E.K. Ross and F. Winslow, 7/23/91, (PB92-129998, A12, MF-A03).
- NCEER-91-0023 "A Study of Reliability-Based Criteria for Seismic Design of Reinforced Concrete Frame Buildings," by H.H.M. Hwang and H-M. Hsu, 8/10/91, (PB92-140235, A09, MF-A02).
- NCEER-91-0024 "Experimental Verification of a Number of Structural System Identification Algorithms," by R.G. Ghanem, H. Gavin and M. Shinozuka, 9/18/91, (PB92-176577, A18, MF-A04).
- NCEER-91-0025 "Probabilistic Evaluation of Liquefaction Potential," by H.H.M. Hwang and C.S. Lee," 11/25/91, (PB92-143429, A05, MF-A01).
- NCEER-91-0026 "Instantaneous Optimal Control for Linear, Nonlinear and Hysteretic Structures - Stable Controllers," by J.N. Yang and Z. Li, 11/15/91, (PB92-163807, A04, MF-A01).
- NCEER-91-0027 "Experimental and Theoretical Study of a Sliding Isolation System for Bridges," by M.C. Constantinou, A. Kartoum, A.M. Reinhorn and P. Bradford, 11/15/91, (PB92-176973, A10, MF-A03).
- NCEER-92-0001 "Case Studies of Liquefaction and Lifeline Performance During Past Earthquakes, Volume 1: Japanese Case Studies," Edited by M. Hamada and T. O'Rourke, 2/17/92, (PB92-197243, A18, MF-A04).
- NCEER-92-0002 "Case Studies of Liquefaction and Lifeline Performance During Past Earthquakes, Volume 2: United States Case Studies," Edited by T. O'Rourke and M. Hamada, 2/17/92, (PB92-197250, A20, MF-A04).
- NCEER-92-0003 "Issues in Earthquake Education," Edited by K. Ross, 2/3/92, (PB92-222389, A07, MF-A02).
- NCEER-92-0004 "Proceedings from the First U.S. - Japan Workshop on Earthquake Protective Systems for Bridges," Edited by I.G. Buckle, 2/4/92, (PB94-142239, A99, MF-A06).
- NCEER-92-0005 "Seismic Ground Motion from a Haskell-Type Source in a Multiple-Layered Half-Space," A.P. Theoharis, G. Deodatis and M. Shinozuka, 1/2/92, not available.
- NCEER-92-0006 "Proceedings from the Site Effects Workshop," Edited by R. Whitman, 2/29/92, (PB92-197201, A04, MF-A01).
- NCEER-92-0007 "Engineering Evaluation of Permanent Ground Deformations Due to Seismically-Induced Liquefaction," by M.H. Baziar, R. Dobry and A-W.M. Elgamal, 3/24/92, (PB92-222421, A13, MF-A03).
- NCEER-92-0008 "A Procedure for the Seismic Evaluation of Buildings in the Central and Eastern United States," by C.D. Poland and J.O. Malley, 4/2/92, (PB92-222439, A20, MF-A04).
- NCEER-92-0009 "Experimental and Analytical Study of a Hybrid Isolation System Using Friction Controllable Sliding Bearings," by M.Q. Feng, S. Fujii and M. Shinozuka, 5/15/92, (PB93-150282, A06, MF-A02).
- NCEER-92-0010 "Seismic Resistance of Slab-Column Connections in Existing Non-Ductile Flat-Plate Buildings," by A.J. Durrani and Y. Du, 5/18/92, (PB93-116812, A06, MF-A02).
- NCEER-92-0011 "The Hysteretic and Dynamic Behavior of Brick Masonry Walls Upgraded by Ferrocement Coatings Under Cyclic Loading and Strong Simulated Ground Motion," by H. Lee and S.P. Prawel, 5/11/92, not available.
- NCEER-92-0012 "Study of Wire Rope Systems for Seismic Protection of Equipment in Buildings," by G.F. Demetriades, M.C. Constantinou and A.M. Reinhorn, 5/20/92, (PB93-116655, A08, MF-A02).

- NCEER-92-0013 "Shape Memory Structural Dampers: Material Properties, Design and Seismic Testing," by P.R. Witting and F.A. Cozzarelli, 5/26/92, (PB93-116663, A05, MF-A01).
- NCEER-92-0014 "Longitudinal Permanent Ground Deformation Effects on Buried Continuous Pipelines," by M.J. O'Rourke, and C. Nordberg, 6/15/92, (PB93-116671, A08, MF-A02).
- NCEER-92-0015 "A Simulation Method for Stationary Gaussian Random Functions Based on the Sampling Theorem," by M. Grigoriu and S. Balopoulou, 6/11/92, (PB93-127496, A05, MF-A01).
- NCEER-92-0016 "Gravity-Load-Designed Reinforced Concrete Buildings: Seismic Evaluation of Existing Construction and Detailing Strategies for Improved Seismic Resistance," by G.W. Hoffmann, S.K. Kunnath, A.M. Reinhorn and J.B. Mander, 7/15/92, (PB94-142007, A08, MF-A02).
- NCEER-92-0017 "Observations on Water System and Pipeline Performance in the Limón Area of Costa Rica Due to the April 22, 1991 Earthquake," by M. O'Rourke and D. Ballantyne, 6/30/92, (PB93-126811, A06, MF-A02).
- NCEER-92-0018 "Fourth Edition of Earthquake Education Materials for Grades K-12," Edited by K.E.K. Ross, 8/10/92, (PB93-114023, A07, MF-A02).
- NCEER-92-0019 "Proceedings from the Fourth Japan-U.S. Workshop on Earthquake Resistant Design of Lifeline Facilities and Countermeasures for Soil Liquefaction," Edited by M. Hamada and T.D. O'Rourke, 8/12/92, (PB93-163939, A99, MF-E11).
- NCEER-92-0020 "Active Bracing System: A Full Scale Implementation of Active Control," by A.M. Reinhorn, T.T. Soong, R.C. Lin, M.A. Riley, Y.P. Wang, S. Aizawa and M. Higashino, 8/14/92, (PB93-127512, A06, MF-A02).
- NCEER-92-0021 "Empirical Analysis of Horizontal Ground Displacement Generated by Liquefaction-Induced Lateral Spreads," by S.F. Bartlett and T.L. Youd, 8/17/92, (PB93-188241, A06, MF-A02).
- NCEER-92-0022 "IDARC Version 3.0: Inelastic Damage Analysis of Reinforced Concrete Structures," by S.K. Kunnath, A.M. Reinhorn and R.F. Lobo, 8/31/92, (PB93-227502, A07, MF-A02).
- NCEER-92-0023 "A Semi-Empirical Analysis of Strong-Motion Peaks in Terms of Seismic Source, Propagation Path and Local Site Conditions, by M. Kamiyama, M.J. O'Rourke and R. Flores-Berrones, 9/9/92, (PB93-150266, A08, MF-A02).
- NCEER-92-0024 "Seismic Behavior of Reinforced Concrete Frame Structures with Nonductile Details, Part I: Summary of Experimental Findings of Full Scale Beam-Column Joint Tests," by A. Beres, R.N. White and P. Gergely, 9/30/92, (PB93-227783, A05, MF-A01).
- NCEER-92-0025 "Experimental Results of Repaired and Retrofitted Beam-Column Joint Tests in Lightly Reinforced Concrete Frame Buildings," by A. Beres, S. El-Borgi, R.N. White and P. Gergely, 10/29/92, (PB93-227791, A05, MF-A01).
- NCEER-92-0026 "A Generalization of Optimal Control Theory: Linear and Nonlinear Structures," by J.N. Yang, Z. Li and S. Vongchavalitkul, 11/2/92, (PB93-188621, A05, MF-A01).
- NCEER-92-0027 "Seismic Resistance of Reinforced Concrete Frame Structures Designed Only for Gravity Loads: Part I - Design and Properties of a One-Third Scale Model Structure," by J.M. Bracci, A.M. Reinhorn and J.B. Mander, 12/1/92, (PB94-104502, A08, MF-A02).
- NCEER-92-0028 "Seismic Resistance of Reinforced Concrete Frame Structures Designed Only for Gravity Loads: Part II - Experimental Performance of Subassemblages," by L.E. Aycaardi, J.B. Mander and A.M. Reinhorn, 12/1/92, (PB94-104510, A08, MF-A02).
- NCEER-92-0029 "Seismic Resistance of Reinforced Concrete Frame Structures Designed Only for Gravity Loads: Part III - Experimental Performance and Analytical Study of a Structural Model," by J.M. Bracci, A.M. Reinhorn and J.B. Mander, 12/1/92, (PB93-227528, A09, MF-A01).

- NCEER-92-0030 "Evaluation of Seismic Retrofit of Reinforced Concrete Frame Structures: Part I - Experimental Performance of Retrofitted Subassemblages," by D. Choudhuri, J.B. Mander and A.M. Reinhorn, 12/8/92, (PB93-198307, A07, MF-A02).
- NCEER-92-0031 "Evaluation of Seismic Retrofit of Reinforced Concrete Frame Structures: Part II - Experimental Performance and Analytical Study of a Retrofitted Structural Model," by J.M. Bracci, A.M. Reinhorn and J.B. Mander, 12/8/92, (PB93-198315, A09, MF-A03).
- NCEER-92-0032 "Experimental and Analytical Investigation of Seismic Response of Structures with Supplemental Fluid Viscous Dampers," by M.C. Constantinou and M.D. Symans, 12/21/92, (PB93-191435, A10, MF-A03). This report is available only through NTIS (see address given above).
- NCEER-92-0033 "Reconnaissance Report on the Cairo, Egypt Earthquake of October 12, 1992," by M. Khater, 12/23/92, (PB93-188621, A03, MF-A01).
- NCEER-92-0034 "Low-Level Dynamic Characteristics of Four Tall Flat-Plate Buildings in New York City," by H. Gavin, S. Yuan, J. Grossman, E. Pekelis and K. Jacob, 12/28/92, (PB93-188217, A07, MF-A02).
- NCEER-93-0001 "An Experimental Study on the Seismic Performance of Brick-Infilled Steel Frames With and Without Retrofit," by J.B. Mander, B. Nair, K. Wojtkowski and J. Ma, 1/29/93, (PB93-227510, A07, MF-A02).
- NCEER-93-0002 "Social Accounting for Disaster Preparedness and Recovery Planning," by S. Cole, E. Pantoja and V. Razak, 2/22/93, (PB94-142114, A12, MF-A03).
- NCEER-93-0003 "Assessment of 1991 NEHRP Provisions for Nonstructural Components and Recommended Revisions," by T.T. Soong, G. Chen, Z. Wu, R-H. Zhang and M. Grigoriu, 3/1/93, (PB93-188639, A06, MF-A02).
- NCEER-93-0004 "Evaluation of Static and Response Spectrum Analysis Procedures of SEAOC/UBC for Seismic Isolated Structures," by C.W. Winters and M.C. Constantinou, 3/23/93, (PB93-198299, A10, MF-A03).
- NCEER-93-0005 "Earthquakes in the Northeast - Are We Ignoring the Hazard? A Workshop on Earthquake Science and Safety for Educators," edited by K.E.K. Ross, 4/2/93, (PB94-103066, A09, MF-A02).
- NCEER-93-0006 "Inelastic Response of Reinforced Concrete Structures with Viscoelastic Braces," by R.F. Lobo, J.M. Bracci, K.L. Shen, A.M. Reinhorn and T.T. Soong, 4/5/93, (PB93-227486, A05, MF-A02).
- NCEER-93-0007 "Seismic Testing of Installation Methods for Computers and Data Processing Equipment," by K. Kosar, T.T. Soong, K.L. Shen, J.A. HoLung and Y.K. Lin, 4/12/93, (PB93-198299, A07, MF-A02).
- NCEER-93-0008 "Retrofit of Reinforced Concrete Frames Using Added Dampers," by A. Reinhorn, M. Constantinou and C. Li, not available.
- NCEER-93-0009 "Seismic Behavior and Design Guidelines for Steel Frame Structures with Added Viscoelastic Dampers," by K.C. Chang, M.L. Lai, T.T. Soong, D.S. Hao and Y.C. Yeh, 5/1/93, (PB94-141959, A07, MF-A02).
- NCEER-93-0010 "Seismic Performance of Shear-Critical Reinforced Concrete Bridge Piers," by J.B. Mander, S.M. Waheed, M.T.A. Chaudhary and S.S. Chen, 5/12/93, (PB93-227494, A08, MF-A02).
- NCEER-93-0011 "3D-BASIS-TABS: Computer Program for Nonlinear Dynamic Analysis of Three Dimensional Base Isolated Structures," by S. Nagarajaiah, C. Li, A.M. Reinhorn and M.C. Constantinou, 8/2/93, (PB94-141819, A09, MF-A02).
- NCEER-93-0012 "Effects of Hydrocarbon Spills from an Oil Pipeline Break on Ground Water," by O.J. Helweg and H.H.M. Hwang, 8/3/93, (PB94-141942, A06, MF-A02).
- NCEER-93-0013 "Simplified Procedures for Seismic Design of Nonstructural Components and Assessment of Current Code Provisions," by M.P. Singh, L.E. Suarez, E.E. Matheu and G.O. Maldonado, 8/4/93, (PB94-141827, A09, MF-A02).
- NCEER-93-0014 "An Energy Approach to Seismic Analysis and Design of Secondary Systems," by G. Chen and T.T. Soong, 8/6/93, (PB94-142767, A11, MF-A03).

- NCEER-93-0015 "Proceedings from School Sites: Becoming Prepared for Earthquakes - Commemorating the Third Anniversary of the Loma Prieta Earthquake," Edited by F.E. Winslow and K.E.K. Ross, 8/16/93, (PB94-154275, A16, MF-A02).
- NCEER-93-0016 "Reconnaissance Report of Damage to Historic Monuments in Cairo, Egypt Following the October 12, 1992 Dahshur Earthquake," by D. Sykora, D. Look, G. Croci, E. Karaesmen and E. Karaesmen, 8/19/93, (PB94-142221, A08, MF-A02).
- NCEER-93-0017 "The Island of Guam Earthquake of August 8, 1993," by S.W. Swan and S.K. Harris, 9/30/93, (PB94-141843, A04, MF-A01).
- NCEER-93-0018 "Engineering Aspects of the October 12, 1992 Egyptian Earthquake," by A.W. Elgamal, M. Amer, K. Adalier and A. Abul-Fadl, 10/7/93, (PB94-141983, A05, MF-A01).
- NCEER-93-0019 "Development of an Earthquake Motion Simulator and its Application in Dynamic Centrifuge Testing," by I. Krstelj, Supervised by J.H. Prevost, 10/23/93, (PB94-181773, A-10, MF-A03).
- NCEER-93-0020 "NCEER-Taisei Corporation Research Program on Sliding Seismic Isolation Systems for Bridges: Experimental and Analytical Study of a Friction Pendulum System (FPS)," by M.C. Constantinou, P. Tsopelas, Y-S. Kim and S. Okamoto, 11/1/93, (PB94-142775, A08, MF-A02).
- NCEER-93-0021 "Finite Element Modeling of Elastomeric Seismic Isolation Bearings," by L.J. Billings, Supervised by R. Shepherd, 11/8/93, not available.
- NCEER-93-0022 "Seismic Vulnerability of Equipment in Critical Facilities: Life-Safety and Operational Consequences," by K. Porter, G.S. Johnson, M.M. Zadeh, C. Scawthorn and S. Eder, 11/24/93, (PB94-181765, A16, MF-A03).
- NCEER-93-0023 "Hokkaido Nansei-oki, Japan Earthquake of July 12, 1993, by P.I. Yanev and C.R. Scawthorn, 12/23/93, (PB94-181500, A07, MF-A01).
- NCEER-94-0001 "An Evaluation of Seismic Serviceability of Water Supply Networks with Application to the San Francisco Auxiliary Water Supply System," by I. Markov, Supervised by M. Grigoriu and T. O'Rourke, 1/21/94, (PB94-204013, A07, MF-A02).
- NCEER-94-0002 "NCEER-Taisei Corporation Research Program on Sliding Seismic Isolation Systems for Bridges: Experimental and Analytical Study of Systems Consisting of Sliding Bearings, Rubber Restoring Force Devices and Fluid Dampers," Volumes I and II, by P. Tsopelas, S. Okamoto, M.C. Constantinou, D. Ozaki and S. Fujii, 2/4/94, (PB94-181740, A09, MF-A02 and PB94-181757, A12, MF-A03).
- NCEER-94-0003 "A Markov Model for Local and Global Damage Indices in Seismic Analysis," by S. Rahman and M. Grigoriu, 2/18/94, (PB94-206000, A12, MF-A03).
- NCEER-94-0004 "Proceedings from the NCEER Workshop on Seismic Response of Masonry Infills," edited by D.P. Abrams, 3/1/94, (PB94-180783, A07, MF-A02).
- NCEER-94-0005 "The Northridge, California Earthquake of January 17, 1994: General Reconnaissance Report," edited by J.D. Goltz, 3/11/94, (PB94-193943, A10, MF-A03).
- NCEER-94-0006 "Seismic Energy Based Fatigue Damage Analysis of Bridge Columns: Part I - Evaluation of Seismic Capacity," by G.A. Chang and J.B. Mander, 3/14/94, (PB94-219185, A11, MF-A03).
- NCEER-94-0007 "Seismic Isolation of Multi-Story Frame Structures Using Spherical Sliding Isolation Systems," by T.M. Al-Hussaini, V.A. Zayas and M.C. Constantinou, 3/17/94, (PB94-193745, A09, MF-A02).
- NCEER-94-0008 "The Northridge, California Earthquake of January 17, 1994: Performance of Highway Bridges," edited by I.G. Buckle, 3/24/94, (PB94-193851, A06, MF-A02).
- NCEER-94-0009 "Proceedings of the Third U.S.-Japan Workshop on Earthquake Protective Systems for Bridges," edited by I.G. Buckle and I. Friedland, 3/31/94, (PB94-195815, A99, MF-A06).

- NCEER-94-0010 "3D-BASIS-ME: Computer Program for Nonlinear Dynamic Analysis of Seismically Isolated Single and Multiple Structures and Liquid Storage Tanks," by P.C. Tsopelas, M.C. Constantinou and A.M. Reinhorn, 4/12/94, (PB94-204922, A09, MF-A02).
- NCEER-94-0011 "The Northridge, California Earthquake of January 17, 1994: Performance of Gas Transmission Pipelines," by T.D. O'Rourke and M.C. Palmer, 5/16/94, (PB94-204989, A05, MF-A01).
- NCEER-94-0012 "Feasibility Study of Replacement Procedures and Earthquake Performance Related to Gas Transmission Pipelines," by T.D. O'Rourke and M.C. Palmer, 5/25/94, (PB94-206638, A09, MF-A02).
- NCEER-94-0013 "Seismic Energy Based Fatigue Damage Analysis of Bridge Columns: Part II - Evaluation of Seismic Demand," by G.A. Chang and J.B. Mander, 6/1/94, (PB95-18106, A08, MF-A02).
- NCEER-94-0014 "NCEER-Taisei Corporation Research Program on Sliding Seismic Isolation Systems for Bridges: Experimental and Analytical Study of a System Consisting of Sliding Bearings and Fluid Restoring Force/Damping Devices," by P. Tsopelas and M.C. Constantinou, 6/13/94, (PB94-219144, A10, MF-A03).
- NCEER-94-0015 "Generation of Hazard-Consistent Fragility Curves for Seismic Loss Estimation Studies," by H. Hwang and J-R. Huo, 6/14/94, (PB95-181996, A09, MF-A02).
- NCEER-94-0016 "Seismic Study of Building Frames with Added Energy-Absorbing Devices," by W.S. Pong, C.S. Tsai and G.C. Lee, 6/20/94, (PB94-219136, A10, A03).
- NCEER-94-0017 "Sliding Mode Control for Seismic-Excited Linear and Nonlinear Civil Engineering Structures," by J. Yang, J. Wu, A. Agrawal and Z. Li, 6/21/94, (PB95-138483, A06, MF-A02).
- NCEER-94-0018 "3D-BASIS-TABS Version 2.0: Computer Program for Nonlinear Dynamic Analysis of Three Dimensional Base Isolated Structures," by A.M. Reinhorn, S. Nagarajaiah, M.C. Constantinou, P. Tsopelas and R. Li, 6/22/94, (PB95-182176, A08, MF-A02).
- NCEER-94-0019 "Proceedings of the International Workshop on Civil Infrastructure Systems: Application of Intelligent Systems and Advanced Materials on Bridge Systems," Edited by G.C. Lee and K.C. Chang, 7/18/94, (PB95-252474, A20, MF-A04).
- NCEER-94-0020 "Study of Seismic Isolation Systems for Computer Floors," by V. Lambrou and M.C. Constantinou, 7/19/94, (PB95-138533, A10, MF-A03).
- NCEER-94-0021 "Proceedings of the U.S.-Italian Workshop on Guidelines for Seismic Evaluation and Rehabilitation of Unreinforced Masonry Buildings," Edited by D.P. Abrams and G.M. Calvi, 7/20/94, (PB95-138749, A13, MF-A03).
- NCEER-94-0022 "NCEER-Taisei Corporation Research Program on Sliding Seismic Isolation Systems for Bridges: Experimental and Analytical Study of a System Consisting of Lubricated PTFE Sliding Bearings and Mild Steel Dampers," by P. Tsopelas and M.C. Constantinou, 7/22/94, (PB95-182184, A08, MF-A02).
- NCEER-94-0023 "Development of Reliability-Based Design Criteria for Buildings Under Seismic Load," by Y.K. Wen, H. Hwang and M. Shinozuka, 8/1/94, (PB95-211934, A08, MF-A02).
- NCEER-94-0024 "Experimental Verification of Acceleration Feedback Control Strategies for an Active Tendon System," by S.J. Dyke, B.F. Spencer, Jr., P. Quast, M.K. Sain, D.C. Kaspari, Jr. and T.T. Soong, 8/29/94, (PB95-212320, A05, MF-A01).
- NCEER-94-0025 "Seismic Retrofitting Manual for Highway Bridges," Edited by I.G. Buckle and I.F. Friedland, published by the Federal Highway Administration (PB95-212676, A15, MF-A03).
- NCEER-94-0026 "Proceedings from the Fifth U.S.-Japan Workshop on Earthquake Resistant Design of Lifeline Facilities and Countermeasures Against Soil Liquefaction," Edited by T.D. O'Rourke and M. Hamada, 11/7/94, (PB95-220802, A99, MF-E08).

- NCEER-95-0001 “Experimental and Analytical Investigation of Seismic Retrofit of Structures with Supplemental Damping: Part 1 - Fluid Viscous Damping Devices,” by A.M. Reinhorn, C. Li and M.C. Constantinou, 1/3/95, (PB95-266599, A09, MF-A02).
- NCEER-95-0002 “Experimental and Analytical Study of Low-Cycle Fatigue Behavior of Semi-Rigid Top-And-Seat Angle Connections,” by G. Pekcan, J.B. Mander and S.S. Chen, 1/5/95, (PB95-220042, A07, MF-A02).
- NCEER-95-0003 “NCEER-ATC Joint Study on Fragility of Buildings,” by T. Anagnos, C. Rojahn and A.S. Kiremidjian, 1/20/95, (PB95-220026, A06, MF-A02).
- NCEER-95-0004 “Nonlinear Control Algorithms for Peak Response Reduction,” by Z. Wu, T.T. Soong, V. Gattulli and R.C. Lin, 2/16/95, (PB95-220349, A05, MF-A01).
- NCEER-95-0005 “Pipeline Replacement Feasibility Study: A Methodology for Minimizing Seismic and Corrosion Risks to Underground Natural Gas Pipelines,” by R.T. Eguchi, H.A. Seligson and D.G. Honegger, 3/2/95, (PB95-252326, A06, MF-A02).
- NCEER-95-0006 “Evaluation of Seismic Performance of an 11-Story Frame Building During the 1994 Northridge Earthquake,” by F. Naeim, R. DiSulio, K. Benuska, A. Reinhorn and C. Li, not available.
- NCEER-95-0007 “Prioritization of Bridges for Seismic Retrofitting,” by N. Basöz and A.S. Kiremidjian, 4/24/95, (PB95-252300, A08, MF-A02).
- NCEER-95-0008 “Method for Developing Motion Damage Relationships for Reinforced Concrete Frames,” by A. Singhal and A.S. Kiremidjian, 5/11/95, (PB95-266607, A06, MF-A02).
- NCEER-95-0009 “Experimental and Analytical Investigation of Seismic Retrofit of Structures with Supplemental Damping: Part II - Friction Devices,” by C. Li and A.M. Reinhorn, 7/6/95, (PB96-128087, A11, MF-A03).
- NCEER-95-0010 “Experimental Performance and Analytical Study of a Non-Ductile Reinforced Concrete Frame Structure Retrofitted with Elastomeric Spring Dampers,” by G. Pekcan, J.B. Mander and S.S. Chen, 7/14/95, (PB96-137161, A08, MF-A02).
- NCEER-95-0011 “Development and Experimental Study of Semi-Active Fluid Damping Devices for Seismic Protection of Structures,” by M.D. Symans and M.C. Constantinou, 8/3/95, (PB96-136940, A23, MF-A04).
- NCEER-95-0012 “Real-Time Structural Parameter Modification (RSPM): Development of Innervated Structures,” by Z. Liang, M. Tong and G.C. Lee, 4/11/95, (PB96-137153, A06, MF-A01).
- NCEER-95-0013 “Experimental and Analytical Investigation of Seismic Retrofit of Structures with Supplemental Damping: Part III - Viscous Damping Walls,” by A.M. Reinhorn and C. Li, 10/1/95, (PB96-176409, A11, MF-A03).
- NCEER-95-0014 “Seismic Fragility Analysis of Equipment and Structures in a Memphis Electric Substation,” by J-R. Huo and H.H.M. Hwang, 8/10/95, (PB96-128087, A09, MF-A02).
- NCEER-95-0015 “The Hanshin-Awaji Earthquake of January 17, 1995: Performance of Lifelines,” Edited by M. Shinozuka, 11/3/95, (PB96-176383, A15, MF-A03).
- NCEER-95-0016 “Highway Culvert Performance During Earthquakes,” by T.L. Youd and C.J. Beckman, available as NCEER-96-0015.
- NCEER-95-0017 “The Hanshin-Awaji Earthquake of January 17, 1995: Performance of Highway Bridges,” Edited by I.G. Buckle, 12/1/95, not available.
- NCEER-95-0018 “Modeling of Masonry Infill Panels for Structural Analysis,” by A.M. Reinhorn, A. Madan, R.E. Valles, Y. Reichmann and J.B. Mander, 12/8/95, (PB97-110886, MF-A01, A06).
- NCEER-95-0019 “Optimal Polynomial Control for Linear and Nonlinear Structures,” by A.K. Agrawal and J.N. Yang, 12/11/95, (PB96-168737, A07, MF-A02).

- NCEER-95-0020 "Retrofit of Non-Ductile Reinforced Concrete Frames Using Friction Dampers," by R.S. Rao, P. Gergely and R.N. White, 12/22/95, (PB97-133508, A10, MF-A02).
- NCEER-95-0021 "Parametric Results for Seismic Response of Pile-Supported Bridge Bents," by G. Mylonakis, A. Nikolaou and G. Gazetas, 12/22/95, (PB97-100242, A12, MF-A03).
- NCEER-95-0022 "Kinematic Bending Moments in Seismically Stressed Piles," by A. Nikolaou, G. Mylonakis and G. Gazetas, 12/23/95, (PB97-113914, MF-A03, A13).
- NCEER-96-0001 "Dynamic Response of Unreinforced Masonry Buildings with Flexible Diaphragms," by A.C. Costley and D.P. Abrams, 10/10/96, (PB97-133573, MF-A03, A15).
- NCEER-96-0002 "State of the Art Review: Foundations and Retaining Structures," by I. Po Lam, not available.
- NCEER-96-0003 "Ductility of Rectangular Reinforced Concrete Bridge Columns with Moderate Confinement," by N. Wehbe, M. Saiidi, D. Sanders and B. Douglas, 11/7/96, (PB97-133557, A06, MF-A02).
- NCEER-96-0004 "Proceedings of the Long-Span Bridge Seismic Research Workshop," edited by I.G. Buckle and I.M. Friedland, not available.
- NCEER-96-0005 "Establish Representative Pier Types for Comprehensive Study: Eastern United States," by J. Kulicki and Z. Prucz, 5/28/96, (PB98-119217, A07, MF-A02).
- NCEER-96-0006 "Establish Representative Pier Types for Comprehensive Study: Western United States," by R. Imbsen, R.A. Schamber and T.A. Osterkamp, 5/28/96, (PB98-118607, A07, MF-A02).
- NCEER-96-0007 "Nonlinear Control Techniques for Dynamical Systems with Uncertain Parameters," by R.G. Ghanem and M.I. Bujakov, 5/27/96, (PB97-100259, A17, MF-A03).
- NCEER-96-0008 "Seismic Evaluation of a 30-Year Old Non-Ductile Highway Bridge Pier and Its Retrofit," by J.B. Mander, B. Mahmoodzadegan, S. Bhadra and S.S. Chen, 5/31/96, (PB97-110902, MF-A03, A10).
- NCEER-96-0009 "Seismic Performance of a Model Reinforced Concrete Bridge Pier Before and After Retrofit," by J.B. Mander, J.H. Kim and C.A. Ligozio, 5/31/96, (PB97-110910, MF-A02, A10).
- NCEER-96-0010 "IDARC2D Version 4.0: A Computer Program for the Inelastic Damage Analysis of Buildings," by R.E. Valles, A.M. Reinhorn, S.K. Kunnath, C. Li and A. Madan, 6/3/96, (PB97-100234, A17, MF-A03).
- NCEER-96-0011 "Estimation of the Economic Impact of Multiple Lifeline Disruption: Memphis Light, Gas and Water Division Case Study," by S.E. Chang, H.A. Seligson and R.T. Eguchi, 8/16/96, (PB97-133490, A11, MF-A03).
- NCEER-96-0012 "Proceedings from the Sixth Japan-U.S. Workshop on Earthquake Resistant Design of Lifeline Facilities and Countermeasures Against Soil Liquefaction, Edited by M. Hamada and T. O'Rourke, 9/11/96, (PB97-133581, A99, MF-A06).
- NCEER-96-0013 "Chemical Hazards, Mitigation and Preparedness in Areas of High Seismic Risk: A Methodology for Estimating the Risk of Post-Earthquake Hazardous Materials Release," by H.A. Seligson, R.T. Eguchi, K.J. Tierney and K. Richmond, 11/7/96, (PB97-133565, MF-A02, A08).
- NCEER-96-0014 "Response of Steel Bridge Bearings to Reversed Cyclic Loading," by J.B. Mander, D-K. Kim, S.S. Chen and G.J. Premus, 11/13/96, (PB97-140735, A12, MF-A03).
- NCEER-96-0015 "Highway Culvert Performance During Past Earthquakes," by T.L. Youd and C.J. Beckman, 11/25/96, (PB97-133532, A06, MF-A01).
- NCEER-97-0001 "Evaluation, Prevention and Mitigation of Pounding Effects in Building Structures," by R.E. Valles and A.M. Reinhorn, 2/20/97, (PB97-159552, A14, MF-A03).
- NCEER-97-0002 "Seismic Design Criteria for Bridges and Other Highway Structures," by C. Rojahn, R. Mayes, D.G. Anderson, J. Clark, J.H. Hom, R.V. Nutt and M.J. O'Rourke, 4/30/97, (PB97-194658, A06, MF-A03).

- NCEER-97-0003 "Proceedings of the U.S.-Italian Workshop on Seismic Evaluation and Retrofit," Edited by D.P. Abrams and G.M. Calvi, 3/19/97, (PB97-194666, A13, MF-A03).
- NCEER-97-0004 "Investigation of Seismic Response of Buildings with Linear and Nonlinear Fluid Viscous Dampers," by A.A. Seleemah and M.C. Constantinou, 5/21/97, (PB98-109002, A15, MF-A03).
- NCEER-97-0005 "Proceedings of the Workshop on Earthquake Engineering Frontiers in Transportation Facilities," edited by G.C. Lee and I.M. Friedland, 8/29/97, (PB98-128911, A25, MR-A04).
- NCEER-97-0006 "Cumulative Seismic Damage of Reinforced Concrete Bridge Piers," by S.K. Kunnath, A. El-Bahy, A. Taylor and W. Stone, 9/2/97, (PB98-108814, A11, MF-A03).
- NCEER-97-0007 "Structural Details to Accommodate Seismic Movements of Highway Bridges and Retaining Walls," by R.A. Imbsen, R.A. Schamber, E. Thorkildsen, A. Kartoum, B.T. Martin, T.N. Rosser and J.M. Kulicki, 9/3/97, (PB98-108996, A09, MF-A02).
- NCEER-97-0008 "A Method for Earthquake Motion-Damage Relationships with Application to Reinforced Concrete Frames," by A. Singhal and A.S. Kiremidjian, 9/10/97, (PB98-108988, A13, MF-A03).
- NCEER-97-0009 "Seismic Analysis and Design of Bridge Abutments Considering Sliding and Rotation," by K. Fishman and R. Richards, Jr., 9/15/97, (PB98-108897, A06, MF-A02).
- NCEER-97-0010 "Proceedings of the FHWA/NCEER Workshop on the National Representation of Seismic Ground Motion for New and Existing Highway Facilities," edited by I.M. Friedland, M.S. Power and R.L. Mayes, 9/22/97, (PB98-128903, A21, MF-A04).
- NCEER-97-0011 "Seismic Analysis for Design or Retrofit of Gravity Bridge Abutments," by K.L. Fishman, R. Richards, Jr. and R.C. Divito, 10/2/97, (PB98-128937, A08, MF-A02).
- NCEER-97-0012 "Evaluation of Simplified Methods of Analysis for Yielding Structures," by P. Tsopelas, M.C. Constantinou, C.A. Kircher and A.S. Whittaker, 10/31/97, (PB98-128929, A10, MF-A03).
- NCEER-97-0013 "Seismic Design of Bridge Columns Based on Control and Repairability of Damage," by C-T. Cheng and J.B. Mander, 12/8/97, (PB98-144249, A11, MF-A03).
- NCEER-97-0014 "Seismic Resistance of Bridge Piers Based on Damage Avoidance Design," by J.B. Mander and C-T. Cheng, 12/10/97, (PB98-144223, A09, MF-A02).
- NCEER-97-0015 "Seismic Response of Nominally Symmetric Systems with Strength Uncertainty," by S. Balopoulou and M. Grigoriu, 12/23/97, (PB98-153422, A11, MF-A03).
- NCEER-97-0016 "Evaluation of Seismic Retrofit Methods for Reinforced Concrete Bridge Columns," by T.J. Wipf, F.W. Klaiber and F.M. Russo, 12/28/97, (PB98-144215, A12, MF-A03).
- NCEER-97-0017 "Seismic Fragility of Existing Conventional Reinforced Concrete Highway Bridges," by C.L. Mullen and A.S. Cakmak, 12/30/97, (PB98-153406, A08, MF-A02).
- NCEER-97-0018 "Loss Assessment of Memphis Buildings," edited by D.P. Abrams and M. Shinozuka, 12/31/97, (PB98-144231, A13, MF-A03).
- NCEER-97-0019 "Seismic Evaluation of Frames with Infill Walls Using Quasi-static Experiments," by K.M. Mosalam, R.N. White and P. Gergely, 12/31/97, (PB98-153455, A07, MF-A02).
- NCEER-97-0020 "Seismic Evaluation of Frames with Infill Walls Using Pseudo-dynamic Experiments," by K.M. Mosalam, R.N. White and P. Gergely, 12/31/97, (PB98-153430, A07, MF-A02).
- NCEER-97-0021 "Computational Strategies for Frames with Infill Walls: Discrete and Smeared Crack Analyses and Seismic Fragility," by K.M. Mosalam, R.N. White and P. Gergely, 12/31/97, (PB98-153414, A10, MF-A02).

- NCEER-97-0022 "Proceedings of the NCEER Workshop on Evaluation of Liquefaction Resistance of Soils," edited by T.L. Youd and I.M. Idriss, 12/31/97, (PB98-155617, A15, MF-A03).
- MCEER-98-0001 "Extraction of Nonlinear Hysteretic Properties of Seismically Isolated Bridges from Quick-Release Field Tests," by Q. Chen, B.M. Douglas, E.M. Maragakis and I.G. Buckle, 5/26/98, (PB99-118838, A06, MF-A01).
- MCEER-98-0002 "Methodologies for Evaluating the Importance of Highway Bridges," by A. Thomas, S. Eshenaur and J. Kulicki, 5/29/98, (PB99-118846, A10, MF-A02).
- MCEER-98-0003 "Capacity Design of Bridge Piers and the Analysis of Overstrength," by J.B. Mander, A. Dutta and P. Goel, 6/1/98, (PB99-118853, A09, MF-A02).
- MCEER-98-0004 "Evaluation of Bridge Damage Data from the Loma Prieta and Northridge, California Earthquakes," by N. Basoz and A. Kiremidjian, 6/2/98, (PB99-118861, A15, MF-A03).
- MCEER-98-0005 "Screening Guide for Rapid Assessment of Liquefaction Hazard at Highway Bridge Sites," by T. L. Youd, 6/16/98, (PB99-118879, A06, not available on microfiche).
- MCEER-98-0006 "Structural Steel and Steel/Concrete Interface Details for Bridges," by P. Ritchie, N. Kauh and J. Kulicki, 7/13/98, (PB99-118945, A06, MF-A01).
- MCEER-98-0007 "Capacity Design and Fatigue Analysis of Confined Concrete Columns," by A. Dutta and J.B. Mander, 7/14/98, (PB99-118960, A14, MF-A03).
- MCEER-98-0008 "Proceedings of the Workshop on Performance Criteria for Telecommunication Services Under Earthquake Conditions," edited by A.J. Schiff, 7/15/98, (PB99-118952, A08, MF-A02).
- MCEER-98-0009 "Fatigue Analysis of Unconfined Concrete Columns," by J.B. Mander, A. Dutta and J.H. Kim, 9/12/98, (PB99-123655, A10, MF-A02).
- MCEER-98-0010 "Centrifuge Modeling of Cyclic Lateral Response of Pile-Cap Systems and Seat-Type Abutments in Dry Sands," by A.D. Gadre and R. Dobry, 10/2/98, (PB99-123606, A13, MF-A03).
- MCEER-98-0011 "IDARC-BRIDGE: A Computational Platform for Seismic Damage Assessment of Bridge Structures," by A.M. Reinhorn, V. Simeonov, G. Mylonakis and Y. Reichman, 10/2/98, (PB99-162919, A15, MF-A03).
- MCEER-98-0012 "Experimental Investigation of the Dynamic Response of Two Bridges Before and After Retrofitting with Elastomeric Bearings," by D.A. Wendichansky, S.S. Chen and J.B. Mander, 10/2/98, (PB99-162927, A15, MF-A03).
- MCEER-98-0013 "Design Procedures for Hinge Restrainers and Hinge Sear Width for Multiple-Frame Bridges," by R. Des Roches and G.L. Fenves, 11/3/98, (PB99-140477, A13, MF-A03).
- MCEER-98-0014 "Response Modification Factors for Seismically Isolated Bridges," by M.C. Constantinou and J.K. Quarshie, 11/3/98, (PB99-140485, A14, MF-A03).
- MCEER-98-0015 "Proceedings of the U.S.-Italy Workshop on Seismic Protective Systems for Bridges," edited by I.M. Friedland and M.C. Constantinou, 11/3/98, (PB2000-101711, A22, MF-A04).
- MCEER-98-0016 "Appropriate Seismic Reliability for Critical Equipment Systems: Recommendations Based on Regional Analysis of Financial and Life Loss," by K. Porter, C. Scawthorn, C. Taylor and N. Blais, 11/10/98, (PB99-157265, A08, MF-A02).
- MCEER-98-0017 "Proceedings of the U.S. Japan Joint Seminar on Civil Infrastructure Systems Research," edited by M. Shinozuka and A. Rose, 11/12/98, (PB99-156713, A16, MF-A03).
- MCEER-98-0018 "Modeling of Pile Footings and Drilled Shafts for Seismic Design," by I. PoLam, M. Kapuskar and D. Chaudhuri, 12/21/98, (PB99-157257, A09, MF-A02).

- MCEER-99-0001 "Seismic Evaluation of a Masonry Infilled Reinforced Concrete Frame by Pseudodynamic Testing," by S.G. Buonopane and R.N. White, 2/16/99, (PB99-162851, A09, MF-A02).
- MCEER-99-0002 "Response History Analysis of Structures with Seismic Isolation and Energy Dissipation Systems: Verification Examples for Program SAP2000," by J. Scheller and M.C. Constantinou, 2/22/99, (PB99-162869, A08, MF-A02).
- MCEER-99-0003 "Experimental Study on the Seismic Design and Retrofit of Bridge Columns Including Axial Load Effects," by A. Dutta, T. Kokorina and J.B. Mander, 2/22/99, (PB99-162877, A09, MF-A02).
- MCEER-99-0004 "Experimental Study of Bridge Elastomeric and Other Isolation and Energy Dissipation Systems with Emphasis on Uplift Prevention and High Velocity Near-source Seismic Excitation," by A. Kasalanati and M. C. Constantinou, 2/26/99, (PB99-162885, A12, MF-A03).
- MCEER-99-0005 "Truss Modeling of Reinforced Concrete Shear-flexure Behavior," by J.H. Kim and J.B. Mander, 3/8/99, (PB99-163693, A12, MF-A03).
- MCEER-99-0006 "Experimental Investigation and Computational Modeling of Seismic Response of a 1:4 Scale Model Steel Structure with a Load Balancing Supplemental Damping System," by G. Pekcan, J.B. Mander and S.S. Chen, 4/2/99, (PB99-162893, A11, MF-A03).
- MCEER-99-0007 "Effect of Vertical Ground Motions on the Structural Response of Highway Bridges," by M.R. Button, C.J. Cronin and R.L. Mayes, 4/10/99, (PB2000-101411, A10, MF-A03).
- MCEER-99-0008 "Seismic Reliability Assessment of Critical Facilities: A Handbook, Supporting Documentation, and Model Code Provisions," by G.S. Johnson, R.E. Sheppard, M.D. Quilici, S.J. Eder and C.R. Scawthorn, 4/12/99, (PB2000-101701, A18, MF-A04).
- MCEER-99-0009 "Impact Assessment of Selected MCEER Highway Project Research on the Seismic Design of Highway Structures," by C. Rojahn, R. Mayes, D.G. Anderson, J.H. Clark, D'Appolonia Engineering, S. Gloyd and R.V. Nutt, 4/14/99, (PB99-162901, A10, MF-A02).
- MCEER-99-0010 "Site Factors and Site Categories in Seismic Codes," by R. Dobry, R. Ramos and M.S. Power, 7/19/99, (PB2000-101705, A08, MF-A02).
- MCEER-99-0011 "Restrainer Design Procedures for Multi-Span Simply-Supported Bridges," by M.J. Randall, M. Saiidi, E. Maragakis and T. Isakovic, 7/20/99, (PB2000-101702, A10, MF-A02).
- MCEER-99-0012 "Property Modification Factors for Seismic Isolation Bearings," by M.C. Constantinou, P. Tsopelas, A. Kasalanati and E. Wolff, 7/20/99, (PB2000-103387, A11, MF-A03).
- MCEER-99-0013 "Critical Seismic Issues for Existing Steel Bridges," by P. Ritchie, N. Kauh and J. Kulicki, 7/20/99, (PB2000-101697, A09, MF-A02).
- MCEER-99-0014 "Nonstructural Damage Database," by A. Kao, T.T. Soong and A. Vender, 7/24/99, (PB2000-101407, A06, MF-A01).
- MCEER-99-0015 "Guide to Remedial Measures for Liquefaction Mitigation at Existing Highway Bridge Sites," by H.G. Cooke and J. K. Mitchell, 7/26/99, (PB2000-101703, A11, MF-A03).
- MCEER-99-0016 "Proceedings of the MCEER Workshop on Ground Motion Methodologies for the Eastern United States," edited by N. Abrahamson and A. Becker, 8/11/99, (PB2000-103385, A07, MF-A02).
- MCEER-99-0017 "Quindío, Colombia Earthquake of January 25, 1999: Reconnaissance Report," by A.P. Asfura and P.J. Flores, 10/4/99, (PB2000-106893, A06, MF-A01).
- MCEER-99-0018 "Hysteretic Models for Cyclic Behavior of Deteriorating Inelastic Structures," by M.V. Sivaselvan and A.M. Reinhorn, 11/5/99, (PB2000-103386, A08, MF-A02).

- MCEER-99-0019 "Proceedings of the 7th U.S.- Japan Workshop on Earthquake Resistant Design of Lifeline Facilities and Countermeasures Against Soil Liquefaction," edited by T.D. O'Rourke, J.P. Bardet and M. Hamada, 11/19/99, (PB2000-103354, A99, MF-A06).
- MCEER-99-0020 "Development of Measurement Capability for Micro-Vibration Evaluations with Application to Chip Fabrication Facilities," by G.C. Lee, Z. Liang, J.W. Song, J.D. Shen and W.C. Liu, 12/1/99, (PB2000-105993, A08, MF-A02).
- MCEER-99-0021 "Design and Retrofit Methodology for Building Structures with Supplemental Energy Dissipating Systems," by G. Pekcan, J.B. Mander and S.S. Chen, 12/31/99, (PB2000-105994, A11, MF-A03).
- MCEER-00-0001 "The Marmara, Turkey Earthquake of August 17, 1999: Reconnaissance Report," edited by C. Scawthorn; with major contributions by M. Bruneau, R. Eguchi, T. Holzer, G. Johnson, J. Mander, J. Mitchell, W. Mitchell, A. Papageorgiou, C. Scaethorn, and G. Webb, 3/23/00, (PB2000-106200, A11, MF-A03).
- MCEER-00-0002 "Proceedings of the MCEER Workshop for Seismic Hazard Mitigation of Health Care Facilities," edited by G.C. Lee, M. Ettouney, M. Grigoriu, J. Hauer and J. Nigg, 3/29/00, (PB2000-106892, A08, MF-A02).
- MCEER-00-0003 "The Chi-Chi, Taiwan Earthquake of September 21, 1999: Reconnaissance Report," edited by G.C. Lee and C.H. Loh, with major contributions by G.C. Lee, M. Bruneau, I.G. Buckle, S.E. Chang, P.J. Flores, T.D. O'Rourke, M. Shinozuka, T.T. Soong, C-H. Loh, K-C. Chang, Z-J. Chen, J-S. Hwang, M-L. Lin, G-Y. Liu, K-C. Tsai, G.C. Yao and C-L. Yen, 4/30/00, (PB2001-100980, A10, MF-A02).
- MCEER-00-0004 "Seismic Retrofit of End-Sway Frames of Steel Deck-Truss Bridges with a Supplemental Tendon System: Experimental and Analytical Investigation," by G. Pekcan, J.B. Mander and S.S. Chen, 7/1/00, (PB2001-100982, A10, MF-A02).
- MCEER-00-0005 "Sliding Fragility of Unrestrained Equipment in Critical Facilities," by W.H. Chong and T.T. Soong, 7/5/00, (PB2001-100983, A08, MF-A02).
- MCEER-00-0006 "Seismic Response of Reinforced Concrete Bridge Pier Walls in the Weak Direction," by N. Abo-Shadi, M. Saiidi and D. Sanders, 7/17/00, (PB2001-100981, A17, MF-A03).
- MCEER-00-0007 "Low-Cycle Fatigue Behavior of Longitudinal Reinforcement in Reinforced Concrete Bridge Columns," by J. Brown and S.K. Kunnath, 7/23/00, (PB2001-104392, A08, MF-A02).
- MCEER-00-0008 "Soil Structure Interaction of Bridges for Seismic Analysis," I. PoLam and H. Law, 9/25/00, (PB2001-105397, A08, MF-A02).
- MCEER-00-0009 "Proceedings of the First MCEER Workshop on Mitigation of Earthquake Disaster by Advanced Technologies (MEDAT-1), edited by M. Shinozuka, D.J. Inman and T.D. O'Rourke, 11/10/00, (PB2001-105399, A14, MF-A03).
- MCEER-00-0010 "Development and Evaluation of Simplified Procedures for Analysis and Design of Buildings with Passive Energy Dissipation Systems, Revision 01," by O.M. Ramirez, M.C. Constantinou, C.A. Kircher, A.S. Whittaker, M.W. Johnson, J.D. Gomez and C. Chrysostomou, 11/16/01, (PB2001-105523, A23, MF-A04).
- MCEER-00-0011 "Dynamic Soil-Foundation-Structure Interaction Analyses of Large Caissons," by C-Y. Chang, C-M. Mok, Z-L. Wang, R. Settgast, F. Waggoner, M.A. Ketchum, H.M. Gonnermann and C-C. Chin, 12/30/00, (PB2001-104373, A07, MF-A02).
- MCEER-00-0012 "Experimental Evaluation of Seismic Performance of Bridge Restrainers," by A.G. Vlassis, E.M. Maragakis and M. Saiid Saiidi, 12/30/00, (PB2001-104354, A09, MF-A02).
- MCEER-00-0013 "Effect of Spatial Variation of Ground Motion on Highway Structures," by M. Shinozuka, V. Saxena and G. Deodatis, 12/31/00, (PB2001-108755, A13, MF-A03).
- MCEER-00-0014 "A Risk-Based Methodology for Assessing the Seismic Performance of Highway Systems," by S.D. Werner, C.E. Taylor, J.E. Moore, II, J.S. Walton and S. Cho, 12/31/00, (PB2001-108756, A14, MF-A03).

- MCEER-01-0001 "Experimental Investigation of P-Delta Effects to Collapse During Earthquakes," by D. Vian and M. Bruneau, 6/25/01, (PB2002-100534, A17, MF-A03).
- MCEER-01-0002 "Proceedings of the Second MCEER Workshop on Mitigation of Earthquake Disaster by Advanced Technologies (MEDAT-2)," edited by M. Bruneau and D.J. Inman, 7/23/01, (PB2002-100434, A16, MF-A03).
- MCEER-01-0003 "Sensitivity Analysis of Dynamic Systems Subjected to Seismic Loads," by C. Roth and M. Grigoriu, 9/18/01, (PB2003-100884, A12, MF-A03).
- MCEER-01-0004 "Overcoming Obstacles to Implementing Earthquake Hazard Mitigation Policies: Stage 1 Report," by D.J. Alesch and W.J. Petak, 12/17/01, (PB2002-107949, A07, MF-A02).
- MCEER-01-0005 "Updating Real-Time Earthquake Loss Estimates: Methods, Problems and Insights," by C.E. Taylor, S.E. Chang and R.T. Eguchi, 12/17/01, (PB2002-107948, A05, MF-A01).
- MCEER-01-0006 "Experimental Investigation and Retrofit of Steel Pile Foundations and Pile Bents Under Cyclic Lateral Loadings," by A. Shama, J. Mander, B. Blabac and S. Chen, 12/31/01, (PB2002-107950, A13, MF-A03).
- MCEER-02-0001 "Assessment of Performance of Bolu Viaduct in the 1999 Duzce Earthquake in Turkey" by P.C. Roussis, M.C. Constantinou, M. Erdik, E. Durukal and M. Dicleli, 5/8/02, (PB2003-100883, A08, MF-A02).
- MCEER-02-0002 "Seismic Behavior of Rail Counterweight Systems of Elevators in Buildings," by M.P. Singh, Rildova and L.E. Suarez, 5/27/02. (PB2003-100882, A11, MF-A03).
- MCEER-02-0003 "Development of Analysis and Design Procedures for Spread Footings," by G. Mylonakis, G. Gazetas, S. Nikolaou and A. Chauncey, 10/02/02, (PB2004-101636, A13, MF-A03, CD-A13).
- MCEER-02-0004 "Bare-Earth Algorithms for Use with SAR and LIDAR Digital Elevation Models," by C.K. Huyck, R.T. Eguchi and B. Houshmand, 10/16/02, (PB2004-101637, A07, CD-A07).
- MCEER-02-0005 "Review of Energy Dissipation of Compression Members in Concentrically Braced Frames," by K.Lee and M. Bruneau, 10/18/02, (PB2004-101638, A10, CD-A10).
- MCEER-03-0001 "Experimental Investigation of Light-Gauge Steel Plate Shear Walls for the Seismic Retrofit of Buildings" by J. Berman and M. Bruneau, 5/2/03, (PB2004-101622, A10, MF-A03, CD-A10).
- MCEER-03-0002 "Statistical Analysis of Fragility Curves," by M. Shinozuka, M.Q. Feng, H. Kim, T. Uzawa and T. Ueda, 6/16/03, (PB2004-101849, A09, CD-A09).
- MCEER-03-0003 "Proceedings of the Eighth U.S.-Japan Workshop on Earthquake Resistant Design of Lifeline Facilities and Countermeasures Against Liquefaction," edited by M. Hamada, J.P. Bardet and T.D. O'Rourke, 6/30/03, (PB2004-104386, A99, CD-A99).
- MCEER-03-0004 "Proceedings of the PRC-US Workshop on Seismic Analysis and Design of Special Bridges," edited by L.C. Fan and G.C. Lee, 7/15/03, (PB2004-104387, A14, CD-A14).
- MCEER-03-0005 "Urban Disaster Recovery: A Framework and Simulation Model," by S.B. Miles and S.E. Chang, 7/25/03, (PB2004-104388, A07, CD-A07).
- MCEER-03-0006 "Behavior of Underground Piping Joints Due to Static and Dynamic Loading," by R.D. Meis, M. Maragakis and R. Siddharthan, 11/17/03, (PB2005-102194, A13, MF-A03, CD-A00).
- MCEER-04-0001 "Experimental Study of Seismic Isolation Systems with Emphasis on Secondary System Response and Verification of Accuracy of Dynamic Response History Analysis Methods," by E. Wolff and M. Constantinou, 1/16/04 (PB2005-102195, A99, MF-E08, CD-A00).
- MCEER-04-0002 "Tension, Compression and Cyclic Testing of Engineered Cementitious Composite Materials," by K. Kesner and S.L. Billington, 3/1/04, (PB2005-102196, A08, CD-A08).

- MCEER-04-0003 “Cyclic Testing of Braces Laterally Restrained by Steel Studs to Enhance Performance During Earthquakes,” by O.C. Celik, J.W. Berman and M. Bruneau, 3/16/04, (PB2005-102197, A13, MF-A03, CD-A00).
- MCEER-04-0004 “Methodologies for Post Earthquake Building Damage Detection Using SAR and Optical Remote Sensing: Application to the August 17, 1999 Marmara, Turkey Earthquake,” by C.K. Huyck, B.J. Adams, S. Cho, R.T. Eguchi, B. Mansouri and B. Houshmand, 6/15/04, (PB2005-104888, A10, CD-A00).
- MCEER-04-0005 “Nonlinear Structural Analysis Towards Collapse Simulation: A Dynamical Systems Approach,” by M.V. Sivaselvan and A.M. Reinhorn, 6/16/04, (PB2005-104889, A11, MF-A03, CD-A00).
- MCEER-04-0006 “Proceedings of the Second PRC-US Workshop on Seismic Analysis and Design of Special Bridges,” edited by G.C. Lee and L.C. Fan, 6/25/04, (PB2005-104890, A16, CD-A00).
- MCEER-04-0007 “Seismic Vulnerability Evaluation of Axially Loaded Steel Built-up Laced Members,” by K. Lee and M. Bruneau, 6/30/04, (PB2005-104891, A16, CD-A00).
- MCEER-04-0008 “Evaluation of Accuracy of Simplified Methods of Analysis and Design of Buildings with Damping Systems for Near-Fault and for Soft-Soil Seismic Motions,” by E.A. Pavlou and M.C. Constantinou, 8/16/04, (PB2005-104892, A08, MF-A02, CD-A00).
- MCEER-04-0009 “Assessment of Geotechnical Issues in Acute Care Facilities in California,” by M. Lew, T.D. O’Rourke, R. Dobry and M. Koch, 9/15/04, (PB2005-104893, A08, CD-A00).
- MCEER-04-0010 “Scissor-Jack-Damper Energy Dissipation System,” by A.N. Sigaher-Boyle and M.C. Constantinou, 12/1/04 (PB2005-108221).
- MCEER-04-0011 “Seismic Retrofit of Bridge Steel Truss Piers Using a Controlled Rocking Approach,” by M. Pollino and M. Bruneau, 12/20/04 (PB2006-105795).
- MCEER-05-0001 “Experimental and Analytical Studies of Structures Seismically Isolated with an Uplift-Restraint Isolation System,” by P.C. Roussis and M.C. Constantinou, 1/10/05 (PB2005-108222).
- MCEER-05-0002 “A Versatile Experimentation Model for Study of Structures Near Collapse Applied to Seismic Evaluation of Irregular Structures,” by D. Kusumastuti, A.M. Reinhorn and A. Rutenberg, 3/31/05 (PB2006-101523).
- MCEER-05-0003 “Proceedings of the Third PRC-US Workshop on Seismic Analysis and Design of Special Bridges,” edited by L.C. Fan and G.C. Lee, 4/20/05, (PB2006-105796).
- MCEER-05-0004 “Approaches for the Seismic Retrofit of Braced Steel Bridge Piers and Proof-of-Concept Testing of an Eccentrically Braced Frame with Tubular Link,” by J.W. Berman and M. Bruneau, 4/21/05 (PB2006-101524).
- MCEER-05-0005 “Simulation of Strong Ground Motions for Seismic Fragility Evaluation of Nonstructural Components in Hospitals,” by A. Wanitkorkul and A. Filiatrault, 5/26/05 (PB2006-500027).
- MCEER-05-0006 “Seismic Safety in California Hospitals: Assessing an Attempt to Accelerate the Replacement or Seismic Retrofit of Older Hospital Facilities,” by D.J. Alesch, L.A. Arendt and W.J. Petak, 6/6/05 (PB2006-105794).
- MCEER-05-0007 “Development of Seismic Strengthening and Retrofit Strategies for Critical Facilities Using Engineered Cementitious Composite Materials,” by K. Kesner and S.L. Billington, 8/29/05 (PB2006-111701).
- MCEER-05-0008 “Experimental and Analytical Studies of Base Isolation Systems for Seismic Protection of Power Transformers,” by N. Murota, M.Q. Feng and G-Y. Liu, 9/30/05 (PB2006-111702).
- MCEER-05-0009 “3D-BASIS-ME-MB: Computer Program for Nonlinear Dynamic Analysis of Seismically Isolated Structures,” by P.C. Tsopelas, P.C. Roussis, M.C. Constantinou, R. Buchanan and A.M. Reinhorn, 10/3/05 (PB2006-111703).
- MCEER-05-0010 “Steel Plate Shear Walls for Seismic Design and Retrofit of Building Structures,” by D. Vian and M. Bruneau, 12/15/05 (PB2006-111704).

- MCEER-05-0011 "The Performance-Based Design Paradigm," by M.J. Astrella and A. Whittaker, 12/15/05 (PB2006-111705).
- MCEER-06-0001 "Seismic Fragility of Suspended Ceiling Systems," H. Badillo-Almaraz, A.S. Whittaker, A.M. Reinhorn and G.P. Cimellaro, 2/4/06 (PB2006-111706).
- MCEER-06-0002 "Multi-Dimensional Fragility of Structures," by G.P. Cimellaro, A.M. Reinhorn and M. Bruneau, 3/1/06 (PB2007-106974, A09, MF-A02, CD A00).
- MCEER-06-0003 "Built-Up Shear Links as Energy Dissipators for Seismic Protection of Bridges," by P. Dusicka, A.M. Itani and I.G. Buckle, 3/15/06 (PB2006-111708).
- MCEER-06-0004 "Analytical Investigation of the Structural Fuse Concept," by R.E. Vargas and M. Bruneau, 3/16/06 (PB2006-111709).
- MCEER-06-0005 "Experimental Investigation of the Structural Fuse Concept," by R.E. Vargas and M. Bruneau, 3/17/06 (PB2006-111710).
- MCEER-06-0006 "Further Development of Tubular Eccentrically Braced Frame Links for the Seismic Retrofit of Braced Steel Truss Bridge Piers," by J.W. Berman and M. Bruneau, 3/27/06 (PB2007-105147).
- MCEER-06-0007 "REDARS Validation Report," by S. Cho, C.K. Huyck, S. Ghosh and R.T. Eguchi, 8/8/06 (PB2007-106983).
- MCEER-06-0008 "Review of Current NDE Technologies for Post-Earthquake Assessment of Retrofitted Bridge Columns," by J.W. Song, Z. Liang and G.C. Lee, 8/21/06 (PB2007-106984).
- MCEER-06-0009 "Liquefaction Remediation in Silty Soils Using Dynamic Compaction and Stone Columns," by S. Thevanayagam, G.R. Martin, R. Nashed, T. Shenthan, T. Kanagalingam and N. Ecemis, 8/28/06 (PB2007-106985).
- MCEER-06-0010 "Conceptual Design and Experimental Investigation of Polymer Matrix Composite Infill Panels for Seismic Retrofitting," by W. Jung, M. Chiewanichakorn and A.J. Aref, 9/21/06 (PB2007-106986).
- MCEER-06-0011 "A Study of the Coupled Horizontal-Vertical Behavior of Elastomeric and Lead-Rubber Seismic Isolation Bearings," by G.P. Warn and A.S. Whittaker, 9/22/06 (PB2007-108679).
- MCEER-06-0012 "Proceedings of the Fourth PRC-US Workshop on Seismic Analysis and Design of Special Bridges: Advancing Bridge Technologies in Research, Design, Construction and Preservation," Edited by L.C. Fan, G.C. Lee and L. Ziang, 10/12/06 (PB2007-109042).
- MCEER-06-0013 "Cyclic Response and Low Cycle Fatigue Characteristics of Plate Steels," by P. Dusicka, A.M. Itani and I.G. Buckle, 11/1/06 (PB2007-106987).
- MCEER-06-0014 "Proceedings of the Second US-Taiwan Bridge Engineering Workshop," edited by W.P. Yen, J. Shen, J-Y. Chen and M. Wang, 11/15/06 (PB2008-500041).
- MCEER-06-0015 "User Manual and Technical Documentation for the REDARSTM Import Wizard," by S. Cho, S. Ghosh, C.K. Huyck and S.D. Werner, 11/30/06 (PB2007-114766).
- MCEER-06-0016 "Hazard Mitigation Strategy and Monitoring Technologies for Urban and Infrastructure Public Buildings: Proceedings of the China-US Workshops," edited by X.Y. Zhou, A.L. Zhang, G.C. Lee and M. Tong, 12/12/06 (PB2008-500018).
- MCEER-07-0001 "Static and Kinetic Coefficients of Friction for Rigid Blocks," by C. Kafali, S. Fathali, M. Grigoriu and A.S. Whittaker, 3/20/07 (PB2007-114767).
- MCEER-07-0002 "Hazard Mitigation Investment Decision Making: Organizational Response to Legislative Mandate," by L.A. Arendt, D.J. Alesch and W.J. Petak, 4/9/07 (PB2007-114768).
- MCEER-07-0003 "Seismic Behavior of Bidirectional-Resistant Ductile End Diaphragms with Unbonded Braces in Straight or Skewed Steel Bridges," by O. Celik and M. Bruneau, 4/11/07 (PB2008-105141).

- MCEER-07-0004 "Modeling Pile Behavior in Large Pile Groups Under Lateral Loading," by A.M. Dodds and G.R. Martin, 4/16/07(PB2008-105142).
- MCEER-07-0005 "Experimental Investigation of Blast Performance of Seismically Resistant Concrete-Filled Steel Tube Bridge Piers," by S. Fujikura, M. Bruneau and D. Lopez-Garcia, 4/20/07 (PB2008-105143).
- MCEER-07-0006 "Seismic Analysis of Conventional and Isolated Liquefied Natural Gas Tanks Using Mechanical Analogs," by I.P. Christovasilis and A.S. Whittaker, 5/1/07, not available.
- MCEER-07-0007 "Experimental Seismic Performance Evaluation of Isolation/Restraint Systems for Mechanical Equipment – Part 1: Heavy Equipment Study," by S. Fathali and A. Filiatrault, 6/6/07 (PB2008-105144).
- MCEER-07-0008 "Seismic Vulnerability of Timber Bridges and Timber Substructures," by A.A. Sharma, J.B. Mander, I.M. Friedland and D.R. Allicock, 6/7/07 (PB2008-105145).
- MCEER-07-0009 "Experimental and Analytical Study of the XY-Friction Pendulum (XY-FP) Bearing for Bridge Applications," by C.C. Marin-Artieda, A.S. Whittaker and M.C. Constantinou, 6/7/07 (PB2008-105191).
- MCEER-07-0010 "Proceedings of the PRC-US Earthquake Engineering Forum for Young Researchers," Edited by G.C. Lee and X.Z. Qi, 6/8/07 (PB2008-500058).
- MCEER-07-0011 "Design Recommendations for Perforated Steel Plate Shear Walls," by R. Purba and M. Bruneau, 6/18/07, (PB2008-105192).
- MCEER-07-0012 "Performance of Seismic Isolation Hardware Under Service and Seismic Loading," by M.C. Constantinou, A.S. Whittaker, Y. Kalpakidis, D.M. Fenz and G.P. Warn, 8/27/07, (PB2008-105193).
- MCEER-07-0013 "Experimental Evaluation of the Seismic Performance of Hospital Piping Subassemblies," by E.R. Goodwin, E. Maragakis and A.M. Itani, 9/4/07, (PB2008-105194).
- MCEER-07-0014 "A Simulation Model of Urban Disaster Recovery and Resilience: Implementation for the 1994 Northridge Earthquake," by S. Miles and S.E. Chang, 9/7/07, (PB2008-106426).
- MCEER-07-0015 "Statistical and Mechanistic Fragility Analysis of Concrete Bridges," by M. Shinozuka, S. Banerjee and S-H. Kim, 9/10/07, (PB2008-106427).
- MCEER-07-0016 "Three-Dimensional Modeling of Inelastic Buckling in Frame Structures," by M. Schachter and AM. Reinhorn, 9/13/07, (PB2008-108125).
- MCEER-07-0017 "Modeling of Seismic Wave Scattering on Pile Groups and Caissons," by I. Po Lam, H. Law and C.T. Yang, 9/17/07 (PB2008-108150).
- MCEER-07-0018 "Bridge Foundations: Modeling Large Pile Groups and Caissons for Seismic Design," by I. Po Lam, H. Law and G.R. Martin (Coordinating Author), 12/1/07 (PB2008-111190).
- MCEER-07-0019 "Principles and Performance of Roller Seismic Isolation Bearings for Highway Bridges," by G.C. Lee, Y.C. Ou, Z. Liang, T.C. Niu and J. Song, 12/10/07 (PB2009-110466).
- MCEER-07-0020 "Centrifuge Modeling of Permeability and Pinning Reinforcement Effects on Pile Response to Lateral Spreading," by L.L. Gonzalez-Lagos, T. Abdoun and R. Dobry, 12/10/07 (PB2008-111191).
- MCEER-07-0021 "Damage to the Highway System from the Pisco, Perú Earthquake of August 15, 2007," by J.S. O'Connor, L. Mesa and M. Nykamp, 12/10/07, (PB2008-108126).
- MCEER-07-0022 "Experimental Seismic Performance Evaluation of Isolation/Restraint Systems for Mechanical Equipment – Part 2: Light Equipment Study," by S. Fathali and A. Filiatrault, 12/13/07 (PB2008-111192).
- MCEER-07-0023 "Fragility Considerations in Highway Bridge Design," by M. Shinozuka, S. Banerjee and S.H. Kim, 12/14/07 (PB2008-111193).

- MCEER-07-0024 "Performance Estimates for Seismically Isolated Bridges," by G.P. Warn and A.S. Whittaker, 12/30/07 (PB2008-112230).
- MCEER-08-0001 "Seismic Performance of Steel Girder Bridge Superstructures with Conventional Cross Frames," by L.P. Carden, A.M. Itani and I.G. Buckle, 1/7/08, (PB2008-112231).
- MCEER-08-0002 "Seismic Performance of Steel Girder Bridge Superstructures with Ductile End Cross Frames with Seismic Isolators," by L.P. Carden, A.M. Itani and I.G. Buckle, 1/7/08 (PB2008-112232).
- MCEER-08-0003 "Analytical and Experimental Investigation of a Controlled Rocking Approach for Seismic Protection of Bridge Steel Truss Piers," by M. Pollino and M. Bruneau, 1/21/08 (PB2008-112233).
- MCEER-08-0004 "Linking Lifeline Infrastructure Performance and Community Disaster Resilience: Models and Multi-Stakeholder Processes," by S.E. Chang, C. Pasion, K. Tatebe and R. Ahmad, 3/3/08 (PB2008-112234).
- MCEER-08-0005 "Modal Analysis of Generally Damped Linear Structures Subjected to Seismic Excitations," by J. Song, Y-L. Chu, Z. Liang and G.C. Lee, 3/4/08 (PB2009-102311).
- MCEER-08-0006 "System Performance Under Multi-Hazard Environments," by C. Kafali and M. Grigoriu, 3/4/08 (PB2008-112235).
- MCEER-08-0007 "Mechanical Behavior of Multi-Spherical Sliding Bearings," by D.M. Fenz and M.C. Constantinou, 3/6/08 (PB2008-112236).
- MCEER-08-0008 "Post-Earthquake Restoration of the Los Angeles Water Supply System," by T.H.P. Tabucchi and R.A. Davidson, 3/7/08 (PB2008-112237).
- MCEER-08-0009 "Fragility Analysis of Water Supply Systems," by A. Jacobson and M. Grigoriu, 3/10/08 (PB2009-105545).
- MCEER-08-0010 "Experimental Investigation of Full-Scale Two-Story Steel Plate Shear Walls with Reduced Beam Section Connections," by B. Qu, M. Bruneau, C-H. Lin and K-C. Tsai, 3/17/08 (PB2009-106368).
- MCEER-08-0011 "Seismic Evaluation and Rehabilitation of Critical Components of Electrical Power Systems," S. Ersoy, B. Feizi, A. Ashrafi and M. Ala Saadeghvaziri, 3/17/08 (PB2009-105546).
- MCEER-08-0012 "Seismic Behavior and Design of Boundary Frame Members of Steel Plate Shear Walls," by B. Qu and M. Bruneau, 4/26/08 . (PB2009-106744).
- MCEER-08-0013 "Development and Appraisal of a Numerical Cyclic Loading Protocol for Quantifying Building System Performance," by A. Filiatrault, A. Wanitkorkul and M. Constantinou, 4/27/08 (PB2009-107906).
- MCEER-08-0014 "Structural and Nonstructural Earthquake Design: The Challenge of Integrating Specialty Areas in Designing Complex, Critical Facilities," by W.J. Petak and D.J. Alesch, 4/30/08 (PB2009-107907).
- MCEER-08-0015 "Seismic Performance Evaluation of Water Systems," by Y. Wang and T.D. O'Rourke, 5/5/08 (PB2009-107908).
- MCEER-08-0016 "Seismic Response Modeling of Water Supply Systems," by P. Shi and T.D. O'Rourke, 5/5/08 (PB2009-107910).
- MCEER-08-0017 "Numerical and Experimental Studies of Self-Centering Post-Tensioned Steel Frames," by D. Wang and A. Filiatrault, 5/12/08 (PB2009-110479).
- MCEER-08-0018 "Development, Implementation and Verification of Dynamic Analysis Models for Multi-Spherical Sliding Bearings," by D.M. Fenz and M.C. Constantinou, 8/15/08 (PB2009-107911).
- MCEER-08-0019 "Performance Assessment of Conventional and Base Isolated Nuclear Power Plants for Earthquake Blast Loadings," by Y.N. Huang, A.S. Whittaker and N. Luco, 10/28/08 (PB2009-107912).

- MCEER-08-0020 “Remote Sensing for Resilient Multi-Hazard Disaster Response – Volume I: Introduction to Damage Assessment Methodologies,” by B.J. Adams and R.T. Eguchi, 11/17/08 (PB2010-102695).
- MCEER-08-0021 “Remote Sensing for Resilient Multi-Hazard Disaster Response – Volume II: Counting the Number of Collapsed Buildings Using an Object-Oriented Analysis: Case Study of the 2003 Bam Earthquake,” by L. Gusella, C.K. Huyck and B.J. Adams, 11/17/08 (PB2010-100925).
- MCEER-08-0022 “Remote Sensing for Resilient Multi-Hazard Disaster Response – Volume III: Multi-Sensor Image Fusion Techniques for Robust Neighborhood-Scale Urban Damage Assessment,” by B.J. Adams and A. McMillan, 11/17/08 (PB2010-100926).
- MCEER-08-0023 “Remote Sensing for Resilient Multi-Hazard Disaster Response – Volume IV: A Study of Multi-Temporal and Multi-Resolution SAR Imagery for Post-Katrina Flood Monitoring in New Orleans,” by A. McMillan, J.G. Morley, B.J. Adams and S. Chesworth, 11/17/08 (PB2010-100927).
- MCEER-08-0024 “Remote Sensing for Resilient Multi-Hazard Disaster Response – Volume V: Integration of Remote Sensing Imagery and VIEWS™ Field Data for Post-Hurricane Charley Building Damage Assessment,” by J.A. Womble, K. Mehta and B.J. Adams, 11/17/08 (PB2009-115532).
- MCEER-08-0025 “Building Inventory Compilation for Disaster Management: Application of Remote Sensing and Statistical Modeling,” by P. Sarabandi, A.S. Kiremidjian, R.T. Eguchi and B. J. Adams, 11/20/08 (PB2009-110484).
- MCEER-08-0026 “New Experimental Capabilities and Loading Protocols for Seismic Qualification and Fragility Assessment of Nonstructural Systems,” by R. Retamales, G. Mosqueda, A. Filiatrault and A. Reinhorn, 11/24/08 (PB2009-110485).
- MCEER-08-0027 “Effects of Heating and Load History on the Behavior of Lead-Rubber Bearings,” by I.V. Kalpakidis and M.C. Constantinou, 12/1/08 (PB2009-115533).
- MCEER-08-0028 “Experimental and Analytical Investigation of Blast Performance of Seismically Resistant Bridge Piers,” by S.Fujikura and M. Bruneau, 12/8/08 (PB2009-115534).
- MCEER-08-0029 “Evolutionary Methodology for Aseismic Decision Support,” by Y. Hu and G. Dargush, 12/15/08.
- MCEER-08-0030 “Development of a Steel Plate Shear Wall Bridge Pier System Conceived from a Multi-Hazard Perspective,” by D. Keller and M. Bruneau, 12/19/08 (PB2010-102696).
- MCEER-09-0001 “Modal Analysis of Arbitrarily Damped Three-Dimensional Linear Structures Subjected to Seismic Excitations,” by Y.L. Chu, J. Song and G.C. Lee, 1/31/09 (PB2010-100922).
- MCEER-09-0002 “Air-Blast Effects on Structural Shapes,” by G. Ballantyne, A.S. Whittaker, A.J. Aref and G.F. Dargush, 2/2/09 (PB2010-102697).
- MCEER-09-0003 “Water Supply Performance During Earthquakes and Extreme Events,” by A.L. Bonneau and T.D. O’Rourke, 2/16/09 (PB2010-100923).
- MCEER-09-0004 “Generalized Linear (Mixed) Models of Post-Earthquake Ignitions,” by R.A. Davidson, 7/20/09 (PB2010-102698).
- MCEER-09-0005 “Seismic Testing of a Full-Scale Two-Story Light-Frame Wood Building: NEESWood Benchmark Test,” by I.P. Christovasilis, A. Filiatrault and A. Wanitkorkul, 7/22/09 (PB2012-102401).
- MCEER-09-0006 “IDARC2D Version 7.0: A Program for the Inelastic Damage Analysis of Structures,” by A.M. Reinhorn, H. Roh, M. Sivaselvan, S.K. Kunnath, R.E. Valles, A. Madan, C. Li, R. Lobo and Y.J. Park, 7/28/09 (PB2010-103199).
- MCEER-09-0007 “Enhancements to Hospital Resiliency: Improving Emergency Planning for and Response to Hurricanes,” by D.B. Hess and L.A. Arendt, 7/30/09 (PB2010-100924).

- MCEER-09-0008 "Assessment of Base-Isolated Nuclear Structures for Design and Beyond-Design Basis Earthquake Shaking," by Y.N. Huang, A.S. Whittaker, R.P. Kennedy and R.L. Mayes, 8/20/09 (PB2010-102699).
- MCEER-09-0009 "Quantification of Disaster Resilience of Health Care Facilities," by G.P. Cimellaro, C. Fumo, A.M. Reinhorn and M. Bruneau, 9/14/09 (PB2010-105384).
- MCEER-09-0010 "Performance-Based Assessment and Design of Squat Reinforced Concrete Shear Walls," by C.K. Gulec and A.S. Whittaker, 9/15/09 (PB2010-102700).
- MCEER-09-0011 "Proceedings of the Fourth US-Taiwan Bridge Engineering Workshop," edited by W.P. Yen, J.J. Shen, T.M. Lee and R.B. Zheng, 10/27/09 (PB2010-500009).
- MCEER-09-0012 "Proceedings of the Special International Workshop on Seismic Connection Details for Segmental Bridge Construction," edited by W. Phillip Yen and George C. Lee, 12/21/09 (PB2012-102402).
- MCEER-10-0001 "Direct Displacement Procedure for Performance-Based Seismic Design of Multistory Woodframe Structures," by W. Pang and D. Rosowsky, 4/26/10 (PB2012-102403).
- MCEER-10-0002 "Simplified Direct Displacement Design of Six-Story NEESWood Capstone Building and Pre-Test Seismic Performance Assessment," by W. Pang, D. Rosowsky, J. van de Lindt and S. Pei, 5/28/10 (PB2012-102404).
- MCEER-10-0003 "Integration of Seismic Protection Systems in Performance-Based Seismic Design of Woodframed Structures," by J.K. Shinde and M.D. Symans, 6/18/10 (PB2012-102405).
- MCEER-10-0004 "Modeling and Seismic Evaluation of Nonstructural Components: Testing Frame for Experimental Evaluation of Suspended Ceiling Systems," by A.M. Reinhorn, K.P. Ryu and G. Maddaloni, 6/30/10 (PB2012-102406).
- MCEER-10-0005 "Analytical Development and Experimental Validation of a Structural-Fuse Bridge Pier Concept," by S. El-Bahey and M. Bruneau, 10/1/10 (PB2012-102407).
- MCEER-10-0006 "A Framework for Defining and Measuring Resilience at the Community Scale: The PEOPLES Resilience Framework," by C.S. Renschler, A.E. Frazier, L.A. Arendt, G.P. Cimellaro, A.M. Reinhorn and M. Bruneau, 10/8/10 (PB2012-102408).
- MCEER-10-0007 "Impact of Horizontal Boundary Elements Design on Seismic Behavior of Steel Plate Shear Walls," by R. Purba and M. Bruneau, 11/14/10 (PB2012-102409).
- MCEER-10-0008 "Seismic Testing of a Full-Scale Mid-Rise Building: The NEESWood Capstone Test," by S. Pei, J.W. van de Lindt, S.E. Pryor, H. Shimizu, H. Isoda and D.R. Rammer, 12/1/10 (PB2012-102410).
- MCEER-10-0009 "Modeling the Effects of Detonations of High Explosives to Inform Blast-Resistant Design," by P. Sherkar, A.S. Whittaker and A.J. Aref, 12/1/10 (PB2012-102411).
- MCEER-10-0010 "L'Aquila Earthquake of April 6, 2009 in Italy: Rebuilding a Resilient City to Withstand Multiple Hazards," by G.P. Cimellaro, I.P. Christovasilis, A.M. Reinhorn, A. De Stefano and T. Kirova, 12/29/10.
- MCEER-11-0001 "Numerical and Experimental Investigation of the Seismic Response of Light-Frame Wood Structures," by I.P. Christovasilis and A. Filiatrault, 8/8/11 (PB2012-102412).
- MCEER-11-0002 "Seismic Design and Analysis of a Precast Segmental Concrete Bridge Model," by M. Anagnostopoulou, A. Filiatrault and A. Aref, 9/15/11.
- MCEER-11-0003 "Proceedings of the Workshop on Improving Earthquake Response of Substation Equipment," Edited by A.M. Reinhorn, 9/19/11 (PB2012-102413).
- MCEER-11-0004 "LRFD-Based Analysis and Design Procedures for Bridge Bearings and Seismic Isolators," by M.C. Constantinou, I. Kalpakidis, A. Filiatrault and R.A. Ecker Lay, 9/26/11.

- MCEER-11-0005 “Experimental Seismic Evaluation, Model Parameterization, and Effects of Cold-Formed Steel-Framed Gypsum Partition Walls on the Seismic Performance of an Essential Facility,” by R. Davies, R. Retamales, G. Mosqueda and A. Filiatrault, 10/12/11.
- MCEER-11-0006 “Modeling and Seismic Performance Evaluation of High Voltage Transformers and Bushings,” by A.M. Reinhorn, K. Oikonomou, H. Roh, A. Schiff and L. Kempner, Jr., 10/3/11.
- MCEER-11-0007 “Extreme Load Combinations: A Survey of State Bridge Engineers,” by G.C. Lee, Z. Liang, J.J. Shen and J.S. O’Connor, 10/14/11.
- MCEER-12-0001 “Simplified Analysis Procedures in Support of Performance Based Seismic Design,” by Y.N. Huang and A.S. Whittaker.
- MCEER-12-0002 “Seismic Protection of Electrical Transformer Bushing Systems by Stiffening Techniques,” by M. Koliou, A. Filiatrault, A.M. Reinhorn and N. Oliveto, 6/1/12.
- MCEER-12-0003 “Post-Earthquake Bridge Inspection Guidelines,” by J.S. O’Connor and S. Alampalli, 6/8/12.
- MCEER-12-0004 “Integrated Design Methodology for Isolated Floor Systems in Single-Degree-of-Freedom Structural Fuse Systems,” by S. Cui, M. Bruneau and M.C. Constantinou, 6/13/12.
- MCEER-12-0005 “Characterizing the Rotational Components of Earthquake Ground Motion,” by D. Basu, A.S. Whittaker and M.C. Constantinou, 6/15/12.
- MCEER-12-0006 “Bayesian Fragility for Nonstructural Systems,” by C.H. Lee and M.D. Grigoriu, 9/12/12.
- MCEER-12-0007 “A Numerical Model for Capturing the In-Plane Seismic Response of Interior Metal Stud Partition Walls,” by R.L. Wood and T.C. Hutchinson, 9/12/12.
- MCEER-12-0008 “Assessment of Floor Accelerations in Yielding Buildings,” by J.D. Wieser, G. Pekcan, A.E. Zaghi, A.M. Itani and E. Maragakis, 10/5/12.
- MCEER-13-0001 “Experimental Seismic Study of Pressurized Fire Sprinkler Piping Systems,” by Y. Tian, A. Filiatrault and G. Mosqueda, 4/8/13.
- MCEER-13-0002 “Enhancing Resource Coordination for Multi-Modal Evacuation Planning,” by D.B. Hess, B.W. Conley and C.M. Farrell, 2/8/13.
- MCEER-13-0003 “Seismic Response of Base Isolated Buildings Considering Pounding to Moat Walls,” by A. Masroor and G. Mosqueda, 2/26/13.
- MCEER-13-0004 “Seismic Response Control of Structures Using a Novel Adaptive Passive Negative Stiffness Device,” by D.T.R. Pasala, A.A. Sarlis, S. Nagarajaiah, A.M. Reinhorn, M.C. Constantinou and D.P. Taylor, 6/10/13.
- MCEER-13-0005 “Negative Stiffness Device for Seismic Protection of Structures,” by A.A. Sarlis, D.T.R. Pasala, M.C. Constantinou, A.M. Reinhorn, S. Nagarajaiah and D.P. Taylor, 6/12/13.
- MCEER-13-0006 “Emilia Earthquake of May 20, 2012 in Northern Italy: Rebuilding a Resilient Community to Withstand Multiple Hazards,” by G.P. Cimellaro, M. Chiriatti, A.M. Reinhorn and L. Tirca, June 30, 2013.
- MCEER-13-0007 “Precast Concrete Segmental Components and Systems for Accelerated Bridge Construction in Seismic Regions,” by A.J. Aref, G.C. Lee, Y.C. Ou and P. Sideris, with contributions from K.C. Chang, S. Chen, A. Filiatrault and Y. Zhou, June 13, 2013.
- MCEER-13-0008 “A Study of U.S. Bridge Failures (1980-2012),” by G.C. Lee, S.B. Mohan, C. Huang and B.N. Fard, June 15, 2013.
- MCEER-13-0009 “Development of a Database Framework for Modeling Damaged Bridges,” by G.C. Lee, J.C. Qi and C. Huang, June 16, 2013.

- MCEER-13-0010 “Model of Triple Friction Pendulum Bearing for General Geometric and Frictional Parameters and for Uplift Conditions,” by A.A. Sarlis and M.C. Constantinou, July 1, 2013.
- MCEER-13-0011 “Shake Table Testing of Triple Friction Pendulum Isolators under Extreme Conditions,” by A.A. Sarlis, M.C. Constantinou and A.M. Reinhorn, July 2, 2013.
- MCEER-13-0012 “Theoretical Framework for the Development of MH-LRFD,” by G.C. Lee (coordinating author), H.A. Capers, Jr., C. Huang, J.M. Kulicki, Z. Liang, T. Murphy, J.J.D. Shen, M. Shinozuka and P.W.H. Yen, July 31, 2013.
- MCEER-13-0013 “Seismic Protection of Highway Bridges with Negative Stiffness Devices,” by N.K.A. Attary, M.D. Symans, S. Nagarajaiah, A.M. Reinhorn, M.C. Constantinou, A.A. Sarlis, D.T.R. Pasala, and D.P. Taylor, September 3, 2014.
- MCEER-14-0001 “Simplified Seismic Collapse Capacity-Based Evaluation and Design of Frame Buildings with and without Supplemental Damping Systems,” by M. Hamidia, A. Filiatrault, and A. Aref, May 19, 2014.
- MCEER-14-0002 “Comprehensive Analytical Seismic Fragility of Fire Sprinkler Piping Systems,” by Siavash Soroushian, Emmanuel “Manos” Maragakis, Arash E. Zaghi, Alicia Echevarria, Yuan Tian and Andre Filiatrault, August 26, 2014.
- MCEER-14-0003 “Hybrid Simulation of the Seismic Response of a Steel Moment Frame Building Structure through Collapse,” by M. Del Carpio Ramos, G. Mosqueda and D.G. Lignos, October 30, 2014.
- MCEER-14-0005 “Seismic Performance of Steel Plate Shear Walls Considering Various Design Approaches,” by R. Purba and M. Bruneau, October 31, 2014.
- MCEER-14-0006 “Air-Blast Effects on Civil Structures,” by Jinwon Shin, Andrew S. Whittaker, Amjad J. Aref and David Cormie, October 30, 2014.
- MCEER-14-0007 “Seismic Performance Evaluation of Precast Girders with Field-Cast Ultra High Performance Concrete (UHPC) Connections,” by G.C. Lee, C. Huang, J. Song, and J. S. O’Connor, July 31, 2014.
- MCEER-14-0008 “Post-Earthquake Fire Resistance of Ductile Concrete-Filled Double-Skin Tube Columns,” by Reza Imani, Gilberto Mosqueda and Michel Bruneau, December 1, 2014.



EARTHQUAKE ENGINEERING TO EXTREME EVENTS

University at Buffalo, The State University of New York

133A Ketter Hall ■ Buffalo, New York 14260-4300

Phone: (716) 645-3391 ■ Fax: (716) 645-3399

Email: mceer@buffalo.edu ■ Web: <http://mceer.buffalo.edu>



University at Buffalo The State University of New York

ISSN 1520-295X